UNIVERSITY OF SOUTHAMPTON

ROTATING GRAVITY CURRENT AND CHANNEL FLOWS

by

Joan Rosemary MARTIN
(*nee de Lacey*)

A dissertation submitted for the degree of

Doctor of Philosophy

in the

School of Ocean and Earth Science

September 1999

UNIVERSITY OF SOUTHAMPTON

ABSTRACT

FACULTY OF SCIENCE

SCHOOL OF OCEAN AND EARTH SCIENCE

Doctor of Philosophy

ROTATING GRAVITY CURRENT AND CHANNEL FLOWS

by Joan Rosemary Martin

A theoretical and laboratory investigation of rotating gravity currents and channel flows is presented. The study is applicable to buoyancy driven flows through straits, mid ocean ridge valleys and fracture zones, and intermittent gravity currents. In the theoretical study two extensions are achieved to the energy conserving theory of Hacker (1996). Hacker considered three flow geometries, case A - weak rotation, case B - intermediate rotation and case C - strong rotation. Firstly, the theory is extended to include dissipation. This is achieved in a similar manner to that used by Benjamin (1968) to include energy loss in the non-rotating gravity current theory. The governing equations and numerical solutions for the three flow geometries are presented. For shallow currents the energy loss theory predicts that the Froude number tends to $2^{\frac{1}{2}}$ irrespective of the rotation rate. For deeper currents the Froude number increases with rotation. The second extension to the energy conserving theory is the inclusion of an upstream potential vorticity boundary condition in the current. The approach taken is based on a method used by van Heijst (1985). The governing equations and preliminary solutions for each case are derived. The potential vorticity theory provides an insight into the circulation that develops within the current. However, varying the pre-set potential vorticity in the source region does not appear to have a significant effect upon the front speed and the other principle variables.

In the laboratory investigation the effects of fractional depth and rotation rate on the velocity and other parameters which characterise the flow are quantified. For weakly rotating currents, $w/R < 0.7$ (where w is the width of the channel and R the Rossby radius), the measured front speed is in fair agreement with the energy loss and potential vorticity theories. At higher rotation rates the front speed is lower than predicted. However, the theories assume that the fluid is inviscid, the no-slip condition is not applied at the boundary, potential vorticity is conserved and that energy loss is uniform across the channel. The theory does not include factors such as the enhanced vertical mixing and the development of a geostrophic eddy. These are associated with strong rotation rates and could account for the divergence of the experimental results from the theory.

PREFACE

This thesis is the result of my own work and it is not the outcome of work done in collaboration. No part has been submitted for a degree or similar qualification at any other university.

However, I do wish to acknowledge the contribution by my PhD Supervisor, Dr. Gregory Lane-Serff, who proof read the manuscript and also wrote a Fortran programme to give an indication of the possible solutions to the energy conserving theory with prescribed potential vorticity, as discussed in § 5.2. I would also like to thank, Dr. David Smeed for his guidance particularly with the theoretical aspect of my research and for always finding time to discuss and advise me regarding the theory. Also, Prof. S. Thorpe for his helpful suggestions regarding the laboratory investigation particularly during the initial stage of my research. Finally I wish to thank my family; my father for all the physics books he bought me; my mother for keeping my home in order enabling me to study; to my dear, patient husband David for all his love and support and my sons Christopher and Andrew for the interest they have always shown in my work.

This research was funded by the Natural Environmental Research Council.

CONTENTS

To my boys
Christopher, Andrew
& David
with all my love

*

CHAPTER 1

Introduction

When a dense fluid is released in the absence of background rotation it spreads radially until it reaches a boundary which prevents further spreading. In the presence of background rotation the fluid spreads laterally and motions normal to the axis of rotation induce Coriolis forces. The Coriolis force is an apparent force that acts normal to the direction of motion and causes a deflection to the right in the northern hemisphere and to the left in the southern hemisphere. Eventually in the absence of dissipation a state of equilibrium will develop where the buoyancy and Coriolis forces balance, preventing further spreading, known as a geostrophic eddy. Plate 1 shows a geostrophic eddy formed by the axial release of a lighter fluid on to a denser fluid rotating at $f = 1$, where f is twice the angular frequency of rotation. If a boundary is introduced, Coriolis forces normal to the border are removed, since flow across the boundary is impossible. A jet forms parallel to the boundary and is held against it by Coriolis forces normal to the direction of flow. The width to which the flow adjusts is known as the Rossby radius of deformation, $R = (g'H)^{\frac{1}{2}}/f$, where g' is the reduced gravity and H the depth (Rossby 1938).

1.1 Applications

In the atmosphere mountain ranges form these boundaries. The occurrence of topographical trapped gravity currents are common along the west coast of North America and against the double barrier of the Coastal and Sierra Nevada Mountains. Other flows with gravity current characteristics influenced by the Coriolis force include the Southerly Buster, a cold wind which runs parallel to the Australian Alps in eastern Australia (Couquhoun, 1985), and sea-breezes in northern Australia, (Physick 1985). The passage of atmospheric phenomena are accompanied by changes in wind, temperature and pressure, which are monitored using instrument towers, balloons, lidar, radar or echo sounders. These sudden meteorological changes have important implications for aviation and shipping

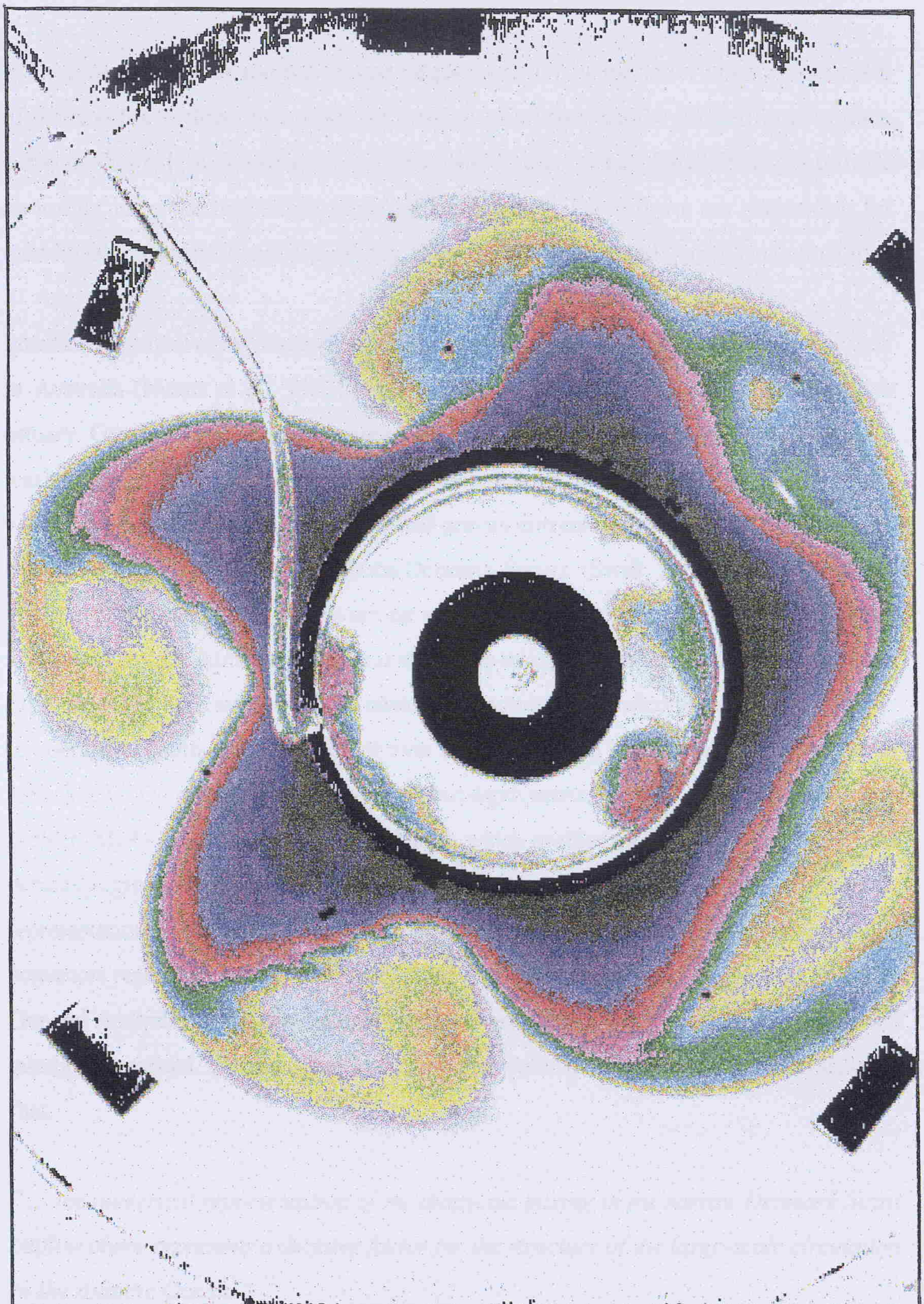

Plate 1 - Geostrophic eddy (f=1). Light fluid is supplied by a central ring source. Initially the fluid moves outwards due to the buoyancy force. An axisymmetric flow develops in order to conserve angular momentum. The resulting Coriolis force balances the radial buoyancy force enabling equilibrium to be reached. The image was taken after several rotation periods when the current had increased in width and wave like disturbances had appeared. (GEFD Summer School, 1996.)

in coastal waters.

In the ocean, coastlines and sub-marine ridges constrain the motion. Numerous examples of density-driven flows influenced by rotation exist, they can be divided in to surface currents, flows through estuaries, overflows and fracture zones. Satellite images provide an insight in to the instabilities of boundary currents. These flows are responsible for meridional transport of heat and salinity. They are large scale and generally continuous.

Intermittent gravity currents are often observed in the estuarine environment. Spencer Gulf in Australia (Nunes et al., 1987) is a particularly well documented case of an inverse estuary. Gravity currents develop here due to the anomalous tidal cycle, which causes a marked reduction in turbulence at fortnightly intervals and is further enhanced by light winds. Spencer Gulf also exhibits a seasonal gravity current (Bowers et al., 1987). Other overflows include the flow through the Denmark Straits (Swift, 1980) and the Straits of Gibraltar (Price et al, 1993), where strong internal tides cause variations in the outflow on a weekly timescale. Atmospheric storms also cause strong fluctuations and pulsations in the flow, however little interannual variability is observed. A detailed picture of the salinity, temperature, depth, and dynamics of over flows is built up using ship borne instruments including: CTD - conductivity, temperature and depth instrument; XCP - extendible current profiler; XDP - extendible dissipation profiler, which profiles the turbulence intensity. It is generally agreed that the improvement of ocean circulation models is dependent on the true representation of the transport and seawater properties of major overflows. Boning in his convenors report for the open session of ocean circulation, European Geophysical Society's General Assembly 1997, highlighted overflows as a key physical process for which open questions remained. In referring to intercomparison studies of ocean models he concluded that,

" ... the numerical representation of the diapycnic mixing in the narrow Denmark Strait outflow plume represents a decisive factor for the structure of the large-scale circulation in the Atlantic Ocean. "

The study of rotating gravity currents has wider applications, benefiting other scientific fields, such as, biology and marine geology. For instance, it is conjectured that the life cycle of the krill is dependent on the transport of its larvae from the Weddell Sea, westward to their nursery grounds, by the South Shetland Islands overflow (Whitehead, 1989). Fishing grounds are known to be affected by the passage of gravity currents, for example, the Kyucho Current which propagates around bays in the Sea of Japan, causes havoc to the fishing grounds (Yamagata, 1980). In the atmosphere sea breezes are responsible for transporting insect pests and pollution inland. Geologically a greater understanding of sediment transport and deposition both now and in the past may be obtained. Further applications are discussed in chapter 2.

1.2 Basic features

The anatomy of the non-rotating gravity current was fully described by Simpson (1987). In plate 2 images taken from the present study are used to illustrate the basic features of non-rotating and rotating gravity currents. The plan view is the upper part and the side view is the lower part of each image.

1.2.1 Non-rotating gravity current

The non-rotating gravity current when viewed from the side has a well defined head and nose (plate 2a). For bottom currents the nose is slightly raised above the tank floor due to bottom friction. Surface currents do not display this feature if the surface is free from contaminants. The following flow behind the head is shallower. This is known as the tail. Immediately behind the head, Kelvin-Helmholtz billows are seen to peel off the outer surface. This is an instability that arises when two fluids move relative to one another. The profile of the current may be modified by viscous effects, fractional depth or an opposing flow in the ambient fluid. In the plan view, the leading edge is broken into a series of lobes and clefts. As the current advances along the tank the lobes swell and engulf or are engulfed by other lobes, producing a shifting pattern. The lobes and clefts are caused by lighter fluid being over run by the denser fluid. The denser fluid is in a position where it is gravitationally unstable and a circulation is set up. Experiments by Simpson (1972) confirm

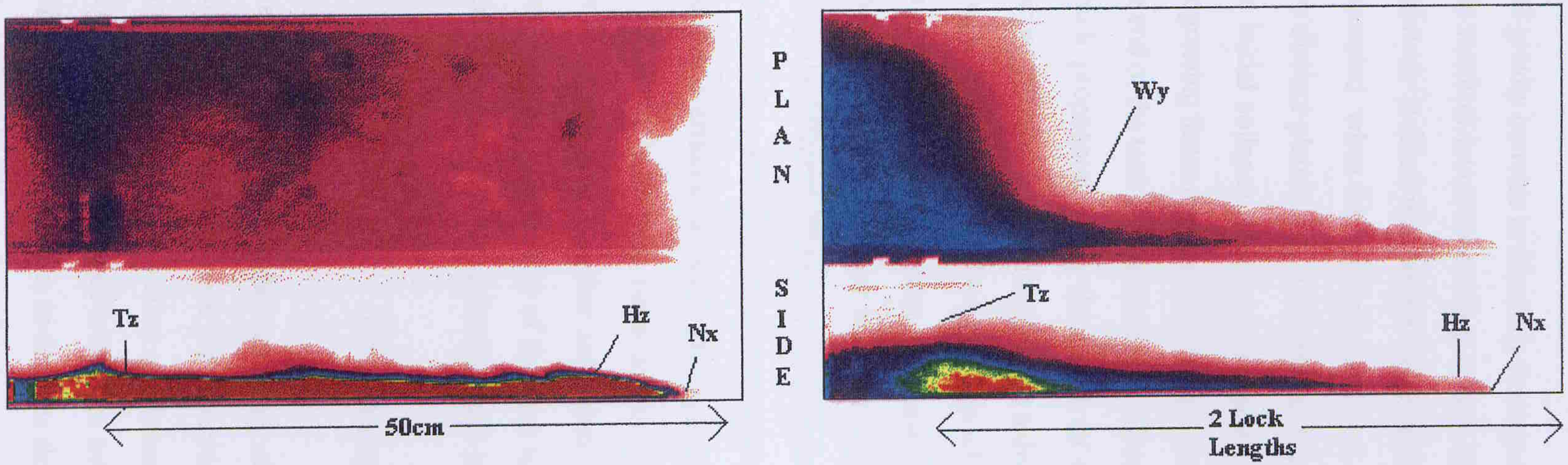

NON-ROTATING GRAVITY CURRENT

ROTATING GRAVITY CURRENT

PLATE 2. Anatomy of a gravity current annotated with the length scales measured in the laboratory investigation, where

T_z	depth of the tail measured at the lock opening
H_z	depth of the gravity current head
W_y	width of the gravity current
N_x	distance the current has progressed from the lock opening

The intensity of light passing through the fluid is illustrated by a false colour palette applied to each image. The intensity range is from 0 to 255 where 0 is saturation level and corresponds to the sequence of colours red, yellow, green, blue, magenta and white.

The initial conditions for (a) and (b) are $h_0/H_0 \sim 0.5$, $Re(h_0) > 3000$.
(a) Non-rotating gravity current ($w/R(h_0) = 0$) showing the distinct head, behind which is the shallower tail. Note the Kelvin-Helmholtz billows in the side view and the 'lobe and cleft' structure in the plan view.
(b) Rotating gravity current (strong rotation, $w/R(h_0) = 2.99$). The current is deflected towards the right hand wall. It is held against the boundary by the Coriolis force normal to the direction of the flow. The head has decreased significantly in both width and depth. Kelvin-Helmholtz billows are again observed. The depth of the current at the source region has increased and a geostrophic eddy has developed.

this for bottom currents.

The gravity currents in this study were generated using the lock-release method. Basically, this method involves dividing a tank into two reservoirs by a removable barrier. One reservoir is filled with saline water and the other with fresh water. A gravity current is generated when the barrier is removed. As a gravity current progresses along a channel two distinct phases may be identified (Simpson, 1972). After the removal of the gate and the initial collapse the two flows propagate in opposite directions, with the upper fluid progressing faster than the lower. This is known as the constant speed phase. On reaching the end of the tank the lighter fluid reflects from the end wall and forms a hydraulic jump, which propagates along the length of the denser gravity current. The hydraulic jump reaches the head of the current within a distance equivalent to 10 lock lengths, where a lock length is the length of the lock from which the saline fluid originates. This results in the constant speed phase ending and phase 2 where the speed of the current decreases with $t^{-\frac{1}{3}}$ begins. If the experiment involves shallow gravity currents in deep water, the situation is slightly different. Phase 1 (the constant speed stage) is observed, but in this case at the fluid interface a long wave of depression propagates. This reflects off the end wall and in due time overtakes the head. This again results in a reduction in velocity, decreasing with $t^{-\frac{1}{2}}$. Eventually in both cases a third phase is reached where viscous effects become dominant, causing a further reduction in velocity. In the present study phase 2 is not observed because the ratio of the tank to the lock length is only 3:1. The transition from inertial to viscous currents is discussed in chapter 7.

1.2.2 Rotating gravity currents

The characteristics of rotating gravity currents (plate 2b) are dependent on the level of rotation. The head and nose are observed but these are modified. The head decreases in depth and width as the rotation rate increases. Behind the head Kelvin-Helmholtz billows are observed on all surfaces in contact with the ambient fluid. The depth at the right hand wall increases with rotation, as does the slope of the interface across stream. The boundary between the head and the tail is less distinct than that observed for non-rotating gravity currents, because it is often obscured by billows. At high rotation rates the current has a wedge like appearance in the side view and an anticyclonic gyre often develops near the opening.

The two distinct phases identified for non-rotating gravity currents are again observed. After the initial collapse the fluid adjusts to a constant velocity phase. However, slight oscillations in the velocity are observed. Griffiths (1983) attributed this oscillation to the growth and decay of the head of the current. The second decelerating phase is also apparent. This was quantified by Griffiths (1983), who established that the velocity of the head decreased exponentially with time. He proposed that the decay in the velocity was dependent on the rotation rate, a Froude number based on lock parameters and, in certain cases, Ekman friction. Only the constant velocity phase is observed in this study.

1.2.3 Basic scales

Plate 2 is annotated with the basic features of the non-rotating and rotating gravity currents measured in this study. The subscripts refer to the plane in which the measurements were taken.

H_z	head
T_z	tail measured at the opening
W_y	width of the rotating current
w	width of the tank
H_0	total depth of fluid
h_0	inflow depth
U	propagation speed of nose

To enable measurements taken in the laboratory to be scaled up to the real world non-dimensionalised numbers are calculated which define the flow. These are written as a function of the parameter on which they are based to ease understanding in the text.

Non-dimensional numbers dependent on pre-set parameters

Front speed	$c(h_0) = U/(g'h_0)^{\frac{1}{2}}$
Rossby radius	$R(h_0) = (g'h_0)^{\frac{1}{2}}/f$
Rotation rate	$W = w/R(h_0)$
Reynolds number	$Re(h_0) = ((g'h_0)^{\frac{1}{2}}\, h_0)/\nu$
Fractional depth	$T_Z/\, h_0$

N.b. The non-dimensional numbers above may also be expressed as a function of H_0.

Non-dimensional numbers dependent on measured parameters

Froude number	$Fr(T_z) = U/(g'T_z)^{\frac{1}{2}}$
Rossby radius	$R(T_z) = (g'T_z)^{\frac{1}{2}}/f$
Reynolds number	$Re(H_z) = ((UH_z)/\nu$
Fractional depth	T_z/H_0

1.3 Aims and thesis outline

So far I have briefly considered the diversity of gravity currents in the environment and their anatomy, (expanded on in chapter 2) but what of the attempts to understand the structure of the flow, the interplay of the various forces and their mathematical representation? The foremost objective of this thesis is to extend the energy conserving theory of rotating gravity currents (Hacker 1996) to include dissipation by quantifying the effect of fractional depth and rotation rate on the velocity and other parameters which characterise the flow. As a first step it was instructive to consider how this is achieved in the non-rotating theory of Benjamin (1968). Next, an understanding of how Hacker derived the energy conserving solution is necessary to decide where it is appropriate to introduce fractional depth. A summary of Benjamin's and Hacker's theories is provided in chapter 3. In chapter 4 energy loss is incorporated into the rotating theory and in chapter 5 the effect of the source conditions, i.e. the prescribed potential vorticity, is also included. In chapters 6 and 7 the method and results of the laboratory investigation are presented. The concluding chapter compares the theoretical predictions and the supporting experimental investigation and suggestions are made for further work.

CHAPTER 2

Environmental Applications

2.1 Introduction

In chapter 1 the effects of rotation upon a fluid released into a rotating system in the laboratory was briefly discussed. Furthermore the introduction of a barrier was shown to generate a jet-like current constrained laterally against the barrier by the Coriolis force. This suggests that if suitable conditions were to occur in the atmosphere or ocean close to a barrier such as a mountain range or a coastline, then an intrusion could develop. Indeed, on examining the literature one finds that there are many examples of flows which could be classified as rotating gravity currents. The aim of this chapter is to compare the characteristics they possess with those currents generated in the laboratory, the arguments for and against classifying them as gravity currents, where they occur, what devices are employed to quantify them and an example of a case study for each.

2.2 Atmospheric Gravity Currents

On researching the subject of atmospheric gravity currents I came across a variety of flows which could be possible candidates for the term gravity current. Before proceeding I shall discuss the nomenclature used in conjunction with these flows as defined by Egger et al, 1991. Firstly, orographic adjustment refers to the adjustment of a large scale flow to a barrier. An orographic jet is a cold front whose nose propagates parallel to a mountain and is confined to within a few kilometers of the mountain range. A particularly well researched example is the Southerly buster which occurs along the southern coast of New South Wales in eastern Australia. Colquhoun et al (1985) describes the arrival of the southerly buster (or burster) which is marked by a sudden increase in wind speed to 15ms^{-1} sometimes exceeding 37ms^{-1} and at the same time a drop in temperature of 10 to 15°C within a few minutes.

Cold air surges may also undergo orographic adjustment, however the horizontal scale associated with these is considerable with widths of up to several thousand kilometers, examples include the cold surges constrained by the Tibetian Plateau (Orlanski, 1983), Andes (Rutlant, 1981) and the Rocky mountains (Lilly, 1981; Shipiro et al, 1985). Along the West coast of North America long shore surges marked by coastal stratus tongues are observed frequently. Mass et al, (1987) describes how the arrival of these events are marked by changes in wind speed, pressure and temperature which occur on a timescale of less than one hour. Similar phenomena are experienced along the coast of South Africa where the topography consists of an abrupt rise from the coastal plain to the interior plateau.

With the aid of surface and upper air stations, and the comparison of measurements from ships, buoys and coastal stations as well as satellite imagery, it is possible to obtain detailed measurements of the extent of these atmospheric flows. The vertical structure can also be discerned using radiosonde measurements. An event for which there are convincing GOES satellite images is the long shore surge caused by synoptic scale changes which occurred along the West coast of North America between 15 - 17 May 1985, see figure 2.1. Mass describes the propagation of the surge thus -

"Moving up the Oregon coast, the surge brought not only a change in wind direction but progressively larger and more abrupt transitions in wind speed, pressure and temperature. Maximum winds increased from 10 ms^{-1} in southern Oregon to 17 ms^{-1} on the northern border, temperature drops varied from 6°C h^{-1} in southern Oregon to 16°C h^{-1} to the north, and pressure rises varied from 0.2 mb h^{-1} to the south to 2 mb h^{-1} in the north. It is well known (e.g., Charba, 1974; Griffiths, 1986) that the forward leading edge of a gravity current can steepen in time. By 00 UTC 17 May (when the surge was just south of Astoria, Oregon) the southerly transition involved a radical and abrupt change of air mass from warm, subsiding continental air to cool, stratus-filled marine flow."

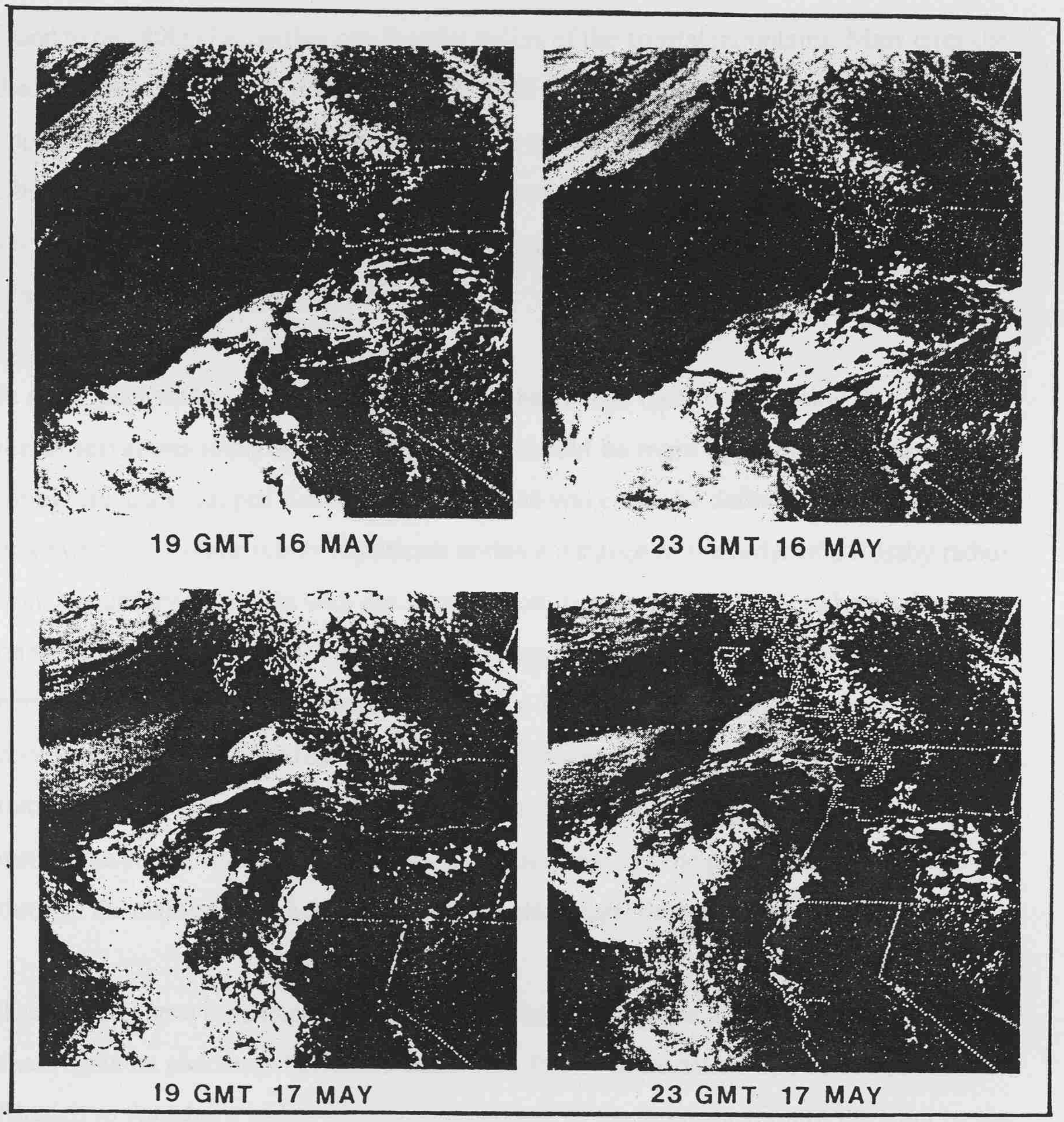

19 GMT 16 MAY

23 GMT 16 MAY

19 GMT 17 MAY

23 GMT 17 MAY

FIGURE 2.1. Topographically trapped gravity current along the western coast of the United States and Canada, imaged using GOES visible satellite between 16-17th May, 1985. This phenomenon is caused by a sudden change in wind direction from northerlies (0 - 10 ms^{-1}) to southerlies (15 ms^{-1}), accompanied by a temperature drop > 10°C and a sudden rise in pressure. The coastal tongue is shallow vertically and its width is within one Rossby radius (170 km). (From Mass et al, 1987)

Mass puts forward a number of arguments for classing the surge as a gravity current. He calculated that the speed closely resembled that of a gravity current based on the theoretical predictions of Seitter and Muench (1985). The width of the southerlies and stratus was found to be 180km i.e., within one Rossby radius of the coastal mountains. Mass cites the theoretical work of Baines, 1980; Griffiths, 1986 and Griffiths and Hopfinger, 1983 which implied that a topographically trapped gravity current should be within this spatial scale. Observations of the vertical structure of the phenomenon showed that the vertical scale was very shallow, constrained to the lower troposphere to below 850 mb, which again is a characteristic of a gravity current.

In many case studies of similar atmospheric phenomena there is discussion as to whether the observations imply a gravity current or should be more appropriately classed as a topographically trapped Kelvin wave. A Kelvin wave may be defined as a unidirectional wave whose amplitude is only significant within a distance of the order of a Rossby radius from a boundary. It travels with the boundary on its right in the Northern hemisphere and on the left in the Southern hemisphere. To distinguish between a Kelvin wave and a gravity current, it is important to consider whether two layers exist. A strong inversion capping a cool marine layer, associated with wave-like disturbances would imply a topographically trapped Kelvin wave. However, if ahead of the surge a two layer system does not exist and instead the vertical structure is created as a consequence of the propagation of the cool air through the uniform subsiding air, then this would suggest the presence of a gravity current.

These phenomena have important implications for shipping and aviation. Indeed the 'papal front' gets its nickname because a helicopter flight due to take Pope John Paul II from Munich to Augsburg had to be canceled because of the intensification of the front by the Alps.

2.3 Estuarine Gravity Currents

Certain conditions are necessary for the development of gravity currents within the estuarine environment. The most common type is known as a 'salt wedge'. These occur in estuaries which are generally narrow relative to their water depth and receive a high volume of fresh water runoff from rivers. They are also associated with a weak tidal cycle that enables stratification to develop. The surface currents tend to be turbulent due to the large input of fresh water, whilst the flow in the saline water is minimal. This exerts a shear on the interface causing internal waves and entrainment of saline water into the turbulent surface flow further increasing its volume. Echo sounding surveys (Geyer, 1983), show that they exhibit many of the features associated with gravity currents including the characteristic 'head'. During the flood stage of the tide the fresh water may be forced back into the estuary. Often the interface between the two fluids on the surface is marked by debris and colour changes, (Simpson & Nunes, 1981).

A further example of a gravity current which occurs in the estuarine environment is that which occurs in shallow estuaries where the local climatic conditions cause evaporation in excess of that lost through precipitation and river run off. This combined with weak tidal currents produces what is known as an inverse estuary. Well documented examples include Spencer Gulf (Bowers & Lennon, 1987) and Gulf St. Vincent (de Silva Samarasinghe, 1987) both situated on the South Australian Coast. Here the lunar and semi-diurnal tidal constituents are equal, which results in a large spring-neap tidal modulation. This causes a considerable reduction in turbulence and mixing on a fortnightly cycle, causing the development of stratification i.e. a baroclinic regime. The switch to stratified conditions occurs abruptly within one hour and lasts for many days, enabling the Earth's rotation to cause the development of a single large scale cyclonic gyre after an inertial period has passed. In each arm of the flow the gyre achieves a velocity of approximately $0.2 \mathrm{ms}^{-1}$. This is considerably greater than the annual mean circulation speed of $0.05 \mathrm{ms}^{-1}$, (Bullock, 1975; Nunes & Lennon, 1986).

At the mouth of the Gulf during the summer months the density contrast between the Gulf and Shelf water is offset by the higher temperatures within the Gulf. However during the autumn and winter the Gulf waters cool and an outflow of saline water forms along the sea floor whilst the less saline shelf waters flow into the Gulf. The Coriolis force causes the interface to be inclined with respect to the horizontal. The outflow continues for 150km. As it travels across the sloping South Australian Shelf it also falls vertically 150m. It is known to local oceanographers as 'Bonaparte's tongue'. Lennon et al, (1987), present the results of a survey carried out by the Royal Australian Navy Vessel, *RV HMAS Cook*. The extent of the survey was from the headwaters of the Gulf to beyond the shelf break. The saline water was found to emerge from the mouth of the Gulf on the eastern side. The salinity and density contours in figure 2.2, clearly show the path of the current as it crosses the end of Investigator Strait and then flows along Kangaroo Island and finally off the shelf edge, close to Du Conedic Canyon. The salinity contours imply a depth of 20- 40m. Its width was found to vary between 50km at the Gulf mouth to 20km at Cape Borda. The effect of the earth's rotation should cause the current to turn into Investigator Strait. Lennon attributes this divergence to the effect of friction, suggesting the since the flow is relatively thin it feels the effect of bottom friction to a greater extent causing it to flow at a steeper angle across depth contours. Lennon estimates the speed of the current as 0.1 ms^{-1} using the Chezy equation. His estimates of continuity of salt and water suggest that the current would have to continue for three months to restore the levels of salt to that prior to the high evaporation rates of the summer. Lennon hypothesizes that the narrowing of the current at Cape Borda could be due to the effects of the anomalous tidal cycle in the Gulf causing pulsations 150km apart.

The intermittent gravity currents which develop within the Gulf and seasonally at its mouth are responsible for the dispersion and exchange of properties between the Gulf and the Shelf waters.

2.4 Overflows

An example of an environmental gravity current which lends itself to the study of gravity currents in the laboratory is that of the overflow or cataract. These dense flows occur at great depth across sills linking ocean basins and their importance in the meridional transfer of heat and salinity should not be underestimated. The Atlantic Ocean boasts several examples of significant overflows including the Iceland Faroe overflow , the flows through the Denmark Strait, the Straits of Gibraltar, and in the Southern hemisphere the Shetland Islands and Filchner Shelf overflows, as well as the flow which occurs between the

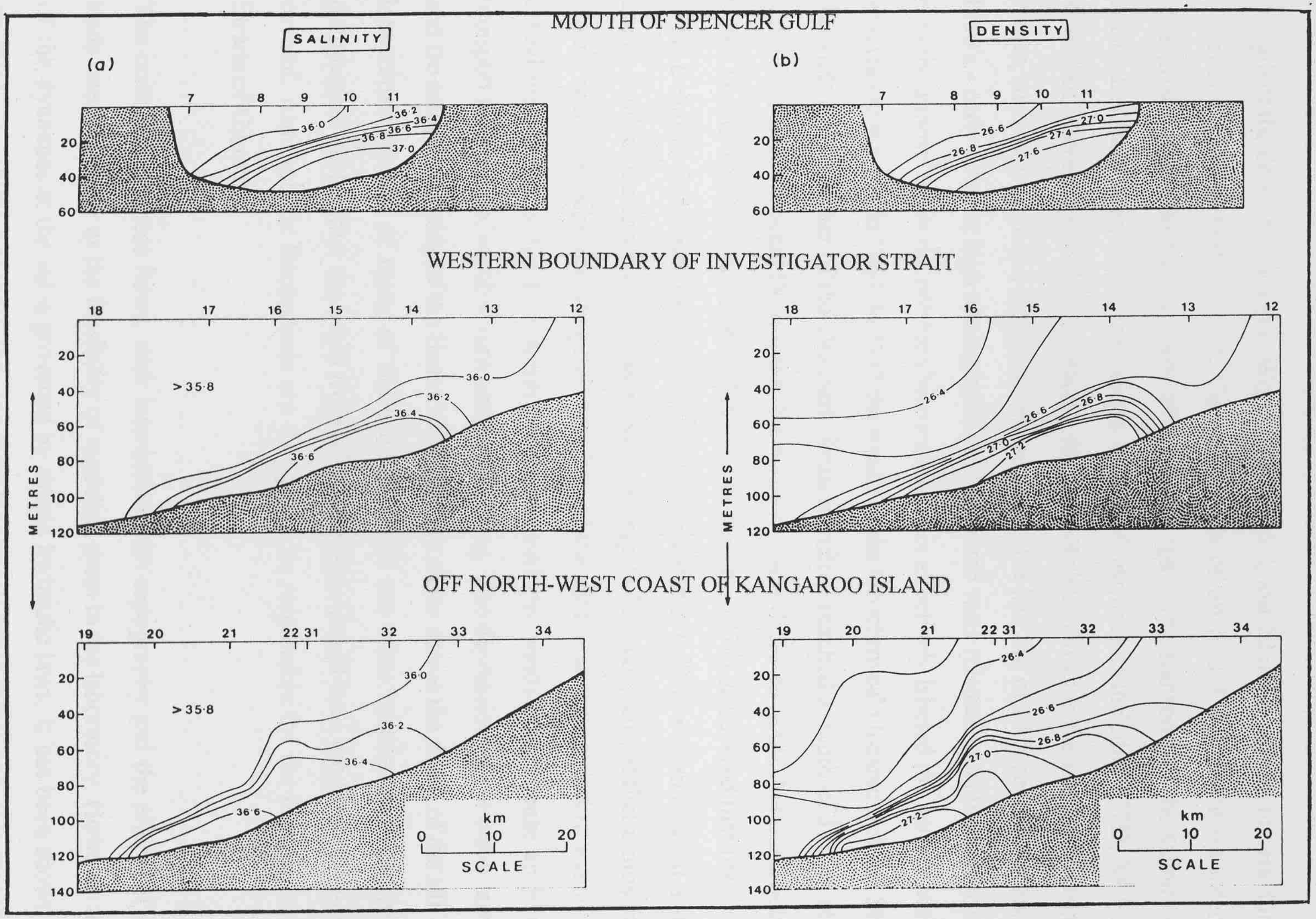

FIGURE 2.2. Spencer Gulf outflow (a) salinity and (b) density section. The gravity current is clearly defined and maintains its density and salinity contrast over the 100km covered by the survey. Width ~ 20km, depth ~ 20m, mean current speed ~ 0.1ms^{-1}, Rossby radius ~ 1km and Reynold's number ~ 10^{6}. (From Bowers et al, 1987)

Brazilian and North Atlantic basin across the Ceara Abyssal Plain.

Measurements of these flows is limited by the depths at which they occur and often the strength of the flows, for example, Worthington (1967), lost 20 of 30 current meters during a survey of the Denmark Strait. Current speeds of up to 1.4 ms^{-1} were recorded in comparison to the surface currents of 0.1 to 0.5 ms^{-1}. The transport of the salinity and density has since been quantified using a variety of instruments including CTD, XCP and XDP. An interesting method of tracing the path of these flows is the use of radioactive tracers, such as, tritium (an isotope of hydrogen with a half life of 12.5 years). During the 1950's - early 60's the high atmospheric nuclear bomb tests released quantities of tritium in to the atmosphere in the northern hemisphere. This effectively labeled the surface waters until testing stopped in 1963. In 1972 the results of the Geochemical Oceanic Section Study showed that the water of the Denmark Strait overflow reached a depth of 3500m at the base of the North Atlantic Deep water, but no tritium was detected in the Antarctic bottom water. Further studies conducted by Peterson & Rooth, (1976) discovered that the source of the Denmark Strait overflow was not the bottom water of the Norwegian Sea but instead from a depth of the upper 1000m. Meincke & Kringe (1978) conjectured that atmospheric forcing was responsible for lifting the water behind the sill to cause an overflow event. The actual mechanism is due to a storm generating cyclonic winds which cause an Ekman transport to be set up, which in turn causes upwelling. The depression of the water surface and the associated rising of the thermocline lifts the water above the depth of the sill. The intermittent nature of many of these flows which are often initiated by atmospheric disturbances implies that the initial front of the intrusion would have the form of a gravity current. Atmospheric fluctuations are thought to be responsible for the flow across the Straits of Gibraltar.

The instability of these flows, their interaction with topography and the effects of tides leads one to wonder at the feasibility of modeling them in the laboratory. However much of the dynamics at the sill is governed by simple hydraulic laws. It has been shown that estimates of volume transport deduced from laboratory experiments compare reasonably well with surveys of environmental overflows. Whitehead et al, (1974), estimated that the volume transport of the Denmark Strait was between 2.1x 10^6 to 4.8 x 10^6 m^3/s. A subsequent survey of the Strait (Dickson et al, 1990), measured a volume transport of 2.9 Sv (1 Sv = $10^6 m^3/s$). Whitehead also modeled the flow through the Straits of Gibraltar and concluded from his experiments that this water was drawn from a great depth, an idea which was previously proposed by Stommel (1973). This too has been confirmed by hydrographic data obtained during a survey of the Mediterranean outflow in November 1986 by Kinder et al (1987). However Whitehead views his results with caution.

" There is still some question however about whether the results of theoretical models and laboratory experiments - which are limited by the size of turntables - can be scaled up to the real ocean where turbulence is likely to be much greater and where the topography of the bottom introduces a largely unknown amount of drag and mixing. "

Indeed if one considers the case of the Arctic bottom water that overflows the sill at the Denmark Strait, one finds that its dynamics and path are the result of a combination of the effects of atmospheric influence, topography, tides and the Coriolis force. The effect of the Earth's rotation has not been mentioned so far. Its influence is shown in figure 2.3 where the overflowing water of the Denmark Strait is seen on the right hand side of the passage in the direction of the flow. The overflow follows the continental slope around Greenland where it encounters the outflow component of the Iceland-Faroe sill and that of the Faroe bank channel (fig. 2.4).

Hence it is seen that these overflows make a significant contribution to the ocean budgets through the transport of salinity, temperature, anthropogenic substances, inorganic and organic matter.

2.5 Surface Currents

Surface currents are a further example of gravity currents which occur in the environment. However many surface currents may be described as continuous and therefore not exhibit the characteristic head associated with the gravity currents described in the previous sections. Despite this the dynamics governing the flow and large scale features observed

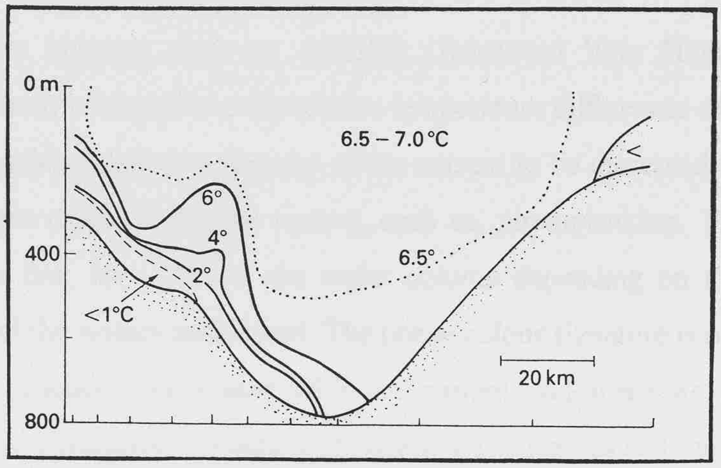

FIGURE 2.3. Denmark Strait overflow temperature section at ~ 65°N. Note the Arctic Bottom Water overflow on the r.h.s. of the channel. (From Worthington, 1969)

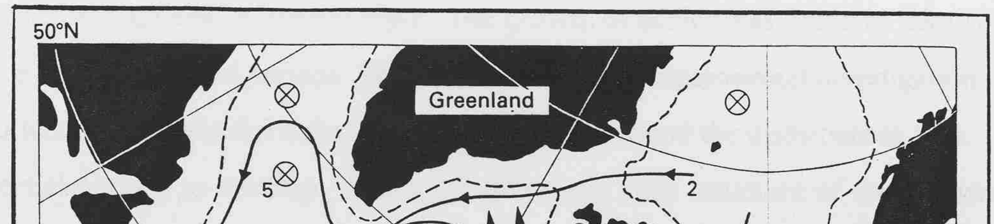

FIGURE 2.4. Map showing the course taken by the Arctic Bottom Water overflow, where
----- 1000m contour

⊗ deep convection

numbers mark the volume transport in Sv .
(From Tomczak and Godfrey, 1994)

in the laboratory may be applied to these flows. Oceanic examples include the Algerian Current (Millot et al, 1990), the East Greenland (Wadhams et al, 1979) and the Norwegian Currents (Mc Climans et al, 1985) and the Leeuwin Current south of Australia (Griffiths & Pearce, 1985).

The use of satellite imagery, such as, AVHRR (Advanced Very High Resolution Radiometer), in the study of these flows can resolve temperature differences of 0.1°C over > $1km^2$ therefore enabling real time features of the current to be discerned and tracked. Ocean colour images utilize biological tracers, such as, phytoplankton. This provides information on the first 10 - 20m of the water column depending on the particular attenuation length of the waters considered. The ocean colour signature is often coupled with the physical processes associated with the current and therefore can provide information on ocean circulation, boundaries between water masses and the evolution of eddies.

Much instability has been documented in observations of the Leeuwin Current (Griffiths et al, 1975). The Leeuwin Current originates near the North West Cape of Australia at 22°S at the south west corner of the continent it rounds the Cape Leeuwin before finally continuing across the Great Australian Bight. The growth of eddies was found to take 10 - 15 days, i.e., 12 to 17 inertial periods. This is consistent with experimental investigation of gravity currents by Griffiths & Linden,(1981, 1982) which found the disturbances took 10 to 20 inertial periods to develop. Figure 2.5 shows the eddy structure of the Leeuwin Current. The eddies were found to have zero phase speed relative to the current, also in agreement with laboratory studies. Griffiths, assuming a Froude number of 1 for the Leeuwin Current in accordance with laboratory results, calculated a velocity of 0.9 to $1.4ms^{-1}$ based on the parameters of the Leeuwin current. This is consistent with the results of a survey carried out in 1982, which measured a maximum velocity of between 0.5 to 1.8 ms^{-1} at the edge of the current. The greatest velocity was measured at Cape Leeuwin where the topography may have imposed critical conditions upon the current. The width of the current was found to be four or more deformation radii. This is greater than the widths observed in the laboratory by Griffiths & Hopfinger (1983), which suggested that the current width approximated to the deformation radius. However dissipation by interaction

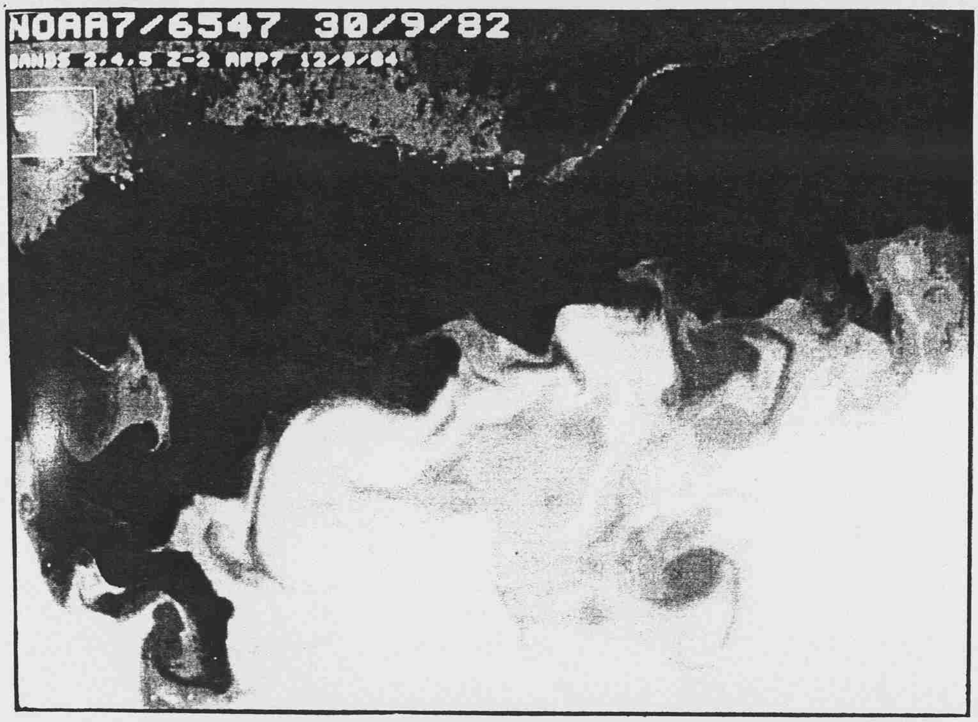

FIGURE 2.5. Leeuwin current imaged using NOAA7 AVHRR, on 30th Sept 1982. The satellite image clearly distinguishes the eddying motions within the warm Leeuwin current (darkest water), which runs parallel to the S.W. coast of Australia. (From Griffiths et al, 1985)

with topography could have caused an increase in width through release of potential energy.

Large scale disturbances are common features of surface currents, indeed the boundary between the Norwegian and East Greenland Current is marked by shear generated eddies of 10 - 20km in diameter, which again have a significant life span of 20 - 30 days. Instabilities are also observed in the Algerian Current (Arnone et al, 1990), see figure 2.6. Eddies are responsible for the transport of nutrients and marine organisms as well as physical properties. Griffiths (1985) established that the warm eddies within the Leeuwin Current were responsible for removing 10 % of the warm water off the south Australian coast in the spring of 1982.

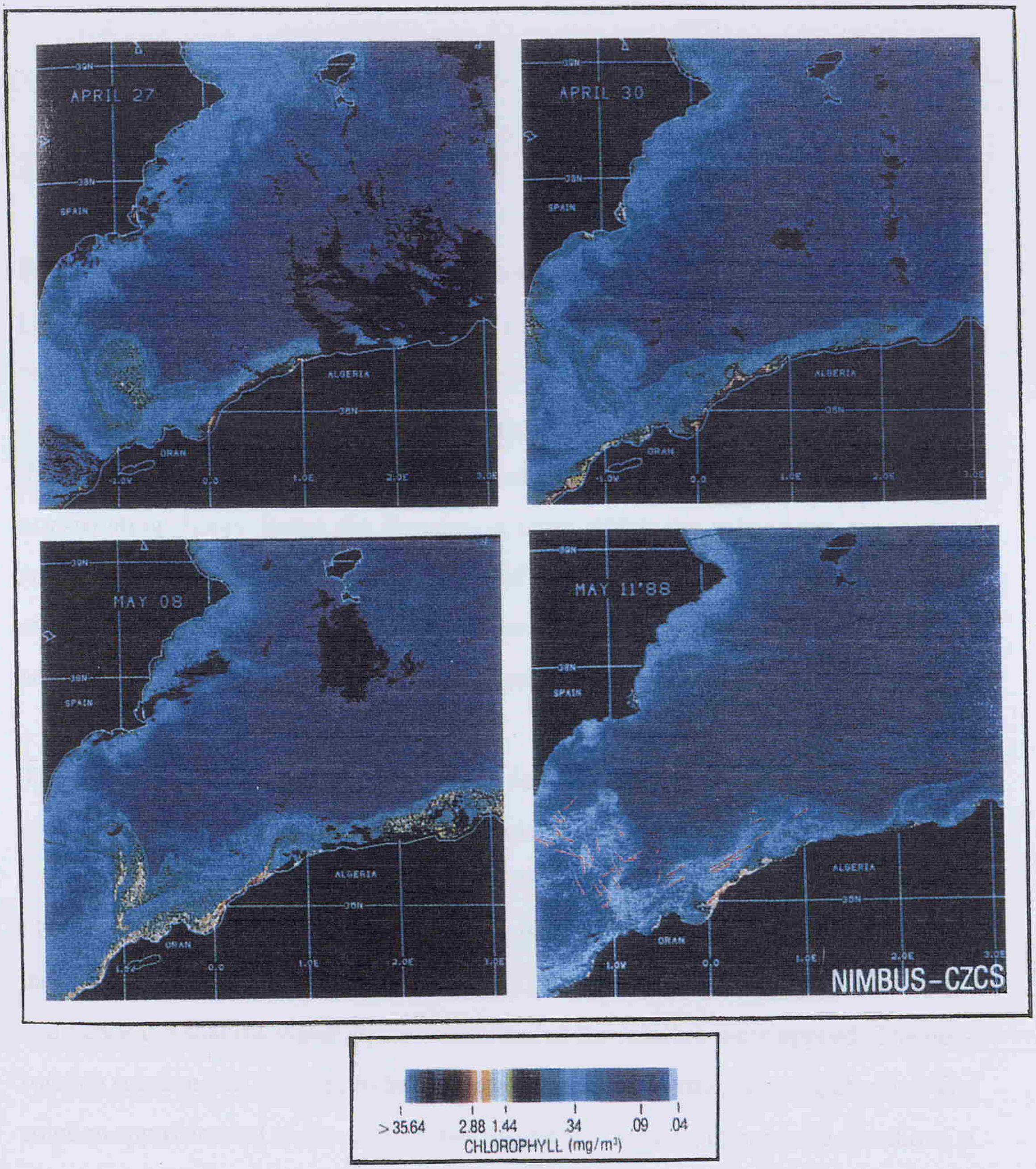

FIGURE 2.6. Algerian Current imaged using Nimbus CZCS between April 27 and May 11, 1986. Beneath the images a non-linear calibration wedge of chlorophyll concentration is shown. The chlorophyll acts as a tracer clearly distinguishing the water masses and the dynamics within the current. (From Arnone et al, 1990)

CHAPTER 3

Theoretical framework

3.1 Literature review

First in importance in a study of gravity currents is the non-rotating theory of Benjamin (1968). The beauty of Benjamin's theory is its simplicity. He avoids the non-hydrostatic region in the vicinity of the nose of the current, by equating the forces acting on the flow at upstream and downstream sections, and the fluxes in and out of this region. For the dissipationless case he predicts a unique velocity and depth of the flow. Benjamin's non-rotating theory forms the foundation upon which the subsequent theories of rotating gravity currents (Stern 1982, Nof 1987, Hacker 1997) are based. It is examined in more detail in § 3.1.1. His extension to include dissipation is discussed separately in § 4.1.1., where it forms the limit to the rotating energy loss theory.

The aim of this literature review is to consider the relevance and limits of previous models associated with rotating gravity currents. Authors in the field of rotating gravity currents include: Gill (1976); van Heijst (1985); Stern (1982); Nof (1987); and Hacker (1996). Gill basically extended the 'Adjustment Problem' to the rotating case. The initial condition was taken as a step function. The hydrostatic approximation was made and hence the shallow water equations corrected for rotation were applied. The non-rotating solution was assumed to be applicable to a very narrow, rotating channel. The solution approximated to the sum of two wavefronts moving in opposite directions at phase speed $(gH)^{\frac{1}{2}}$, where H is the total depth of fluid. In the rotating case the solution was taken as the sum of Poincare modes and two Kelvin waves. The Kelvin waves propagated at a uniform speed along opposite sides of the channel. The resulting disturbance was strongly asymmetrical. Gill subsequently considered hydraulic control in a rotating system (1977).

Gill's work is not directly relevant to the present study, as it is a one layer shallow water model. However the actual geostrophic adjustment process is utilised in § 5.1 where the initial potential vorticity distribution is incorporated into the energy conserving theory. This method is similar to that used by van Heijst (1985). He considered the adjustment of a three-layer system from rest within a rotating reference frame to a state of equilibrium, after the removal of a hypothetical barrier separating the density fronts. His work forms an extension to the two layer adjustment models of Csanady (1971, 1978), Stommel and Veronis (1980), Ou (1983) and Hsueh and Cushman-Roisin (1983). The method firstly considers conservation of potential vorticity between the initial and adjusted state in each layer. Margules' equation (5.1.13), is then used to determine the relationship between the slope of the interface between two layers and the velocity jump across the interface. It is assumed that the channel has a rigid lid. From these relationships van Heijst derives general solutions for the depth of each layer, which are solved by considering boundary conditions particular to the equilibrium state and conservation of momentum and mass. In § 5.1 this method is applied to give the general solution for the depth of the interface.

Stern et al (1982) presented a theoretical model of rotating gravity currents based on laboratory observations and Stern's previous work (1980). He proposed that the current width could be divided into a steady and unsteady region seperated by what he called a 'dividing streamline'. Conservation of volume flux within this region was not used, instead he formulated an expression for what he called a detrainment coefficient, that was based on the ratio of the volume transport to the absolute transport. By using the shallow water equations and a generalisation of his previous work (1980), he derived a solution for long waves on a uniform potential vorticity current. Stern found that there were two possible sets of solutions. These he interpreted as either a wedge or bore intrusion, based on the shape of the current. The wedge solution was discarded as it was not consistent with his laboratory observations. He proceeded with a particular bore solution which he called the 'limiting bore'. This predicted a maximum width, L, for all intrusive bores of $0.413 \lesssim \mathrm{L} \lesssim 0.516$, where $\mathrm{L} = L^* f/(g'h^*)^{\frac{1}{2}}$ i.e. the ratio of the measured current width to the Rossby Radius, based on the dimensional current depth. The width, nose speed and the detrainment coefficient were all found to be essentially independent of the prescribed potential vorticity and the finite depth of the lower layer. The non-dimensional nose speed or internal Froude number $Fr(h) = c^*/(g'h^*)^{\frac{1}{2}} = 1.57$ and the detrainment coefficient, $\delta = 0.32$. Stern recognised that the long wave theory would fail when the first shock formed at the nose and he envisaged that the short wave theory would alter and accelerate the nose region. He assumed this would have no effect upstream in the intrusion. Griffiths (1986) questions the assumption of no upstream influence. It is surprising that Stern rejected the 'thinning wedge' solution in favour of the 'limiting bore', because in my experiments a strongly rotating current does have a wedge-like profile and the propagation rate does appear to increase towards the nose. Stern also found that the theoretical nose speed was unaffected by the fractional depth of the current whereas in the non-rotating case Benjamin found that there was a strong dependence on the finite depth of the lower layer. In § 7 I present the results of my laboratory investigation which covers a wide range of depths and rotation rates. In contradiction to Stern I have found that the nose speed is sensitive to the fractional depth of the current. Stern's work is an interesting forerunner to the contemporary theories of Hacker and Nof. However its weakness is that it only considers a shallow, strongly rotating current of limited width, on which there is no upstream influence. Here I develop a theory that covers all levels of rotation and fractional depths.

Nof (1987) criticised the use of the long wave equations in Stern's theory, since the current is non-hydrostatic in the nose region and instead used a similar method to Benjamin applying conservation of energy, momentum and continuity to a control volume connecting the flow behind and ahead of the nose. His model includes a free surface and considers a current of wedge-like cross-section, with zero potential vorticity and finite depth. He derived five algebraic equations in terms of five unknowns and solved them using an algebraic manipulation programme known as 'Macsyma'. Steady solutions were found for a limited range of finite depths where the fractional depth varied between ~ 0.65 to 1 (Nof, 1987). The propagation rate of the nose was found to be approximately constant, increasing slightly with increasing fractional depth from $0.811(g'h)^{\frac{1}{2}}$ to $0.824(g'h)^{\frac{1}{2}}$ where h is the depth of the current. For a particular fractional depth a unique current width was predicted which varied between 0.724

$(g'h)^{\frac{1}{2}}/f$ to 0.772 $(g'h)^{\frac{1}{2}}/f$. Unfortunately, Nof found that steady solutions did not exist for an infinitely deep, broad ocean, so it is not possible to compare his results directly with those of Stern. However his results can be compared with those of Hacker (1996).

Hacker used a similar approach to Nof. He assumed that the fluids (ambient and current) were immiscible and inviscid, and that the flow was steady. This enabled him to meet the conditions necessary to apply conservation of momentum, energy, volume flux and potential vorticity between the upstream and downstream cross-sections and hence avoid the hydrostatic problem. Hacker did not assume zero potential vorticity and he introduced a rigid lid. He applied the governing equations describing the structure of the flow to three flow geometries, based on the width of the current as the rotation rate increases. For each case a solution was found for the speed of the current. He provided a steady solution for all levels of rotation, with a smooth progression between the non-rotating and weak rotating case. Nof's solutions can be compared with Hacker's solutions for intermediate rotation rate and despite the inclusion of a free surface and the assumption of zero P.V. in Nof's analysis the results compare quite well. While Hacker's theory does not include dissipation and the effect of the potential vorticity distribution at the source region on the ensuing flow, it is by far the most comprehensive. Hence it is Hacker's energy conserving theory which I have chosen to extend. The inclusion of energy loss and the P.V. distribution are addressed in §4 and §5 respectively. The framework upon which these extensions are made is summarised in §3.2.. Before proceeding with the effects of rotation, the non-rotating energy conserving theory of Benjamin is considered in more detail. Benjamin's solutions provide the end points ($W = 0$) for both Hacker's rotating energy conserving theory and the energy loss theory described in chapter 4. Indeed, it is shown in § 4.2.1.2 that the governing equations of the energy loss theory reduce to those of the non-rotating case described in § 3.1.1.

3.1.1 Non-rotating energy conserving theory

Benjamin's model of a gravity current considers the analogous flow of a steady, inviscid fluid of density ρ, past a cavity (fig.3.1). The cavity may be filled with air or empty. The flow is confined between two horizontal planes. The pressure at the free surface is taken as zero. Upstream the fluid has depth, *H*, and propagates at a constant velocity, c_1. Beneath the cavity far downstream the flow is uniform with depth, *h*, and constant velocity, c_2.

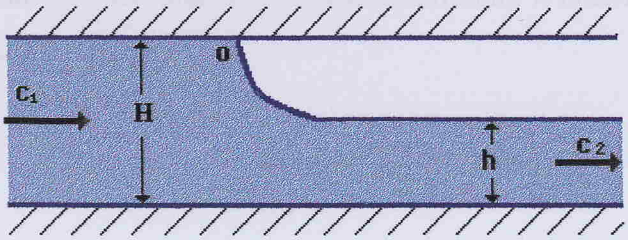

Fig. 3.1 Benjamin's (1968) model of the flow of an inviscid fluid past a cavity of air.

Benjamin obtains an expression for c_2 by applying the Bernoulli equation along a streamline connecting the stagnation point, 0 and a point downstream on the free surface, where

$$c_2^2 = 2g\,(H - h) \tag{3.1.1}$$

To obtain the pressure on the upper boundary the Bernoulli equation is applied between the stagnation point and the flow far upstream, hence

$$-\tfrac{1}{2}\,c_1^2\rho = p_0\,. \tag{3.1.2}$$

Since the pressure in the liquid far up and downstream varies hydrostatically with depth, conservation of momentum between the two locations, or the 'flow force balance' as Benjamin refers to it, yields

$$\tfrac{1}{2}\rho\,(\,c_1^2H + gH^2\,) = \rho\,(\,c_2^2h + \tfrac{1}{2}\,gh^2\,). \tag{3.1.3}$$

The term on the l.h.s. is the total pressure force acting on a section far upstream plus the momentum flux. The r.h. is the same but applies to the downstream flow. Applying the continuity equation, gives a second equation for the downstream velocity, c_2.

$$c_1 H = c_2 h, \tag{3.1.4}$$

This is equated with (3.1) to obtain a quadratic equation for h in terms of H. The roots of this equation are $h = H$ and

$$h = \tfrac{1}{2} H. \tag{3.1.5}$$

Therefore the condition of energy conservation dictates that the receding flow must occupy half the full depth, H. Substituting (3.5) and (3.4) into (3.1) gives the Froude numbers for the up and downstream flows,

$$c_1 / (gH)^{\frac{1}{2}} = \tfrac{1}{2}, \tag{3.1.6}$$

$$c_2 / (gH)^{\frac{1}{2}} = (2)^{\frac{1}{2}} \tag{3.1.7}$$

where the receding flow is supercritical.

3.2 Governing equations

3.2.1 Model description

The energy conserving model of Hacker is based on three flow geometries as the rotation rate is increased (fig. 3.2). In case A the current fills the full width of the channel, 'weak rotation'. In case B the current detaches from the left hand wall and outcrops on the free surface, at position d. For strong rotation rates, case C, the current fills the full depth of the channel, outcropping on the bottom of the tank at position b.

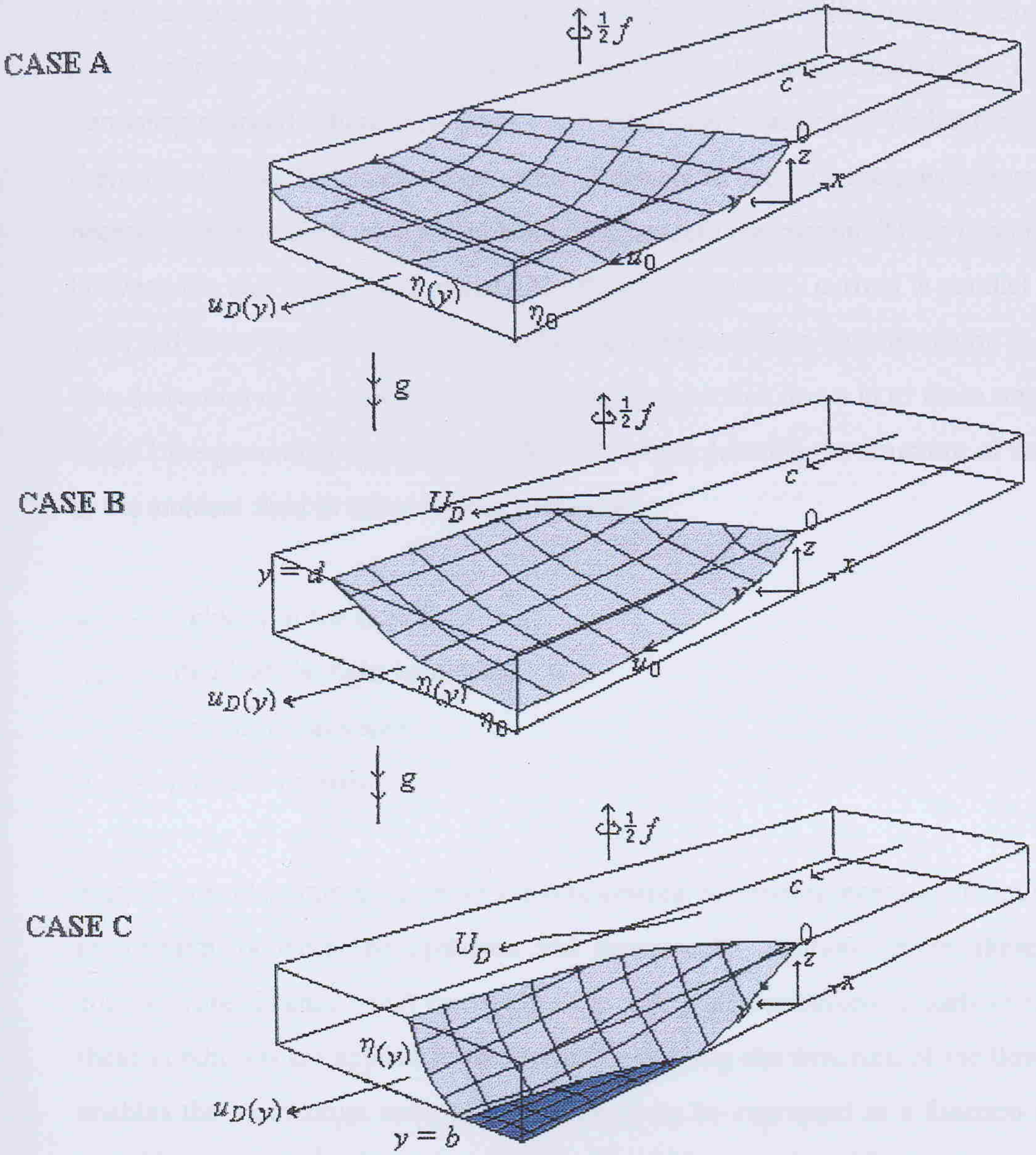

FIGURE 3.2. Flow geometries for 3 levels of background rotation in the steady reference frame. The surface gravity current is shown in blue, whilst the ambient fluid is clear. Upstream in the ambient fluid there is no flow. The interface between the current and ambient fluid propagates at speed c parallel to the channel walls and floor. Hence, the gravity current appears stationary to an observer moving with current, whilst the oncoming ambient fluid has speed c. This is known as the steady reference frame.

Case A (low rotation) - current fills the full width of the channel

Case B (moderate rotation) - current outcrops on the upper boundary at $y = d$

Case C (strong rotation) - current outcrops on the upper boundary and fills the full depth of channel, intersecting the bottom boundary at $y = b$.

Structure of the flow is defined in terms of:

u_0	velocity of the ambient fluid at the r.h. wall
η_0	depth of the ambient fluid at the r.h. wall
c	speed of translation of the reference frame
U_D	downstream velocity in the ambient fluid
$u_D(y)$	velocity of the ambient fluid at y
$\eta(y)$	depth of the ambient fluid at y

(Adapted from Hacker, 1996)

The model considers a surface gravity current. The interface of the current propagates at a constant speed c. The reference frame is rotating at angular frequency $=f/2$ and translating at speed c, hence the gravity current appears stationary. Within the current there is no flow. The role of the current is merely to produce the pressure gradient necessary to drive the flow in the ambient fluid beneath the current. There is no mixing between the two fluids. Downstream the flow in the gravity current is parallel to the walls and floor. The channel has a rigid lid and the Boussinesq approximation is made. The derivation of the energy conserving theory is broken down in to three stages. In Stage 1 the governing equations are derived, which describe the structure of the flow in the ambient fluid in terms of four parameters:

u_0 - velocity at the right hand wall.
η_0 - depth at the right hand wall
c - speed of translation
p_0 - pressure upstream

Stage 2 considers conservation of the fundamental properties, energy, continuity and momentum, between the upstream and downstream locations. From these three equations are obtained which contain the four unknown parameters. Finally in stage 3, these conditions are applied to the equations defining the structure of the flow. This enables the momentum integral for each case to be expressed as a function of one variable and solved using a numerical method for cases A and B, and an analytical method for case C. From these the other variables are calculated.

3.2.2 Basic scales

The variables in the model are defined and non-dimensionalised as follows. The dimensional variables are marked with an asterisk. Vectors are in bold type. The subscripts c and a refer to the current and ambient fluid respectively, with U the upstream and D the downstream locations. The subscript 0 specifies a variable measured at the r.h. wall which is therefore a constant. Where a symbol appears only once it is defined in the text. Note that the scaling of the pressure term removes the hydrostatic pressure within the ambient fluid. An important parameter is the strength of the rotation, this is characterised by the ratio of the width of the channel to the Rossby radius of deformation.

Dimensional parameters

reduced gravity	$g' = g\,\Delta\rho/\rho_a$ where $\Delta\rho = \rho_a - \rho_c$
channel width	D
channel depth	H
Coriolis parameter	f
Rossby radius	$R = f/(g'H)^{\frac{1}{2}}$

Non-dimensional parameters

independent variables	$x = x^*/D,$	$y = y^*/D,$	$z = z^*/H$
vertical aspect ratio	$\lambda_H = H/D$		
depth of the flow	$h = h^*/H$		
density ratio	$\rho = \rho_c{}^*/\rho_a{}^* = 1 - \Delta\rho^*/\rho_a{}^*$		
velocity	$\mathbf{u} = \mathbf{u}^*/(g'H)^{\frac{1}{2}}$		
velocity of the leading edge	$c = c^*/(g'H)^{\frac{1}{2}}$		
pressure	$p = (p^* + \rho_a{}^* g\, z^*)/(\rho_a{}^*\, g'H)$		
Strength of rotation	$W = f\,D/(g'H)^{\frac{1}{2}}$		

3.2.3 Stage 1 - governing equations

3.2.3.1 Momentum equation

The momentum equation for steady flow in the rotating, translating reference frame is

$$\rho^*\mathbf{u}^*.\nabla^*\mathbf{u}^* \;+\; \rho^* f(\mathbf{k} \times \mathbf{u}^*) \;=\; -\nabla^* p^* - \rho^* f c^* \mathbf{j} + \rho^* g \mathbf{k}. \qquad (3.2.1)$$

The second term on the r.h.s of the momentum equation (3.2.1), $\rho f c^*\mathbf{j}$, is the Coriolis force experienced by the frame of reference and it is known as the 'body force of translation'. It is a result of the change from the steady rest frame to a reference frame translating at the speed c, i.e.

$$\mathbf{u}^*_r\,(t^*, x^*_r, y^*, z^*) = \mathbf{u}^*_t\,(x^*_t, y^*, z^*) + c^*\mathbf{i}$$

where the subscripts r and t refer to the rest frame and translating frame respectively. The non-dimensional form of the momentum equation (3.2.1) for the current is

$$\rho\mathbf{u}_c.\nabla\mathbf{u}_c + \rho W\mathbf{k} \times \mathbf{u}_c = -\nabla p_c - \rho Wc\mathbf{j} + \lambda_H^{-1}\,\mathbf{k} \qquad (3.2.2)$$

and for the ambient fluid is

$$\mathbf{u}_a.\nabla\mathbf{u}_a + W\mathbf{k} \times \mathbf{u}_a = -\nabla p_a - Wc\mathbf{j}. \qquad (3.2.3)$$

3.2.3.2 *Geostrophic equations*

The following sign convention is used for the flow velocities in upstream and downstream areas where the flow is parallel to the channel walls.

$$\mathbf{u}_c = (-u_c(y, z), 0, 0) \qquad (3.2.4)$$

$$\mathbf{u}_a = (u_a(y, z), 0, 0) \qquad (3.2.5)$$

The non-dimensionalised momentum equations (3.2.2) and (3.2.3) are decomposed into x, y and z components making use of (3.2.4) and (3.2.5)

$$\frac{\partial p_c}{\partial x} = 0, \qquad \frac{\partial p_c}{\partial y} = -\rho W(u_c + c) \qquad \frac{\partial p_c}{\partial z} = 1 \qquad (3.2.6)$$

$$\frac{\partial p_a}{\partial x} = 0 \qquad \frac{\partial p_a}{\partial y} = W(u_a - c) \qquad \frac{\partial p_a}{\partial z} = 0 \qquad (3.2.7)$$

and hence the geostrophic relationships for the current

$$\frac{dp_c}{dy} = -\rho W(u_c + c) \qquad (3.2.8)$$

and the ambient fluid

$$\frac{dp_D}{dy} = W(u_D - c) \qquad (3.2.9)$$

are obtained. The subscript D refers to the ambient fluid downstream.

3.2.3.3 Across-stream pressure

To determine the across stream pressure variation in the current the velocity, u_c, is set to zero in (3.2.6). This enables the geostrophic equation to be integrated easily using the boundary condition that the pressure is zero at the foremost stagnation point (0,0,1). At this stage in the calculation the Boussinesq approximation is made, $\rho = 1$.

$$p_c = (z - 1) - Wcy \qquad (3.2.10)$$

By applying (3.2.7) to the ambient fluid upstream where the velocity $u_U = c$, the pressure becomes a constant, hence

$$p_U = p_0, \qquad (3.2.11)$$

where the subscript U refers to the ambient fluid upstream. In the ambient fluid downstream the pressure is set by that of the current at the interface, $z = 1 - \eta$, because the hydrostatic pressure variation in the ambient fluid has been removed, so (3.2.10) becomes

$$y \in [0, d] \qquad p_D = -\eta(y) - Wcy \qquad (3.2.12)$$

To obtain the pressure in the free stream around the current, the geostrophic equation (3.2.9) is integrated using the boundary condition that at

$$y = d \qquad p_D(d) = -Wcd,$$

hence

$y \in [d,1]$ $$p_D(y) = WU_D(y-d) - Wcd. \qquad (3.2.13)$$

3.2.3.4 Conservation of potential vorticity

Potential vorticity is materially conserved between the two upstream and downstream locations in the ambient fluid where the flow is hydrostatic. The shallow water potential vorticity is

$$q^* = \frac{f+\omega^*}{h^*}. \qquad (3.2.14)$$

Non-dimensionalising (3.2.14) gives

$$q = \frac{H}{f} q^* = \frac{1 - W^1 du/dy}{h} \qquad (3.2.15)$$

Hence upstream the potential vorticity becomes

$$q_U = 1,$$

and downstream we have

$$q_D = \frac{1 + W^1 du_D/dy}{1-\eta}.$$

Hence conservation of potential vorticity gives

$$du_D/dy = -W\eta. \qquad (3.2.16)$$

3.2.3.5 Flow structure equations

The structure of the flow is defined in terms of the depth of the flow, η_0, and the velocity at the right hand wall of the channel, u_0. The general solutions for the across stream depth $\eta(y)$ and velocity $u(y)$ are applicable to for the whole of case A, and for $y \in [0, d]$ in case B. In the free stream around the current in case B the solution where $y \in [d, 1]$ is applied. In case C the solution for case B is still applicable for $y \in [b, 1]$

but now $\eta(b)$ and $u(b)$ become the depth and velocity at the lateral boundary of the ambient fluid. The general solutions are derived by firstly substituting the across-stream pressure (3.2.12) into the geostrophic equation (3.2.9) which gives

$$d\eta/dy = -Wu_D. \qquad (3.2.17)$$

This expression is then differentiated and by applying (3.2.16) gives

$$\frac{d^2\eta}{dy^2} - W^2\eta = 0, \qquad (3.2.18)$$

which has the general solution for the across-stream depth,

$$y \in [b, d] \qquad \eta(y) = \eta_0 \cosh Wy - u_0 \sinh Wy. \qquad (3.2.19)$$

In the free stream $\eta = 0$ hence (3.2.19) gives

$$y \in [d, 1] \qquad d = W^{-1} \operatorname{arctanh} (\eta_0 / u_0) \qquad (3.2.20)$$

When the current is the full depth of the channel at the right hand wall (case C) and outcrops at position b on the bottom boundary $y=b$, so (3.2.19) becomes

$$y = b \qquad \eta(b) = \eta_0 \cosh Wb - u_0 \sinh Wb = 1 \qquad (3.2.21)$$

The general solution for the across-stream velocity is derived using (3.2.17) and gives

$$y \in [b, d] \qquad u(y) = u_0 \cosh Wy - \eta_0 \sinh Wy. \qquad (3.2.22)$$

In the free stream around the current $\eta = 0$, therefore (3.2.16) implies that there is no shear. So $u_D(y)$ is a constant, U_D, and it is continuous at $y = d$, hence

$$y \in [d, 1] \qquad U_D = u_0 \cosh Wd - \eta_0 \sinh Wd \qquad (3.2.23)$$

At strong rotation rates when the current outcrops on the bottom (3.2.22) becomes,

$$y = b \qquad u(b) = u_0 \cosh Wb - \eta_0 \sinh Wb. \qquad (3.2.24)$$

3.2.4 Stage 2 - Conservation of fundamental properties

3.2.4.1 Conservation of energy

The momentum equation for the ambient fluid (3.2.3) is simplified using the vector identity for $\mathbf{u}.\nabla\mathbf{u}$ to give,

$$\nabla\left(\tfrac{1}{2}\,|\mathbf{u}|^2 + p + Wcy\right) = \mathbf{u} \times \boldsymbol{\omega} + W\mathbf{u} \times \mathbf{k}$$

where $\boldsymbol{\omega} \equiv \nabla \times \mathbf{u}$. Since the rhs is perpendicular to **u** taking the scalar product with **u** gives zero. Integrating with respect to y gives the Bernoulli equation,

$$\mathrm{B} = \tfrac{1}{2}\,|\mathbf{u}|^2 + p + Wcy = \text{constant along streamlines.} \qquad (3.2.25)$$

The third term on the r.h.s. is the potential energy a fluid element possesses due to its position in the potential field of the body force of translation. This is equivalent to the gravitational potential energy in the non-rotating Bernoulli equation. As the fluid element moves across-stream work must done against the body force of translation, therefore it gains potential energy. In order for the total energy to remain constant the fluid element must move in to a region of lower pressure or decelerate.

The first of the unknown parameters, p_0, is obtained by applying the Bernoulli equation to a streamline along the right hand wall, joining the foremost stagnation point (0,0,1) to the upstream flow, hence

$$\mathrm{p}_0 = -\tfrac{1}{2}\,c^2. \qquad (3.2.26)$$

Substituting (3.2.26) into (3.2.25) upstream gives,

$$\mathrm{B_U}(y) = Wcy. \qquad (3.2.27)$$

Consider the streamline connecting downstream location y to the upstream location Y(y). Then according to (3.2.25) and (3.2.27),

$$\mathrm{B_D}(y) = \mathrm{B_U}(\mathrm{Y}(y))$$

$$\tfrac{1}{2}u_{\mathrm{D}}^{2} + p_{\mathrm{D}} + Wcy = Wc(Y(y)). \qquad (3.2.28)$$

Since rigid boundaries are composed of streamlines $Y(y)$ is known for,

$$Y(b) = 0$$

and

$$Y(1) = 1.$$

Substituting the above into (3.2.28) along with the pressure fields (3.2.12) and (3.2.13) gives

$$\mathrm{B_U}(b) = 0 = \tfrac{1}{2}u_{\mathrm{D}}^{2}(b) - \eta(b) \qquad (3.2.29)$$

and

$$\mathrm{B_U}(1) = Wc = \tfrac{1}{2}u_{\mathrm{D}}^{2}(1) - \eta(1) + WU_{\mathrm{D}}(1\text{-}d) \qquad (3.2.30)$$

These two equations may be written in terms of three of the unknown parameters, u_0, η_0 and c. Hence only one more equation is required to close the problem.

3.2.4.2 Conservation of volume flux

The inward flux must equal the outward flux across the up and downstream cross-sections. This is described by the following integral where the upstream discharge is simply c,

$$c = \int_b^1 \int_0^{1-\eta} u_{\mathrm{D}}(y)\, dz\, dy,$$

$$(3.2.31)$$

$$= \int_b^1 u_{\mathrm{D}}(y)\,(1-\eta)\, dy$$

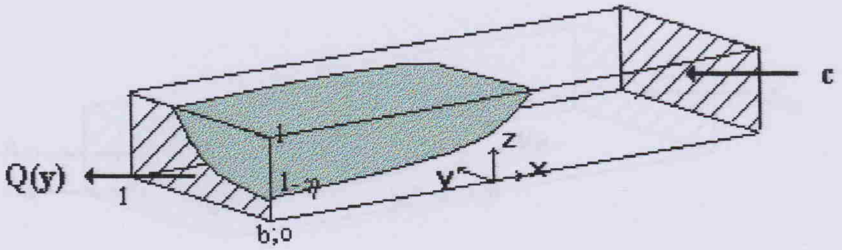

Fig. 3.3 Illustration of the cross-sectional area over which the downstream velocity is integrated.

To integrate (3.2.31) the potential vorticity (3.2.16) and geostrophic relationship (3.2.9) are substituted hence the terms are expressed as exact integrals.

$$c = \frac{1}{W}\left[\tfrac{1}{2}u_D^{\,2} + p_D + Wcy\right]_b^1 \qquad (3.2.32)$$

The term within the brackets is equivalent to the downstream Bernoulli function. Hacker found that if the continuity equation (3.2.32) was simplified using the Bernoulli equation (3.2.29) where B(b) = 0, the continuity equation became equivalent to (3.2.30). Hence conservation of volume flux did not offer any further information for the energy conserving solution, than the Bernoulli equation. However the continuity equation is of importance in the energy loss model where the use of the Bernoulli equation is avoided, § 4.1.2

3.2.4.3 Conservation of Momentum

The condition of conservation of momentum is satisfied by integrating the momentum equations (3.2.2) and (3.2.3) over the rectangular volume, *V*, connecting up and downstream cross-sections. In order to simplify the integral the divergence theorem is applied to the advective and pressure terms enabling them to be expressed as surface integrals. At rigid boundaries **u.n** = 0.

$$\int_{A_U + A_D} \mathbf{u}(\mathbf{u.n})\, dS + \int_{\partial V} p\mathbf{n}\, dS = -\int_{Va} W\mathbf{k} \times \mathbf{u}\, dV - Wc\mathbf{j}\int_{V} dV + \mathbf{k}\int_{V_c} dV \qquad (3.2.33)$$

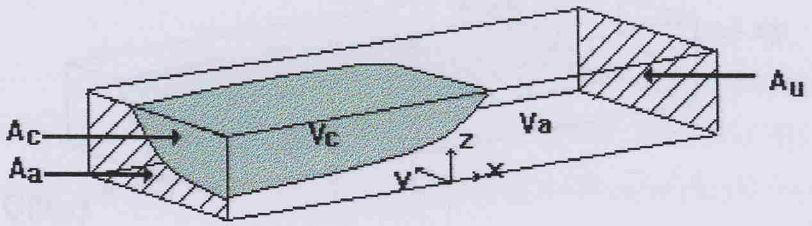

Fig. 3.4 Illustrates the volume, V, bounded by ∂V, over which the momentum equation is integrated.The parts of V containing the ambient fluid and the current are V_a and V_c respectively. The up and downstream faces of ∂V are A_U and A_D.

The j and k components of (3.2.33) merely express the balance between the pressure force, and coriolis and buoyancy forces respectively. The i component is the useful part of the equation,

$$\int_{A_U} (u_U{}^2 + p_U)\, dA = \int_{Aa} (u_D{}^2 + p_D)\, dA + \int_{A_c} p_c\, dA + W \int_{Va} \mathrm{v}\, dV \qquad (3.2.34)$$

where the surface A_D consists of A_c the current and A_a the ambient fluid. The term on the l.h.s. and the first term on the r.h.s. of (3.2.34) are the momentum flux plus cross-sectional pressure acting on the ambient fluid up and downstream respectively. The second term is the cross-sectional pressure acting on the current. In the third term, v is the across stream component of the ambient fluid velocity, which induces a Coriolis force aimed upstream as the ambient fluid is accelerated around the current. This integral is equivalent to

$$W \int_{Va} \mathrm{v}\, dV = W \int_{0}^{1} Q_c\,(y)\, dy \qquad (3.2.35)$$

where $Q_c(y)$ is the volume flux at y across a vertical plane. Hence $Q_c(y)$ can be evaluated knowing the flux in, cy, and out, $Q(0; y)$, of a region connecting up and downstream i.e.

$$Q_c(y) = cy - Q(0; y). \qquad (3.2.36)$$

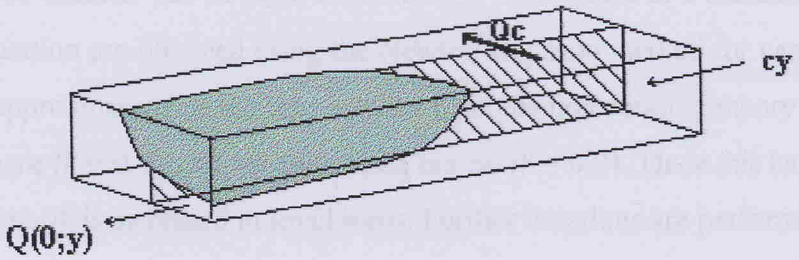

Fig. 3.5 Illustrates the fluxes in and out of a volume bounded by a vertical plane at *y* where the across stream flux is Q_c.

Using the fact that

$$Q(0; y) = \tfrac{1}{W}\left[B_D\right]_{y_o}^{y_1} \qquad (3.2.37)$$

(3.2.37) is substituted into (3.2.36) enabling the momentum integral (3.2.34) to be solved. This provides the third equation necessary to close the problem. The method used to evaluate (3.2.34) is similar to that described in detail in § 4.1.4. for the solution of the momentum integral in the energy loss model. Note that in order to incorporate dissipation the discharge, Q(0; *y*), is retained, enabling the Bernoulli equation (3.2.25) to be side stepped.

The solution of the energy conserving momentum integral is,

$$c^2 = {}^{1}\!/_{W}\left[\tfrac{2}{3}\,u_D^{\,3} - u_D\,\eta\right]_b^d + U_D^{\,2}(1 - d) - b \qquad (3.2.38)$$

On substitution of the flow structure equations § *3.2.3.5*, (3.2.38) becomes a function of u_0, η_0 and *c*. Hacker simplified this equation further using the Bernoulli equations (3.2.29) and (3.2.30).

3.2.5 Stage 3 - Numerical solution

For each of the flow geometries the respective Bernoulli equations (3.2.29) and (3.2.30), and the momentum integral (3.2.38) are determined. Substituting the Bernoulli equations into the momentum integral enables (3.2.38) to be expressed in terms of one variable. The strength of rotation, W, is retained as a constant. The roots of this equation are obtained using the Newton-Raphson method for cases A and B. The first approximation to the root is taken from the non-rotating theory (Benjamin, 1968) where $W = 0$. Iterations are carried out on $W = 0.01$. Once this has converged to a solution, W is increased in small steps. Further iterations are performed using the previous solution as the next initial approximation. For each level of rotation a unique solution is found, from which the other variables can be solved. An analytical solution is possible for case C because at b, $\eta(b) = 1$ and according to (3.2.29) $u_D = (2)^{\frac{1}{2}}$.

3.3 Review of results with no energy loss and simple flow

3.3.1 Results and discussion

The set of solutions for Hacker's energy conserving model form the starting point of the energy loss theory § 4.1.2. Figure 3.6 shows the solution of the five main variables, u_0, η_0, c, b, and d. Despite the abrupt change in the geometries between each of the cases, one can see that the transitions between the cases are smooth and continuous. The curves for the velocity, u_0, and depth, η_0 at the r.h. wall are similar due to their simple relationship in the Bernoulli equation (3.2.29). At weak rotation rates c increases linearly. This increase becomes more gradual as c tends towards 1 at strong levels of rotation. In case A the current fills the full width of the channel. In case B the current is deflected away from the l.h. wall and the surface width, d, decreases quickly until it is less than half the width of the channel at the onset of case C. During case C the decrease in d slows and the current now fills the full depth of the channel outcropping at b on the channel floor. The bottom width, b, remains less than 5% of the channel width even at strong rotation rates.

Recalculating Hacker's solutions enabled me to display the results in a manner in which they had not been previously presented, i.e. in 3-D graphs. Figure 3.7(a) is a 3-D interface profile for all three cases. For the non-rotating case the interface is horizontal, but as the level of rotation is increased the interface tilts, deepens slightly at the r.h.

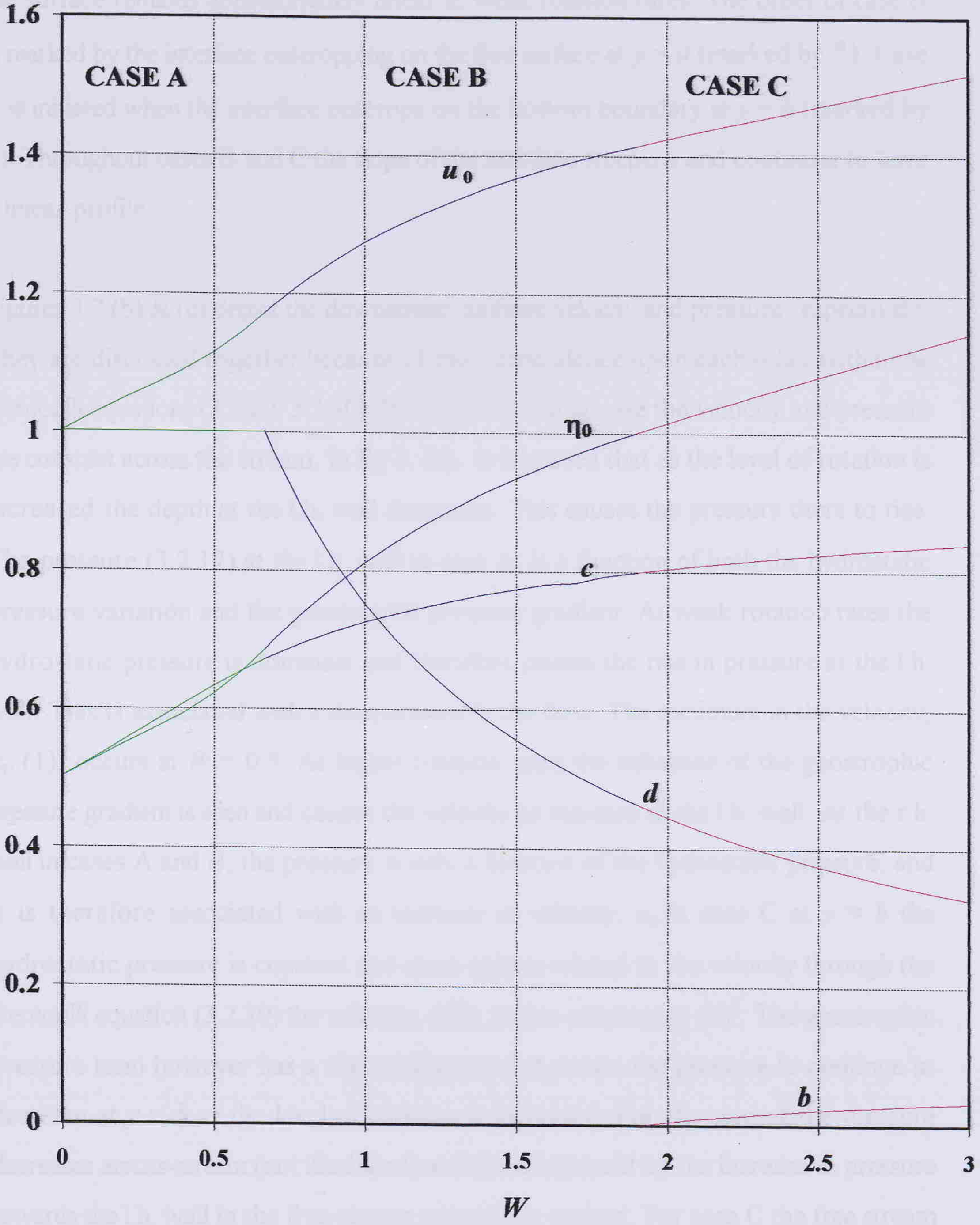

Figure 3.6. Solution of the five main variables of the rotating energy conserving model of Hacker (1996) for each flow geometry, i.e cases A, B & C where

u_0	velocity of the current at the r.h. wall
η_0	depth of the current at the r.h. wall
c	front speed
d	width of the current outcropping on the free surface
b	width of the current outcropping on the bottom of the channel

wall, ($y = 0$) and becomes increasingly shallower at the l.h. wall, ($y = 1$). The slope of the surface remains approximately linear at weak rotation rates. The onset of case B is marked by the interface outcropping on the free surface at $y = d$ (marked by *). Case C is initiated when the interface outcrops on the bottom boundary at $y = b$ (marked by +). Throughout cases B and C the slope of the interface steepens and continues to have a linear profile.

Figures 3.7 (b) & (c) depict the downstream ambient velocity and pressure respectively. They are discussed together because of their dependence upon each other within the Bernoulli equations (3.2.29, 3.2.30). In the non-rotating case the velocity and pressure are constant across the stream. In fig 3. (a), it was seen that as the level of rotation is increased the depth at the l.h. wall decreases. This causes the pressure there to rise. The pressure (3.2.12) at the l.h. wall in case A, is a function of both the hydrostatic pressure variation and the geostrophic pressure gradient. At weak rotation rates the hydrostatic pressure is dominant and therefore causes the rise in pressure at the l.h. wall. This is associated with a deceleration in the flow. The minimum in the velocity, u_D (1), occurs at $W = 0.5$. At higher rotation rates the influence of the geostrophic pressure gradient is seen and causes the velocity to increase at the l.h. wall. At the r.h. wall in cases A and B, the pressure is only a function of the hydrostatic pressure, and it is therefore associated with an increase in velocity, u_0.In case C at $y = b$ the hydrostatic pressure is constant and since $\eta(b)$ is related to the velocity through the Bernoulli equation (3.2.29) the velocity, $u(b)$, is also constant at $(2)^{\frac{1}{2}}$. The geostrophic pressure term however has a slight influence and causes the pressure to continue to decrease at $y = b$ as the level of rotation is increased. For the current the pressure decreases across-stream (not illustrated) and this is balanced by the increase in pressure towards the l.h. wall in the free-stream around the current. For case C the free stream velocity, U_D, is a constant. We are now in a position to proceed from the energy conserving theory for simple flow to the inclusion of dissipation § 4.1.2.

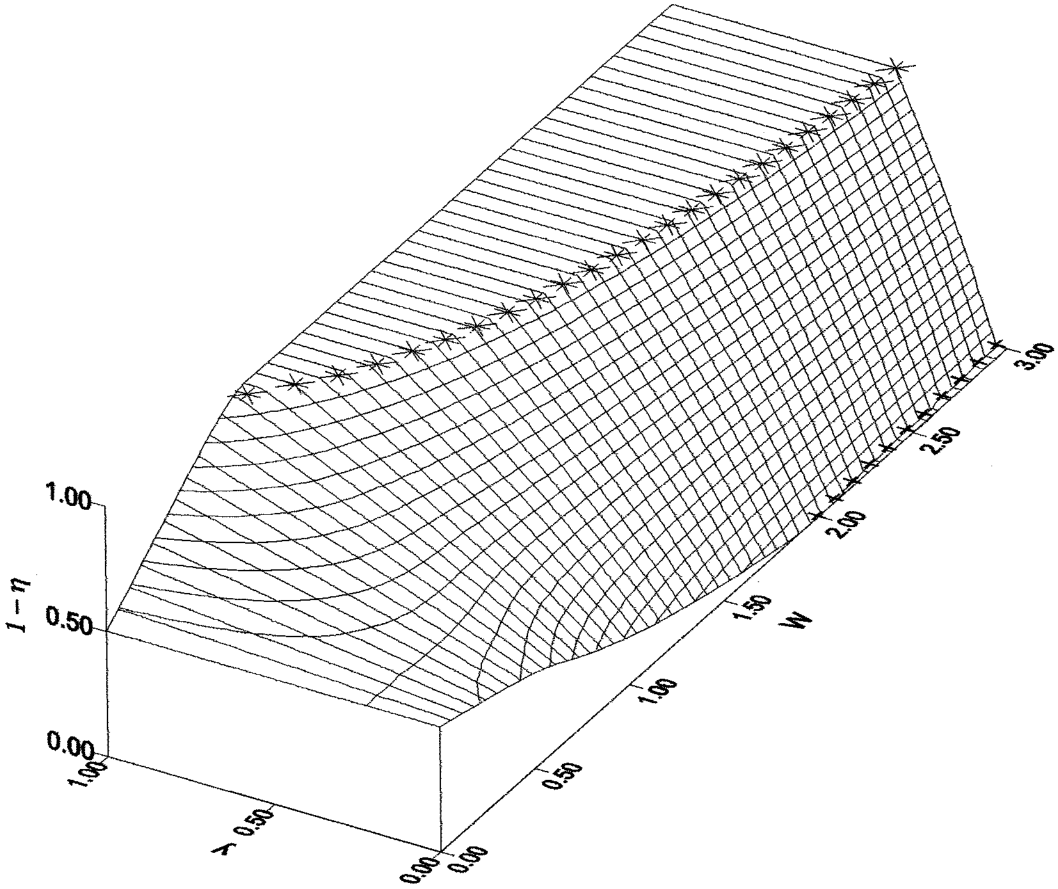

FIGURE 3.7a. Surface plot to illustrate the across stream variation of current depth $\eta(y)$, as the level of rotation, W is increased.

✳	$y = d$ the current outcrops on the free surface (Case B)
+	$y = b$ the current outcrops on the bottom boundary (Case C)

Case A -For non-rotating currents, ($W = 0$) the interface is horizontal. As the level of rotation is increased the interface tilts with the current depth $\eta(y)$ at the l.h. wall ($y = 1$) decreasing, whilst the depth at the r.h. wall ($y = 0$) increases.

Case B - When $\eta(1) = 0$ the current outcrops on the free surface at $y = d$ and the interface continues to tilt as the level of rotation increases further.

Case C - When $\eta(0) = 1$ the current outcrops on the bottom boundary at $y = b$. The current continues to outcrop on the top boundary and moves towards the r.h. wall. The interface is approximately linear.

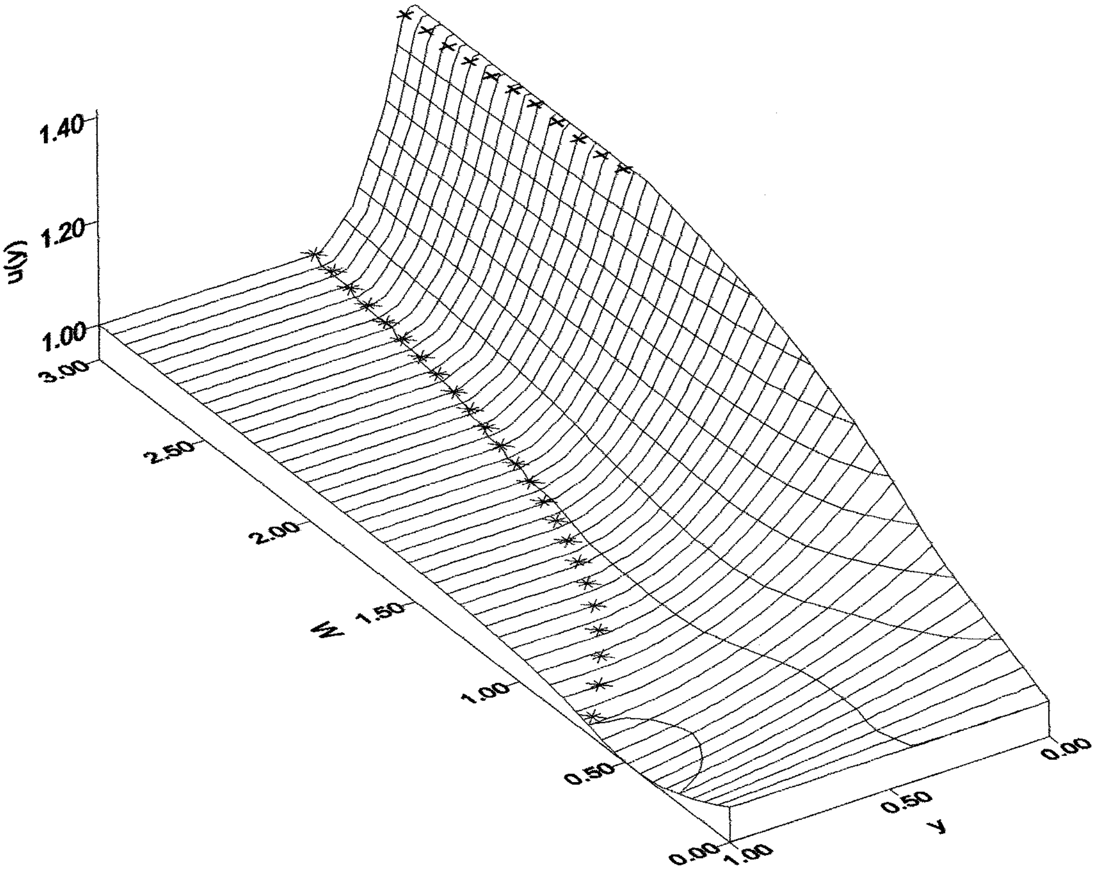

FIGURE 3.7b. Surface plot to illustrate the across stream velocity, $u_D(y)$ versus rotation rate for the ambient fluid.

✳ $y = d$ the current outcrops on the free surface (Case B)
\+ $y = b$ the current outcrops on the bottom boundary (Case C)

Case A - For non-rotating currents, ($W = 0$) the velocity of the ambient fluid is constant across the stream. As the level of rotation is increased to $W = 0.5$, a minimum in the velocity occurs at the l.h. wall ($y = 1$), whilst at the r.h. wall ($y = 0$) the velocity increases steadily.

Case B - In the free stream the velocity, U_D between $1 < y < d$ is constant and tends to 1 as W is increased. Beneath the current the velocity of the ambient fluid increases towards the r.h. wall ($y = 0$). The gradient of $u_D(y)$ increases at greater levels of rotation.

Case C - Beneath the current there is a strong shear across stream. At $y = b$ the velocity is constant $u_D(b) = 2^{\frac{1}{2}}$, whilst at $y = d$ the velocity $u_D(d) = 1$.

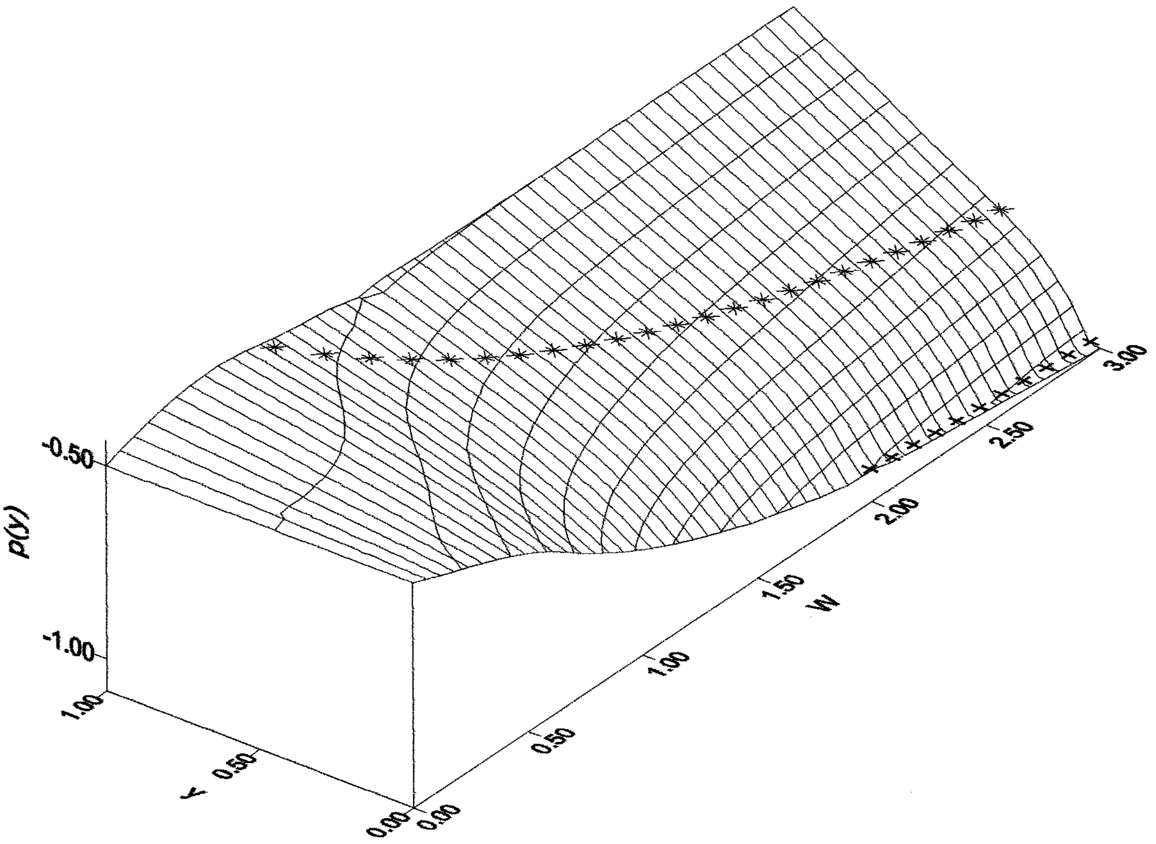

FIGURE 3.7c. Surface plot to illustrate the across stream pressure, $p(y)$ versus rotation rate for the ambient fluid.

✳ $y = d$ the current outcrops on the free surface (Case B)
+ $y = b$ the current outcrops on the bottom boundary (Case C)

Case A - For non-rotating currents, ($W = 0$) the across stream pressure is constant. As the level of rotation is increased to $W = 0.5$, the pressure rises to a maximum at the l.h. wall ($y = 1$), whilst at the r.h. wall ($y = 0$) the pressure decreases steadily.

Case B - In the free stream the pressure is greatest at the l.h. wall increasing linearly between $y = d$ and $y = 1$. Beneath the current the pressure continues to decrease to a minimum value at the r.h. wall. The pressure at $y = 0$ decreases as the level of rotation is increased..

Case C - At y = b the pressure continues to decrease as W increases.

CHAPTER 4

Theoretical results (1)

4.1 Energy dissipation

By way of an introduction I shall begin this chapter by summarising the method used to include energy loss in the non-rotating gravity current theory (Benjamin, 1968). This forms the foundation on which I have based the extension of the rotating energy conserving theory. In considering the difficulty of including dissipation Hacker suggested examining the case of uniform energy loss across the channel and indeed it is this assumption which is made in the subsequent analysis.

4.1.1 Background to the energy loss theory

Benjamin (1968) approached the problem of including the effects of energy loss by considering the propagation of a cavity of air along the upper boundary of a horizontal box as fluid is discharged at one end freely under gravity. When the flow has become steady the energy conserving theory predicts that the cavity will fill half the depth of the box and will propagate at speed c_1 as defined in (3.1.6). Therefore the rate of discharge of the fluid and the flux of air into the cavity, per unit width, will be,

$$Q = c_1 (H - h). \tag{4.1.1}$$

Benjamin conjectures that in order to allow different rates of discharge then dissipation must occur, through the fluid experiencing a uniform loss of total head. The head loss term, Δe, is incorporated into the Bernoulli equation (3.1.1) to give,

$$c_2^2 = 2g(H - h - \Delta e). \tag{4.1.2}$$

Since momentum is conserved between positions far upstream and downstream, (3.1.3) may be rearranged and the continuity equation (3.1.4) applied, to give an expression for c_2,

$$c_2^2 = \frac{g(H^2 - h^2)H}{(2H - h)h}. \tag{4.1.3}$$

An expression for Δe is obtained by equating (4.1.3) with (4.1.2) to give,

$$\Delta e = \frac{(2h - H)(H - h)^2}{2h(2H - h)} \tag{4.1.4}$$

(4.1.4) confirms that the energy conserving depth is $h = \frac{1}{2}H$. Energy loss is possible when h is greater than this depth. Depths less than the dissipationless depth are unlikely as these would require a gain in energy. In order to quantify the rate of discharge an expression is first required for c_1. This is obtained by substituting the continuity equation (3.1.4) in to the momentum equation (4.1.3) which becomes,

$$\frac{c_1}{(gH)^{\frac{1}{2}}} = \frac{\{h(H^2 - h^2)\}^{\frac{1}{2}}}{\{H^2(2H - h)\}^{\frac{1}{2}}}. \tag{4.1.5}$$

Substituting (4.1.5) into the expression for the discharge (4.1.1) and non-dimensionalising gives,

$$\frac{Q}{(gH^3)^{\frac{1}{2}}} = \frac{\{ (H - h)^2 h\, (H^2 - h^2)\}^{\frac{1}{2}}}{\{H^4(2H - h)\}^{\frac{1}{2}}} \tag{4.1.6}$$

Figure 4.1 illustrates the relationship between the non-dimensional variables, Q, c_1 and Δe, which are plotted against h/H.

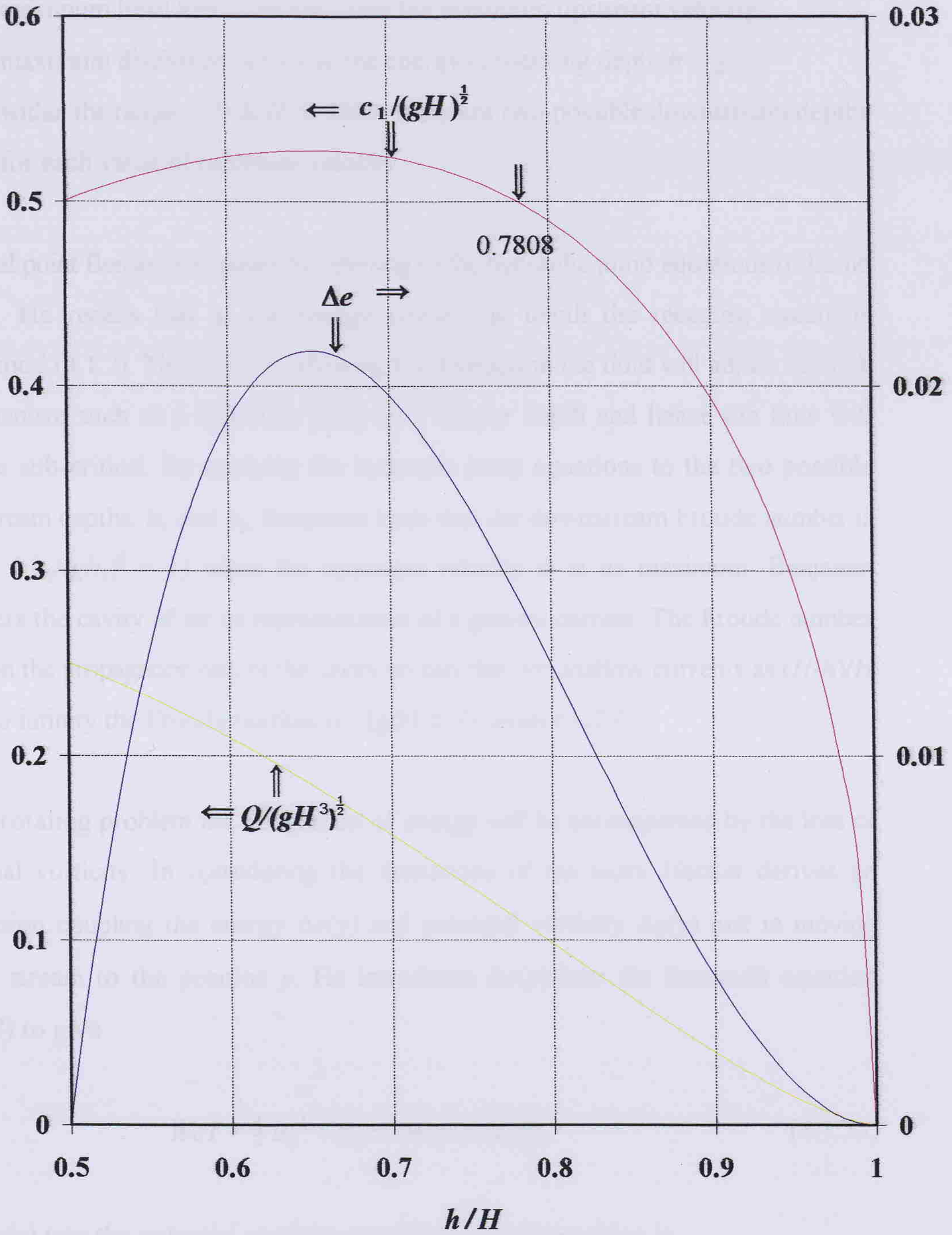

FIGURE 4.1. Solutions of the non-rotating energy loss theory (Benjamin 1968) for the upstream velocity, $c_1/(gH)^{\frac{1}{2}}$, head loss, Δe and non-dimensionalised discharge $Q/(gH^3)^{\frac{1}{2}}$ versus fractional depth, h/H as defined in figure 3.1.

Note that the -

- maximum head loss coincides with the maximum upstream velocity.
- maximum discharge occurs at the energy conserving depth $h = \frac{1}{2}H$.
- within the range $0.5<h/H<0.7808$ there are two possible downstream depths for each value of upstream velocity.

This final point Benjamin explains by referring to the hydraulic jump equations of Lamb (1932). He recalls that at the energy conserving depth the receding stream is supercritical (3.1.7). Therefore, by allowing for dissipation the fluid will adjust through a mechanism such as a hydraulic jump to a deeper depth and hence the flow will become sub-critical. By applying the hydraulic jump equations to the two possible downstream depths, h_1 and h_2, Benjamin finds that the downstream Froude number is critical ($c_2/(gh_1)^{\frac{1}{2}} = 1$) when the upstream velocity is at its maximum. Benjamin considers the cavity of air as representative of a gravity current. The Froude number based on the propagation rate of the cavity reveals that for shallow currents as $(H\text{-}h)/H$ tends to infinity the Froude number $(c_1/(g(H\text{-}h))^{\frac{1}{2}})$ tends to $(2)^{\frac{1}{2}}$.

In the rotating problem the dissipation of energy will be accompanied by the loss of potential vorticity. In considering the limitations of his work Hacker derives an expression coupling the energy $\Delta e(y)$ and potential vorticity $\Delta q(y)$ lost in moving across stream to the position y. He introduces $\Delta e(y)$ into the Bernoulli equation (3.2.28) to give

$$WcY = \tfrac{1}{2}\, u_D^{\frac{1}{2}} + p_D + \ Wcy + \Delta e(y), \qquad (4.1.7a)$$

and $\Delta q(y)$ into the potential vorticity equation (3.2.15) resulting in

$$\frac{du_D}{dy} + W(1-\eta)\Delta q(y) = -W\eta_{.} \qquad (4.1.7b)$$

Continuity of volume flux (3.2.31) between the positions b and y yields

$$cY(y) = \int_b^y u_D(s)\,(1-\eta(s))\,ds. \tag{4.1.8}$$

Substituting (4.1.7*a&b*) and (3.2.9) into (4.1.8) gives

$$\Delta e(y) - \Delta e(b) = W\int_b^y u_D(s)\Delta q(s)(1-\eta(s))\,ds. \tag{4.1.9}$$

which shows that if there is variation in energy loss across stream then there will be an associated pertubation in the potential vorticity flux . Hacker identified the difficulties in solving (4.1.9) due to insufficient information. However as a first step he suggests examining the case of

$$\Delta e(y) = \text{constant},$$

where according to (4.1.9)

$$\Delta q(y) = 0$$

This concludes the discussion of the background to the energy loss theory. In the following section (4.1.2) the rotating energy loss theory is presented. The approach taken to include dissipation in the present study is based on the method used by Benjamin for the non-rotating case. In § 4.1.2. a head loss term is introduced into the Bernoulli equation (3.2.25) and the assumption of uniform energy loss across the stream is made. Next in § 4.1.3. a solution for the propagation rate of the interface, c, is obtained using the continuity equation, which replaces the Bernoulli equation (3.2.30) in the energy conserving solution. In § 4.1.4. the momentum integral is solved using a similar method to that employed by Hacker for the energy conserving case, however here the volume flux, $Q(0;y)$ is retained, rather than the equivalent Bernoulli function (3.2.37). For each case the momentum equation is expressed in terms of one of the principle variables, with W and η_0 retained as pre-set constants, and solved numerically using the Newton-Raphson method. The governing equation for the energy loss is applied to each of the flow geometries and this completes § 4.2. The results are discussed in § 4.3 and a comparison with the non-rotating theory is made in the final section § 4.4.

4.1.2 Governing equation quantifying energy loss

The energy conserving theory predicts a unique upstream volume flux in the current for each level of rotation. If the volume flux is restricted in some way, then the energy conserving state will not be possible. The volume flux and hence the level of dissipation is set by the fractional depth of the current. To quantify this dissipation a head loss term is introduced into the Bernoulli equation (3.2.25) and applied at the right hand boundary of the ambient fluid to give

$$B_D(b) = \tfrac{1}{2}\, u_D{}^2 + p_D + Wcb + \Delta e(b). \qquad (4.1.10)$$

According to equation (4.1.9) the only case where potential vorticity is conserved whilst energy is lost, is that where the energy loss is uniform across the stream, that is

$$\Delta e(b) = \Delta E = \text{constant}.$$

To obtain a solution for ΔE the momentum integral (3.2.34) is solved as follows. Firstly the upstream integral is evaluated using (3.2.11), (3.2.26) and recalling that $u_u = c$ (3.2.34) becomes

$$\tfrac{1}{2}\, c^2 = \int_{Aa} (\, u_D{}^2 + p_D \,)\, dA + \int_{A_c} p_c\, dA + W \int_{Va} v\, dV. \qquad (4.1.11)$$

Integrating the first integral with respect to z gives

$$\int_{Aa} (u_D{}^2 + p_D\,)\, dA = \int_b^1 (u_D{}^2 + p_D\,)\,(1 - \eta)\, dy. \qquad (4.1.12)$$

To solve (4.1.12) the following substitution is required. Continuity of volume flux (3.2.31) between y_0 and y gives

$$Q_D(y_0; y) = \int_{y_0}^{y} u_D(y)\,(1 - \eta(y))\, dy$$

which according to (3.2.32) and (3.2.37) becomes

$$Q_D(y_0; y_1) = \frac{1}{W}\left[\tfrac{1}{2}u_D^2 + p_D + Wcy\right]_{y_0}^{y} = \frac{1}{W}\left[B_D\right]_{y_0}^{y} \qquad (4.1.13)$$

therefore

$$(\tfrac{1}{2}u_D^2 + p_D)\big|_{y} = B_D(y) - B_D(y_0) + (\tfrac{1}{2}u_D^2 + p_D)\big|_{y_0} - Wcy\big|_{y} + Wcy\big|_{y_0}. \qquad (4.1.14)$$

Substituting (4.1.14) into(4.1.12) gives

$$\int_b^1 (u_D^2 + p_D)(1 - \eta)\, dy = \int_b^1 (B_D(y) - Wcy + \tfrac{1}{2}u_D^2 - \eta(u_D^2 + p_D)\, dy +$$

$$(1 - b)\left\{-B_D(b) + Wcb + \tfrac{1}{2}u_D^2(b) + p_D(b)\right\}. \qquad (4.1.15)$$

The third integral in (4.1.11) is simplified by substituting (3.2.36) into (3.2.35) and noting that $Q_D(0, y) = 0$ when $y \in [0, b]$ gives

$$W\int_{V_a} v\, dV = W\int_0^b cy + W\int_b^1 (cy - Q_D(y))\, dy.$$

Using (3.2.37) the above becomes

$$W\int_{V_a} v\, dV = \tfrac{1}{2}Wcb^2 + \int_b^1 (Wcy - B_D(y))\, dy. \qquad (4.1.16)$$

Substituting (4.1.15) and (4.1.16) into the momentum integral (4.1.11) gives

$$\tfrac{1}{2}c^2 = \int_b^1 (\tfrac{1}{2}u_D^2 - \eta(u_D^2 + p_D))\, dy + (1 - b)\left\{-B_D(b) + Wcb + \tfrac{1}{2}u_D^2(b) + p_D(b)\right\} +$$

$$\int_{A_c} p_c\, dA + \tfrac{1}{2}Wcb^2 \qquad (4.1.17)$$

The pressure fields (3.2.12) and (3.2.13) are substituted into the first integral in (4.1.17), noting that $\eta = 0$ for $y \in [d, 1]$

$$\int_b^1 \tfrac{1}{2}u_D^2 - \eta(u_D^2 + p_D)\, dy =$$

$$\int_b^d (\tfrac{1}{2}u_D^2 - \eta u_D^2 + \eta^2 + \eta Wcy)\, dy + \tfrac{1}{2}U_D^2(1 - d). \qquad (4.1.18)$$

The pressure field for the current (3.2.10) is substituted into the second integral in (4.1.17), noting that $\eta = 1$ for $y \in [0, b]$

$$\int_{A_c} p_c\, dA = -\tfrac{1}{2}\, b - \tfrac{1}{2} Wcb^2 + \int_b^d -\tfrac{1}{2}\,\eta^2 - Wcy\eta\; dy. \qquad (4.1.19)$$

When (4.1.18) and (4.1.19) are substituted into (4.1.17) the momentum integral becomes

$$\tfrac{1}{2}c^2 = \int_b^d \left(\tfrac{1}{2}\, u_D{}^2 - \eta u_D{}^2 + \tfrac{1}{2}\eta^2\right)\, dy + \tfrac{1}{2}\, U_D^2(1 - d) - \tfrac{1}{2}\, b + (1 - b)\left\{-B_D(b) + Wcb + \tfrac{1}{2}\, u_D{}^2(b) + p_D(b)\right\} \qquad (4.1.20)$$

The head loss term is introduced into (4.1.20) through the Bernoulli function (4.1.10), hence (4.1.20) becomes

$$\tfrac{1}{2}c^2 = \int_b^d \left(\tfrac{1}{2}\, u_D{}^2 - \eta u_D{}^2 + \tfrac{1}{2}\eta^2\right) dy + \tfrac{1}{2}\, U_D^2(1 - d) - \tfrac{1}{2}\, b + (1 - b)\, \{-\Delta E\}. \qquad (4.1.21)$$

Making use of the potential vorticity equation (3.2.16), the geostrophic equation (3.2.9) and the across stream ambient pressure (3.2.12) enables (4.1.21) to be expressed in terms of exact differentials. It is then easily integrated to give

$$c^2 = \frac{1}{W}\left[\tfrac{2}{3}u_D{}^3 - \eta u_D\right]_b^d + U_D^2(1 - d) - b + 2(1 - b)\, \{-\Delta E\}. \qquad (4.1.22)$$

Rearranging (4.1.22) gives the governing energy loss equation with

$$\Delta E = \frac{1}{2\,(1 - b)} \left\{\frac{1}{W}\left[\tfrac{2}{3}u_D{}^3 - \eta u_D\right]_b^d + U_D^2(1 - d) - b - c^2\right\}. \qquad (4.1.23)$$

The solutions for ΔE as W and η_0 are varied are illustrated in figure 4.2(a).

4.1.3 Continuity of volume flux

Continuity of volume flux is described by the integral (3.2.31). To integrate (3.2.31) the potential vorticity equation (3.2.16) and the geostrophic equation (3.2.9) are used, enabling (3.2.31) to be expressed in terms of exact differentials, hence

$$c = \int_b^1 u_D(y)\,(1 - \eta(y))\,dy$$

$$= \frac{1}{W}\left(\int_b^d + \int_d^1\right)\left(\frac{dp_D}{dy} + Wc + u_D\frac{du_D}{dy}\right)dy$$

$$= \frac{1}{W}\left[\,p_D + Wcy + \tfrac{1}{2}\,u_D^{\,2}\right]_b^d + \frac{1}{W}\left[\,p_D + Wcy + \tfrac{1}{2}\,u_D^{\,2}\right]_d^1$$

Substituting for the downstream pressure fields, (3.2.12) and (3.2.13), yields

$$c = \frac{1}{W}\left[\tfrac{1}{2}\,u_D^{\,2}(1) - \eta(d) + WU_D(1-d) + \eta(b) - \tfrac{1}{2}\,u_D^{\,2}(b)\right]. \qquad (4.1.24)$$

Comparing this to the expression for c derived previously using the Bernoulli function (3.2.30) it is apparent that there are two new terms $(\eta(b), -\frac{1}{2}u_D^{\,2}(b))$. In the dissipationless case these terms cancel because of their relationship through the Bernoulli function, $B_D(b) = 0$ (3.2.29).

4.1.4 Conservation of momentum

The momentum integral is solved in a similar manner to that used in § 4.1.2, however the discharge, Q_D, is retained and the substitution of the Bernoulli function does not take place. A substitution is once again required for the first integral (4.1.12) in the momentum equation (4.1.11). According to (4.1.13)

$$W\left[Q_D\right]_{y_0}^{y} = \left[\tfrac{1}{2}\,u_D^{\,2} + p_D + Wcy\right]_{y_0}^{y}$$

therefore

$$\left(\tfrac{1}{2}\,u_D^{\,2} + p_D\right)\Big|_y = W(Q_D(y) - Q_D(y_0)) + \left(\tfrac{1}{2}\,u_D^{\,2} + p_D\right)\Big|_{y_0} - Wcy\big|_y + Wcy\big|_{y_0}. \qquad (4.1.25)$$

Substituting (4.1.25) into (4.1.12) gives

$$\int_b^1 \left(u_D^{\,2} + p_D\right)(1 - \eta)\,dy = \int_b^1 \left(W\left(Q_D(y) - cy\right) + \tfrac{1}{2}\,u_D^{\,2} - \eta\left(u_D^{\,2} + p_D\right)\right)dy\ +$$

$$(1-b)\left\{W(-Q_D(b) + cb) + \tfrac{1}{2}\,u_D^{\,2}(b) + p_D(b)\right\}. \qquad (4.1.26)$$

The expression derived previously for the cross stream velocity volume integral (4.1.16) and (4.1.26) are substituted into the momentum integral (4.1.11) which becomes

$$\tfrac{1}{2}c^2 = \int_b^1 \tfrac{1}{2}\, u_D{}^2 - \eta(u_D{}^2 + p_D)\, dy + (1-b)\left\{\, W(-Q_D(b) + cb) + \tfrac{1}{2}\, u_D{}^2(b) + p_D(b)\right\}$$
$$+ \int_{A_c} p_c\, dA + \tfrac{1}{2}Wcb^2 \qquad (4.1.27)$$

The pressure fields (3.2.12) and (3.2.13) are substituted into the first integral in (4.1.27) to give (4.1.18) and the across stream pressure for the current (3.2.10) is substituted into the second integral to give (4.1.19), as in § 4.1.2. These are then substituted into (4.1.27) which becomes

$$\tfrac{1}{2}c^2 = \int_b^d \tfrac{1}{2}\, u_D{}^2 - \eta u_D{}^2 + \tfrac{1}{2}\eta^2\, dy + \tfrac{1}{2}\, U_D{}^2(1-d) - \tfrac{1}{2}\, b +$$
$$(1-b)\left\{\, W(-Q_D(b) + cb) + \tfrac{1}{2}\, u_D{}^2(b) + p_D(b)\right\} \qquad (4.1.28)$$

Assuming $Q(b) = 0$ and applying (3.2.12) at $y = b$ the expression above becomes

$$c^2 = \int_b^d (\, u_D{}^2 - 2\eta u_D{}^2 + \eta^2)\, dy + U_D{}^2(1-d) - b + 2(1-b)\left\{\tfrac{1}{2}\, u_D{}^2(b) - \eta(b)\right\}.$$

(4.1.29)

As in § 4.1.2. the potential vorticity equation (3.2.16) and the geostrophic equation (3.2.9) along with the across stream pressure (3.2.12) are used to express (4.1.29) in terms of exact differentials.

$$c^2 = \frac{1}{W}\left[\tfrac{2}{3}u_D{}^3 - \eta u_D\right]_b^d + U_D{}^2(1-d) - b + 2(1-b)\,\{\tfrac{1}{2}\, u_D{}^2(b) - \eta(b)\}. \qquad (4.1.30)$$

As with the continuity equation (4.1.24) there are two new terms which would cancel in the dissipationless case where $\tfrac{1}{2}\, u_D{}^2(b) = \eta(b)$ according to (3.2.29).

4.1.5 Governing equations

To summarise, the governing equations are as follows:

Energy loss

$$\Delta E = \frac{1}{2\,(1-b)}\left\{\frac{1}{W}\left[\tfrac{2}{3}u_D{}^3 - \eta u_D\right]_b^d + U_D^2(1-d) - b - c^2\right\} \qquad (4.1.23)$$

Continuity

$$c = \frac{1}{W}\left[\tfrac{1}{2}\,u_D{}^2(1) - \eta(d) + WU_D(1-d) + \eta(b) - \tfrac{1}{2}\,u_D{}^2(b)\right] \qquad (4.1.24)$$

Momentum

$$c^2 = \frac{1}{W}\left[\tfrac{2}{3}u_D{}^3 - \eta u_D\right]_b^d + U_D^2(1-d) - b + 2(1-b)\left\{\tfrac{1}{2}\,u_D{}^2(b) - \eta(b)\right\}. \qquad (4.1.30)$$

The governing equations are defined in terms of $\eta(y)$, $u_D(y)$, c,b and d, which are all functions of u_0 and the pre-set constants W and η_0, where

$y \in [b, d]$ $\quad \eta(y) = \eta_0 \cosh Wy - u_0 \sinh Wy$ (3.2.19)

$y \in [0, b]$ $\quad \eta(y) = 1$

$y \in [d, 1]$ $\quad \eta(y) = 0$

$y \in [b, d]$ $\quad u_D(y) = u_0 \cosh Wy - \eta_0 \sinh Wy$ (3.2.22)

$y \in [d, 1]$ $\quad u_D(y) = U_D = \text{constant}$

$U_D = u_0 \cosh Wd - \eta_0 \sinh Wd.$ (3.2.23)

For

Case A $\quad b = 0 \qquad d = 1$

Case B $\quad b = 0 \qquad d = W^{-1} \operatorname{arctanh}(\eta_0 / u_0)$ (3.2.20)

$U_D = u_0 \cosh Wd - \eta_0 \sinh Wd$ (3.2.23)

Case C $\quad d$ and U_D as for Case B

$\eta(b) = 1 = \eta_0 \cosh Wb - u_0 \sinh Wb.$ (3.2.21)

4.2 Solution of the governing equations

4.2.1 Case A

4.2.1.1 Solution for Case A

For case A the governing equations (4.1.23), (4.1.24) and (4.1.30) become

Energy loss

$$\Delta E = \frac{1}{W}\left[\tfrac{1}{3}\, u_D(1)^3 - \tfrac{1}{2}\, \eta(1)u_D(1) - \tfrac{1}{3}\, u_0^3 + \tfrac{1}{2}\, \eta_0\, u_0\right] - \tfrac{1}{2}\, c^2. \qquad (4.2.1)$$

Continuity

$$c = \frac{1}{W}\left[\tfrac{1}{2}\, u_D^2(1) - \eta(1) + \eta_0 - \tfrac{1}{2}\, u_0^2\right]. \qquad (4.2.2)$$

Momentum

$$c^2 = \frac{1}{W}\left[\tfrac{2}{3}\, u_D^3(1) - \eta(1)u_D(1) - \tfrac{2}{3}\, u_0^3 + \eta_0 u_0\right] + u_0^2 - 2\eta_0\,. \qquad (4.2.3)$$

The flow structure equations (3.2.19) and (3.2.22) for case A become

$$\eta(1) = \eta_0 \cosh W - u_0 \sinh W \qquad (4.2.4)$$

and

$$u_D(1) = u_0 \cosh W - \eta_0 \sinh W \qquad (4.2.5)$$

respectively. The momentum equation (4.2.3) is rearranged to give

$$0 = \tfrac{2}{3}\, u_D^3(1) - \eta(1)u_D(1) - \tfrac{2}{3}\, u_0^3 + \eta_0 u_0 + W\left(u_0^2 - 2\eta_0 - c^2\right). \qquad (4.2.6)$$

By substituting the continuity (4.2.2) and the flow structure equations (4.2.4) and (4.2.5), into (4.2.6) an equation as a function of u_0 with η_0 and W as constants is obtained. This is then solved using a numerical method.

4.2.1.2 Asymptotic solution as W⇒0

Before proceeding with the solution for case A ($y \in [0, 1]$), it is important to confirm that as W approaches zero the governing equations reduce to those of the non-rotating case. Using the Maclaurin expansion for hyperbolic functions the expressions (3.2.19) and (3.2.22) become

$$\eta(y) = \eta_0 - Wy\, u_0 \tag{4.2.7a}$$

and

$$u_D(y) = u_0 - Wy\, \eta_0 \tag{4.2.7b}$$

respectively. Applying (4.2.7 a&b) at $y = 1$ gives

$$\eta(1) = \eta_0 - W u_0 \tag{4.2.8a}$$

and

$$u_D(1) = u_0 - W \eta_0 \tag{4.2.8b}$$

Substituting (4.2.8 a&b) into the continuity equation (4.2.2) gives

$$c = u_0(1 - \eta_0) + O(W). \tag{4.2.9}$$

Substituting (4.2.8 a&b) into (4.2.3) gives

$$c^2 = -2u_0^2\eta_0 + 2u_0^2 + \eta_0^2 - 2\eta_0 + O(W) \tag{4.2.10}$$

On substituting (4.2.8 a&b) and making use of (4.2.10) the expression for energy loss (4.2.1) becomes

$$\Delta E = \eta_0 - \tfrac{1}{2}\, u_0^2 + O(W). \tag{4.2.11}$$

Now to compare the leading order terms in the expressions above with the non-rotating governing equations described in § 3.1.1 and § 4.1.1. The non-rotating expressions are non-dimensionalised and the notation used for the rotating theory is applied. The continuity equation (3.1.4) becomes

$$c = u_0(1 - \eta_0). \tag{4.2.12}$$

Hence (4.2.12) is equivalent to (4.2.9). The expression for the non-rotating conservation of momentum (3.1.3) becomes

$$c^2 = -2u_0^2\eta_0 + 2u_0^2 + \eta_0^2 - 2\eta_0, \tag{4.2.13}$$

confirming that (4.2.13) is equivalent to (4.2.10). Finally rearranging (4.1.2) to give an expression for the non-rotating energy loss as a function of the downstream depth and velocity gives

$$\Delta E = \eta_0 - \tfrac{1}{2}\, u_0^2, \tag{4.2.14}$$

which is equivalent to (4.2.11). Therefore the rotating energy loss solution tends to the non-rotating solution as W tends to zero, where $\eta_0 = \frac{1}{2}$, $u_0 = 1$ and $c = \frac{1}{2}$.

4.2.1.3 Transition point between cases A and B

In the energy loss solution the principle variables are a function of the two constants η_0 and W. As successive values of η_0 are considered for a particular level of rotation the depth at the l.h.wall, $\eta(1)$, will decrease until $\eta(1)$=0 i.e. the transition point between cases A and B. Therefore for every level of rotation for which the dissipationless geometry is that of case A, W_A, a transition will occur at some value of η_0. As W_A is increased the slope of the interface is greater and hence the transition will occur at larger values of η_0. To obtain the value of η_0 which coincides with the end-point of case A for each value of W_A, $\eta(1)$=0 is substituted into (4.2.4), (4.2.5) and (4.2.2) to give

$$u_0 = \frac{\eta_0}{\tanh W_A}, \tag{4.2.15}$$

$$u_D(1) = \frac{\eta_0}{\sinh W_A}, \tag{4.2.16}$$

$$c = \frac{1}{W_A}\left[\eta_0 - \frac{\eta_0^2}{2\tanh^2 W_A} + \frac{\eta_0^2}{2\sinh^2 W_A}\right] \tag{4.2.17}$$

respectively. Substituting the above into (4.2.6) gives the momentum equation in terms of η_0, which is solved numerically to give

W	η_0	u_0	c
0.67	0.6842	1.1697	0.6719
0.6	0.5686	1.0588	0.6783
0.5	0.4166	0.9016	0.6597
0.4	0.2813	0.7405	0.6044
0.3	0.1663	0.5710	0.5083
0.2	0.0770	0.3904	0.3704
0.1	0.0198	0.1987	0.1961

TABLE 4.1 Values of W, η_0, u_0 and c (to 4d.p) for the transition points between cases A and B.

From table 1 it is apparent that for $W = 0.1$ the current fills the full width of the channel for all but very shallow depths $\eta_0 < 0.020$, whilst for $W = 0.67$ the case A geometry only occurs between the energy conserving depth $\eta_0 = 0.685$ and $\eta_0 = 0.684$. The transition between case A and B in the energy conserving solution occurs at $W = 0.671$.

4.2.1.4 Numerical solution for case A

The roots of (4.2.6) are obtained using the Newton-Raphson method. The first approximation is taken as the energy conserving solution of u_0 for a particular value of η_0 and W. The aim is to obtain a set of solutions for u_0 at successive values of η_0 for which $\eta(1)$ is positive i.e. case A. η_0 is decreased in steps of 0.01. At each step a number of iterations are performed until u_0 converges to a solution. Generally a solution to 4 d.p. is obtained within 4 iterations. The initial approximation at each step is taken as the previous solution for u_0. The full solutions are plotted in § 4.3.

4.2.2 Case B

4.2.2.1 Solution for Case B

For case B the governing equations (4.1.23), (4.1.24) and (4.1.30) become

Energy loss

$$\Delta E = \frac{1}{W}\left[\tfrac{1}{3} U_D^3 - \tfrac{1}{3} u_0^3 + \tfrac{1}{2}\eta_0 u_0 \right] + \tfrac{1}{2}U_D^2(1-d) - \tfrac{1}{2} c^2 \tag{4.2.18}$$

Continuity

$$c = \frac{1}{W}\left[\tfrac{1}{2}U_D^2 + WU_D(1-d) + \eta_0 - \tfrac{1}{2} u_0^2 \right] \tag{4.2.19}$$

Momentum

$$c^2 = \frac{1}{W}\left[\tfrac{2}{3}U_D^3 - \tfrac{2}{3} u_0^3 + \eta_0 u_0 \right] + U_D^2(1-d) - 2\eta_0 + u_0^2 \tag{4.2.20}$$

The flow structure equations (3.2.19) and (3.2.22) for case B become

$$\eta(d) = 0 = \eta_0 \cosh Wd - u_0 \sinh Wd \tag{4.2.21}$$

and

$$u_D(d) = U_D = u_0 \cosh Wd - \eta_0 \sinh Wd \tag{3.2.23}$$

respectively. In the free-stream $\eta_0 = 0$ hence

$$d = W^{-1} \operatorname{arctanh} (\eta_0 / u_0) \qquad (3.2.20)$$

The momentum equation (4.2.20) is rearranged to give

$$0 = \tfrac{2}{3} U_D^3 - \tfrac{2}{3} u_0^3 + \eta_0 u_0 + W U_D^2 (1 - d) + W (u_0^2 - 2\eta_0 - c^2). \qquad (4.2.22)$$

4.2.2.2 Transition between cases C and B

For the energy conserving solution the transition from case B to C occurs at $W = 1.898$ (to 3 d.p). To obtain the dissipative solutions for case C ($1.898 \leq W \leq 3.0$) the value of η_0 is decreased from the respective energy conserving value until $\eta_0 = 1$ and $b = 0$, i.e. the starting point of case B. To obtain the transition values $\eta_0 = 1$ is inserted into the flow structure equations (4.2.21) and (3.2.23), and the continuity equation (4.2.19) to give

$$u_0 = \frac{1}{\tanh Wd}, \qquad (4.2.23)$$

$$U_D = \frac{1}{\sinh Wd}, \qquad (4.2.24)$$

$$c = \frac{1}{W} \left[\frac{1}{2} + \frac{W(1 - d)}{\sinh Wd} \right]. \qquad (4.2.25)$$

respectively. Substituting the above into (4.2.20) enables the momentum equation to be expressed in terms of d and solved numerically.

W	η_0	u_0	d	c
3.0	1	1.4108	0.2949	0.8684
2.9	1	1.4109	0.3051	0.8641
2.8	1	1.4110	0.3159	0.8596
2.7	1	1.4112	0.3276	0.8547
2.6	1	1.4113	0.3401	0.8495
2.5	1	1.4115	0.3536	0.8439
2.4	1	1.4118	0.3683	0.8379
2.3	1	1.4121	0.3841	0.8314
2.2	1	1.4125	0.4014	0.8244
2.1	1	1.4129	0.4203	0.8167
2.0	1	1.4135	0.4410	0.8084
1.9	1	1.4142	0.4639	0.7993

TABLE 4.2 Values for W, η_0, u_0, d and c (to 4 d.p.) for the transition points between cases C to B.

4.2.2.3 Numerical solution for case B

By substituting the continuity (4.2.19) and the flow structure equations (4.2.21), (3.2.23) and (3.2.20), into (4.2.22) an equation as a function of u_0 with η_0 and W as constants is obtained. This is solved using the numerical method described in § 4.2.1.4, with the exception that the first initial approximations for $0 < W < 0.671$ are taken as the end-points of case A (table 4.1). For the range $0.671 < W < 1.898$ the energy conserving values for case B are used. In the range $1.898 < W < 3.0$ the transition points between case C-B are required (table 4.2). The full solutions for case B are discussed in § 4.3.

4.2.3 Case C

4.2.3.1 Solution for case C

For case C the governing equations (4.1.23), (4.1.24) and (4.1.30) become

Energy loss

$$\Delta E = \frac{1}{2\,(1-b)} \left\{ \frac{1}{W} \left[\tfrac{2}{3} U_D{}^3 - \tfrac{2}{3} u_D(b)^3 + u_D(b) \right] + U_D{}^2(1-d) - b - c^2 \right\} \qquad (4.2.26)$$

Continuity

$$c = \frac{1}{W} \left[\tfrac{1}{2} U_D{}^2 + W U_D(1-d) + \eta(b) - \tfrac{1}{2}\, u_D(b)^2 \right] \qquad (4.2.27)$$

Momentum

$$c^2 = \frac{1}{W} \left[\tfrac{2}{3} U_D{}^3 - \tfrac{2}{3}\, u_D(b)^3 + u_D(b) \right] + U_D{}^2(1-d) - 2 - u_D(b)^2 - b u_D(b)^2 + b \qquad (4.2.28)$$

The flow structure equations (3.2.19) and (3.2.22) for case B become

$$\eta(b) = 1 = \eta_0 \cosh Wb - u_0 \sinh Wb \qquad (3.2.21)$$

and

$$u_D(b) = u_0 \cosh Wb - \eta_0 \sinh Wb \qquad (3.2.24)$$

respectively. In the free-stream $\eta(d) = 0$ hence

$$d = W^{-1} \operatorname{arctanh}\,(\eta_0 / u_0) \qquad (3.2.20)$$

remains valid. Rearranging (3.2.21) and equating with (3.2.20) gives

$$Wd = \operatorname{arctanh}[\,(u_0 \cosh Wb)^{-1} + \tanh Wb\,] \qquad (4.2.29)$$

The momentum equation (4.2.28) is rearranged to give

$$0 = \tfrac{2}{3}U_D{}^3 - \tfrac{2}{3}u(b)^3 + u_D(b) + WU_D{}^2(1 - d) + W\{u_D(b)^2 - 2 - bu_D(b)^2 + b - c^2\}. \tag{4.2.30}$$

4.2.3.2 Numerical solution for Case C

By substituting the continuity (4.2.27) and the flow structure equations (3.2.21), (3.2.24), (3.2.20) and (4.2.29), into the momentum equation (4.2.30) an equation as a function of b with η_0 and W as constants is obtained. This is solved using the numerical method described in § 4.2.1.4, where the first approximations are taken as the energy conserving solutions for b within the range $1.898<W<3.0$. The end-points of case C are listed in table 4.2. The full solutions for case C along with those for cases A and B are discussed in § 4.3.

4.3 Review of results with energy loss and simple flow

4.3.1 Properties of the solution

In the energy loss theory the principal variables are a function of two parameters, i.e. η_0 and W. To illustrate the solutions the results are plotted on contour graphs. The following symbols are used; ▽ dissipationless solution, + transition from case A to B, and ✳ transition from case B to C. Each symbol is labelled with its respective value. The method used to contour the results is Delaunay Triangulation and the data set consists of more than 3000 data points. Figs. 4.2 a & b show the solutions for ΔE and c. These two variables show similar behaviour. As η_0 is decreased from the energy conserving value at a particular level of rotation ΔE and c increase until they reach a maximum value. The maxima are marked with (.) and labelled with their respective values. The maxima for ΔE and c both occur in the same positions (W, η_0). However, for ΔE the values of the maxima generally decrease with increasing rotation, whilst for c the values increase. For each level of rotation within a certain range two depths are possible for a particular value of ΔE and c. For shallow depths, c becomes relatively

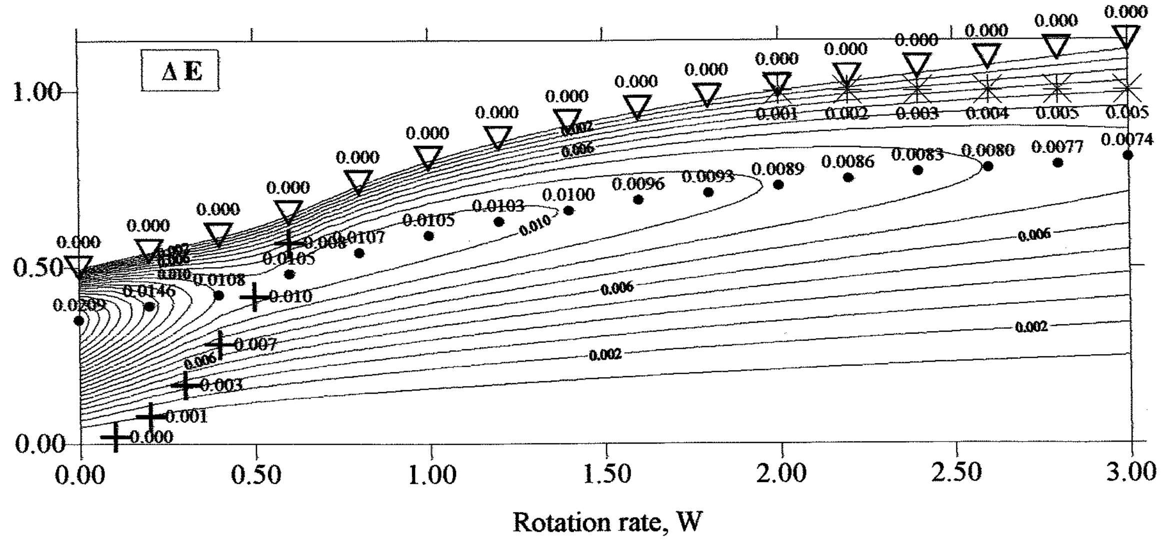

FIGURE 4.2a Contour plot of the solutions for the energy loss, ΔE, as the rotation rate, *W* and fractional depth, η(0) are varied.

▽ dissipationless solution (Hacker)
+ transition between Case A and B
✳ transition between Case B and C
● maximum value

If the upstream volume flux is restricted, then the energy conserving solution will not be possible. The volume flux and hence the level of dissipation are set by the fractional depth of the current. As the level of rotation is increased for a particular fractional depth, the energy loss decreases. For shallow currents the energy loss tends zero. A result consistent with that obtained by Benjamin for non-rotating gravity currents.

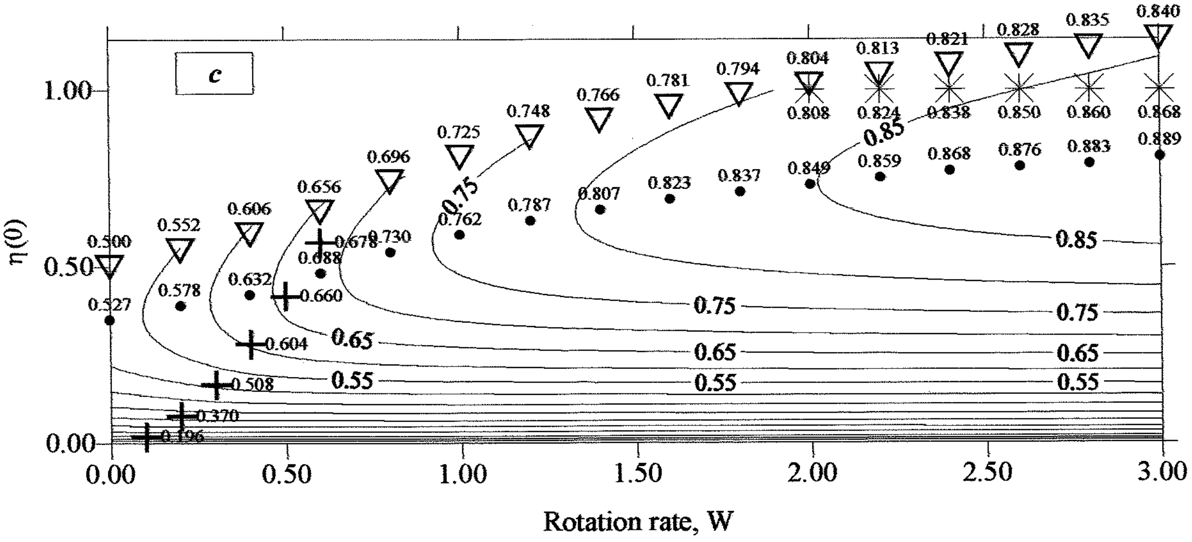

FIGURE 4.2b. Contour plot of the solutions for the front speed, *c* as the rotation rate, *W* and fractional depth, η(0) are varied. The maximum front speed coincides with the maximum energy loss, ΔE. Generally the front speed increases with rotation rate. However, at shallow depths the front speed becomes constant irrespective of the rotation rate.
(See figure 4.2a for explanation of symbols used)

constant and rotation has little effect. It is interesting to note that the energy loss tends to zero for shallow currents at all levels of rotation.

Figures 4.3 a and b, show the solutions for the ambient fluid velocities, u_0 and $u_D(d)$ respectively. In case A, where the current fills the full width of the channel, as the rotation rate increases for a particular depth, η_0, the velocity at the r.h. wall, u_0, decreases minimally from the non-rotating solution. Whilst at the l.h. wall the velocity, $u_D(1)$, increases. However, at very shallow depths rotation has no discernable effect on either of the velocities. What is striking is that once the current has departed from the l.h. wall the strength of rotation becomes ineffectual and consequently the velocity is primarily dependent on the depth, η_0. The velocity, $u_D(b)$, for the dissipationless case equals $(2)^{\frac{1}{2}}$, as the depth of the current is reduced this velocity decreases until the current no longer outcrops on the bottom boundary. The transition from $u_D(b)$ to u_0 at $\eta_0 = 1$ occurs smoothly. Figs 4.4 a & b illustrate the solutions for the widths b and d. In case C, b decreases from the dissipationless solution. For shallow currents the onset of case B, where the current outcrops on the surface ($y = d$), occurs at much lower levels of rotation than in the energy conserving case. As W increases the ratio of d/η_0 decreases as expected.

To investigate the effect of reducing the current depth on the ambient fluid across the stream, 3-D graphs similar to those in § 3.4 are presented. Note that here η_0 is varied rather than W. The surfaces in figs. 4.5 a & b are the across stream pressure, $p(y)$, and velocity, $u_D(y)$, respectively, for $W = 3.0$. The equations governing the structure of the flow in the energy conserving case are still applicable. Therefore as discussed in § 3.4 the pressure is a result of the hydrostatic and geostrophic pressure gradients. At the r.h. wall ($y = 0$) as η_0 is decreased the pressure increases. This is associated with a reduction in the velocity. In the energy conserving case the geostrophic pressure gradient causes the pressure to increase across the stream. As the depth is decreased the difference in pressure from b to d lessens, until the pressure becomes relatively constant across the stream. Hence the hydrostatic and geostrophic pressure gradients become virtually equivalent and the shear in the free stream around the current becomes insignificant. For the current the pressure is also constant across the stream

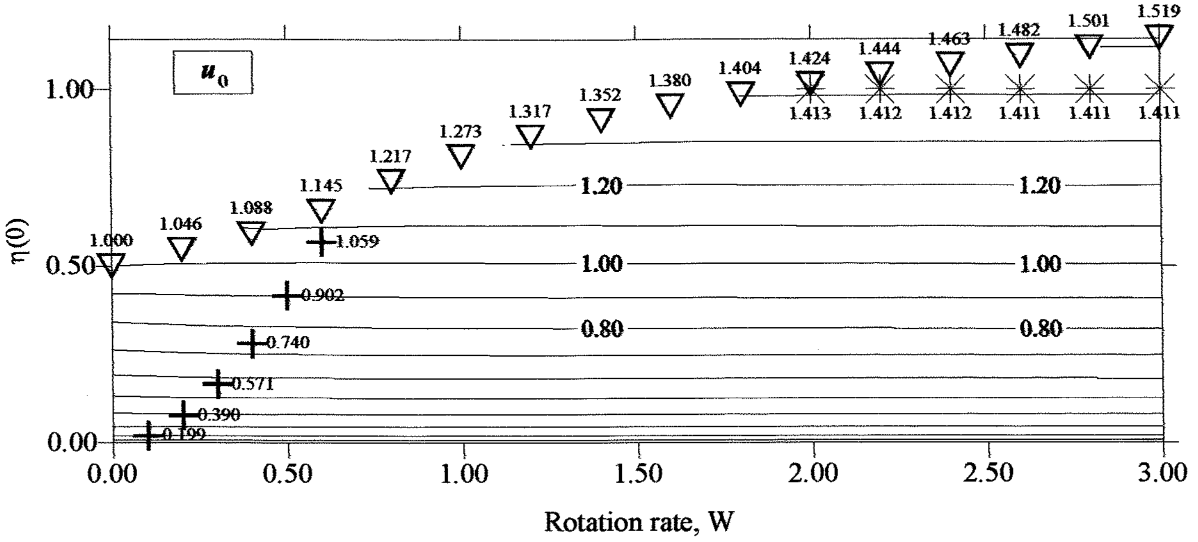

FIGURE 4.3a. Contour plot of the solutions for the ambient fluid velocity at the r.h. wall, u_0 as the rotation rate,W and the fractional depth,η(0) are varied. The velocity u_0 is dependent on the fractional depth of the current. The level of rotation has a minimal effect.
(see figure 4.2a for an explanation of the symbols used)

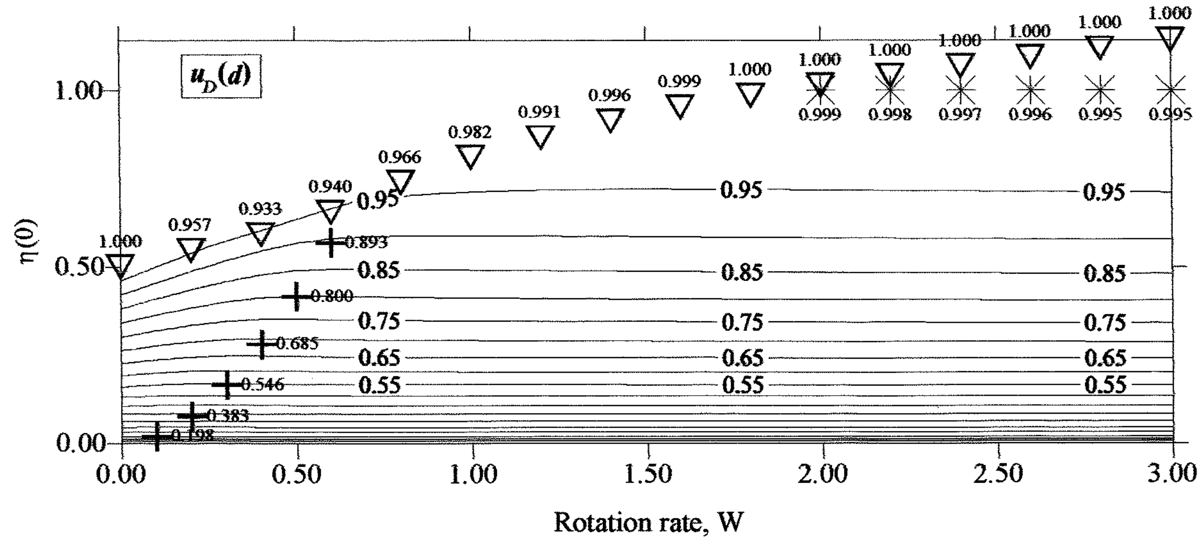

FIGURE 4.3b Contour plot of the solutions for the ambient fluid velocity $u_D(d)$, as the rotation rate, $W$and the fractional depth,η(0) are varied. For low rotation rates (Case A) the velocity increases with rotation for a particular fractional depth. At higher rotation rates the velocity, $u_D(d)$ is dependent on the fractional depth only.
(see figure 4.2a for an explanation of the symbols used)

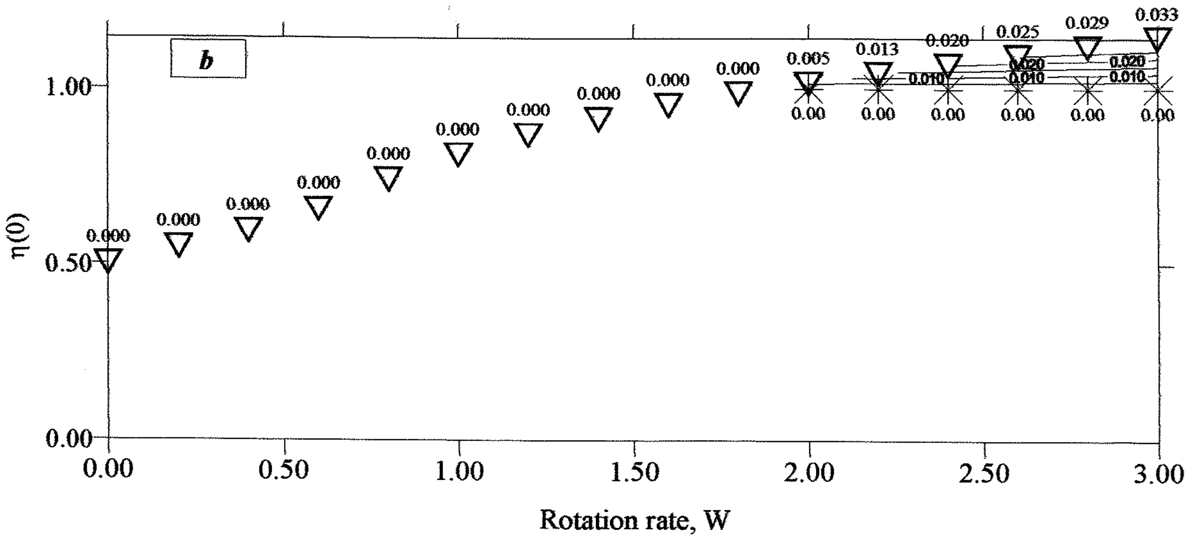

FIGURE 4.4a Contour plot of the solutions for the width of the current on the bottom boundary, *b* for Case C, as the rotation rate, *W* and fractional depth, η(0) are varied. In case C, *b* is seen to decrease from Hacker's dissipationless solution to zero at η(0)= 1, i.e. the transition from case B to C. (see figure 4.2a for an explanation of the symbols)

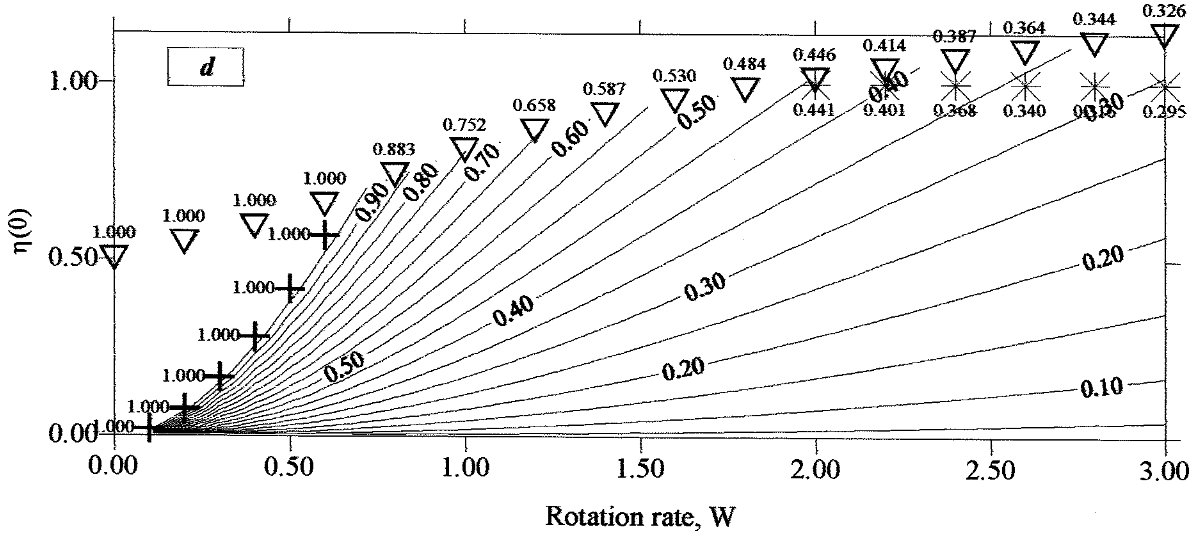

FIGURE 4.4b Contour plot of the width at which the current outcrops on the top boundary, *d* as the rotation rate, *W* and the fractional depth, η(0) are varied. The transition to case B occurs at much lower levels of rotation for shallower currents with energy loss. (see figure 4.2a for an explanation of the symbols used)

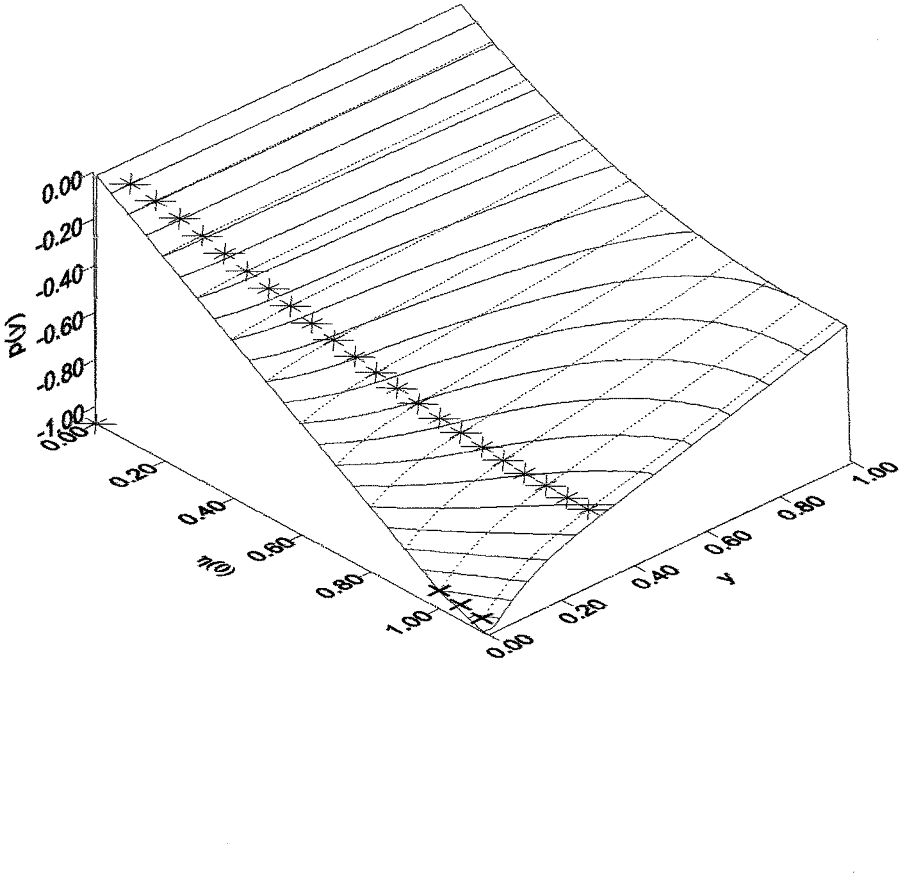

FIGURE 4.5a Surface plot to illustrate the across stream variation in pressure $p(y)$ for the ambient fluid where $W = 3.0$ (strongly rotating current), as the fractional depth η_0 is varied.

✳ $y = d$ the current outcrops on the free surface (transition from case A to B)

\+ $y = b$ the current outcrops on the bottom boundary (transition from case B to C)

For $W = 3.0$ the current has departed from the l.h. wall ($y = 1$) and outcrops at $y = d$ on the free surface. For the energy conserving depth the current fills the full depth of the channel, outcropping on the bottom boundary at $y = b$. Here the pressure increases across stream with the greastest pressure gradient beneath the current. As the fractional depth is decreased ,the across stream pressure increases, particularly at the r.h. wall ($y = 0$). At shallow depths the pressure is constant.

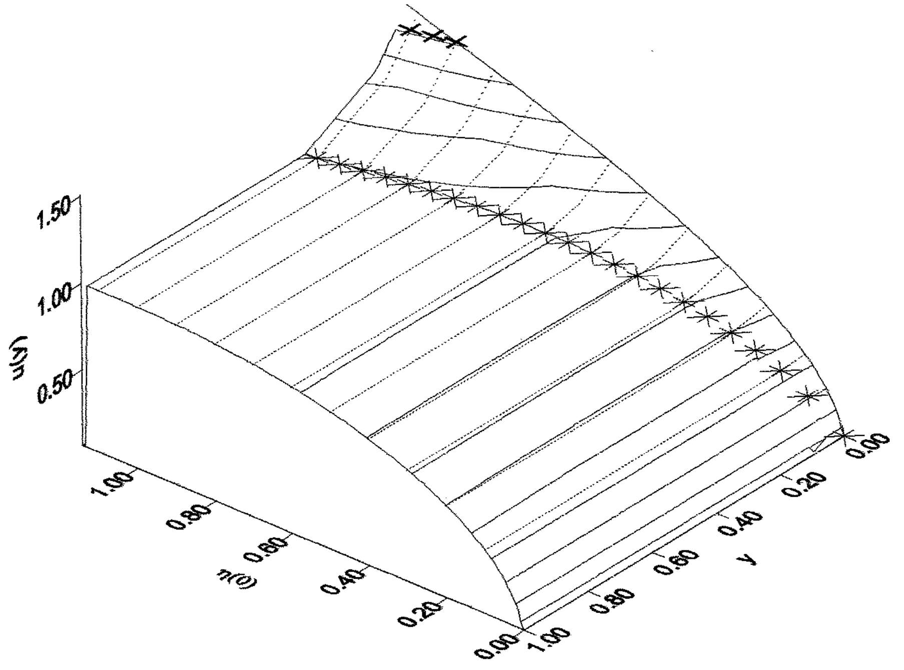

FIGURE 4.5b Surface plot to illustrate the across stream variation in velocity, $u_D(y)$ for the ambient fluid where $W = 3.0$ (strongly rotating current), as the fractional depth, η_0 is varied.

✳ $y = d$ the current outcrops on the free surface (transition from case A to B)
\+ $y = b$ the current outcrops on the bottom boundary (transition from case B to C)

For $W = 3.0$ the current has departed from the l.h. wall ($y = 1$) and outcrops at $y = d$ on the free surface. For the energy conserving depth the current fills the full depth of the channel, outcropping on the bottom boundary at $y = b$. Here there is a strong shear beneath the current. As the fractional depth is reduced the velocity is seen to decrease at the r.h. wall from $u_D(b) = 2^{\frac{1}{2}}$ tending to zero for shallow currents. In the free stream ($d \leq y \leq 1$) the velocity is constant and decreases for shallow currents.

according to (3.2.10). Although the pressure difference across the stream is minimal for shallow currents, if the ambient fluid is to be accelerated from up to downstream there must be a positive net momentum flux between up and downstream cross-sections, i.e. the pressure forces acting upstream must be greater than those due to buoyancy and the Coriolis forces acting downstream.

To consider this further the net momentum flux for the ambient fluid is calculated as η_0 and W are varied. The net momentum flux, M, i.e. the net force acting on the control volume is derived from (3.2.34) to give the same expression as in the energy conserving case where

$$M = \int_{Aa} (u_D{}^2)\, dA - \int_{Au} (c^2)\, dA. \tag{4.3.1}$$

The subscripts $_{Aa}$ and $_{Au}$ refer to the ambient fluid downstream and upstream respectively. By substituting (3.2.16) and (3.2.22) and using the hyperbolic identity for cosh $2x$ the integral (4.3.1) is solved for each of the cases A, B and C. Fig. 4.6 a shows the net momentum flux in the ambient fluid. For the energy conserving case the momentum flux decreases with greater rotation. This trend is also apparent when η_0 is held constant at a value less the dissipationless depth and the level of rotation is increased. However, M is more sensitive to a reduction in η_0. Initially M decreases nearly linearly until at shallower depths the decrease slows as M tends to zero. This implies that the forces acting downstream on the ambient fluid cross-section diminish considerably with decreasing η_0. Therefore, one would expect the mean velocity across the ambient cross-section to show a significant reduction as η_0 decreases. The mean velocity is as defined in Hacker's dissipationless theory, since the flow structure equations are unaltered by the loss of energy for this simple case, where

$$\bar{u}_D = \frac{\int_{Aa} (u_D(y))\, dA}{\int_{Aa} dA} = \frac{c}{\int_b^1 (1-\eta(y))\, dy}. \tag{4.3.2}$$

The integral in (4.3.2) is evaluated by substituting the exact differential (3.2.16). Hence the general solution is obtained which is solved for each flow geometry. The results are plotted in fig. 4.6 b. As expected the mean velocity, $\bar{u}_D$, decreases as the current becomes shallower. However there is not a decrease in $\bar{u}_D$ corresponding to the reduction in M as the level of rotation is increased. In fact $\bar{u}_D$ remains relatively constant for case B where $\eta_0 < 0.5$. As the level of rotation increases the cross-sectional area of the ambient fluid must also increase. To quantify the change in the cross-sectional area downstream in the ambient fluid, A_D, the following integral is evaluated,

$$A_D = \int_{Aa} dA = \int_b^1 (1 - \eta(y))\, dy. \tag{4.3.3}$$

The solutions for A_D are plotted in fig. 4.6 c. As W increases A_D increases in a similar manner to the decrease in the momentum flux. These theoretical results can be explained simply using a similar argument to that proposed by Hacker in his explanation for the increase in c with W. In the energy conserving case with simple flow, as W increases it causes A_D to become greater, however $\bar{u}_D$ remains relatively constant. Therefore, the downstream volume flux will increase. Hacker reasoned that the greater volume flux downstream would by continuity require an increase in the speed of the oncoming flow c. In the energy loss case from fig. 4.2 b one can see that when η_0 is large c increases as the level of rotation rises, however at shallow depths c becomes relatively constant. From fig. 4.6 a it is observed that at shallow depths as W is increased M remains close to zero. Therefore increasing W at shallow depths no longer causes a marked acceleration of the ambient fluid as it reaches the downstream cross-section. The cross-sectional area, A_D, is tending to 1 hence $\bar{u}_D$ tends to c. The effect on c of lowering the depth, η_0, for a constant value of W is that initially c increases until it reaches a maximum value which coincides with the maximum energy loss (fig. 4.2 b). Further reduction of η_0 causes c to decrease. Therefore the initial response to a reduction in η_0 is that the downstream volume flux in the ambient fluid must increase, in order to accommodate the increased speed of the upstream flow. In the range of depths greater than that at the maximum value of c this is indeed the case. The cross-sectional area increases, whilst the decrease in $\bar{u}_D$ is only slight. Below the

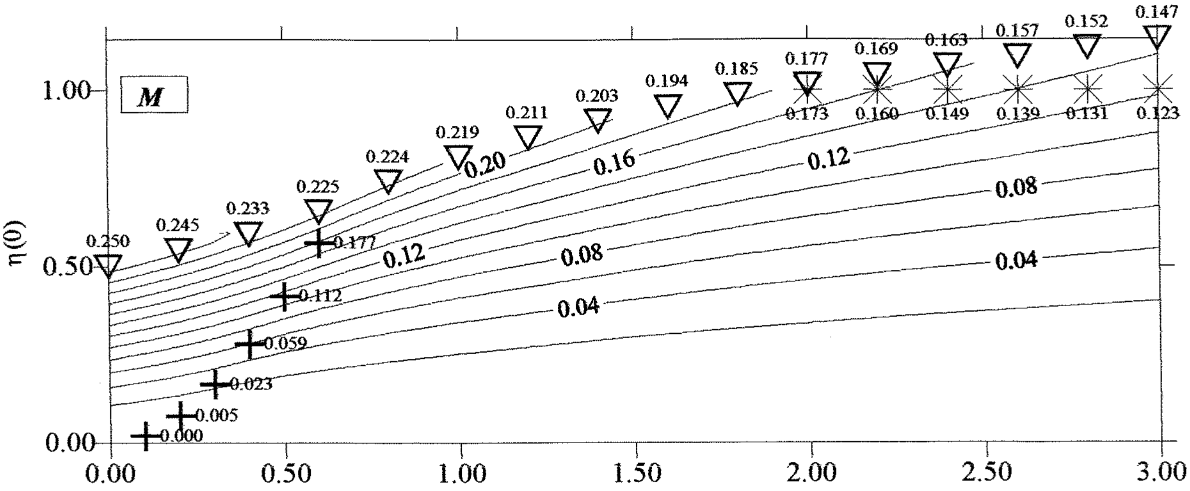

FIGURE 4.6(a) Net momentum flux, *M* in the ambient fluid as the rotation rate, *W* and the fractional depth, η(0) are varied. (see fig. 4.2a for an explanation of symbols)

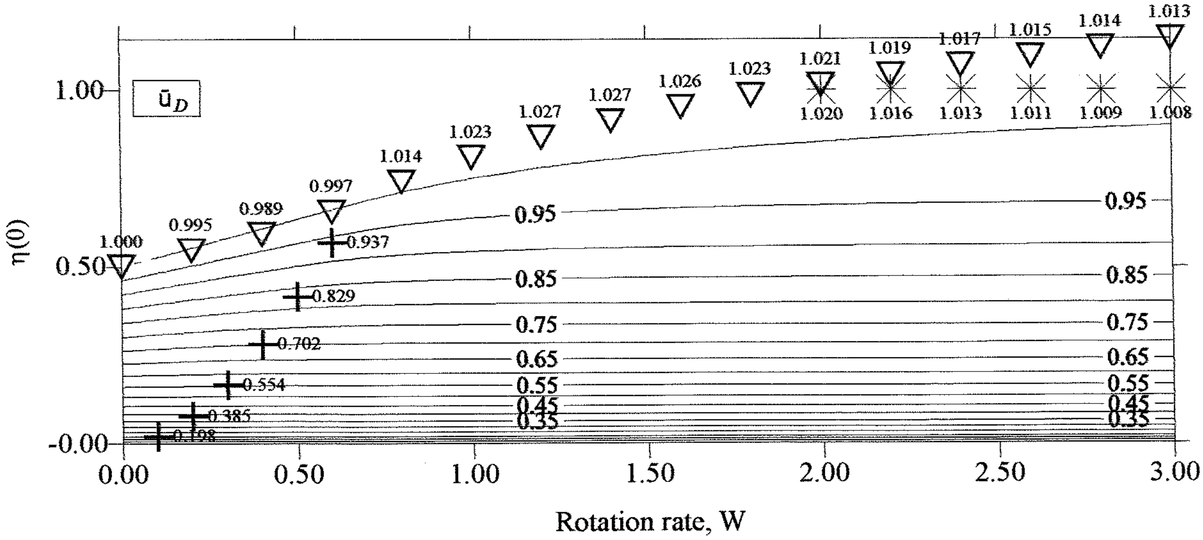

(b) Mean velocity, $\bar{u}_D$ of the ambient fluid as the rotation rate, *W* and the fractional depth, η(0) are varied.

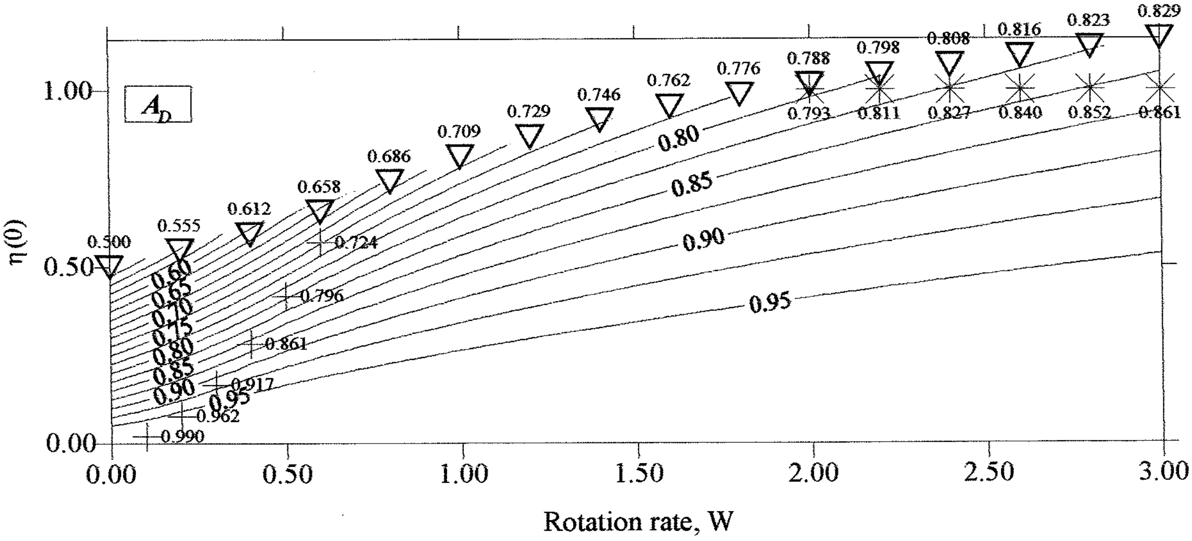

(c) Cross-sectional area, A_D of the ambient fluid as the rotation rate, *W* and the fractional depth, η(0) are varied.

maximum A_D continues to increase, whilst the decrease in $\bar{u}_D$ now becomes significant. Therefore, there is a reduction in the volume flux downstream requiring c to decrease. This argument is based on the assumption that the velocity is uniform across the stream. Although this is not the case close to the energy conserving solutions, at shallow depths the velocity is indeed constant across the channel, as shown in fig.4.5b. Therefore this simple argument based on continuity does give an explanation for the variation of c as η_0 and W are varied.

4.3.2 Comparison with previous work

In § 4.1.1 the method used to include energy loss in the non-rotating theory of Benjamin (1968) was discussed. The non-rotating solutions have been included at $W = 0$ in the contour graphs of § 4.3.1. However, to provide a clearer comparison with fig. 4.1, which illustrates the non-rotating solutions for the variables Q, c, and ΔE, 2-D graphs are plotted for $0 \leq W \leq 3$. The non-rotating solutions are shown in black, whilst the solutions as W is varied are displayed in different colours to illustrate the smooth transitions between the different flow geometries. The endpoints on the r.h. side of each curve are the energy conserving solutions. The horizontal axis is the depth η_0 and the variables ΔE, Q and c are plotted on the vertical axis in figs. 4.7 a, b & c respectively. The trends identified in § 4.1.1 for the non-rotating case are again apparent. In fig. 4.7 a the energy loss is found to equal zero at the energy conserving solution and as η_0 tends to zero for all values of W. The magnitude of the maximum value of ΔE initially decreases significantly as the level of rotation increases for case A. At $W \sim 0.5$ there is a slight increase in ΔE there after it continues to decrease at a reduced rate. In fig. 4.7 b the front speed exhibits the characteristic curve identified by Benjamin in the non-rotating case, where c corresponds to two values of η_0 within a certain range. The maximum values for c coincide with the maxima for ΔE. As W increases c also increases, however at shallow depths c becomes relatively constant for all values of W. Note that c is equivalent to the downstream volume flux of the ambient fluid (3.2.31). The volume flux of the current, Q, is shown in fig. 4.7 c. As in the non-rotating case the maximum discharge of the current occurs at the energy conserving depth. Q decreases as the current becomes shallower and the level of rotation is

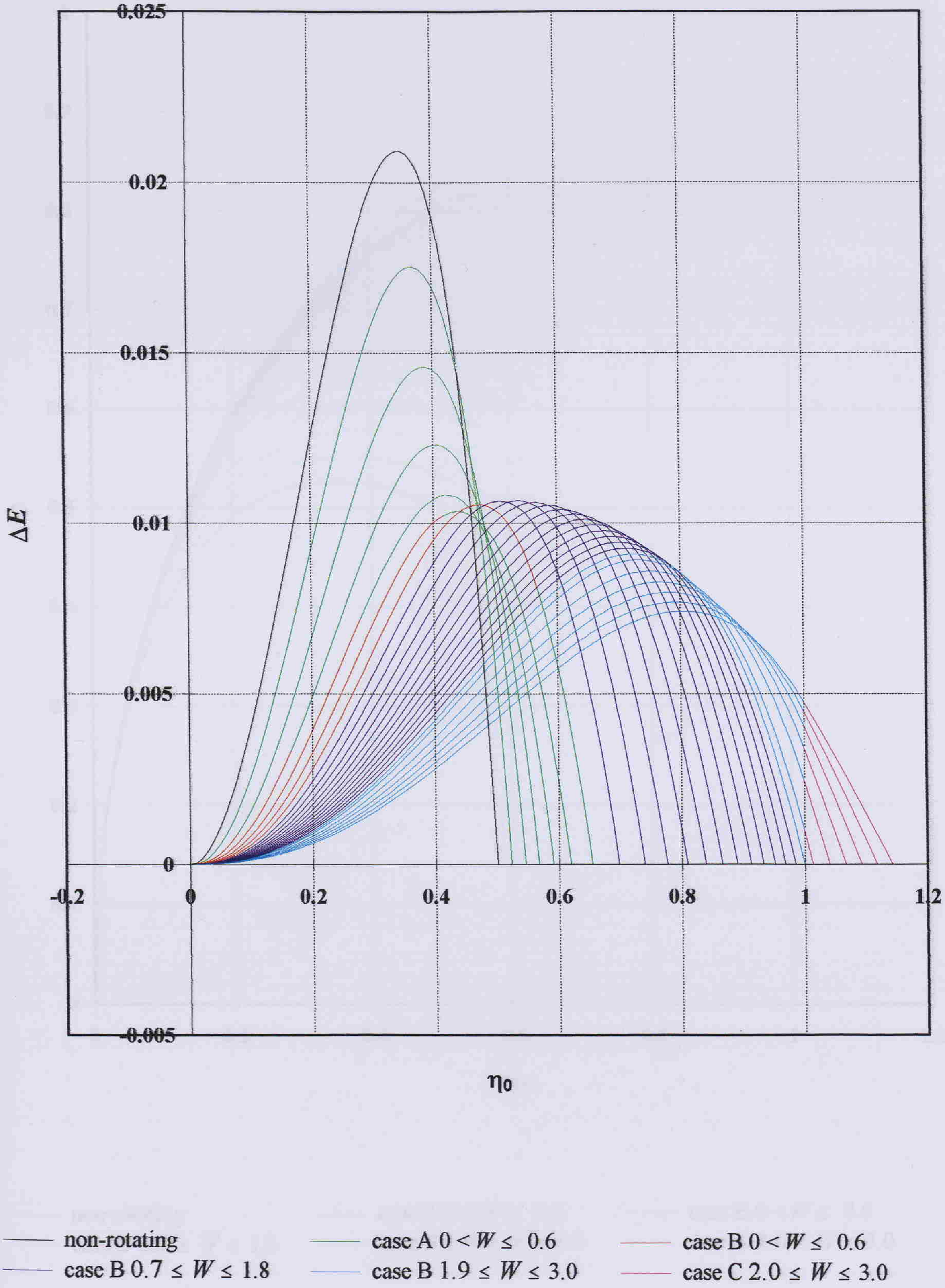

FIGURE 4.7. (a) Energy loss ΔE, versus fractional depth η_0. As the fractional depth is decreased below the dissipationless value there is a positive loss of energy.

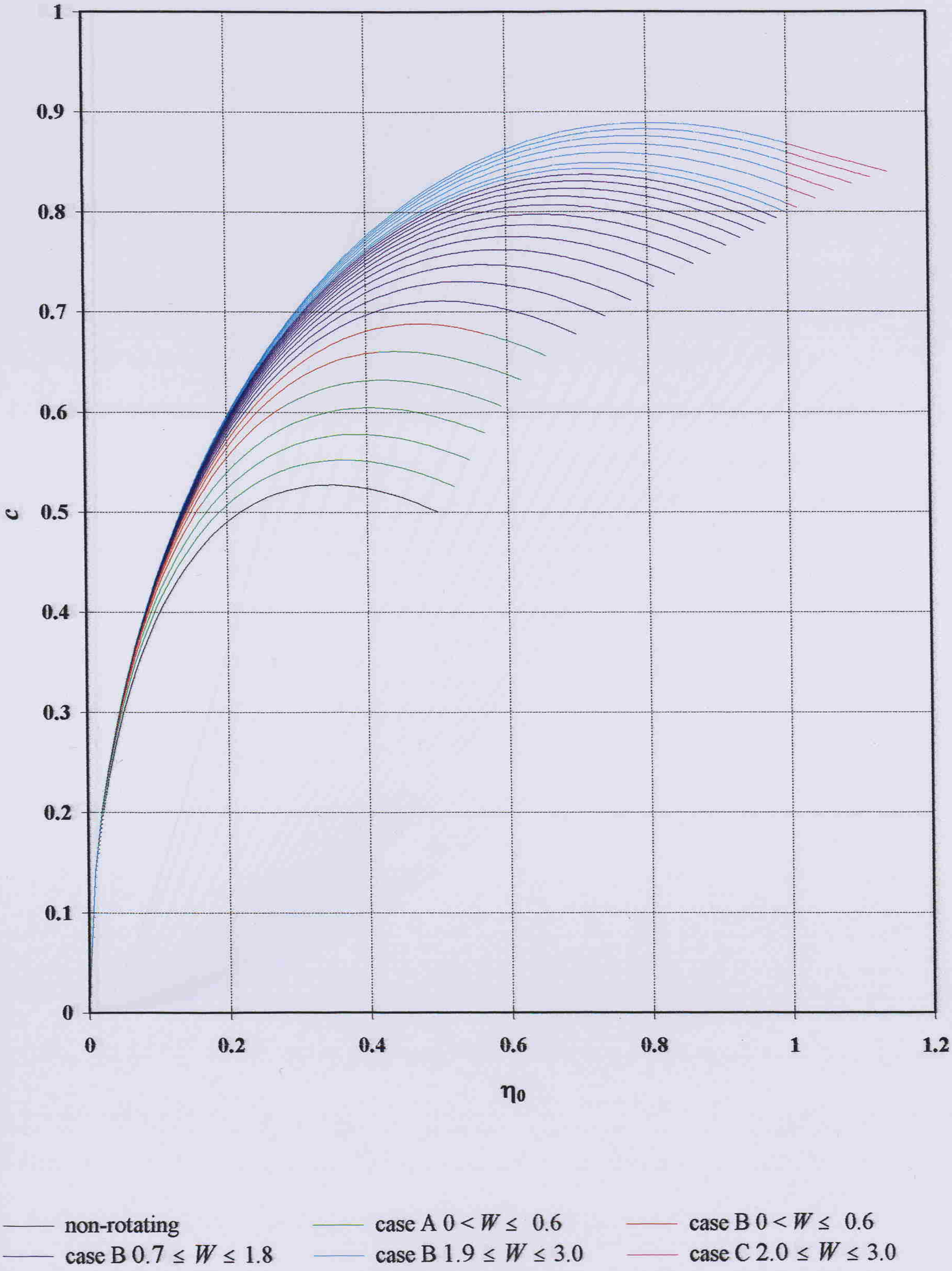

FIGURE 4.7. (b) Front speed c, versus fractional depth η_0. In agreement with the non-rotating energy loss theory (Benjamin, 1968) two values of η_0 correspond to c within a certain range. The maximum value of c also coincides with the maximum energy loss, ΔE.

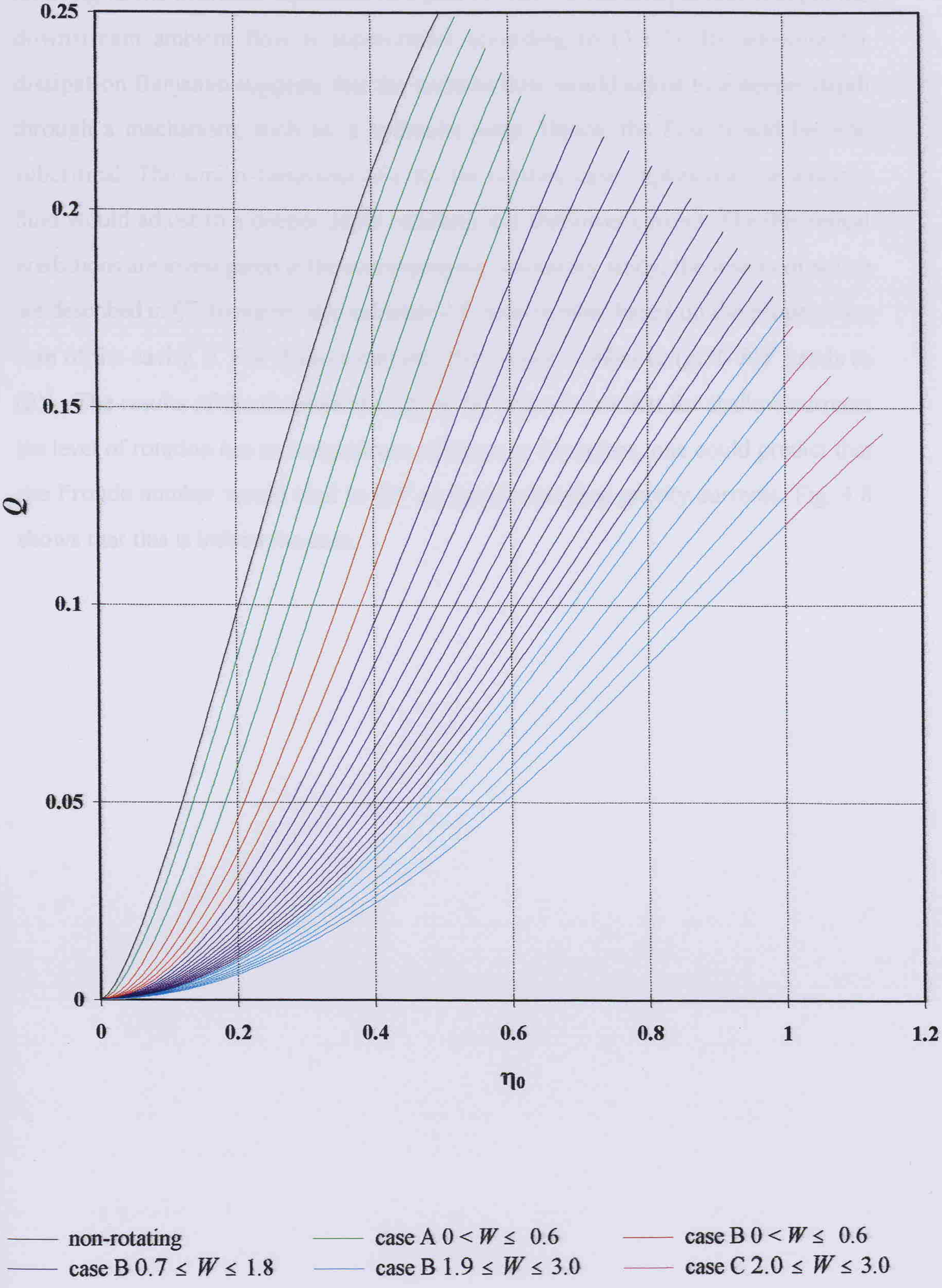

FIGURE 4.7. (c) Discharge Q, versus fractional depth η_0. In agreement with the non-rotating energy loss theory (Benjamin, 1968) the maximum discharge occurs at the energy conserving depth.

increased, as one would expect. Benjamin explained the two alternative depths for c by referring to the hydraulic equations of Lamb (1932). At the dissipationless depth the downstream ambient flow is supercritical according to (3.1.7). By allowing for dissipation Benjamin suggests that the ambient flow would adjust to a deeper depth through a mechanism, such as, a hydraulic jump. Hence, the flow would become subcritical. The similar behaviour of c for the rotating case implies that the ambient fluid would adjust to a deeper depth resulting in a shallower current. The theoretical predictions are investigated in the accompanying laboratory study, the results of which are described in §7. Benjamin also calculate a Froude number based on the propagation rate of the cavity, c. For shallow currents the Froude number $(c/(g(H- h))^{\frac{1}{2}}$ tends to $(2)^{\frac{1}{2}}$. The results of the theoretical study so far have shown that for shallow currents the level of rotation has an insignificant effect on c. Therefore, one could predict that the Froude number would tend to $(2)^{\frac{1}{2}}$ as for non-rotating gravity currents. Fig. 4.8 shows that this is indeed the case.

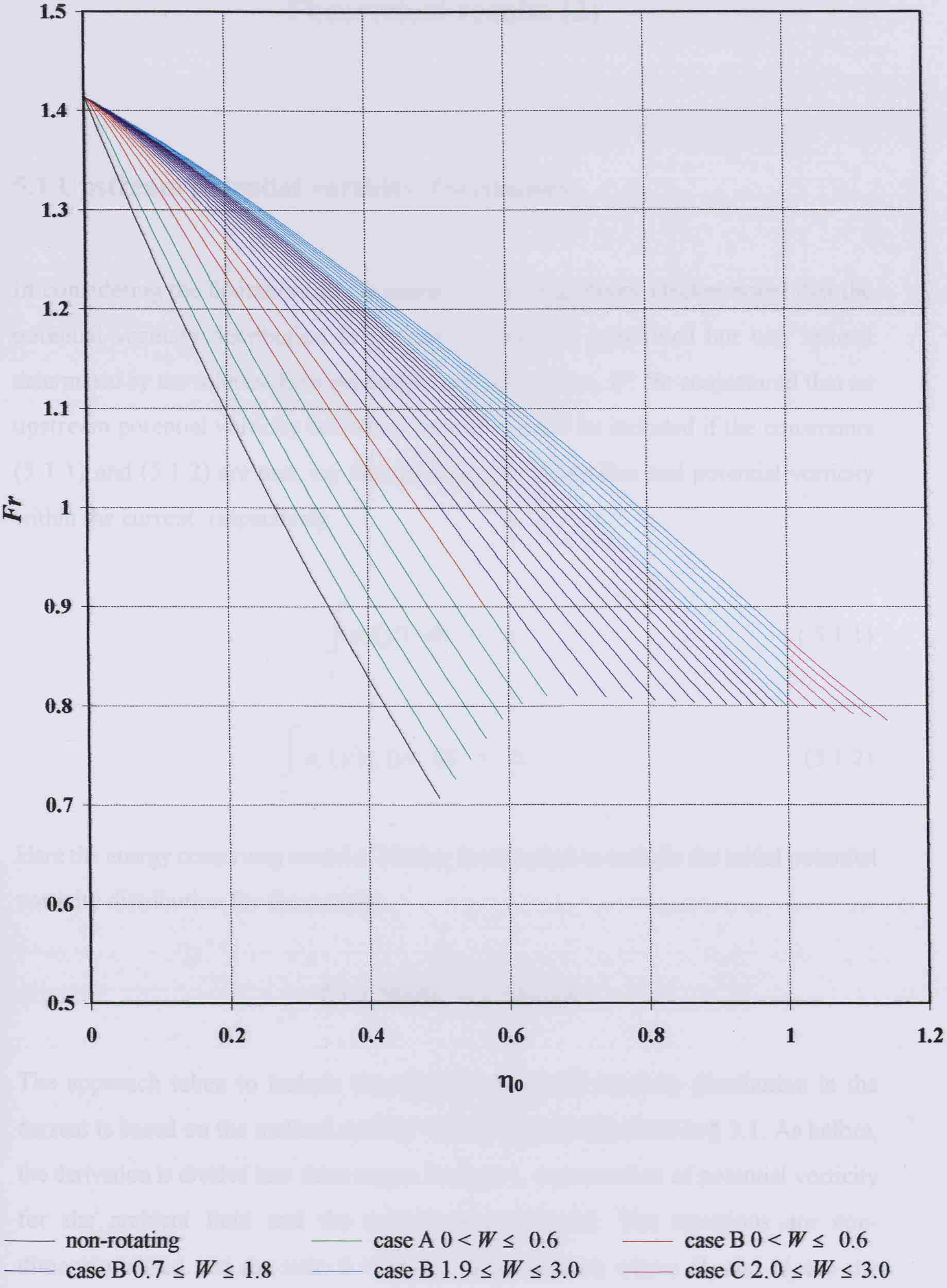

FIGURE 4.8. Froude number *Fr*, versus fractional depth η_0. In agreement with the non-rotating energy loss theory (Benjamin 1968) the Froude number tends to $2^{\frac{1}{2}}$ as η_0 tends to zero.

CHAPTER 5

Theoretical results (2)

5.1 Upstream potential vorticity distribution

In considering the limitations of his energy conserving theory Hacker noted that the potential vorticity distribution in the current was not prescribed but was instead determined by the solution for a particular level of rotation, W. He conjectured that an upstream potential vorticity boundary condition could be included if the constraints (5.1.1) and (5.1.2) are met, i.e. conservation of volume flux and potential vorticity within the current, respectively.

$$\int_S u_c(y)\ dS \ = \ 0 \tag{5.1.1}$$

$$\int_S u_c(y) q_c(y)\ dS \ = \ 0. \tag{5.1.2}$$

Here the energy conserving model of Hacker is extended to include the initial potential vorticity distribution for the current.

5.1.1 Model description

The approach taken to include the upstream potential vorticity distribution in the current is based on the method used by Van Heijst and described in § 3.1. As before, the derivation is divided into three stages. In stage 1, conservation of potential vorticity for the ambient fluid and the current is considered. The equations are non-dimensionalised and the ratio $\delta = H_1/H_2$ is introduced, where H_1 and H_2 are the reference depth of the current and the ambient fluid upstream respectively, as defined in fig. 5.1. This allows the potential vorticity to be preset. Next the Margules equation is used to determine the relationship between the slope of the interface between the two layers and the velocity jump across the interface. From these, general solutions defining the structure of the flow in terms of the functional parameters are obtained, where

$u_c(0)$ - downstream velocity of the current at the r.h. wall

$u_D(0)$ - downstream velocity of the ambient fluid at the r.h. wall

η_0 - depth of the current at the r.h. wall

c - speed of translation of the reference frame

p_0 - upstream pressure in the ambient fluid.

In stage 2 conservation of the fundamental properties energy, mass and momentum between up and downstream cross sections are considered. Finally in stage 3 these conditions are applied to each of the three flow geometries as defined in § 3.2.1. This results in a complex set of simultaneous equations for each case. Note that the assumptions made in § 3.2.1 are still applicable with the exception that a recirculating flow is allowed in the current. The adjustment of the current from the initial source conditions is assumed to be inviscid, with no energy loss in the current, hence potential vorticity is conserved, i.e. there is no net flux of potential vorticity into the current.

To allow the flow in the current and the ambient fluid to have the same sign when they are flowing in the same direction, a different sign convention is adopted for u_a to that used in § 3.2.3.2. As before u_c is positive when the flow in the current is towards the forward stagnation point. Since the flow in the current is recirculating u_c may take either sign. The flow in the ambient fluid is now expected to be in the negative direction therefore (3.2.4) and (3.2.5) become

$$\mathbf{u}_c = (u_c(y, z), 0, 0) \tag{5.1.3}$$

and

$$\mathbf{u}_a = (u_a(y, z), 0, 0). \tag{5.1.4}$$

The subscript a refers to the ambient fluid, which can be further divided into the ambient fluid up and downstream, i.e. the subscripts U and D respectively. The subscript c refers to the current.

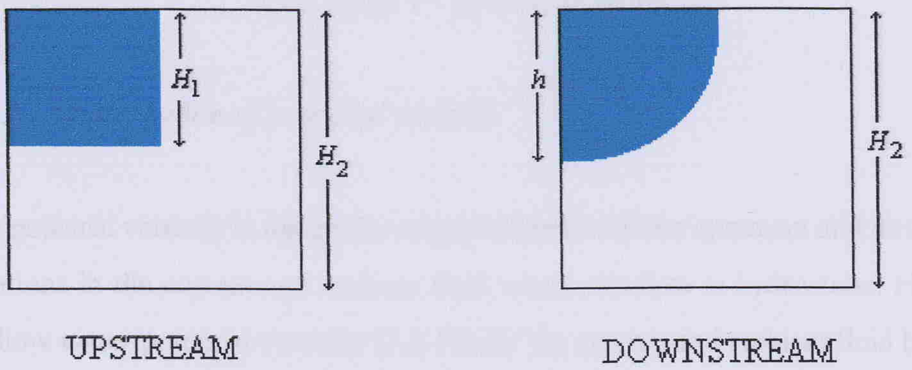

Figure 5.1. Schematic to illustrate the upstream reference depth H_1 and the depth to which the current adjusts downstream, *h*.

5.1.2 Basic scales

The new parameters are defined and non-dimensionalised below, note that those listed in § 3.2.2 are still applicable.

Dimensional parameters	
reference depth of the current	H_1
upstream depth of ambient fluid	H_2
channel depth	H

N.b $H_2 = H$

Non-dimensional parameters	
depth of the flow	$h = h^* / H$
Upstream depth ratio	$\delta = H_1 / H_2$
Strength of rotation	$W'^2 = W^2 (1+\delta)/\delta = \dfrac{f^2 D^2}{g'} \dfrac{(H_1 + H_2)}{H_1 H_2}$

where $W^2 = f^2 D^2 / (g' H_2)$

5.1.3 Stage 1 - governing equations

5.1.3.1 Conservation of potential vorticity

The potential vorticity is materially conserved between the upstream and downstream locations in the current and ambient fluid where the flow is hydrostatic. Hence the shallow water potential vorticity (3.2.14) for the current and ambient fluid becomes

$$\frac{f - (du_c/dy)}{h} = \frac{f}{H_1} \tag{5.1.5}$$

and

$$\frac{f - (du_D/dy)}{H_2 - h} = \frac{f}{H_2}, \tag{5.1.6}$$

respectively. Non-dimensionalising (5.1.5) and (5.1.6) become for the current

$$\frac{du_c}{dy} = W(1 - \eta/\delta) \tag{5.1.7}$$

and the ambient fluid

$$\frac{du_D}{dy} = W\eta. \tag{5.1.8}$$

N.b. the change of sign in (5.1.8) compared to (3.2.16). This is due to the different sign convention used in this model.

5.1.3.2 Geostrophic equations and Margules relationship

To remove the hydrostatic pressure variation with depth in the current p_c may be written as

$$p_c = P_c + (z - 1). \tag{5.1.9}$$

The non-dimensionalised momentum equations for the current (3.2.2) and the ambient fluid (3.2.3) are still applicable. Applying the Boussinesq Approximation ($\rho = 1$) and (5.1.9) the geostrophic relationship for the current becomes

$$\frac{dp_c}{dy} = \frac{dP_c}{dy} = -W(u_c + c). \tag{5.1.10}$$

For the ambient fluid the new sign convention (5.1.4) implies

$$\frac{dp_D}{dy} = -W(u_D + c). \tag{5.1.11}$$

Since the pressure is continous at the interface between the two fluids where $z = 1 - \eta$, this implies that

$$p_D = P_c - \eta. \tag{5.1.12}$$

Differentiating (5.1.12) and substituting (5.1.10) and (5.1.11) gives the Margules (1906) relationship, where the slope of the interface between the two fluids is given by the difference in velocity across the interface

$$u_c - u_D = -W^{-1}\, d\eta/dy. \tag{5.1.13}$$

5.1.3.3 Flow structure equations

The structure of the flow is defined in terms of the depth of the flow and the respective velocities of the current and the ambient fluid at the r.h. wall, η_0, $u_c(0)$ and $u_a(0)$. The general solution for the velocity of the current, $u_c(y)$, holds for all the levels of rotation, since $y \in [0, d]$ for cases A, B and C. For the ambient fluid the boundary conditions associated with each of the flow geometries are applied to the downstream depth $\eta(y)$ and velocity $u_D(y)$, as described in §3.2.3.5.

The general solution for $\eta(y)$ is derived by firstly diffentiating (5.1.13) with respect to y, and substituting (5.1.7) and (5.1.8) to give

$$-W^2 = d^2\eta/\, dy^2 - W'^2\eta. \tag{5.1.14}$$

The general solution of (5.1.14) is

$$\eta(y) = \delta/(1+\delta) + A \cosh W'y + B \sinh W'y\,, \tag{5.1.15}$$

where A and B are constants of integration which are solved subsequently. The general solutions for $u_c\,(y)$ and $u_D(y)$ are obtained by substituting (5.1.15) into (5.1.7) and

(5.1.8) respectively to give

$$u_c(y) = E + W(\delta/(1+\delta))y - (W/\delta W')[A \sinh W'y + B \cosh W'y] \tag{5.1.16}$$

and

$$u_D(y) = F + W(\delta/(1+\delta))y + (W/W')[A \sinh W'y + B \cosh W'y]. \tag{5.1.17}$$

Subtracting (5.1.17) from (5.1.16) and equating with (5.1.13) shows that the two constants in the above equations are equivalent, i.e. $E = F$. Returning to the constants A and B in the above equations these are obtained by considering the solutions of (5.1.5) at $y = 0$. Hence, (5.1.15) becomes

$$A = \eta_0 -(\delta/(1+\delta)). \tag{5.1.18}$$

The constant B is obtained by subtracting the solution at $y = 0$ of (5.1.17) from that at (5.1.16) which gives

$$B = -W/W'(u_c(0) - u_D(0)). \tag{5.1.19}$$

Substituting the expressions for the constants A (5.1.18) and B (5.1.19) into the general solutions (5.1.16) and (5.1.17) and evaluating them at $y = 0$ enables the remaining constant F to be determined, where

$$\begin{aligned} F = u_c(0) - (W^2/\delta W'^2)(u_c(0) - u_D(0)) &= u_D(0) + (W^2/W'^2)(u_c(0) - u_D(0)) \\ &= u_c(0) - (1+\delta)^{-1}(u_c(0) - u_D(0)) \end{aligned} \tag{5.1.20}$$

Substituting the expressions for the coefficients A and B into (5.1.15) enables the general solution for $\eta(y)$ to be written as

$$\eta(y) = \delta/(1+\delta) + (\eta_0 - \delta/(1+\delta)) \cosh W'y + ((-W/W')(u_c(0) - u_D(0))) \sinh W'y. \tag{5.1.21}$$

In the free stream $\eta(d) = 0$ for cases B and C. By applying (5.1.21) at d, and making use of the hyperbolic identity for $\sinh^2 W'd$, a quadratic equation is obtained which is solved for $\cosh W'd$. Hence an expression for d in terms of η_0, $u_c(0)$ and $u_D(0)$ is obtained,

$$d = W'^{-1}\cosh^{-1}\left[\frac{-(W^2/W'^2)A \mp \left(B^2\left((W^4/W'^4) + B^2 - A^2\right)\right)^{\frac{1}{2}}}{(A^2 - B^2)}\right] \tag{5.1.22}$$

where A and B are the constants defined in (5.1.18) and (5.1.19).

For case C where the current outcrops on the bottom boundary at $y = b$ (5.1.21) becomes

$$\eta(b) = 1 = \delta/(1+\delta) + \left(\eta_0 - \delta/(1+\delta)\right)\cosh W'b + \left((-W/W')(u_c(0) - u_D(0))\right)\sinh W'b. \tag{5.1.23}$$

An expression for b in terms of η_0, $u_c(0)$ and $u_D(0)$, is obtained by rearranging (5.1.23) and again making use of the hyperbolic identity for $\sinh^2 W'd$. Hence for

$$b = W'^{-1}\cosh^{-1}\left[\frac{-(1+\delta)^{-1}A \mp \left(B^2\left((1+\delta)^{-2} + B^2 - A^2\right)\right)^{\frac{1}{2}}}{(A^2 - B^2)}\right] \tag{5.1.24}$$

where A and B are the constants defined in (5.1.18) and (5.1.19).

Substituting the expression for the remaining integration constant F (5.1.20) into (5.1.16) and (5.1.17) enables the general solutions to be obtained for the downstream velocity of the current and ambient fluid respectively where,

$$u_c(y) = u_c(0) - (W^2/\delta W'^2)(u_c(0) - u_D(0)) + W(\delta/(1+\delta))y - (W/\delta W')\left[\left(\eta_0 - \delta/(1+\delta)\right)\sinh W'y + \left((-W/W')(u_c(0) - u_D(0))\right)\cosh W'y\right] \tag{5.1.25}$$

and

$$u_D(y) = u_D(0) + (W^2/W'^2)(u_c(0) - u_D(0)) + W(\delta/(1+\delta))y + (W/W')\left[\left(\eta_0 - \delta/(1+\delta)\right)\sinh W'y + \left((-W/W')(u_c(0) - u_D(0))\right)\cosh W'y\right]. \tag{5.1.26}$$

5.1.3.4 Pressure equations (1)

In the energy conserving theory of Hacker the velocity of the current, u_c, was set to zero to enable (3.2.6) to be integrated easily. In this model (3.2.6) is integrated with u_c as defined in (5.1.25), to give an expression for the downstream pressure of the current, where

$$\begin{aligned} p_c = k - Wcy - W\Big[&\left(u_c(0) - (W^2/\delta W'^2)\left(u_c(0) - u_D(0)\right)\right)y + \tfrac{1}{2}W(\delta/(1+\delta))y^2 - \\ &(W/\delta W'^2)\Big(\left(\eta_0 - \delta/(1+\delta)\right)\cosh W'y + \left((-W/W')(u_c(0) - u_D(0))\right)\sinh W'y\Big)\Big] + z. \end{aligned} \qquad (5.1.27)$$

Removing the hydrostatic pressure variation in the fluid according to (5.1.9), (5.1.27) becomes

$$\begin{aligned} P_c = k + 1 - Wcy - W\Big[&\left(u_c(0) - (W^2/\delta W'^2)\left(u_c(0) - u_D(0)\right)\right)y + \tfrac{1}{2}W(\delta/(1+\delta))y^2 - \\ &(W/\delta W'^2)\Big(\left(\eta_0 - \delta/(1+\delta)\right)\cosh W'y + \left((-W/W')(u_c(0) - u_D(0))\right)\sinh W'y\Big)\Big]. \end{aligned} \qquad (5.1.28)$$

The constant of integration k is determined subsequently. Applying (5.1.11) to the ambient fluid upstream where $u_U = -c$, the pressure becomes constant, as in (3.2.11) where $p_U = p_0$. The subscript U refers to the upstream flow in the ambient fluid. According to (5.1.12) the downstream pressure $p_D = P_c - \eta$, because the pressure is continuous across the interface, hence (5.1.28) becomes

$$\begin{aligned} p_D = k - Wcy - W\Big[&\left(u_c(0) - (W^2/\delta W'^2)\left(u_c(0) - u_D(0)\right)\right)y + \tfrac{1}{2}W(\delta/(1+\delta))y^2 - \\ &(W/\delta W'^2)\Big(\left(\eta_0 - \delta/(1+\delta)\right)\cosh W'y + \left((-W/W')(u_c(0) - u_D(0))\right)\sinh W'y\Big)\Big] + 1 - \eta. \end{aligned} \qquad (5.1.29)$$

(Note $(\delta/(1+\delta)) = W^2/W'^2$)

Stage 1 - Summary

The general solutions for the flow structure equations

$y \in [b, d]$

$$\eta(y) = \delta/(1+\delta) + \big(\eta_0 - \delta/(1+\delta)\big) \cosh W'y + \big((-W/W')(u_c(0) - u_D(0))\big) \sinh W'y \tag{5.1.21}$$

$$y \in [0, b] \quad \eta(y) = 1$$

$$y \in [d, 1] \quad \eta(y) = 0$$

$y \in [0, d]$

$$\begin{aligned} u_c(y) = {} & u_c(0) - (W^2/\delta W'^2)(u_c(0) - u_D(0)) + W(\delta/(1+\delta))y - \\ & (W/\delta W')\big[\big(\eta_0 - \delta/(1+\delta)\big) \sinh W'y + \big((-W/W')(u_c(0) - u_D(0))\big) \cosh W'y\big] \end{aligned} \tag{5.1.25}$$

$y \in [b, d]$

$$\begin{aligned} u_D(y) = {} & u_D(0) + (W^2/W'^2)(u_c(0) - u_D(0)) + W(\delta/(1+\delta))y + \\ & (W/W')\big[\big(\eta_0 - \delta/(1+\delta)\big) \sinh W'y + \big((-W/W')(u_c(0) - u_D(0))\big) \cosh W'y\big] \end{aligned} \tag{5.1.26}$$

$$y \in [d, 1] \quad u_D(y) = U_D = \text{constant}$$

The boundary conditions

$$d = W^{-1}\cosh^{-1}\left[\frac{-(W^2/W'^2)A \mp \big(B^2((W^4/W'^4) + B^2 - A^2)\big)^{\frac{1}{2}}}{(A^2 - B^2)}\right] \tag{5.1.22}$$

$$b = W^{-1}\cosh^{-1}\left[\frac{-(1+\delta)^{-1}A \mp \big(B^2((1+\delta)^{-2} + B^2 - A^2)\big)^{\frac{1}{2}}}{(A^2 - B^2)}\right] \tag{5.1.24}$$

where A and B are the constants defined in (5.1.18) and (5.1.19).

The general form of the pressure equations

$y \in [b, d]$

$$P_c(y) = k + 1 - Wcy - W\Big[\,(u_c(0) - (W^2/\delta W'^2)\,(u_c(0) - u_D(0)\,))y + \tfrac{1}{2}W(\delta/(1+\delta))y^2 -$$

$$(W/\delta W'^2)\big(\,(\eta_0 - \delta/(1+\delta))\cosh W'y + ((-W/W')(u_c(0) - u_D(0)\,))\sinh W'y\big)\Big].$$

(5.1.28)

$$p_D(y) = k - Wcy - W\Big[\,(u_c(0) - (W^2/\delta W'^2)\,(u_c(0) - u_D(0)\,))y + \tfrac{1}{2}W(\delta/(1+\delta))y^2 -$$

$$(W/\delta W'^2)\big(\,(\eta_0 - \delta/(1+\delta))\cosh W'y + (\,(-W/W')(u_c(0) - u_D(0)\,))\sinh W'y\big)\Big] + 1 - \eta.$$

(5.1.29)

(k is determined subsequently)

This completes stage 1, where the general solutions for the flow structure equations, boundary conditions and the downstream pressure equations were determinded in terms of η_0, $u_c(0)$ and $u_D(0)$. To obtain expressions for the remaining functional parameters, c and p_0, the method adopted in the non-rotating theory is applied. In the following section conservation of the energy, mass and momentum through the control volume connecting up and downstream cross-sections is considered.

5.1.4 Stage 2 - Conservation of the fundamental properties

5.1.4.1 Conservation of energy

The vector identity

$$(\mathbf{u}.\nabla)\mathbf{u} = \nabla(\tfrac{1}{2}\, u^2) - \mathbf{u} \times (\nabla \times \mathbf{u}) \quad \text{where } u = |\mathbf{u}|$$

is substituted into the momentum equation for the current (3.2.2). Using the definition of the differential operator, defined in § 3.2.2, (3.2.2) becomes

$$\nabla\left(\tfrac{1}{2}\,|\mathbf{u}_c|^2 + p_c + Wcy - z\right) \; = \; \mathbf{u}_c \times \boldsymbol{\omega} + W\mathbf{u}_c \times \mathbf{k}$$

where $\boldsymbol{\omega} = \nabla \times \mathbf{u}_c$. Taking the scalar product of each side of the above expression with $\mathbf{u}_c$, gives

$$\frac{d}{dy}\left(\tfrac{1}{2}\,|\mathbf{u}_c|^2 + p_c + Wcy - z\right) \; = \; 0,$$

where *d/dy* means the derivative along the streamline. The l.h. side equals zero because the scalar product of perpendicular vectors is zero. Integrating the above expression with respect to y gives the Bernoulli equation

$$B_c = \tfrac{1}{2}\,|\mathbf{u}_c|^2 + P_c(y) + Wcy = \text{constant along streamlines.} \qquad (5.1.30)$$

Applying the Bernoulli equation for the current along a streamline connecting the forward stagnation point (0, 0, 1) to a point on the r.h. boundary downstream in the current gives

$$B_c(0) = 0 = \tfrac{1}{2}\, u_c(0)^2 + P_c(0). \qquad (5.1.31)$$

Hence the downstream pressure in the current is quantified as

$$-\tfrac{1}{2}\, u_c(0)^2 = P_c(0). \qquad (5.1.32)$$

To obtain the value of $B_c(d)$, firstly (5.1.30) is differentiated and use is made of the geostrophic and the potential vorticity equations (5.1.10) and (5.1.7) respectively to give

$$\frac{dB_c}{dy} = \frac{-W\eta u_c}{\delta}.$$

Integrating the above expression and making use of the condition (5.1.1) which states that there is no flux of fluid in to or out of the current gives

$$\begin{aligned} B_c(d) - B_c(0) &= -\frac{W}{\delta}\int_0^d u_c(y)\,\eta(y)\,dy \\ &= -\frac{W}{\delta}\Big[\,Q_c(y)\Big]_0^d = 0. \end{aligned} \qquad (5.1.33)$$

According to (5.1.32) $B_c(0) = 0$, which implies that $B_c(d) = 0$, therefore (5.1.33) becomes

$$B_c(d) = \tfrac{1}{2}\,u_c(d)^2 + P_c(d) + Wcd = 0. \qquad (5.1.34)$$

Hence, the Bernoulli equations (5.1.31) and (5.1.34) for the current are defined. At this stage the pressure has not been fully specified. This will be dealt with in the following section, where the constant of integration k is solved. Next I will consider the Bernoulli relationship for the ambient fluid. As in § 3.2.4.1 simplifying the momentum equation for the ambient fluid (3.2.3), taking the scalar product with **u** and integrating results in

$$B = \tfrac{1}{2}\,|\mathbf{u}|^2 + p + Wcy = \text{constant along streamlines.} \qquad (3.2.25)$$

The expressions derived in § 3.2.4.1 still hold therefore applying (3.2.25) along a streamline connecting the forward stagnation point at (0, 0, 1) and the upstream ambient flow gives

$$p_0 = -\tfrac{1}{2}\,c^2. \qquad (3.2.26)$$

The upstream Bernoulli equation is obtained by substituting (3.2.26) into (3.2.25) to give

$$B_U(y) = Wcy. \tag{3.2.27}$$

According to (3.2.25) and (3.2.27) a streamline connecting the downstream location y to the upstream location $Y(y)$ is expressed as

$$\begin{aligned} B_D(y) &= B_U(Y(y)) \\ \tfrac{1}{2}u_D{}^2 + p_D + Wcy &= Wc(Y(y)). \end{aligned} \tag{3.2.28}$$

$Y(y)$ is known for streamlines running along rigid boundaries where

$$Y(b) = 0$$

and

$$Y(1) = 1.$$

Hence evaluating (3.2.25) where $Y(y)$ is known the Bernoulli equation becomes

$$B_D(b) = 0 = \tfrac{1}{2}u_D{}^2(b) + p_D(b) + Wcb \tag{5.1.35}$$

and

$$B_D(1) = Wc = \tfrac{1}{2}u_D{}^2(1) + p_D(1) + Wc. \tag{5.1.36}$$

In cases A and B where $b = 0$, $B_D(0)$ becomes

$$B_D(0) = \tfrac{1}{2}u_D(0)^2 + p_D(0).$$

Applying (5.1.12) at $b = 0$ and making use of (5.1.32) gives

$$\eta_0 = \tfrac{1}{2}u_D(0)^2 - \tfrac{1}{2}u_c(0)^2. \tag{5.1.37}$$

Next integrating the relationship obtained in the derivation of (5.1.32), for case C where $y \in [0, b]$ yields

$$B_c(b) - B_c(0) = -\frac{W}{\delta}\int_0^b u_c(y)\,\eta(y)\,dy. \tag{5.1.38}$$

Applying $B_c(0) = 0$ (5.1.31) and (5.1.7), (5.1.38) becomes

$$B_c(b) = \frac{u_c^2(b)}{2(1-\delta)} - \frac{u_c^2(0)}{2(1-\delta)} \tag{5.1.39}$$

Equating (5.1.39) with (5.1.30) applied at $y = b$ gives

$$-\tfrac{1}{2}\, u_c^2(b)\, \frac{\delta}{1-\delta} + P_c(b) + Wcb + \frac{1}{2(1-\delta)}\, u_c^2(0) = 0. \tag{5.1.40}$$

Substituting (5.1.12) into (5.1.35) and equating with (5.1.40) gives

$$-\tfrac{1}{2}\, u_c^2(b)\, \frac{\delta}{1-\delta} + \frac{1}{2(1-\delta)}\, u_c^2(0) = \tfrac{1}{2}\, u_D^2(b) - \eta(y). \tag{5.1.41}$$

The integral of (5.1.7) for $y \in [0, b]$ is

$$u_c(b) - u_c(0) = Wb\,(\,(\delta-1)/\delta), \tag{5.1.42}$$

which is substituted into (5.1.41) to give

$$\tfrac{1}{2}\, u_D^2(b) = \tfrac{1}{2}\, u_c^2(b) + \frac{Wb}{\delta}\, u_c(b) + W^2b^2\, \frac{1-\delta}{2\delta^2} + \eta(y)\,. \tag{5.1.43}$$

The relationship (5.1.43) defines $u_D(b)$ in terms of $u_c(b)$ and b, which can be further defined in terms of η_0, $u_c(0)$ and $u_D(0)$ for $y = 0$. (5.1.43) forms the first equation in the set of four necessary to complete the solution.

In order to define the Bernoulli equations for the downstream flow in the ambient fluid, for $y \in [b, d]$ and $y \in [d, 1]$, in terms of the principal variables expressions for the pressure $p_D(y)$ are required. Firstly, the constant of integration k in the pressure equations (5.1.28) and (5.1.29), (5.1.28) is evaluated at $y = 0$ and the substitution (5.1.31) is applied to give

$$k = -\tfrac{1}{2}u_c(0)^2 - 1 - (W^2/\delta W'^2)\left(\eta_0 - (W^2/W'^2)\right). \qquad (5.1.44)$$

Hence (5.1.28) becomes $y \in [b, d]$

$$\begin{aligned} P_c(y) = &-\tfrac{1}{2}u_c(0)^2 - (W^2/\delta W'^2)\eta_0 + (W^4/\delta W'^4) - Wcy \\ &- W\left(u_c(0) - (W^2/\delta W'^2)(u_c(0) - u_D(0))\right)y - (\tfrac{1}{2}W^4/W'^2)y^2 \\ &+ (W^2/\delta W'^2)\left(\eta(y) - W^2/W'^2\right). \end{aligned} \qquad (5.1.45)$$

For the ambient fluid (5.1.29) at $y \in [b, d]$ becomes

$y \in [b, d]$

$$\begin{aligned} p_D(y) = &-\tfrac{1}{2}u_c(0)^2 - (W^2/\delta W'^2)\eta_0 + (W^4/\delta W'^4) - Wcy \\ &- W\left(u_c(0) - (W^2/\delta W'^2)(u_c(0) - u_D(0))\right)y - (\tfrac{1}{2}W^4/W'^2)y^2 \\ &+ (W^2/\delta W'^2)\left(\eta(y) - (W^2/W'^2)\right). \end{aligned} \qquad (5.1.46)$$

In the free stream around the current $\eta(d) = 0$, hence the pressure at $y \in [d, 1]$ is obtained by firstly substituting (5.1.21) applied at $y = d$ into (5.1.46) to give the boundary condition

$y \in [d, 1]$

$$\begin{aligned} p_D(d) = &-\tfrac{1}{2}u_c(0)^2 - (W^2/\delta W'^2)\eta_0 - Wcd \\ &- W\left(u_c(0) - (W^2/\delta W'^2)(u_c(0) - u_D(0))\right)d - (\tfrac{1}{2}W^4/W'^2)d^2. \end{aligned} \qquad (5.1.47)$$

An expression for the pressure in the free stream is obtained by integrating the geostrophic equation (5.1.11) which gives

$$p_D(y) = -WU_D\,y - Wcy + H.$$

Applying the above expression at $y = d$ and equating with (5.1.47) enables the integration constant H to be solved, hence

$y \in [d, 1]$

$$p_D(y) = WU_D\,(d - y)\ - Wcy - \tfrac{1}{2}\,u_c(0)^2 - (W^2/\delta W'^2)\,\eta_0$$
$$- W\Big(\,u_\mathrm{D}(0) - (W^2/W'^2)(u_\mathrm{c}(0) - u_\mathrm{D}(0))\Big)d - (\tfrac{1}{2}W^4/W'^2)\,d^2. \qquad (5.1.48)$$

Applying (5.1.48) at $y = 1$ gives

$y = 1$

$$p_D(1) = WU_D\,(d - 1)\ - Wc - \tfrac{1}{2}\,u_c(0)^2 - (W^2/\delta W'^2)\,\eta_0$$
$$- W\Big(\,u_\mathrm{D}(0) - (W^2/W'^2)(u_\mathrm{c}(0) - u_\mathrm{D}(0))\Big)d - (\tfrac{1}{2}W^4/W'^2)\,d^2. \qquad (5.1.49)$$

It is now possible to write the expressions for conservation of energy in the ambient fluid in terms of the principal variables and parameters defining the flow structure, therefore substituting (5.1.46) into (3.2.28) gives

$y \in [b, d]$

$$B_D(y) = WcY(y) = \tfrac{1}{2}\,u_D(\mathrm{y})^2 - \tfrac{1}{2}\,u_c(0)^2 - (W^2/\delta W'^2)\,\eta_0 + (W^4/\delta W'^4)$$
$$- W\Big(\,u_\mathrm{D}(0) - (W^2/W'^2)(u_\mathrm{c}(0) - u_\mathrm{D}(0))\Big)y - (\tfrac{1}{2}W^4/W'^2)\,y^2$$
$$+ (W^2/\delta W'^2)\Big(\,(\eta_0 - (W^2/W'^2))\cosh W'y + ((-W/W')(\,u_c(0) - u_\mathrm{D}(0)\,))\sinh W'y\Big) - \eta(y). \qquad (5.1.50)$$

Substituting (5.1.48) into (3.2.28) gives

$y \in [d, 1]$

$$B_D(y) = WcY(y) = \tfrac{1}{2}\,U_D{}^2 + WU_D\,(d - y)\ - \tfrac{1}{2}\,u_c(0)^2 - (W^2/\delta W'^2)\,\eta_0$$
$$- W\Big(\,u_\mathrm{D}(0) - (W^2/W'^2)\,(u_\mathrm{c}(0) - u_\mathrm{D}(0))\Big)d - (\tfrac{1}{2}\,W^4/W'^2)\,d^2. \qquad (5.1.51)$$

Applying (5.1.51) at $y = d$ and $y = 1$ the following relationship is obtained

$y \in [d, 1]$

$$B_D(d) = B_D(1) + WU_D\,(1 - d). \qquad (5.1.52)$$

At $y = d$, $\eta = 0$ which according to (5.1.12) implies that $P_\mathrm{c} = p_D$, hence

$$B_D(d) = \tfrac{1}{2}\,U_D{}^2 + P_\mathrm{c}(d) + Wcd$$
$$= \tfrac{1}{2}\,(U_D{}^2 - u_c(d)^2). \qquad (5.1.53)$$

It is now possible to complete the expressions for conservation of energy in the ambient fluid by firstly substituting (5.1.46) applied at $y = b$ into (5.1.35), which becomes

$$B_D(b) = 0 = \tfrac{1}{2}\, u_D(\mathrm{b})^2 - \tfrac{1}{2}\, u_c(0)^2 - (W^2/\delta W'^2)\,\eta_0$$
$$- W\big(\, u_D(0) - (W^2/W'^2)\,(u_c(0) - u_D(0))\big)b - (\tfrac{1}{2}W^4/W'^2)\,b^2 \; -\delta/(1+\delta). \qquad (5.1.54)$$

Secondly $B_D(1)$ is calculated where $Y(1) = 1$. An equation which may be applied to all the flow geometries is obtained by combining the expressions for $B_D(1)$ for case A with that for cases B and C. The equation for case A is found by substituting (5.1.46) applied at $y = 1$ into (5.1.36). For cases B and C (5.1.49) is substituted into (5.1.36). The resulting equation becomes

$$B_D(1) = Wc = \tfrac{1}{2}\, u_D(1)^2 + WU_D\,(d - 1) - \tfrac{1}{2}\, u_c(0)^2 - (W^2/\delta W'^2)\,\eta_0$$
$$- W\big(\, u_D(0) - (W^2/W'^2)(u_c(0) - u_D(0))\big)d - (\tfrac{1}{2}W^4/W'^2)\,d^2$$
$$+ (W^2/\delta W'^2)\,\eta(d) - \eta(d). \qquad (5.1.55)$$

According to (5.1.34)

$$- \tfrac{1}{2}\, u_c(d)^2 = P_c(d) + Wcd. \qquad (5.1.56)$$

Substituting (5.1.12) into (5.1.56) and noting (5.1.20), enables (5.1.55) to be simplified. It is now possible to define c in terms of the principal variables where,

$$c = W^{-1}\left[\, \tfrac{1}{2}\, u_D(1)^2 - \tfrac{1}{2}\, u_c(d)^2 + WU_D\,(d - 1) - \eta(d) \,\right] \qquad (5.1.57)$$

(5.1.57) is the second general equation required to close the problem. Note that when $u_c = 0$ is substituted into (5.1.57) expressions are obtained for each of the cases, that are equivalent to those derived in the energy conserving theory with simple flow § 3.2.4.

The conditions for $y \in [b, d]$ are now considered. Substituting (5.1.14) in to the potential vorticity equation (5.1.8) enables it to be integrated between the limits $y \in [b, y]$. The substitution (5.1.13) is then introduced and the expression is rearranged to become

$$u_D(y) + \delta u_c(y) - W \delta y \;=\; u_D(b) + \delta u_c(b) - W \delta b\,. \tag{5.1.58}$$

Using

$$u_c = \frac{1}{1+\delta}\left((u_c - u_D) + (u_D + \delta u_c)\right). \tag{5.1.59}$$

The differential (5.1.13) replaces the first term in the brackets. To obtain a substitution for the second term the following integral is considered and equated with (5.1.58) to give

$$\begin{aligned} \delta \int_b^Y \frac{du_c}{dy}\, dy &= \delta\left(u_c(y) - u_c(b)\right) \\ &= u_D(b) - u_D(y) + W\delta\,(y - b). \end{aligned}$$

The integral above enables a substitution for the second term in (5.1.59) to be obtained, hence (5.1.59) becomes

$$u_c(y) = \frac{1}{1+\delta}\left(- \frac{1}{W}\frac{d\eta}{dy} + W\delta(y - b) + (u_D(b) + \delta u_c(b)\right). \tag{5.1.60}$$

Integrating (5.1.60) between the limits $y \in [b, d]$ gives

$$\int_b^d u_c(y)\, dy = \frac{1}{1+\delta}\left[\frac{\eta(b) - \eta(y)}{W} + W\delta(\tfrac{1}{2}(d^2 - b^2) - db + b^2) + (d - b)(u_D(b) + \delta u_c(b)\right] \tag{5.1.61}$$

(5.1.61) enables the geostrophic equation (5.1.10) to be integrated to become

$$\begin{aligned} P_c(d) - P_c(b) &= - (d - b)\left\{Wc + \frac{W}{1+\delta}\,(u_D(b) + \delta u_c(b))\right\} \\ &\quad - \frac{1}{1+\delta}\left\{\eta(b) - \eta(y) + W^2\delta\left(\tfrac{1}{2}(d - b)^2\right)\right\}. \end{aligned} \tag{5.1.62}$$

Substituting (5.1.12) applied at $y = b$ and (5.1.43), into the Bernoulli function (5.1.35), yields

$$P_c(b) = -\tfrac{1}{2}u_c^2(b) - \frac{Wb}{\delta}u_c(b) - W^2b^2\,\frac{1-\delta}{2\delta^2} - Wcb. \tag{5.1.63}$$

Rearranging the Bernoulli function (5.1.53) gives

$$P_c(d) = -\tfrac{1}{2}u_c^2(d) - Wcd. \tag{5.1.64}$$

Evaluating the difference between (5.1.64) and (5.1.63)

$$P_c(d) - P_c(b) = \tfrac{1}{2}\left(u_c^2(b) - u_c^2(d)\right) + \frac{Wb}{\delta}\,u_c(b) + W^2b^2\frac{1-\delta}{2\delta^2} + Wc\,(b-d). \tag{5.1.65}$$

Equating (5.1.65) with the previous expression for $P_c(d) - P_c(b)$, (5.1.62), results in the third general equation required to close the problem, i.e.

$$\begin{aligned}\tfrac{1}{2}\left(u_c^2(d) - u_c^2(b)\right) &= \frac{(d-b)}{(1+\delta)}\Big(W\left(u_D(b) + \delta u_c(b)\right)\Big)\\ &\quad + \frac{1}{(1+\delta)}\left(\eta(b) - \eta(d) + \tfrac{1}{2}W^2\delta(d-b)^2\right)\\ &\quad + \frac{Wb}{\delta}u_c(b) + W^2b^2\,\frac{1-\delta}{2\delta^2}.\end{aligned} \tag{5.1.66}$$

5.1.4.2 Conservation of volume flux

Earlier it was stated that the condition of conservation of volume flux for the current implies that the fluid within the current must be recirculating. Evaluating (5.1.1) gives

$$\int_0^d \int_{1-\eta}^1 u_c(y)\,dz\,dy = 0 \tag{5.1.67}$$

$$\int_0^d u_c(y)\,\eta(y)\,dy = \int_0^b u_c(y)\,dy + \int_b^d u_c(y)\,\eta(y)\,dy.$$

The integrals in the above equation may be written as exact differentials by substituting the potential vorticity (5.1.7) and geostrophic equation (5.1.10). (5.1.67) can then be easily integrated to give

$$-\left[\frac{1}{W}P_c+cy\right]_0^b-\left[\frac{\delta}{W}P_c+\delta\, cy+\frac{\delta}{2W}u_c(y)^2\right]_b^d = 0. \tag{5.1.68}$$

For the ambient fluid the condition of conservation of volume flux is represented by the following integral. Note the change in sign from (3.2.31), because of the new sign convention.

$$\begin{aligned} -c &= \int_b^1 \int_0^{1-\eta} u_D(y)\, dz\, dy \\ &= \int_b^1 u_D(y)\,(1-\eta)\, dy. \end{aligned} \tag{5.1.69}$$

The above expression is evaluated using the potential vorticity (5.1.8) and the geostrophic (5.1.11) relationships. Hence (5.1.69) becomes

$$c = W^{-1}\left[\tfrac{1}{2}\, u_D{}^2 + p_D + Wcy\right]_b^1 \tag{5.1.70}$$

which is equivalent to (3.2.32).Therefore, as in the energy conserving solution for simple flow the continuity equation offers no further information over the Bernoulli equation for the ambient fluid.

5.1.4.3 Conservation of Momentum

Conservation of momentum is evaluated as in §3.2.4.3. The momentum equations (3.2.2) and (3.2.3) are integrated over the rectangular volume between the up and downstream cross sections (fig. 3.2.3). However in this model the velocity of the current is not assumed to equal zero and therefore must be included. The divergence theorem is again used to express the advective and pressure terms as surface integrals. Note that at rigid boundaries **u.n** = 0.

$$\int_{A_U+A_D+A_c} \mathbf{u}(\mathbf{u.n})\, dS + \int_{\partial Va+\partial V_c} p\mathbf{n}\, dS = -\int_{Va+V_c} W\boldsymbol{k}\times\mathbf{u}\, dV - Wcj\int_{Va+V_c} dV + \mathbf{k}\int_{V_c} dV. \tag{5.1.71}$$

The subscripts are defined in § 3.2.4.3. Considering the different components of (5.1.71), one finds that the total Coriolis force acting in the *i* direction is equivalent to the sum of the net fluxes of the momentum plus the pressure force acting on the wall in the *i* direction, where

$$\mathbf{i}: \int_{A_U} (u_U^2 + p_U)\, dA - \int_{Aa} (u_D^2 + p_D)\, dA - \int_{A_c} (u_c^2 + p_c)\, dA = W \int_{Va + V_c} \mathrm{v}\, dV . \quad (5.1.72)$$

Note that the expression of conservation of momentum derived in §3.2.4.3 has been altered to include the non-zero velocity of the current. There now also exists an across stream velocity, v_c, in the current. This induces a Coriolis force directed upstream, with respect to the current, which acts to retard the current.

The *j* component expresses the balance between the net pressure force on the side walls, and the sum of the Coriolis force and the body force of translation. The *k* component represents the balance between the net pressure force on the top and bottom walls, and the buoyancy force acting on the current. The remaining unknowns are determined from the *i* component.

Using the fact that $u_U = -c$ and the substitution for the upstream pressure (3.2.26), the above expression (5.1.72), becomes

$$\tfrac{1}{2}c^2 = \int_{A_c} (u_c^2 + p_c)\, dA + \int_{Aa} (u_D^2 + p_D)\, dA + W \int_{V_c} \mathrm{v}_c\, dV + W \int_{Va} \mathrm{v}_D\, dV . \quad (5.1.73)$$

The solution of (5.1.73) is quite complex. To enable the reader to easily follow the derivation it is broken down into a number of steps.

Step 1: The integrals associated with firstly the current, and secondly the ambient fluid, are reduced to single integrals.

Step 2: The terms used previously in § 3 in deriving conservation of energy with simple flow, are then considered.

Step 3: The remaining terms for the current, which result from relaxing the zero velocity assumption, are considered next.

Step 4: The terms derived in steps 2 & 3 are combined to produce a simplified version of (5.1.73), which contains two single integrals.

Step 5: These are evaluated, where possible by substituting exact differentials and making use of the Bernoulli equations, to produce the general solution for the momentum integral.

Step 6: To confirm that the momentum integral reduces to that for simple flow, $u_c = 0$ is substituted into the general solution obtained in step 5.

Step 1 - The terms within the double integrals in (5.1.73) associated with the current and the ambient fluid are integrated as follows.

Current

The velocity term in the first integral becomes

$$\int_{A_c} u_c^{\,2}\, dA = \int_0^d \int_{1-\eta}^{1} u_c^{\,2}\, dz\, dy = \int_0^b u_c^{\,2}\, dy + \int_b^d u_c^{\,2} \eta\, dy. \tag{5.1.74}$$

The substitution (5.1.9) is used to replace the pressure term in the first integral and it is integrated to give

$$\int_{A_c} P_c\, dA = \int_0^d \int_{1-\eta}^{1} P_c + z - 1\ \, dz\, dy$$

$$= \int_0^b P_c\, dy + \int_b^d \left(P_c \eta - \tfrac{1}{2}\eta^2 \right) dy - \tfrac{1}{2}\, b. \tag{5.1.75}$$

The third integral,which describes the Coriolis force associated with the across stream flow within the current, is simplified using the physical argument that since the flow is recirculating and there is no flux into or out of the current, then the volume flux across a vertical plane at y must be equivalent to $Q_c(0; y)$. The substitution (5.1.33) is also applied, resulting in

$$W \int_{V_c} \mathrm{v}_c \, dV \;=\; W \int_0^d Q_c(y)\ dy \;=\; -\delta \int_0^d B\,(y)\, dy. \qquad (5.1.76)$$

<u>Ambient fluid</u>

The second integral in (5.1.73) is associated with the downstream ambient fluid. This is integrated with respect to z, then (3.2.25), applied downstream, is substituted to give

$$\int_{Aa} (\, u_D{}^2 + p_D\,)\, dA \;=\; \int_b^1 B_D(y) + \tfrac{1}{2}\, u_D{}^2\ - Wcy\ - \eta(\, u_D{}^2 + p_D)\, dy\,. \qquad (5.1.77)$$

The forth integral, which concerns the flow of the ambient fluid around the head of the current, is evaluated as in § 3.2.4.3 using (3.2.35), (3.2.36) and (3.2.37) to give

$$W \int_{Va} \mathrm{v}_D \, dV = \tfrac{1}{2} Wcb^2 + \int_b^1 Wcy\ - B_D(y)\, dy. \qquad (5.1.78)$$

Adding (5.1.77) and (5.1.78) the Bernoulli terms cancel and the expression for the ambient fluid becomes

$$\int_{Aa} (\, u_D{}^2 + p_D\,)\, dA \ + W \int_{Va} \mathrm{v}_D \, dV =$$

$$\int_b^d (\tfrac{1}{2}\, u_D{}^2\ -\ \eta u_D{}^2\ -\ \eta\, p_D)\, dy\ + \tfrac{1}{2}\, U_D{}^2\, (1 - d)\ + \tfrac{1}{2}\, Wcb^2. \qquad (5.1.79)$$

Step 2 - in the energy conserving theory for simple flow the velocity of the current equalled zero, therefore the momentum integral consisted of the second and forth integrals in (5.1.73), plus the integral describing the cross-sectional pressure acting on the current. Hence adding (5.1.79) to (5.1.75) gives

$$\int_{Aa} (u_D{}^2 + p_D)\, dA \;+\; W \int_{Va} \nu_D \, dV \;+\; \int_{A_c} p_c \, dA =$$

$$\int_0^b P_c \, dy + \int_b^d (\tfrac{1}{2}\, u_D{}^2 \;-\; \eta u_D{}^2 + \tfrac{1}{2}\, \eta^2)\, dy \;+ \tfrac{1}{2}\, U_D{}^2 (1 - d) + \tfrac{1}{2}\, Wcb^2 - \tfrac{1}{2}\; b. \tag{5.1.80}$$

Step 3 - the sum of the remaining terms in (5.1.73) for the current equals (5.1.74) plus (5.1.76), which gives

$$\int_{A_c} u_c{}^2 \; dA \;\; + W \int_{V_c} \nu_c \, dV = \int_0^b u_c{}^2 - \delta B_c(y)\, dy \;+\; \int_b^d u_c{}^2 \eta - \delta B_c(y)\, dy. \tag{5.1.81}$$

The first term in the second integral is integrated by parts using the relationship obtained in the derivation of (5.1.33)

$$\frac{-\delta}{W} \frac{dB_c}{dy} = \eta u_c . \tag{5.1.82}$$

Then the substitution (5.1.7) is applied, hence (5.1.81) becomes

$$\int_{A_c} u_c{}^2 \; dA \;\; + W \int_{V_c} \nu_c \; dV \;=\; \int_0^b u_c{}^2 - \delta B_c(y)\, dy \;+\; \int_b^d - \eta B_c(y)\, dy - \left[\tfrac{\delta}{W} u_c B_c(y)\right]_b^d . \tag{5.1.83}$$

Step 4 - by combining (5.1.80) and (5.1.83) the momentum integral (5.1.73) becomes

$$\int_0^b (P_c \;+\; u_c{}^2 - \delta B_c(y))\, dy \;+\; \int_b^d (\tfrac{1}{2}\; u_D{}^2 \;+ \tfrac{1}{2}\, \eta^2 - \eta u_D{}^2 - \eta B_c(y))\, dy$$

$$- \left[\frac{\delta}{W} u_c B_c(y)\right]_b^d \;+ \tfrac{1}{2}\, U_D{}^2 (1 - d) \;+ \tfrac{1}{2}\, Wcb^2 - \tfrac{1}{2}\, b \;\; = \tfrac{1}{2}\, c^2 . \tag{5.1.84}$$

Step 5 - the Bernoulli function (5.1.30) is used to remove the pressure term in the first integral above. This integral is then solved using two substitutions of (5.1.7), and (5.1.82), (noting that $\eta = 1$ where $y \in [0, b]$). Hence the first integral in (5.1.84) becomes

$$\int_0^b (P_c + u_c^2 - \delta B_c(y))\, dy = -\frac{\delta}{W}\left[\frac{u_c^3}{6(1-\delta)} + u_c B_c(y)\right]_0^b - \tfrac{1}{2}Wcb^2. \tag{5.1.85}$$

The second integral in (5.1.84) is solved as follows: the substitution (5.1.13) is applied to the first two terms; (5.1.8) is used to express the third term as an exact differential; the forth term is integrated by parts making use of (5.1.8) and (5.1.82). Hence the second integral becomes

$$\int_b^d (\tfrac{1}{2}\ u_D^2 + \tfrac{1}{2}\,\eta^2 - \eta u_D^2 - \eta B_c(y))\, dy =$$

$$\int_b^d (\tfrac{1}{2}\ u_D u_c - \frac{\eta}{\delta}\, u_D u_c)\, dy + W^{-1}\left[\tfrac{1}{2}\ u_D\eta - \tfrac{1}{3}\, u_D^3 - u_D B_c(y)\right]_b^d. \tag{5.1.86}$$

The second term in the remaining integral is simplified further by: substituting a differential for η using (5.1.7); integrating by parts; substituting the potential vorticity equations (5.1.8) and (5.1.7). Hence the momentum integral (5.1.84) becomes

$$\int_b^d \tfrac{1}{2}\ (-\,u_c(u_D + \delta\, u_c))\, dy + W^{-1}\left[\frac{\delta}{6(1-\delta)}u_c^3 - \delta\, u_c B_c\right]_0^b$$

$$W^{-1}\left[\ \tfrac{1}{6}\ \delta\, u_c^3 + \tfrac{1}{2}\, u_c^2 u_D - \tfrac{1}{3}\, u_D^2 + \tfrac{1}{2}\ u_D\eta - \delta\ u_c B_c(y) -\ u_D B_c(y)\ \right]_b^d$$

$$+ \tfrac{1}{2}\, U_D^2(1-d) - \tfrac{1}{2}\ b = \tfrac{1}{2}\, c^2. \tag{5.1.87}$$

There does not exist an exact differential which could be used as a substitution to solve the final integral. However a solution is possible by substituting the velocity equations (5.1.25) and (5.1.26) into the respective terms and integrating directly to give

$$\int_b^d \tfrac{1}{2}\ (-\,u_c(u_D + \delta\, u_c))\, dy = \int_b^d -\tfrac{1}{2}\, u_c(\,u_D(0) + \delta\, u_c(0) + W\delta y\,))\, dy$$

$$= \Big[y\big((\ u_c(0)\ u_D(0))(-(W^2/W'^2)) + \tfrac{1}{2}\, u_D(0)^2(-(W^2/\delta W'^2)) + \tfrac{1}{2}\, u_c(0)^2((W^2/W'^2) - \delta)\big)$$

$$+\ y^2\left(\tfrac{1}{4}(u_c(0)\,)(-W\delta + (W^3/W'^2) - \delta(W^3/W'^2)) + \tfrac{1}{2}\, u_D(0)(-(W^3/W'^2))\right) +$$

$$+\, y^3\left(-\tfrac{1}{6}\ (W^4/W'^2)\delta\right) + \lambda\left(-\tfrac{1}{2}\ (W^2/W'^2)\right) + \lambda'\left(\tfrac{1}{2}\ u_D(0)(W/\delta W'^2) + \tfrac{1}{2}\ u_c(0)(W/W'^2)\ \right)$$

$$+\tfrac{1}{2}\ y\lambda'\left(W^2/W'^2\right)\Big]_b^d \tag{5.1.88}$$

where $\lambda = W'^{-1}\big((\eta_0 - (W^2/W'^2)) \sinh W'y + (-(W/W')(u_c(0) - u_D(0)) \cosh W'y)\big)$

and $\lambda' = d\lambda/dy$.

To clarify the momentum equation (5.1.87), firstly, the cross product terms $\frac{1}{2} u_c^2 u_D$ and $u_D B_c(y)$ are replaced using (5.1.30), (3.2.25) and (5.1.12), to give

$\frac{1}{2} u_c^2 u_D - u_D B_c(y) = \frac{1}{2} u_D^3 - u_D B_D(y) - u_D \eta.$

Secondly, the terms within the brackets are rearranged to refer to either the current or the ambient fluid. Note that for $y \in [0, d]$ $B_c = 0$, according to (5.1.31). Hence, the general solution to the momentum equation (5.1.73) becomes

$$\frac{1}{2} c^2 = \int_b^d \frac{1}{2} (-u_c(u_D + \delta u_c))\, dy + W^{-1}\left[\frac{\delta^2}{6(1-\delta)} u_c^3\right]_0^b + \left[\frac{\delta}{6W} u_c^3\right]_0^d + W^{-1}\left[\frac{1}{6} u_D^3 - \frac{1}{2} u_D \eta - u_D B_D(y)\right]_b^d + \frac{1}{2} U_D^2 (1-d) - \frac{1}{2} b. \tag{5.1.89}$$

where the integral in the above expression is given by (5.1.88). Note, for $y \in [0, b]$, $B_D = 0$ and at $y = d$, $B_D = W(c + (1-d)U_D)$ where (5.1.36) is substituted into (5.1.52). This equation (5.1.89) is the final general equation required to close the problem.

Step 6 - in order to confirm that the general solution for the momentum integral (5.1.89) reduces to that for the energy conserving model with simple flow (3.2.38), the case of $u_c = 0$ is considered. The assumption of zero velocity for the current will affect the derivation of the ambient fluid pressure and consequently the Bernoulli function, $B_D(y)$ in the above expression. Substituting $u_c = 0$ into the geostrophic equation (5.1.10), the dependent ambient fluid pressure for $y \in [b, d]$ becomes (3.2.12), as derived in § 3.2.3.3. Therefore, the Bernoulli function (3.2.25) applied downstream becomes

$$y \in [b, d] \qquad B_D = \frac{1}{2} u_D^2 - \eta \tag{5.1.90}$$

Substituting (5.1.90) and $u_c = 0$ into (5.1.89) gives

$$c^2 = W^{-1}\left[-\frac{2}{3} u_D^3 + u_D \eta\right]_b^d + U_D^2(1-d) - b. \tag{5.1.91}$$

The above expression is equivalent to (3.2.28) where the sign convention (3.2.5) is adopted.

5.1.5 Summary of the general form of the governing equations

The problem is now fully specified. There are four general equations - momentum integral (5.1.89) and three Bernoulli equations (5.1.44), (5.1.57) and (5.1.66). For each case the relevant boundary conditions b and d are applied to these general equations. Next the flow structure equations are substituted enabling the resulting equations to be expressed in terms of the parameters, $u_c(0)$, $u_D(0)$, $\eta(0)$ and c, which are a function of W and δ. These four equations can then be solved simultaneously for each level of rotation.

Momentum equation

$$\begin{aligned} \tfrac{1}{2}c^2 = & \int_b^d \tfrac{1}{2}\left(-u_c(u_D+\delta\, u_c)\right) dy + W^{-1}\left[\frac{\delta^2}{6(1-\delta)}u_c{}^3\right]_0^b + \left[\frac{\delta}{6W}u_c{}^3\right]_0^d \\ & + W^{-1}\left[\tfrac{1}{6}u_D{}^3 + \tfrac{1}{2}\, u_D\eta - u_D B_D(y)\right]_b^d + \tfrac{1}{2}U_D{}^2(1-d) - \tfrac{1}{2}\, b \end{aligned} \qquad (5.1.89)$$

N.b. the integral in (5.1.89) is given by (5.1.88)

Bernoulli equations

$$\tfrac{1}{2}u_D{}^2(b) = \tfrac{1}{2}u_c{}^2(b) + \frac{Wb}{\delta}u_c(b) + W^2b^2\,\frac{1-\delta}{2\delta^2} + \eta(b) \qquad (5.1.44)$$

$$c = W^{-1}\left[\tfrac{1}{2}u_D(1)^2 - \tfrac{1}{2}u_c(d)^2 + WU_D(d-1) - \eta(d)\right] \qquad (5.1.57)$$

$$\begin{aligned} \tfrac{1}{2}\left(u_c{}^2(d) - u_c{}^2(b)\right) = & \frac{(d-b)}{(1+\delta)}\Big(W\left(u_D(b) + \delta\, u_c(b)\right)\Big) \\ & + \frac{1}{(1+\delta)}\left(\eta(b) - \eta(d) + \tfrac{1}{2}W^2\delta(d-b)^2\right) \\ & + \frac{Wb}{\delta}u_c(b) + W^2b^2\,\frac{1-\delta}{2\delta^2}. \end{aligned} \qquad (5.1.66)$$

Flow structure equations

$y \in [b, d]$

$$\eta(y) = \delta/(1+\delta) + \big(\eta_0 - \delta/(1+\delta)\big) \cosh W'y + \big(-(W/W')(u_c(0) - u_D(0))\big) \sinh W'y \tag{5.1.21}$$

$$y \in [0, b] \quad \eta(y) = 1$$

$$y \in [d, 1] \quad \eta(y) = 0$$

$y \in [0, d]$

$$u_c(y) = u_{0\,c} - (W^2/\delta W'^2)\,(u_c(0) - u_D(0)) + W\big(\delta/(1+\delta)\big)y - (W/\delta W')\big[\big(\eta_0 - \delta/(1+\delta)\big) \sinh W'y + \big(-(W/W')(u_c(0) - u_D(0))\big) \cosh W'y\big] \tag{5.1.25}$$

$y \in [b, d]$

$$u_D(y) = u_{0\,D} - (W^2/W'^2)\,(u_c(0) - u_{\mathrm{D}}(0)) + W\big(\delta/(1+\delta)\big)y + (W/W')\big[\big(\eta_0 - \delta/(1+\delta)\big) \sinh W'y + \big(-(W/W')(u_c(0) - u_D(0))\big) \cosh W'y\big] \tag{5.1.26}$$

$y \in [d, 1] \quad u_D(y) = U_D = \text{constant}$

$$U_D = u_{0\,D} + (W^2/W'^2)\,(u_c(0) - u_D(0)) + W\big(\delta/(1+\delta)\big)d + (W/W')\big[\big(\eta_0 - \delta/(1+\delta)\big) \sinh W'd + \big(-(W/W')(u_c(0) - u_D(0))\big) \cosh W'd\big] \tag{5.1.92}$$

The boundary conditions

$$d = W^{-1}\cosh^{-1}\left[\frac{-(W^2/W'^2)A \mp \big(B^2\,((W^4/W'^4) + B^2 - A^2)\big)^{\frac{1}{2}}}{(A^2 - B^2)}\right] \tag{5.1.22}$$

$$b = W^{-1}\cosh^{-1}\left[\frac{-(1+\delta)^{-1}A \mp \big(B^2\,((1+\delta)^{-2} + B^2 - A^2)\big)^{\frac{1}{2}}}{(A^2 - B^2)}\right] \tag{5.1.24}$$

where A and B are the constants defined in (5.1.18) and (5.1.19).

5.1.6 The governing equations for each case

The general form of the governing equations can now be applied to each of the flow geometries, which are dependent upon the strength of the rotation.

5.1.6.1 Case A

First I shall present case A which corresponds to a weak rotation rate, where the current continues to fill the full width of the channel. The boundary conditions for case A are

$$b = 0 \qquad d = 1$$

The governing equations (5.1.89), (5.1.44), (5.1.57) and (5.1.66) become

Momentum equation

$$\tfrac{1}{2}c^2 = \int_0^1 \tfrac{1}{2}\left(-u_c(u_D + \delta\, u_c)\right) dy + \frac{\delta}{6W}\left(u_c(1)^3 - u_c(0)^3\right)$$
$$+ W^{-1}\left[\tfrac{1}{6}\left(u_D(1)^3 - u_D(0)^3\right) + \tfrac{1}{2}\left(u_D(1)\,\eta(1) - u_D(0)\,\eta(0)\right)\right] - u_D(1)c \qquad (5.1.93)$$

N.b. the integral in (5.1.93) is given by (5.1.88) applied at $y \in [0, 1]$

Bernoulli equations

$$\eta_0 = \tfrac{1}{2}\, u_D(0)^2 - \tfrac{1}{2}\, u_c(0)^2 \qquad (5.1.37)$$

$$c = W^{-1}\left[\tfrac{1}{2}\, u_D(1)^2 - \tfrac{1}{2}\, u_c(1)^2 - \eta(1)\right] \qquad (5.1.94)$$

$$\tfrac{1}{2}\left(u_c^2(1) - u_c^2(0)\right) = \frac{W}{(1+\delta)}\left(u_D(0) + \delta\, u_c(0)\right)$$
$$+ \frac{1}{(1+\delta)}\left(\eta(0) - \eta(1) + \tfrac{1}{2} W^2 \delta\right) \qquad (5.1.95)$$

Flow structure equations

$$\eta(1) = \delta/(1+\delta) + (\eta_0 - \delta/(1+\delta))\cosh W' + (-(W/W')(u_c(0) - u_D(0)))\sinh W \quad (5.1.96)$$

$$u_c(1) = u_c(0) - (W^2/\delta W'^2)\,(u_c(0) - u_D(0)) + W(\delta/(1+\delta)) - (W/\delta W')[(\eta_0 - \delta/(1+\delta))\sinh W' + (-(W/W')(u_c(0) - u_D(0)))\cosh W'] \quad (5.1.97)$$

$$u_D(1) = u_D(0) + (W^2/W'^2)\,(u_c(0) - u_D(0)) + W(\delta/(1+\delta)) + (W/W')[(\eta_0 - \delta/(1+\delta))\sinh W' + (-(W/W')(u_c(0) - u_D(0)))\cosh W'] \quad (5.1.98)$$

5.1.6.2 Case B

Case B corresponds to a moderate rotation rate, where the current banks up against the right hand wall and outcrops on the surface at $y = d$. Note that there is no shear in the free stream since $\eta(y) = 0$ for $y \in [d, 1]$, therefore the boundary conditions for case B become

$$b = 0$$

$$d = W^{-1}\cosh^{-1}\left[\frac{-(W^2/W'^2)A \mp \left(B^2\left((W^4/W'^4) + B^2 - A^2\right)\right)^{\frac{1}{2}}}{(A^2 - B^2)}\right] \quad (5.1.22)$$

where A and B are the constants defined in (5.1.18) and (5.1.19).

For case B the general equations (5.1.89), (5.1.44), (5.1.57) and (5.1.66) become

Momentum equation

$$\tfrac{1}{2}c^2 = \int_0^d \tfrac{1}{2}(-u_c(u_D + \delta u_c))\,dy + \frac{\delta}{6W}(u_c(d)^3 - u_c(0)^3) + W^{-1}\left[\tfrac{1}{6}(U_D^3 - u_D(0)^3) - \tfrac{1}{2}u_D(0)\eta(0) - \tfrac{1}{2}(U_D^3 - U_D u_c(d)^2\right] + \tfrac{1}{2}U_D^2(1 - d) \quad (5.1.99)$$

N.b. the integral in (5.1.99) is given by (5.1.88) applied at $y \in [0, d]$

Bernoulli equations

$$\eta_0 = \tfrac{1}{2} u_D(0)^2 - \tfrac{1}{2} u_c(0)^2 \qquad (5.1.37)$$

$$c = W^{-1} \left[\tfrac{1}{2} U_D{}^2 - \tfrac{1}{2} u_c(d)^2 + W U_D (d - 1) \right] \qquad (5.1.100)$$

$$\begin{aligned} \tfrac{1}{2} \left(u_c{}^2(d) - u_c{}^2(0) \right) &= \frac{W d}{(1+\delta)} \left(u_D(0) + \delta u_c(0) \right) \\ &+ \frac{1}{(1+\delta)} \left(\eta(0) + \tfrac{1}{2} W^2 \delta d^2 \right) \qquad (5.1.101) \end{aligned}$$

Flow Structure Equations

$$\eta(d) = 0 = \mathrm{d}/(1+\delta) + (\eta_0 - \delta/(1+\delta)) \cosh W'd + (-(W/W')(u_c(0) - u_D(0))) \sinh W'd \qquad (5.1.102)$$

$$\begin{aligned} u_c(d) = u_{0\,c} &- (W^2/\delta W'^2)\,(u_c(0) - u_D(0)) + W(\delta/(1+\delta))d - \\ &(W/\delta W')[(\eta_0 - \delta/(1+\delta)) \sinh W'd + (-(W/W')(u_c(0) - u_D(0))) \cosh W'd] \qquad (5.1.103) \end{aligned}$$

$$\begin{aligned} u_D(d) = U_D = u_{0\,D} &+ (W^2/W'^2)\,(u_c(0) - u_D(0)) + W(\delta/(1+\delta))d + \\ &(W/W')[(\eta_0 - \delta/(1+\delta)) \sinh W'd + (-(W/W')(u_c(0) - u_D(0))) \cosh W'd]. \qquad (5.1.91) \end{aligned}$$

5.1.6.3 Case C

Case C corresponds to a strong rotation rate, where the current has banked up against the right hand wall to such an extent that it fills the full depth of the channel and outcrops on the bottom boundary at $y = b$. Therefore, the boundary conditions for case C are

$$d = W^{-1} \cosh^{-1} \left[\frac{-(W^2/W'^2)A \mp \left(B^2 \left((W^4/W'^4 + B^2 - A^2) \right) \right)^{\frac{1}{2}}}{(A^2 - B^2)} \right] \qquad (5.1.22)$$

$$b = W^{-1}\cosh^{-1}\left[\frac{-(1+\delta)^{-1}A \mp \left(B^2\left((1+\delta)^{-2}+B^2-A^2\right)\right)^{\frac{1}{2}}}{(A^2-B^2)}\right] \tag{5.1.24}$$

where A and B are the constants defined in (5.1.18) and (5.1.19).

The general equations (5.1.89), (5.1.44), (5.1.57) and (5.1.66) become

Momentum equation

$$\tfrac{1}{2}c^2 = \int_b^d \tfrac{1}{2}\,(-u_c(u_D+\delta\,u_c))\,dy + \frac{\delta^2}{W6(1-\delta)}\left(u_c(b)^3 - u_c(0)^3\right) + \frac{\delta}{6W}\left(u_c(d)^3 - u_c(0)^3\right)$$
$$+ W^{-1}\left[\tfrac{1}{6}(U_D^{\,3} - u_D(b)^3) - \tfrac{1}{2}\,u_D(b) - \tfrac{1}{2}\left(U_D^{\,3} - u_c(d)^2 U_D\right)\right] + \tfrac{1}{2}U_D^{\,2}(1-d) - \tfrac{1}{2}\,b \tag{5.1.104}$$

N.b. the integral in (5.1.104) is given by (5.1.88) applied at $y \in [b, d]$

Bernoulli equations

$$\tfrac{1}{2}u_D^{\,2}(b) = \tfrac{1}{2}u_c^{\,2}(b) + \frac{Wb}{\delta}u_c(b) + W^2b^2\,\frac{1-\delta}{2\delta^2} + 1 \tag{5.1.105}$$

$$c = W^{-1}\left[\tfrac{1}{2}U_D^{\,2} - \tfrac{1}{2}u_c(d)^2 + WU_D\,(d-1)\right] \tag{5.1.100}$$

$$\tfrac{1}{2}\left(u_c^2(d) - u_c^2(b)\right) = \frac{(d-b)}{(1+\delta)}\left(W\left(u_D(b) + \delta\,u_c(b)\right)\right)$$
$$+ \frac{1}{(1+\delta)}\left(\eta(b) + \tfrac{1}{2}W^2\delta(d-b)^2\right)$$
$$+ \frac{Wb}{\delta}u_c(b) + W^2b^2\,\frac{1-\delta}{2\delta^2}. \tag{5.1.66}$$

Flow structure equations

$$\eta(b) = 1 = \delta/(1+\delta) + (\eta_0 - \delta/(1+\delta)) \cosh W'b + (-(W/W')(u_c(0) - u_D(0))) \sinh W'b \qquad (5.1.23)$$

$$u_c(b) = u_{0\,c} - (W^2/\delta W'^2)\,(u_c(0) - u_D(0)) + W(\delta/(1+\delta))b - (W/\delta W')[(\eta_0 - \delta/(1+\delta)) \sinh W'b + (-(W/W')(u_c(0) - u_D(0))) \cosh W'b] \qquad (5.1.106)$$

$$u_D(b) = u_D(0) + (W^2/W'^2)\,(u_c(0) - u_D(0)) + W(\delta/(1+\delta))b + (W/W')[(\eta_0 - \delta/(1+\delta)) \sinh W'b + (-(W/W')(u_c(0) - u_D(0))) \cosh W'b]. \qquad (5.1.107)$$

$u_c(d)$ and U_D are as defined for case B

5.2 Numerical solution

Due to the complexity of the governing equations and the absence of a simple relationship between $u_c(0)$ and $u_D(0)$, a computer programme is required to solve the equations for each case. I am indebted to G. Lane-Serff for developing such a programme (written in Fortran using standard NAG routines). Using this he has calculated approximate solutions to give an indication of the numerical results which will be obtained. The parameter range for which solutions were obtained are illustrated in figure 5.2. Lane-Serff's initial results reveal a fourth possible flow geometry, labelled BII in figure 5.2. This flow has $d = 0$ and $b > 0$ and thus outcrops only on the bottom boundary. Further investigations are necessary to discover whether this structure is realisable in the laboratory.

Note $\delta = 1$ corresponds to currents whose source region is of an equivalent depth to the full depth of the channel downstream. $\delta < 1$ is applicable to currents originating from a shallow source region, whilst $\delta > 1$ could be applied to currents where the source region is deeper than the downstream depth, for example where a deep ocean flow encounters a plateau. Therefore, the current has to undergo vortex compression and hence loss of relative vorticity resulting in an anticyclonic circulation.

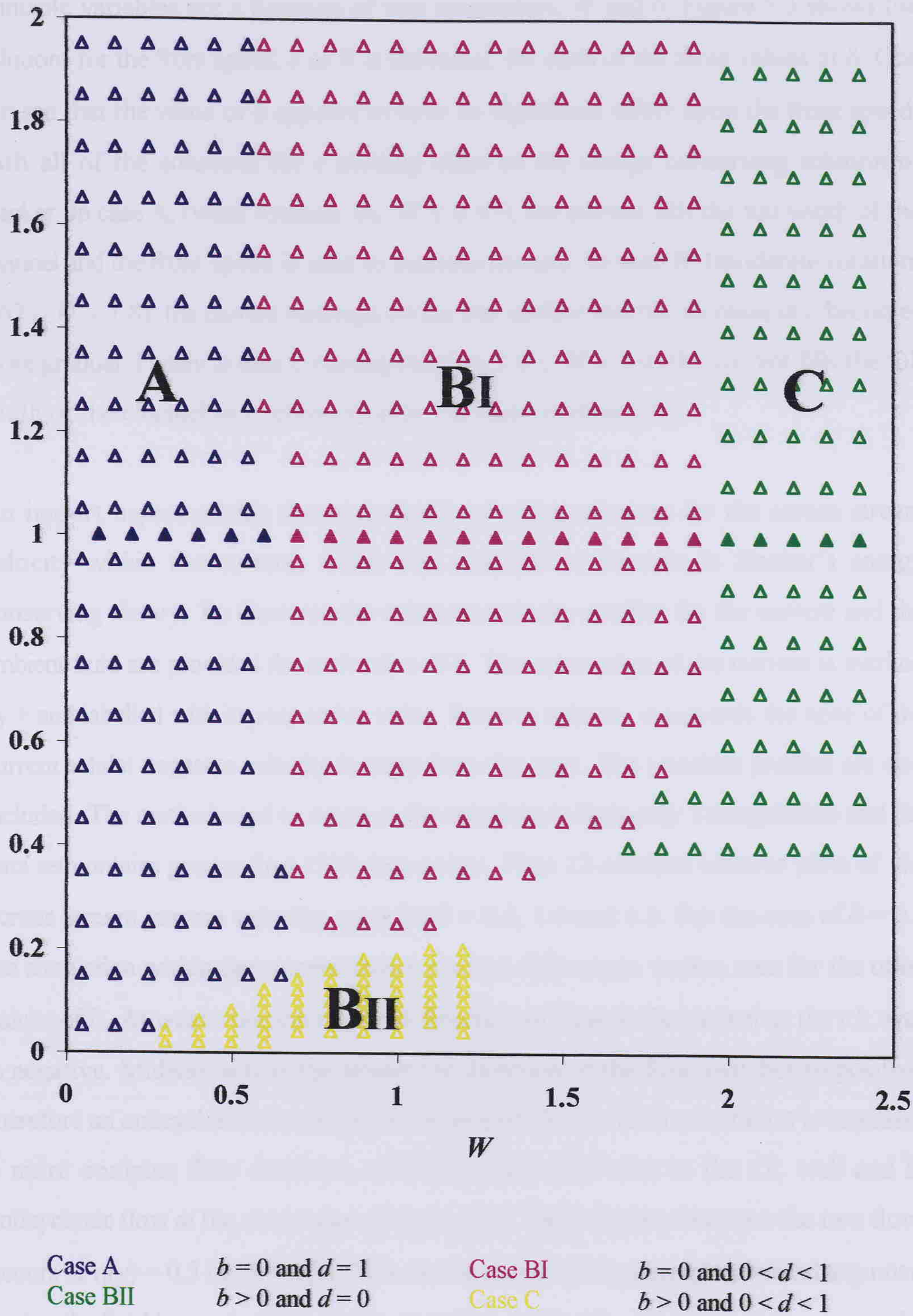

FIGURE 5.2 Parameter range for which preliminary solutions to the governing equations were obtained by Lane-Serff ,using a Fortran programme, for the energy conserving theory with prescribed potential vorticity. Note the presence of a fourth flow geometry BII.

Solutions have been obtained for 3 cases where $\delta = 0.5$, 1.0 and 1.5. In this theory the principle variables are a function of two parameters, W and δ. Figure 5.3 shows the solutions for the front speed, c as W is increased, for each of the three values of δ. One can see that the value of δ appears to have no significant effect upon the front speed, with all of the solutions for c plotting close to the energy conserving solution of Hacker. In case A, (weak rotation, $0 \leq W \leq 0.67$), the current fills the full width of the channel and the front speed is seen to increase linearly. In case B, (moderate rotation, $0.67 \leq W \leq 1.8$) the current outcrops on the free surface and the increase in c becomes more gradual. Finally in case C (strong rotation, $1.8 \leq W \leq 3.0$) the current fills the full width of the channel as c tends towards 1 at high rotation rates.

An import aspect of this theory is that it provides solutions for the across stream velocity within the current, which was assumed to be zero in Hacker's energy conserving theory. To illustrate the solutions velocity profiles for the current and the ambient fluid are provided for each value of δ. The outer edge of the current is marked by + and labelled with its respective value. Positive velocity is towards the nose of the current whilst negative velocity is away from the nose. The interface profiles are also included. The method used to contour the solutions is Delaunay Triangulation and the data set contains greater than 1500 data points. Plate 12 contains contour plots of the across stream current velocity, $u_c(y)$ for $\delta = 0.5$, 1.0 and 1.5. For the case of $\delta = 0.5$ the circulation within the current shows marked differences to that seen for the other values of δ. At weak rotation rates the direction of flow in the current at the r.h. wall is negative. Midway across the stream the direction of the flow switches to positive, therefore an anticyclonic circulation has developed. As the level of rotation is increased a more complex flow develops, with a cyclonic flow next to the r.h. wall and an anticyclonic flow at the outer edge of the current. The boundary between the two flows occurs at $\eta(y) = 0.5$ i.e. $\delta = \eta(y)$. This can be explained by a simple physical argument in that the fluid has undergone vortex stretching at the r.h.wall whilst at the outer edge of the current the fluid has experienced vortex compression. The stretching of the vortex lines requires that the water column has to take on additional cyclonic relative vorticity to conserve its potential vorticity, whilst the compression requires additional anticyclonic relative vorticity. Mathematically this behaviour is described by the

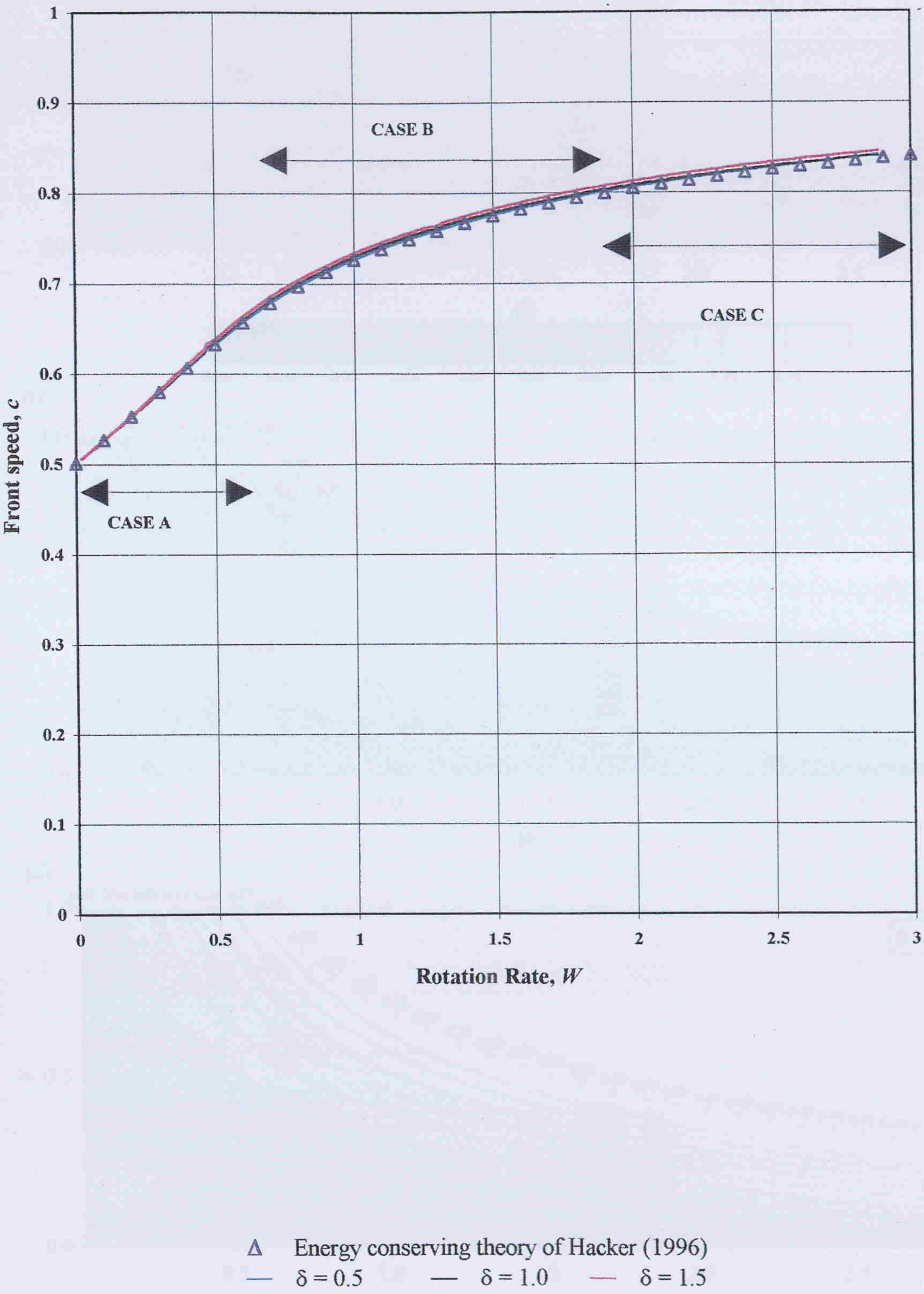

Figure 5.3. Comparison of front speed, c, versus rotation rate, W, for each of the values of δ and the energy conserving theory of Hacker.

PLATE 12

Across-stream Velocity of the Current, $u_c(y)$

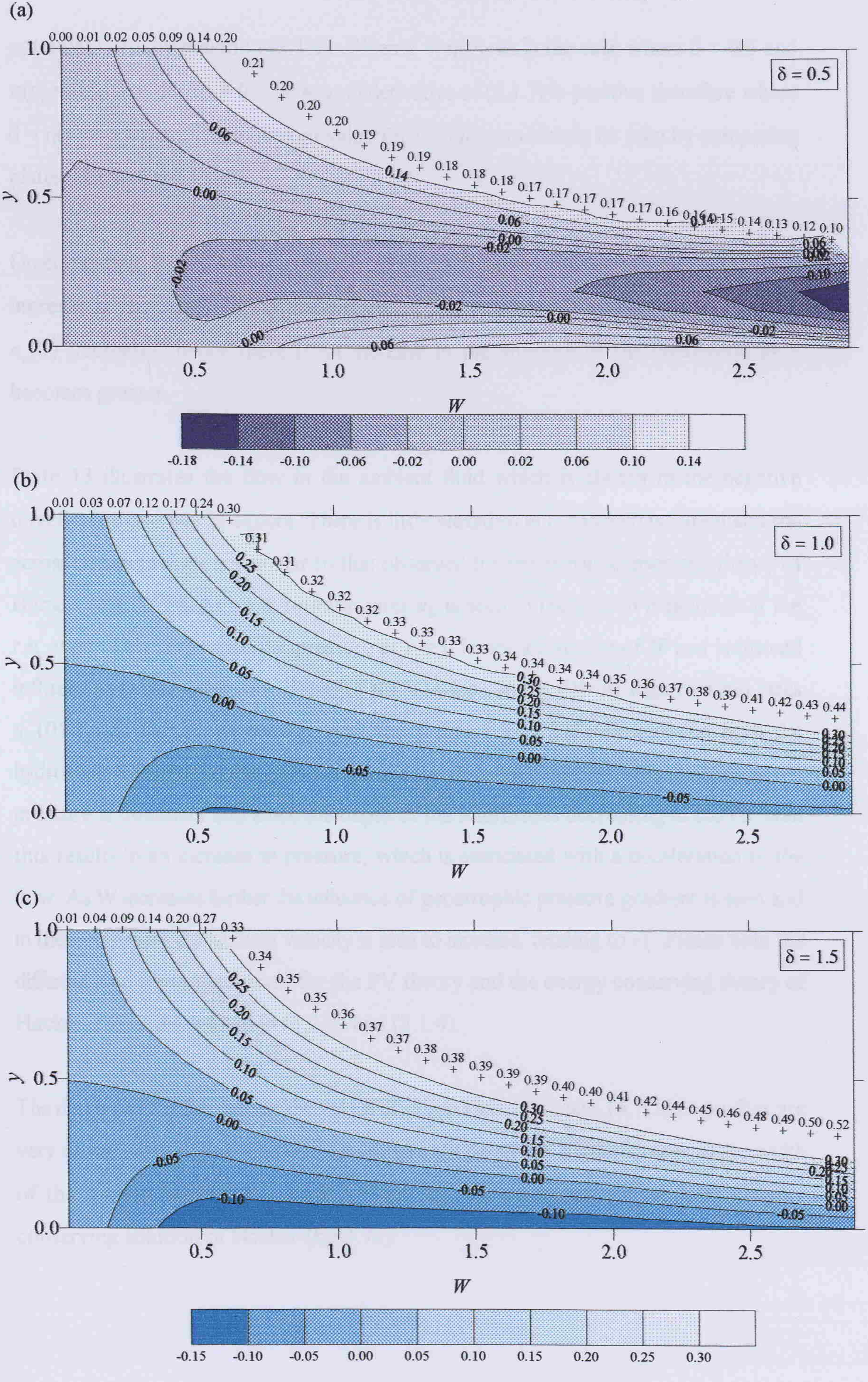

potential vorticity equation (5.1.7). When $\delta = \eta(y)$, as is the case where $\delta = 0.5$ and $\eta(y) = 0.5$, then $du_c/dy = 0$. The second derivative of (5.1.7) is positive therefore where $\delta = \eta(y) = 0.5$ there is a minimum value for u_c. This can clearly be seen by comparing plates 12a and 14a.

On comparing the velocity, $u_c(y)$ at $y = d$ for each value of δ, the velocity is found to increase at the outer edge of the current as δ is increased. However at the r.h. wall $u_c(0)$ decreases, hence there is an increase in the strength of the circulation as δ becomes greater.

Plate 13 illustrates the flow in the ambient fluid which is always in the negative direction as one would expect. There is little variation in $u_D(y)$ as δ is varied and the across stream profiles are similar to that observed for the energy conserving theory of Hacker (fig. 3.7b). At weak rotation rates u_D is seen to increase in magnitude at the r.h. wall. This is because the pressure at $y = 0$ is not a function of W and is instead influenced by the increasing depth of the interface and $u_c(0)$. At high rotation rates $u_D(0)$ tends to $-2^{\frac{1}{2}}$. At the l.h. wall the pressure is a balance between both the hydrostatic and geostrophic pressure gradients. At weak rotation rates the hydrostatic pressure is dominant and since the depth of the interface is decreasing at the l.h. wall this results in an increase in pressure, which is associated with a deceleration of the flow. As W increases further the influence of geostrophic pressure gradient is seen and in the free stream the ambient velocity is seen to increase, tending to -1. Please note the different sign conventions used for the PV theory and the energy conserving theory of Hacker, these are defined in (3.2.5) and (5.1.4).

The depth profiles for each of the values of δ are shown in plate 14. These profiles are very similar, with the only discernable difference being the slight increase in the width of the current for $\delta = 0.5$. Both $\delta = 1.0$ and 1.5 were very similar to the energy conserving solution of Hacker (fig 3.7a).

PLATE 13

Across-stream Velocity of the Ambient Fluid, $u_D(y)$

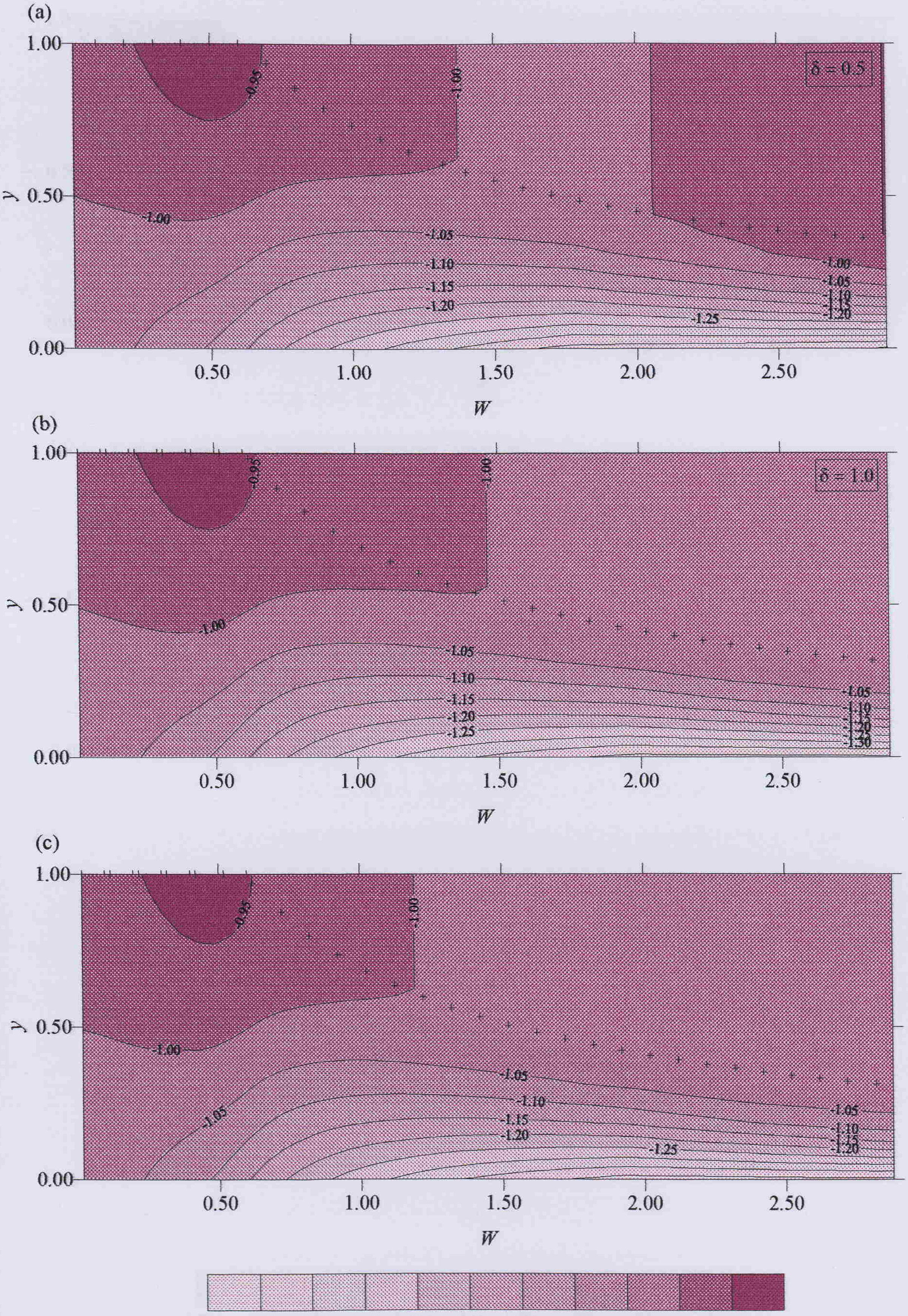

PLATE 14

Across-stream Depth of the Current, $\eta(y)$

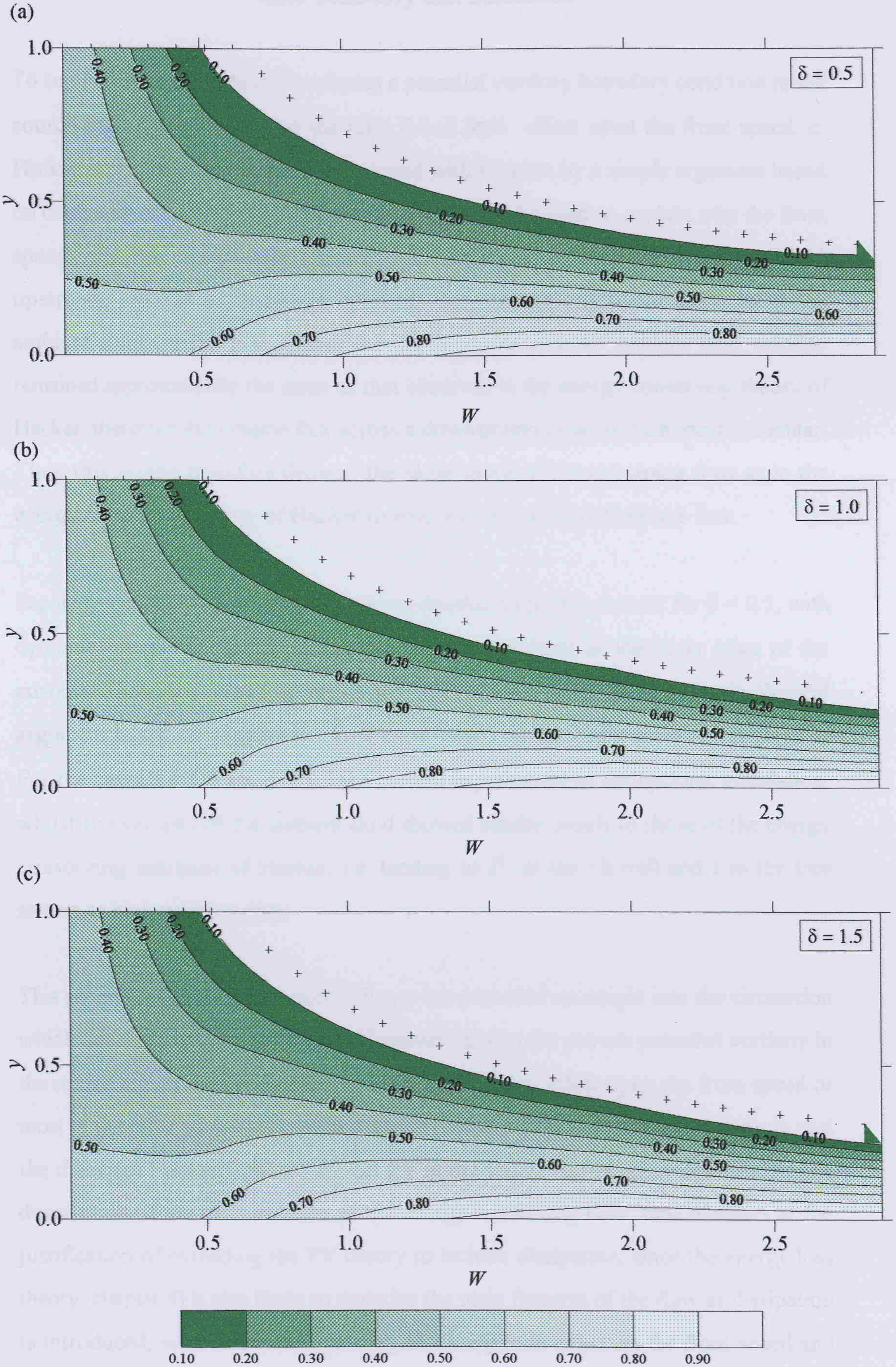

5.2.1 Summary and Discussion

To summarise, the effects of introducing a potential vorticity boundary condition in the source region are firstly, that the ratio δ had little effect upon the front speed, c. Hacker explained the variation in front speed with rotation by a simple argument based on continuity of volume flux. This same argument can be used to explain why the front speed was not significantly altered by the inclusion of potential vorticity (P.V.) upstream, since it is dependent upon the downstream cross-sectional area of the ambient fluid. In the P.V. theory the depth profile and the ambient fluid velocity remained approximately the same as that observed in the energy conserving theory of Hacker, therefore the volume flux across a downstream cross section must be similar. Thus this would therefore demand the same speed of the oncoming flow as in the energy conserving theory of Hacker to ensure conservation of volume flux.

Secondly a complex circulation was seen to develop within the current for $\delta = 0.5$, with cyclonic circulation nearest the r.h.wall and anticyclonic at the outer edge of the current. These converged at $\eta(y) = 0.5$. This was explained using a simple physical argument based on whether the flow experienced vortex compression or stretching. For the cases $\delta = 1.0$ and $\delta = 1.5$ the current experienced an anticyclonic circulation, whilst the velocity of the ambient fluid showed similar trends to those of the energy conserving solutions of Hacker, i.e. tending to $2^{\frac{1}{2}}$ at the r.h.wall and 1 in the free stream at high rotation rates.

This second extension to Hacker's theory has provided an insight into the circulation which develops within the current. However varying the pre-set potential vorticity in the source region does not appear to have a significant effect upon the front speed or most of the other parameters which describe the flow. Therefore one may conclude that the theory of Hacker (with no pre-set PV in the source region) provides an adequate description of the main features of the energy conserving flow. One wonders at the justification of extending the PV theory to include dissipation, since the energy loss theory (chapter 4) is also likely to describe the main features of the flow as dissipation is introduced, with variations in PV again having little effect on the front speed and most of the other parameters.

CHAPTER 6

Laboratory Investigation

6.1 Aims of the Laboratory Investigation

In order to gain a general understanding of the diversity of non and rotating gravity currents a set of preliminary experiments (sets 1 & 2) were performed. The aim of these experiments was to cover as large a range of parameters as possible. Hence, shallow to deep currents, weak to strong rotation, and viscous to inviscid currents were examined. To satisfy these limits three density differences were used, 0.24%, 2.5% and 4.5%. For each rotating experiment an equivalent non-rotating experiment was performed, to act as a control. The main parameter varied was fractional depth, which was controlled using a permanent barrier. Four levels of rotation were examined, see tables 6.1 & 6.2.

Sets 3 to 6 form the main body of the experimental work. Their function was to support the theoretical investigation previously discussed in chapters 3 to 5. Firstly, one of the main assumptions of the theory is that the flow is inviscid. To achieve this a density difference of 2% was chosen to maintain a Reynolds number > 1000. Secondly, the principal variables of the theory are shown in § 4.3.1 to be a function of the two parameters η_0 and W. Therefore, in the experiments only the initial fractional depth, h_0/H_0, and the rotation rate, W, as defined in § 1.2.3, were varied. The remaining parameters, which included the initial depth of fresh water, lock geometry and density difference, were held constant. The permanent barrier used in the preliminary experiments was discarded, since it was difficult to quantify its effect on the flow. The fractional depth was controlled using a method outlined by Griffiths et al (1983), see § 6.2. The fractional depths, $0.2 \leq h_0/H_0 \leq 0.85$, were considered in set 3. The remaining fractional depths i.e. shallow and full depth currents were addressed in sets 4 & 5 where $h_0/H_0 \leq 0.2$ and $h_0/H_0 = 1$ respectively. The range of rotation rates investigated was $0 \leq W \leq 3$, as in the theoretical study.

Exp	g' (cm/s^2)	h_0/H_0	f (s^{-1})	$w/R(h_0)$	$Re(h_0)$
1	2.1	0.12	0.000	0.000	255
2	2.4	0.14	0.000	0.000	349
3	2.4	0.18	0.000	0.000	558
4	2.4	0.20	0.000	0.000	695
5	23.6	0.11	0.000	0.000	704
6	25.0	0.14	0.000	0.000	1118
7	25.0	0.17	0.000	0.000	1598
8	25.0	0.21	0.000	0.000	2367
9	48.7	0.13	0.000	0.000	1412
10	47.8	0.16	0.000	0.000	2043
11	46.8	0.19	0.000	0.000	2559
12	46.8	0.20	0.000	0.000	3068
13	2.7	0.08	1.232	11.34	158
14	2.4	0.11	1.269	10.78	230
15	2.4	0.17	1.412	9.31	492
16	2.1	0.19	1.571	10.42	563
17	2.4	0.10	0.232	2.03	211
18	2.4	0.14	0.253	1.83	371
19	2.4	0.20	0.290	1.72	676
20	2.4	0.18	0.326	2.11	523
21	24.6	0.11	0.367	0.95	796
22	25.0	0.16	0.395	0.84	1424
23	25.7	0.20	0.524	0.95	2173
24	25.0	0.21	0.564	1.02	2267
25	49.3	0.13	0.058	0.10	1382
26	49.3	0.15	0.060	0.09	1782
27	48.0	0.19	0.076	0.10	2738
28	47.4	0.20	0.078	0.10	2919

Table 6.1 Parameters of set 1(preliminary) experiments. Experiments 1 to 12 are non-rotating, 13 to 28 are rotating gravity currents. All the currents are shallow, $h_0/H_0 \leq 0.21$.

Exp	g' (cm/s^2)	h_0/H_0	f (s^{-1})	$w/R(h_0)$	$Re(h_0)$
29	2.4	0.25	0.000	0.000	1049
30	2.4	0.34	0.000	0.000	1927
31	2.4	0.49	0.000	0.000	5178
32	2.4	1.00	0.000	0.000	15286
33	26.6	0.25	0.000	0.000	3320
34	27.6	0.34	0.000	0.000	6570
35	26.0	0.51	0.000	0.000	19148
36	23.6	1.00	0.000	0.000	50066
37	46.1	0.27	0.000	0.000	5110
38	45.1	0.35	0.000	0.000	8990
39	46.4	0.51	0.000	0.000	24999
40	42.4	1.00	0.000	0.000	66852
41	2.4	0.25	0.388	1.98	1058
42	2.4	0.35	0.483	1.95	2141
43	2.4	0.51	0.658	1.90	5804
44	2.4	1.00	0.997	2.06	15989
45	26.6	0.26	0.654	0.98	3761
46	25.3	0.36	0.771	0.95	7210
47	26.3	0.51	1.220	1.07	19242
48	23.3	1.00	1.514	1.01	48906
49	44.8	0.27	0.072	0.08	5154
50	48.0	0.35	0.127	0.11	9454
51	44.1	0.52	0.132	0.09	25446
52	47.4	1.00	0.212	0.10	71158

Table 6.2 Parameters of set 2 (preliminary) experiments. Experiments 29 to 40 are non-rotating, 41 to 52 are rotating. The initial depths range from moderately shallow to full depth, $0.25 \leq h_0/H_0 \leq 1.00$.

In chapter 5 the role of the initial potential vorticity distribution was considered. The theory assumes that potential vorticity is conserved; to investigate this a final set of experiments was performed using particle tracking. This gives a qualitative insight into the direction of flow within the current. The range of parameters investigated in sets 3 to 6 are listed in tables 6.3 to 6.6.

Exp	***g'*** **(cm/s²)**	h_0/H_0	***f*** **(s⁻¹)**	$w/R(h_0)$	$Re(h_0)$
53	18.9	0.27	0.000	0.00	4013
54	19.9	0.24	0.289	0.49	3435
55	18.9	0.26	0.582	0.99	3610
56	19.6	0.24	0.884	1.53	3407
57	19.6	0.25	1.154	1.95	3539
58	20.2	0.25	1.486	2.47	3598
59	20.2	0.25	1.767	2.95	3598
60	20.2	0.34	0.000	0.00	3734
61	19.6	0.34	0.314	0.52	3672
62	19.6	0.33	0.567	0.95	3672
63	19.6	0.33	0.857	1.46	3539
64	19.6	0.34	1.155	1.92	3807
65	19.6	0.34	1.479	2.48	3672
66	19.6	0.33	1.776	3.02	3539
67	19.6	0.51	0.000	0.00	3807
68	19.6	0.50	0.281	0.47	3672
69	19.6	0.53	0.564	0.92	4083
70	19.6	0.54	1.152	1.88	3944
71	19.6	0.50	1.476	2.50	3539
72	19.6	0.50	1.747	2.99	3407
73	19.6	0.83	0.000	0.00	3807
74	19.6	0.80	0.279	0.47	3539
75	19.6	0.84	0.562	0.93	3807
76	19.6	0.74	0.880	1.52	3407
77	19.6	0.78	1.168	1.99	3539
78	18.9	0.79	1.450	2.52	3349
79	19.6	0.75	1.747	3.00	3407

Table 6.3 Parameters of set 3 (main) experiments. Four fractional depths are considered ~ 0.25, 0.33, 0.50 and 0.8. For each fractional depth the rate of rotation is varied between $0 \leq W/R(h_0) \leq 3.0$.

Exp	g' (cm/s^2)	h_0/H_0	f (s^{-1})	$w/R(h_0)$	$Re(h_0)$
80	20.2	0.10	0.000	0.00	1310
81	19.6	0.08	0.281	0.35	963
82	19.6	0.10	0.841	0.98	1205
83	19.6	0.10	1.256	1.46	1214
84	19.6	0.10	1.690	1.92	1298
85	20.2	0.10	2.132	2.39	1310

Table 6.4 Parameters of set 4 (shallow) experiments. The initial depth is held constant, $h_0/H_0 \sim 0.1$. The rotation is rate is varied between $0 \leq W/R(h_0) \leq 2.4$.

Exp	g' (cm/s^2)	h_0/H_0	f (s^{-1})	$w/R(h_0)$	$Re(h_0)$
86	19.6	1.00	0.000	0.00	3849
87	18.8	1.00	0.283	0.48	3590
88	19.6	1.00	0.577	0.98	3513
89	20.2	1.00	0.875	1.43	3815
90	18.9	1.00	1.151	1.99	3463
91	20.2	1.00	1.475	2.41	3829
92	18.5	1.00	1.766	3.03	3598

Table 6.5 Parameters of set 5 (full depth) experiments. The initial depth is held constant, $h_0/H_0 = 1$. The rotation is rate is varied between $0 \leq W/R(h_0) \leq 3.0$.

Exp	g' (cm/s^2)	h_0/H_0	f (s^{-1})	$w/R(h_0)$	$Re(h_0)$
93	19.9	0.25	0.000	0.00	3568
94	19.9	0.25	0.590	0.99	3568
95	19.2	0.25	1.236	2.11	3509

able 6.6 Parameters of set 6 (particle tracking) experiments. The initial depth is held constant, $h_0/H_0 = 0.25$. The rotation is rate is varied between $0 \leq W/R(h_0) \leq 2.1$.

The gravity currents were generated on the surface of the fluid for all of the sets. By using this isopotential surface the effect of topography experienced by bottom currents due to the parabolic shape of the free surface was removed. Bottom friction was also avoided.

6.2 Review of others' experimental findings

Before continuing with the laboratory investigation of the present study, it is useful to discuss the extent of previous authors investigations. The main contributors to the field of rotating gravity currents are Stern et al., (1982), Griffiths, (1983) and more recently Hacker (1996). Table 6.7 lists the range of parameters considered by these authors. Stern and Griffiths focused on surface currents with small initial fractional depth, whilst Hacker investigated full depth locks only. The Reynolds numbers of Stern were lower than the other studies, therefore his currents were more viscous (see table 6.7). Both Stern and Griffiths neglected the transition from the non-rotating to the weakly rotating case. This range was subsequently considered by Hacker, for full depth locks, for both surface and floor currents.

These authors described how when rotating fluid is released into fluid of a different density, in the proximity of a wall, a jet of fluid will form parallel to the boundary either on the surface or bottom of the channel, depending on its relative density. They described many of the features of the gravity current previously associated with non-rotating currents (Simpson, 1987), including, a phase where the leading edge of the current propagates at a constant speed, Kelvin-Helmholtz billows peeling off the outer surface of the current and a pinched neck region behind the head. Griffiths however identified a number of characteristics that were unique to the rotating case. These included the following observations: a considerable increase in the amount of vertical mixing beneath the current; oscillations in the nose velocity associated with the head breaking up and the growth of a new billow at the head; a decrease in the size of the nose and a broadening of the current with time. Stern also described how in some experiments a vortex sheet was observed separating a laminar inner region from a turbulent surface. The main concern of Stern was to quantify the width of the boundary current. He defined the distance from the wall to the vortex sheet as the current width, L. The hydrostatic number, $g'/f^2h_0 = (R(h_0)/h_0)^2$, was as taken as a measure of the strength of rotation, where h_0 is the initial depth of fresh water and $R(h_0)$ is the Rossby radius based on h_0. Stern found that the current width, L, non-dimensionalised by the local Rossby radius, $L/R(h_Z)$, based on the head height h_Z, tended to a constant value of (0.423 +/- 0.056) for $(R(h_0)/h_0)^2 > 5$. However the vortex sheet was not observed by Griffiths who studied streak photographs and particle motions. It is probable that this feature is only identifiable in viscous currents under certain lighting conditions. Griffiths instead defined a head width that for $R(h_0)/h_0 > 1$ was (0.6 +/- 0.1) $R(h_Z)$. Hacker found the head width approximated to $0.2R(h_Z)$ increasing to $0.7R(h_Z)$ as the level of rotation was increased.

AUTHOR	LOCK PARAMETERS (cm)			h_0/H_0	g' (cm/s^2)	$w/R(h_0)$	$Re(h_0)$	COMMENTS
	w	x_0	H_0					
STERN WHITEHEAD & HUA (1982)	20	49	9.5-21.0	0.15-0.41	3.1-17.5	0.94-3.70 *	750-7500	Surface currents 2 sets of experiments barrier at 90° & 45°
GRIFFITHS & HOPFINGER (1983)	A 30	20	50	0.06-0.24	2.0-15.0	0.67-9.80 *	1000-12000	Surface currents 3 lock geometries - A, B and C
	B 10	50	50					
	C 10	15	50					
	A 30	20	10	0.80-0.87				
HACKER (1996)	P 42.5	10	20	1.00	3.2-24.0	0.0-7.9	10000-46800	3 sets of experiments P preliminary exp F floor currents S surface currents 2 lock geometries
	F, S 42.5	20.3	10-20.9					
PRESENT STUDY (1999)	15	25	5 - 22	0.08-1.00	2.4-49.3	0.0-11.3	160-71200	Surface currents 6 sets of experiments permanent barrier: (preliminary exps.) (1) $0.1 \leq h_0/H_0 \leq 0.2$ (2) $0.25 \leq h_0/H_0 \leq 1$ no permanent barrier: (3) $0.25 \leq h_0/H_0 \leq 0.85$ (4) $h_0/H_0 \sim 0.1$ (5) $h_0/H_0 = 1$ (6) particle tracking
	N.b. For set 4 (shallow currents), the ratio of the width of the large reservoir to the lock width = $\frac{1}{2}$.							

* not stated by author, calculated from values of f, g' and h_0 given.

Table 6.7 Comparison of the parameters of previous studies with the present laboratory investigation.

Stern defined a non-dimensional front speed, $c = U/(g'H_Z)^2$, where U is the propagation speed of the nose. No relationship was found between the degree of rotation and the front speed. However the speed was found to increase with Reynolds number, tending to c =1.56. Griffiths found that for small fractional depths ($0.05 \leq T_Z/H_Z \leq 0.1$) c = (1.3 +/- 0.2), where T_Z is the upstream depth of the tail. Again no dependence on rotation rate was identified. Hacker however, found that the variation of front speed ($c(h_0)$) for surface currents with rotation rate, $W/R(h_0)$, could be approximated to a $tanh(W/R(h_0))$ profile, where w is the tank width. He showed that there was a smooth transition from the non-rotating regime through to strong rotation. His experiments concerned full depth locks only.

Griffiths was eager to quantify the decay of front speed and the stagnation of currents observed by Stern. Griffiths established that the timescale for the decay in the front speed was dependent upon the rotation rate and a global Froude number $(Fr = fA_0^{\frac{1}{2}}/(g'h_0)^{\frac{1}{2}})$, where A_0 is the horizontal area of the lock. For flows where the Ekman number was small the decay time was decreased by Ekman friction. For $E_0 > 10$, the decay was attributed to the dissipation of momentum by inertial waves and Taylor columns (for $h_0/H > 0.5$). Hacker agreed that this could be a contributing factor in the decay of the front speed. His results were inconclusive with respect to the decay timescale, however they did indicate some dependence on the buoyancy frequency and rotation rate.

Griffiths obtained time exposure photographs using neutrally buoyant particles, which showed wave and vortex motions in the lower layer and ahead of the current. In some instances Griffiths reported seeing an interfacial Kelvin wave propagating anticlockwise around the lock and along the current. This was proposed to be equivalent to the interfacial gravity wave, that results from the reflection of the return flow from the back of the channel in the non-rotating experiments. Rottman & Simpson (1983), proposed that this wave causes a reduction in the nose velocity on reaching the leading edge of the bore. Griffiths suggested that the Kelvin wave observed in the rotating experiments could be a further factor in the decay of the front speed. Hacker argues that if this were true then the front speed of the current would be controlled at the head as in the non-rotating case. Instead Hacker proposes that in the rotating case the point of control moves to the source region and that the formation of the geostrophic eddy in this region is responsible for effectively trapping and restricting the supply to the current. Griffiths did consider the effect of the eddy in the source region, but he found no correlation with the decay in the front speed.

The main aim of the experimental investigation was to cover the full range of fractional depths from shallow to full depth currents for the range of rotation rates covered by Hacker ($0 \leq W \leq 3$). This will therefore provide a complete comparison with the theoretical results (chapters 4 and 5) and is discussed in § 7.3.

6.3 Experimental procedure

The first question to address is, what is the most appropriate method for generating rotating gravity currents in the laboratory? There are two main techniques, continuous flux of fluid and the lock-release. The continuous flux approach consists of introducing a buoyant fluid from a point source on to the surface of saline water in a rotating tank. This has been previously used by Stern (1980), Griffiths & Linden (1981, 1982) and Chabert d'Hières, Didelle & Obaton (1991). In this case the initial conditions are not ideal, since the inflow has zero potential vorticity and angular momentum. The small source may be allied with low Reynolds number, resulting in a laminar current. The main assumption of the theoretical study is that the fluid is inviscid, therefore it is important to ensure that the Reynolds numbers for the experiments are much greater than 1000. Therefore, the continuous flux method was not adopted for this investigation.

The lock-release method involves releasing a finite volume of fluid from a reservoir in to another fluid of different density, where both are in solid body rotation. This method was introduced in the 1930's by O'Brian & Cherno and has been used extensively in the investigation of non-rotating gravity currents, (Simpson, 1982). It is simple to perform, the source conditions are quantifiable and initially, in the rotating case, the fluid has uniform potential vorticity. An important consideration is whether this method adequately models gravity currents in the environment. To justify the simple laboratory experiment I cite an example previously discussed, Spencer Gulf, where there is a sudden cessation in tidal forcing and development of a gravity current on a timescale of only one hour. Nunes (1987), surveyed this current and commented that the abrupt release from the dissipative regime was analogous to the lock release method. Hence, the lock-release is the chosen method for this laboratory investigation.

6.3.1 Apparatus

The apparatus consisted of a 1m diameter rotating table, levelled manually to an error of 1mm/m = 0.057°. On this was mounted a perspex tank, 15 cm wide, 100cm length and 25cm depth. The tank was lit from above using four neon lamps which were attached to a metal frame suspended above the tank. The frame was painted black to prevent specular reflections. The tank was divided in to two reservoirs in the ratio 3:1 by a removable perspex barrier (width 0.5cm). The barrier was held in place using foam guides attached to the sides of the tank. These guides were positioned above the water surface and therefore did not interfere with the flow or obscure the current. To the edges of the barrier were attached strips of rubber which when smeared with a small amount of silicon gel provided excellent seals. The use of silicon gel was kept to a minimum because it was found to contaminate the water surface.

The tank was supported by lab jacks. A mirror was positioned at approximately 45° to the r.h. side of the tank. This provided a side view of the current. The mirror extended beneath the tank to illuminate the base, by reflecting light from the lamps above. The lab jacks enabled the height above the table to be altered, to ensure the free surface was normal to the plane of the mirror. The angle of the mirror could be adjusted for the same reason. A camera was attached to the table top and viewed the tank through a second mirror which was positioned above the tank at an angle of approximately 5° to the horizontal. This increased the path length of the light and therefore reduced the parallax problem. Hence both plan and side views were observed simultaneously (fig. 6.1 a & b). To ensure the light was evenly distributed, the underside of the tank was covered in light diffusing paper and white card was attached to the l.h. side of the tank. Black card was positioned at either end of the tank, to prevent water dripping from the barrier disturbing the water surface as the barrier was removed.

6.3.2 Method

For the preliminary experiments (sets 1 & 2) three density differences ($\Delta\rho/\rho_2$) were used - 0.25%, 2.5% and 4.5%. For the main experiments (sets 3 to 6) a density difference of 2%

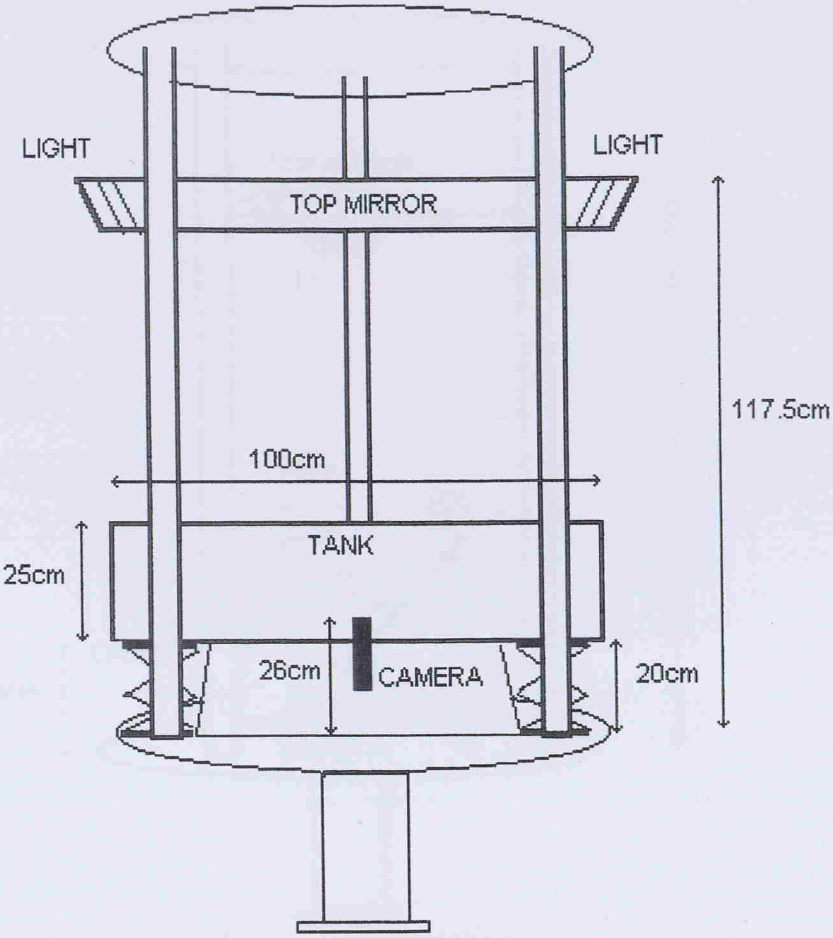

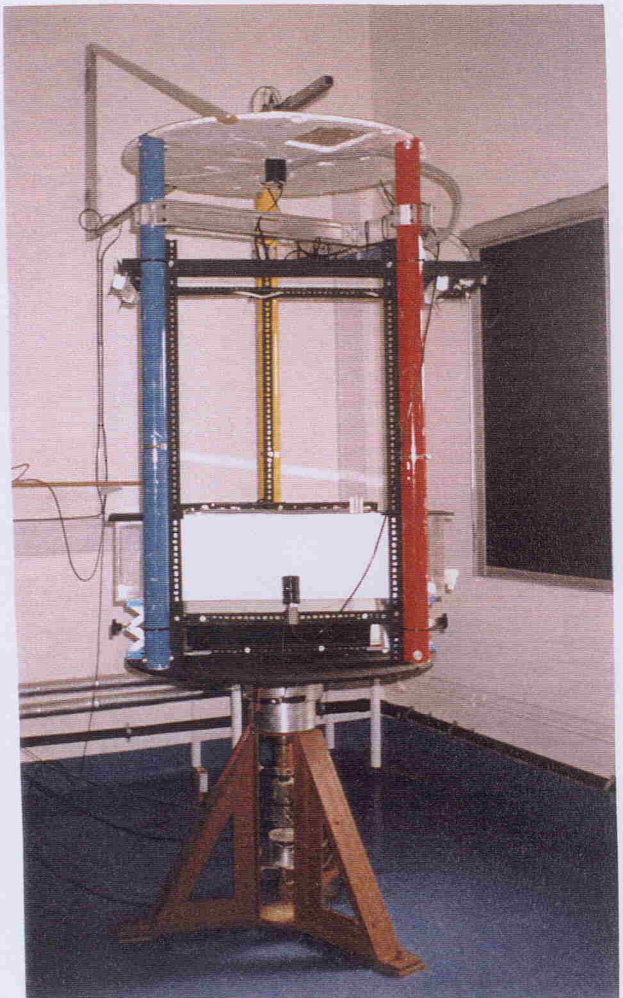

FIGURE 6.1

Apparatus (a) front view

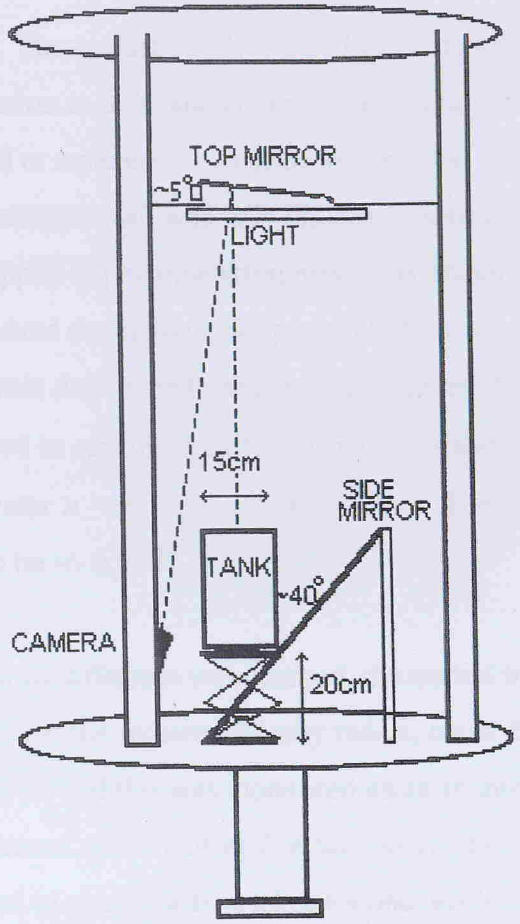

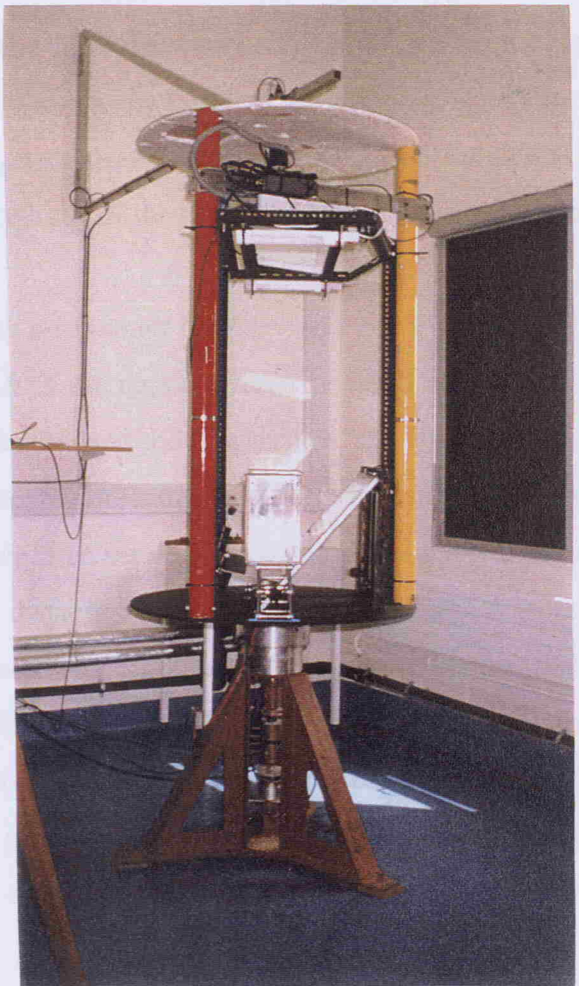

FIGURE 6.1

Apparatus (b) side view

was required. The amount of salt required was determined using standard tables for sodium chloride solution at 20°C and either mixed in situ with fresh filtered tap water in the tank (sets 1,2 & 6) or separately in a bucket and then the saline solution was filtered as it entered the tank, ensuring the salt was fully dissolved (sets 3 to 5). To ensure a clean free surface, a frame wrapped in phytoplankton mesh was drawn vertically through the water and the tank was covered during the spin up period. Prior to rotating the table, the densities of the two fluids were determined using a refractometer. The refractive index, n, was measured and converted to specific density, ρ using the standard tables for sodium chloride, where for fresh water $n = 1.3330$ and $\rho = 1.0000$. The accuracy of the specific density was estimated to be +/- 0.0007.

Once the density difference was obtained, the inertial frequency and hence the rotation rate of the table, for the required Rossby radius, could then be calculated. The rotation rate could be pre-set and this was monitored using an interval timer. Prior to and immediately after the removal of the barrier five successive interval times were recorded. These were then averaged to obtain the time taken for one revolution in seconds (s), therefore enabling the inertial frequency, f, to be calculated where $f = 4\pi/s$. The standard deviation in f was generally within 0.5%. However some problems were experienced with the timer in set 5. The actual values for the standard deviation are stated in tables 7.1 to 7.9. The depth of the water, H_0, was measured using an anodised aluminium ruler which could placed in the tank. The accuracy of the depth measurements were estimated to be within 2mm.

6.3.2.1 With permanent barrier - sets 1 & 2

For sets 1 & 2 the depth of fluid released was varied by altering the gap between a permanent barrier and the free surface, see fig. 6.2. The tank was filled with filtered tap water to the required depth. The removable barrier was inserted, leaving a gap of approximately 2mm between the base of the tank and the permanent barrier. This reduced the pressure disparity between the two reservoirs. A measured quantity of salt was added to the main reservoir and mixed thoroughly. When the salt had dissolved, the density of the fluids in the two reservoirs were measured. The barrier was fully inserted and dye (concentration 1*ml*/*l*) was added to the fresh water in the small reservoir. Calibration panels for side and plan views were recorded. The table was rotated until the water was in solid

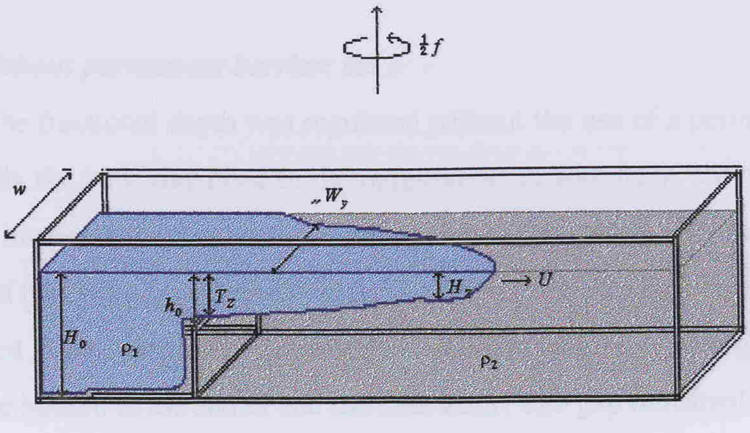

FIGURE 6.2 Tank set up for sets 1 & 2 (preliminary experiments). The fractional depth is controlled by varying the depth of water above the permanent barrier.

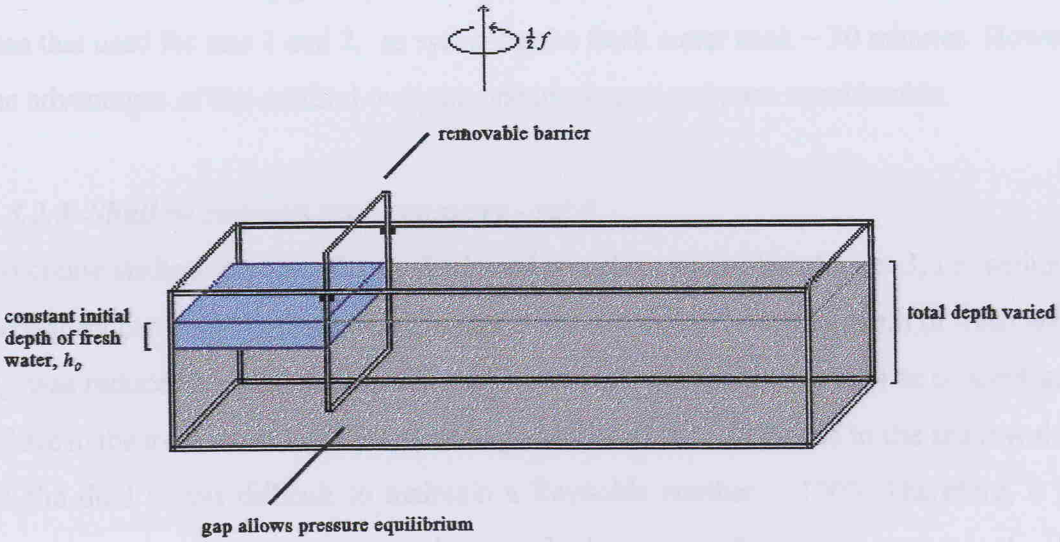

FIGURE 6.3 Tank set up for set 3. The fractional depth is controlled without the use of a permanent barrier. The particle experiments (set 6) were performed using this set up, but the tank was covered internally with a black vinyl and white strips were attached to the top edge of the tank to act as reference points.

body rotation, approximately 1 hour. The room was blacked out, the tank illuminated and a background image was recorded. Finally the barrier was removed and a gravity current generated.

6.3.2.2 Without permanent barrier: set 3

For set 3, the fractional depth was regulated without the use of a permanent barrier, (fig. 6.3). Initially the tank was filled to the required depth with fresh water. Background and calibration images were recorded. Obtaining these at this stage prevented the subsequent distortion of the background divided image by the barrier. The tank was emptied and filled with filtered saline water. The removable barrier was inserted. A large opening was left between the bottom of the barrier and the tank floor. The gap remained for the duration of the experiment, preventing the formation of a pressure head. When the saline water had spun up, after approximately 1 hour, fresh, dyed water (dye concentration *0.5 ml/l*) was carefully syringed on to the surface of the saline water in the small reservoir. For all the experiments, irrespective of the required fractional depth, the initial depth of fresh water, $h_0 \sim 4cm$. Therefore the fractional depth was altered by varying the full depth H_0. The fresh water was allowed to reach solid body rotation, approximately 15 minutes. The barrier was removed and the ensuing gravity current videoed. This method was more time consuming than that used for sets 1 and 2, as syringing the fresh water took ~ 30 minutes. However the advantages of this method over the one used previously are considerable.

6.3.2.3 Shallow currents tank geometry - set 4

To create shallow currents the method used was the same as that for set 3, i.e. without a permanent barrier and a density difference of 2%. However the initial depth of fresh water, h_0, was reduced to 2cm, because of the geometric constraints of tank. The concentration of dye in the fresh water was correspondingly increased to *1ml/l.* Due to the shallow depth of the fluid it was difficult to maintain a Reynolds number > 1000. Therefore, it was necessary to increase the relative volume of fluid in the small reservoir to that in the large reservoir, so that the current had a sufficient volume of fluid to draw upon. This was achieved by inserting a permanent L-shaped barrier, which halved the width of the large reservoir, see fig 6.4. The barrier was made of perspex and held in place using rubber pressure seals and a small amount of silicon gel. A removable barrier, half the width of the

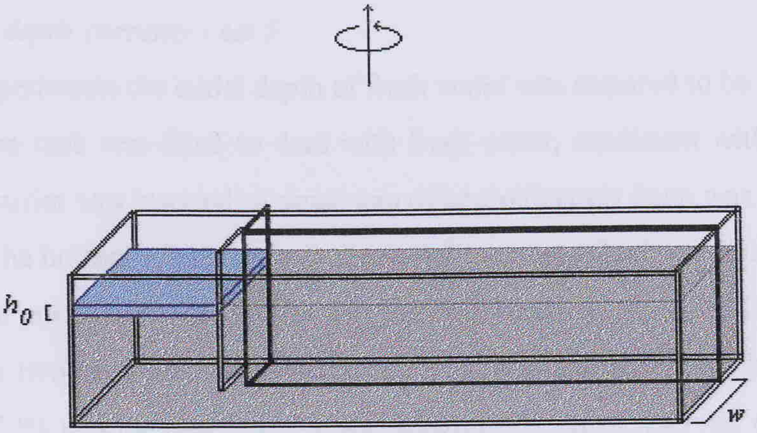

FIGURE 6.4 Tank set up for set 4 (shallow currents). The L shaped barrier is used to increase the relative volume of the fluid in the small reservoir to that in the large reservoir, in order to maintain an adequate volume of fluid within the lock for the shallow current to draw upon as it progresses along the channel.

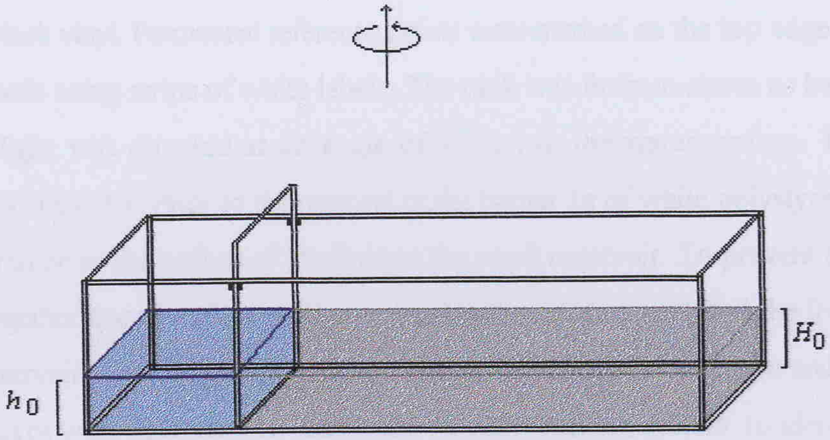

FIGURE 6.5 Tank set up for set 5 (full depth). A small gap is left between the bottom of the tank and the removable barrier whilst the salt is being mixed. The barrier is then fully inserted and the density of the two fluids is measured just prior to running the experiment.

channel, separated the two reservoirs. The method proceeded as in § 6.3.3.

6.3.2.4 Full depth currents - set 5

For these experiments the initial depth of fresh water was required to be the full depth of the tank. The tank was filled to 4cm with fresh water, consistent with set 3, and the removable barrier was inserted. A small gap of approximately 5mm was left between the barrier and the bottom of the tank. A measured quantity of salt was added to the large reservoir and mixed well. The barrier was then fully inserted (fig.6.5). The density of the fluids in the two reservoirs was measured and g' was calculated. As before, a density difference of 2% was the aim. The dye was added to the small reservoir (0.5*ml/l*) and the fluid was spun up for approximately 1 hour. The barrier was removed and the resulting gravity current videoed.

6.3.2.5 Particle tracking - set 6

The aim here was to measure the velocity gradient across the current at the free surface using particle tracking. The method used was the same as for set 3, with $h_0 = 4$cm, density difference of 2% and a dye concentration of 0.5 *ml/l*. For all of these experiments $h_0/H_0 = 0.25$ and the only parameter varied was the rotation rate W. The walls of the tank were covered in black vinyl. Permanent reference points were marked on the top edge of the tank at 5cm intervals using strips of white labels. The tank was lit from above as before and an additional light was directed at an angle of 45° on to the water surface. The method proceeded as in § 6.3.3. Prior to the removal of the barrier 1g of white polystyrene particles were scattered on to the surface of the fluid in the small reservoir. To prevent the particles clumping together due to surface tension, a weak soap solution replaced the fresh water in the small reservoir. The particles were also washed before use in detergent and then dried. These measures were necessary to enable the particle tracking system to identify discrete particle paths.

6.3.2.6 Image processing

Prior to each experiment a background image was recorded. For the preliminary experiments the background was recorded whilst the table was at rest. In the following experiments the table was rotated for a time interval equivalent to the rotation period and then averaged. This improved the quality of the background removal. Calibration panels were videoed for side and plan views. In sets 1 and 2 the calibration panel for the plan view was placed on the floor of the tank. This was found to give inaccurate width measurements due to the changing parallax as the depth of the fluid was altered. In subsequent experiments the calibration panel was floated on the surface of the water to overcome the parallax problems. Width measurements are therefore not presented for the preliminary experiments. For the side view the calibration panel was placed at the right hand wall. The experiment was then recorded. The video tapes were analysed using the image processing system Digimage developed by Dalziel (1993, 1994). The image processing may be divided into two stages, firstly acquiring and secondly analysing the images. The first stage is applicable to all of the experiments.

Firstly a time pulse was recorded on to the video tape on an audio track. Then a sequence of images were grabbed to buffers on the c: drive of a pc using a frame grabber card. In sets 3, 4 and 5 the images were grabbed 2s after the release of the fluid, at intervals of 0.16s to 0.32s, to avoid the accelerating phase identified in the preliminary experiments. In set 6 the aim was to quantify the velocity gradient across the current far downstream of the head, therefore buffers were grabbed when the head had travelled $\frac{2}{3}$ the length of the channel, at intervals of 0.08s onto 31 buffers. The calibration images were used to assign world co-ordinates to the images. For sets 1 to 5 this enabled measurements to be taken of the width, depth and the distance progressed by the nose of the current along the channel to a resolution of (0.12+/-0.02) in the vertical and (0.08+/-0.02) in the horizontal. For the particle tracking experiments permanent reference points were also specified. Each image was digitised in an array of 512 x 512 pixels. The images were filtered. This was necessary because each frame grabbed to the computer is made up of two video fields recorded at slightly different times. This can cause the image to shimmer, so one of the fields was removed using an intralace filter. The particle tracking images in set 6 were not filtered because filtering has the draw back of reducing the vertical resolution from 512 to 256 lines, since the area of a particle approximated the size of a pixel a reduction in resolution was unacceptable.

In the second stage the digitised images were analysed. Each pixel contains the value of light intensity recorded at that point, in the range 0 to 255, where 0 is black (saturation level) and 255 is white. In sets 1 to 5 the image of the gravity current marked by dye was divided by the background image. It is assumed that the amount of light passing vertically through the fluid is related to some function of the dye concentration and the depth of the fluid. If there is no mixing, the variation in the intensity values can give an indication of the depth or width of the fluid in the plan view or side views respectively. A false colour palette was applied to the image to enable the cross stream depth and physical features of the current to be revealed. Unfortunately, problems were encountered with the camera where saturation (intensity of light = 0) occurred at moderate light intensities. This happened in set 2 where the dye in the deep currents attenuated the light passing through the fluid. To over come this problem a number of experiments were performed to ascertain the optimum concentration of dye. This was found to be 0.5ml/l. Hence in the plan views in sets 3 to 5 the intensity of light passing through the fluid was maintained above the saturation level. However because of the difference in vertical and horizontal scales, saturation could not be prevented in some of the side views.

In the particle experiments white particles were observed against a black background. A threshold intensity range was pre-set to enable areas of the image which matched this to be identified and marked. Further analysis then took place to determine whether these matched the criteria which specified the characteristics of a particle, such as, volume, shape (ellipticity limit) and its intensity distribution. The accuracy to which the position of a particle is known is dependent upon the size of a particle. To increase the apparent particle size the camera was defocused. For particles whose dimensions where greater than that of a pixel the positional accuracy according to Dalziel is greater than one pixel. To trace the particles from one image to the next Digimage uses modification of a Transportation algorithm. The spatial resolution is dependent on the number of particles, the greater the number the higher the resolution. However each particle must be clearly identified within the constraints of the tank. The optimum number for these experiments was found to be 150. The velocity of each particle was calculated by knowing its location over a series of times. Track2DVel a subroutine within Digimage configures the data and plots the velocity information as a series of arrows based on a least squares approach. The error for a single velocity vector is +/- 5 to10%.

CHAPTER 7

Laboratory Results

The objective of sets 1 & 2 was to consider as large a parameter range as possible. The fractional depth in the first two sets of experiments was controlled using a permanent barrier. Set 1, that is, fractional depths $0.1 \leq h_0/H_0 \leq 0.2$, and rotation rates, $0 \leq w/R(h_0) \leq 2$, provide an interesting insight into the transition between viscous and inviscid flows. Set 2 investigates deeper currents including the full depth case, where $0.25 \leq h_0/H_0 \leq 1$ at rotation rates $0 \leq w/R(h_0) \leq 2$. The qualitative and quantitative results are discussed in § 7.1. The permanent barrier although useful for controlling the depth of the inflow did appear to disturb the flow and cause enhanced mixing. This problem, together with the aim of extending the experimental and theoretical work of Hacker, were the impetus for set 3. Here the fractional depth was controlled without the use of a permanent barrier. In set 3 the Reynolds number, $Re(h_0)$, was maintained at greater than 3000 to remove unwanted viscous effects. The concentration of dye used to mark the current was reviewed to prevent saturation occurring, in order that confident comparisons of vertical mixing between currents of differing rotation rates could be obtained. The range of $w/R(H_0)$ considered was increased to 7 levels in the range $0 \leq w/R(h_0) \leq 3$, for fractional depths $0.25 \leq h_0/H_0 \leq 0.85$. A qualitative description of the flows together with the results for set 3 are presented in § 7.2. To complete the parameter range, shallow and full depth currents are examined in § 7.2.2 and § 7.2.3 respectively. Reflected flows are considered in § 7.2.4. In § 7.2.5 the results of the particle tracking experiments are discussed, which provide a qualitative insight into the flow within the current. A comparison between the experiments (sets 3, 4 and 5) with the theories presented in chapters 4 and 5, is provided in § 7.3.

A consistent layout of the images is used throughout. The upper portion of each image is the plan view, whilst the lower portion is the side view with the free surface at the bottom. The images of set 2 are in monochrome because of the saturation problems. If a palette were applied it would give a false impression of the across stream variation in depth. The results of set 3, 4 and 5 are illustrated by both simple and contour graphs. The 2-D graphs are included to give the reader an idea of the general trends displayed by the data and to aid the interpretation of the contour graphs.

7.1 With a permanent barrier

7.1.1 Qualitative features: sets 1 & 2

On examining sequences of images mapping the development of certain flows in set 1, it was observed that initially the leading edge of the current had the characteristic "lobe and cleft" structure identified for non-rotating currents by Simpson (1982). On progressing some distance along the tank a sudden change in the shape of the front was noticed. The lobe structure disappeared and a smooth profile was seen. The head also decreased in size. This was seen for non-rotating and rotating currents in the range $0 \leq w/R(h_0) \leq 2$, it is discussed further in section 7.1.2 and illustrated in plate 5.

Another interesting phenomenon was the development of undular bores. These are visible indications that the flow is supercritical and hence that the Froude number exceeds unity. This occurs when the depth of the current is less than the critical depth of the channel, that is, when the specific energy of the flow is at its minimum. The critical flow occurs somewhere before the first wave crest. Plate 3 shows a sequence of images of a non-rotating experiment (Exp. 6), where undulations occurred on the interface between the fresh and saline water. The undulations have a small amplitude and a long wavelength. The bore is seen as a series of bars across the current in plan view. The associated increase in depth was seen in the side view. Generally the bore was stationary.

Set 2 concentrated on the range $0.25 \leq h_0/H_0 \leq 1$. No undulations were observed, indicating that the flows were all subcritical, that is, had a Froude number less than 1. I shall describe the features of these gravity currents as the rotation rate is increased. Plate 4, shows a sequence of images for each level of rotation ($0 \leq w/R(h_0) \leq 2$) as the current progresses along the tank. Nb that this is a mirror image and the current is deflected to the r.h. wall. The non-rotating gravity current (plate 4a) exhibits all the features described in section 1.2.

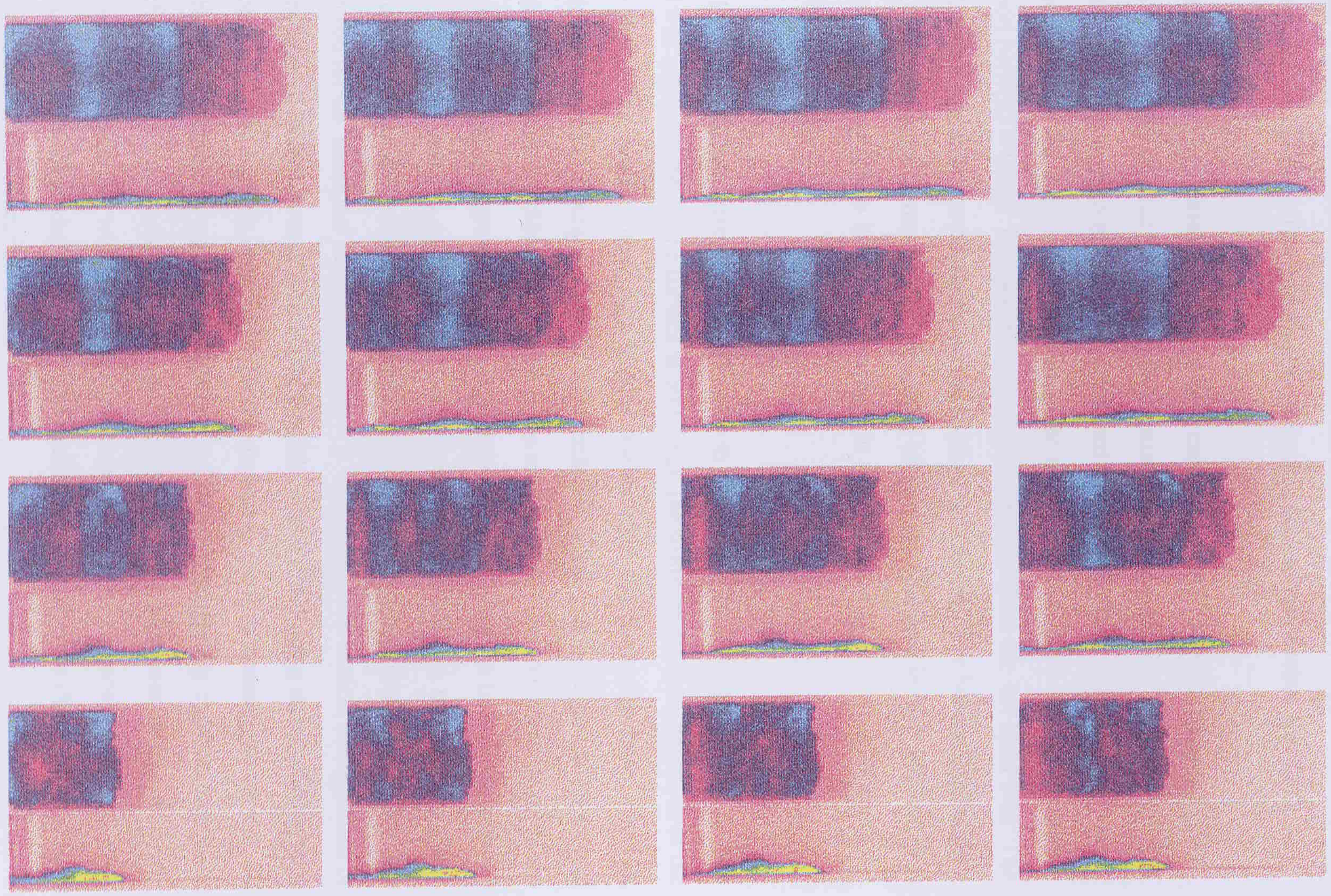

PLATE 3. Undular bore - $h_0/H_0 = 0.14$, $w/R(h_0) = 0$ and $Re(h_0) = 1118$

At the front of the current is a bulbous head, behind which Kelvin-Helmholtz billows are just discernable. The following flow is shallower than the head and is approximately half the depth of the opening. The leading edge is broken by a series of lobes and clefts.

The second sequence (plate 4b) is of a gravity current exposed to weak rotation, ($w/R(h_0)$ = 0.11). The head and tail are now approximately the same depth. In the plan view the leading edge of the current is further advanced at the right hand wall, but the current continues to fill the full width of the tank. The third sequence (plate 4c) is at moderate rotation ($w/R(h_0)$ = 0.95). The gravity current has detached from the left hand wall. The width of the current is approximately half the width of the channel. The head is smaller than that of a non-rotating current. Kelvin-Helmholtz billows are observed in both side and plan views. There appears to be a slight increase in mixing with the ambient fluid along the length of the current.

The strongly rotating current ($w/R(h_0)$ = 1.95) in plate 4d, is deflected away from the left hand wall and outcrops on the surface at about half the width of the tank, as shown in the plan view. The head is now significantly smaller than the following flow. There is considerable vertical mixing during the initial collapse. What may be described as a cloud of mixed fluid forms and fills the full depth of the tank. In plan view the mixed fluid has the appearance of a rotating gravity current and slowly advances along the tank. Following the initial collapse, there is an abrupt flow of denser fluid through the mixed fluid, which overtakes the front and the current progresses at a faster speed. This unusual behaviour was observed for all fractional depths at $w/R(h_0) \sim 2$. The increase in vertical mixing could be a consequence of the increase in rotation. Griffiths et al, (1983) using streak photography of rotating gravity currents identified cyclonic vortices in the flow beneath the current. He attributed the increase in vertical mixing observed for rotating gravity currents, compared to the equivalent non-rotating currents, to these vortices. However in this study the interaction of the current with the permanent barrier as it adjusts to geostrophic flow could also contribute to the mixing observed in the preliminary experiments (Sets 1 & 2). This is investigated further in section 7.2.

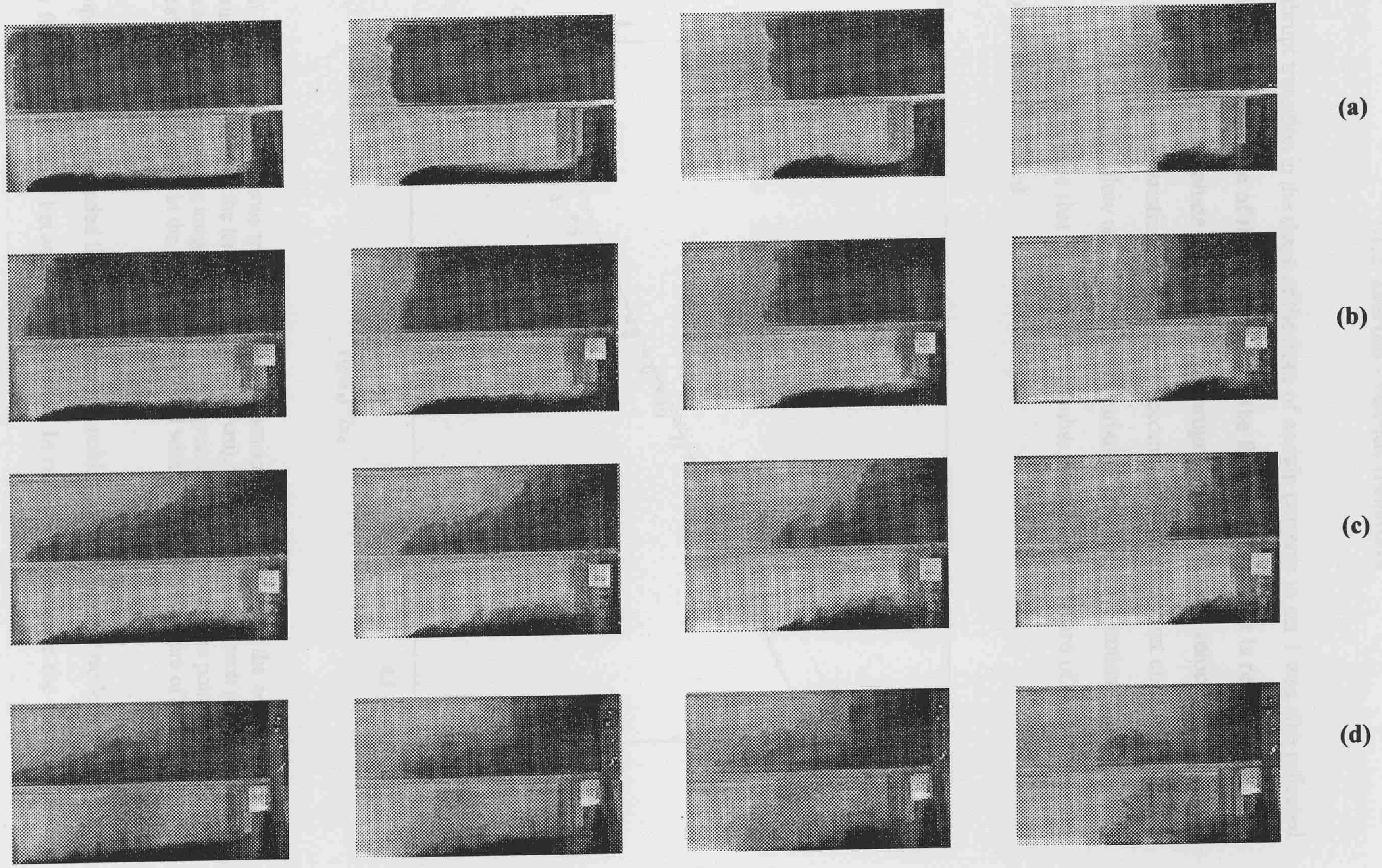

PLATE 4. Set 2 $h_0/H_0 \sim 0.33$, $Re(h_0) > 1000$ - (a) $w/R(h_0) = 0$, (b) $w/R(h_0) = 0.11$, (c) $w/R(h_0) = 0.95$, (d) $w/R(h_0) = 1.95$.

7.1.2 Inertial - viscous transition

The abrupt transition in the shape of the front of certain currents in set 1 was also reflected in the propagation rate of the nose. Initially the fluid collapses as it is released from the lock. Next there is a phase where the nose progresses at constant velocity. The sudden change in the characteristics of the flow is accompanied by an abrupt change to a lower constant velocity. The flow no longer appears turbulent and instead a laminar flow develops (fig. 7.1). This suggests that the Reynolds number, which is a measure of the influence of viscosity, has decreased.

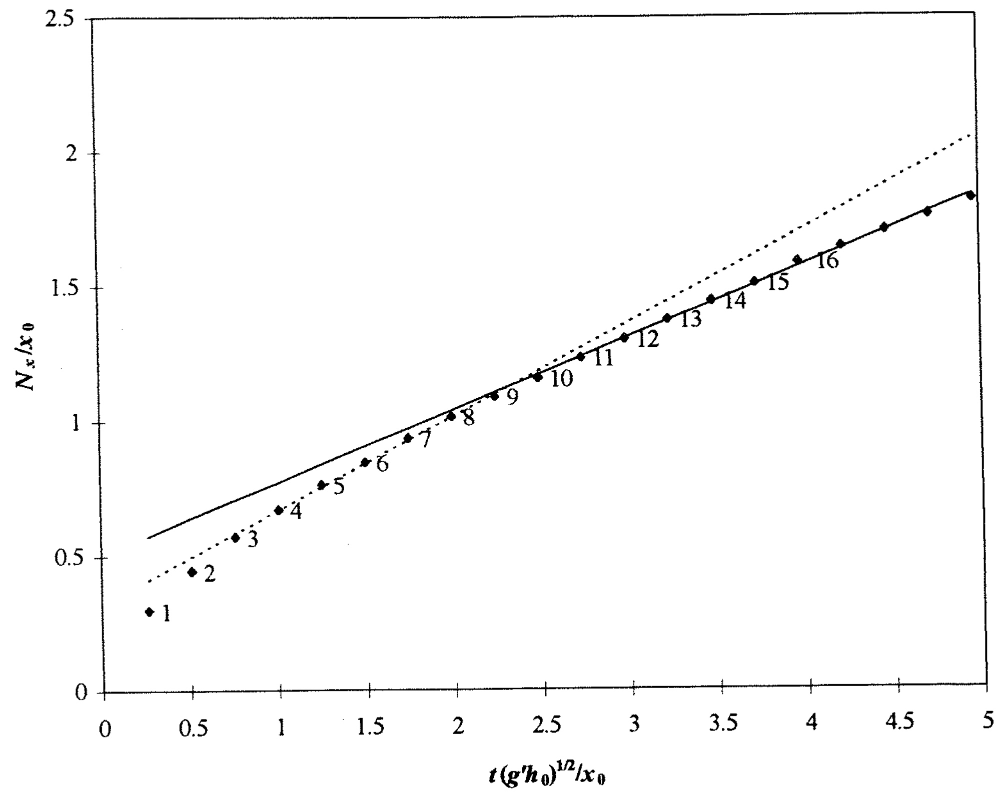

FIGURE 7.1 Inertia-viscous transition - Non-dimensionalised position of the nose of the current versus time, where x_0 is the length of the lock (25cm). The number above each point on the graph indicates the corresponding image in plate 5. The regression lines through data points 1- 8 and 9 -16 reveal the abrupt change in the velocity, associated with the evolving structure of the current.

Simpson (1979), concluded that the critical Reynolds number, where it no longer influenced the flow was situated between 500 to 1000. In order to investigate the influence of the

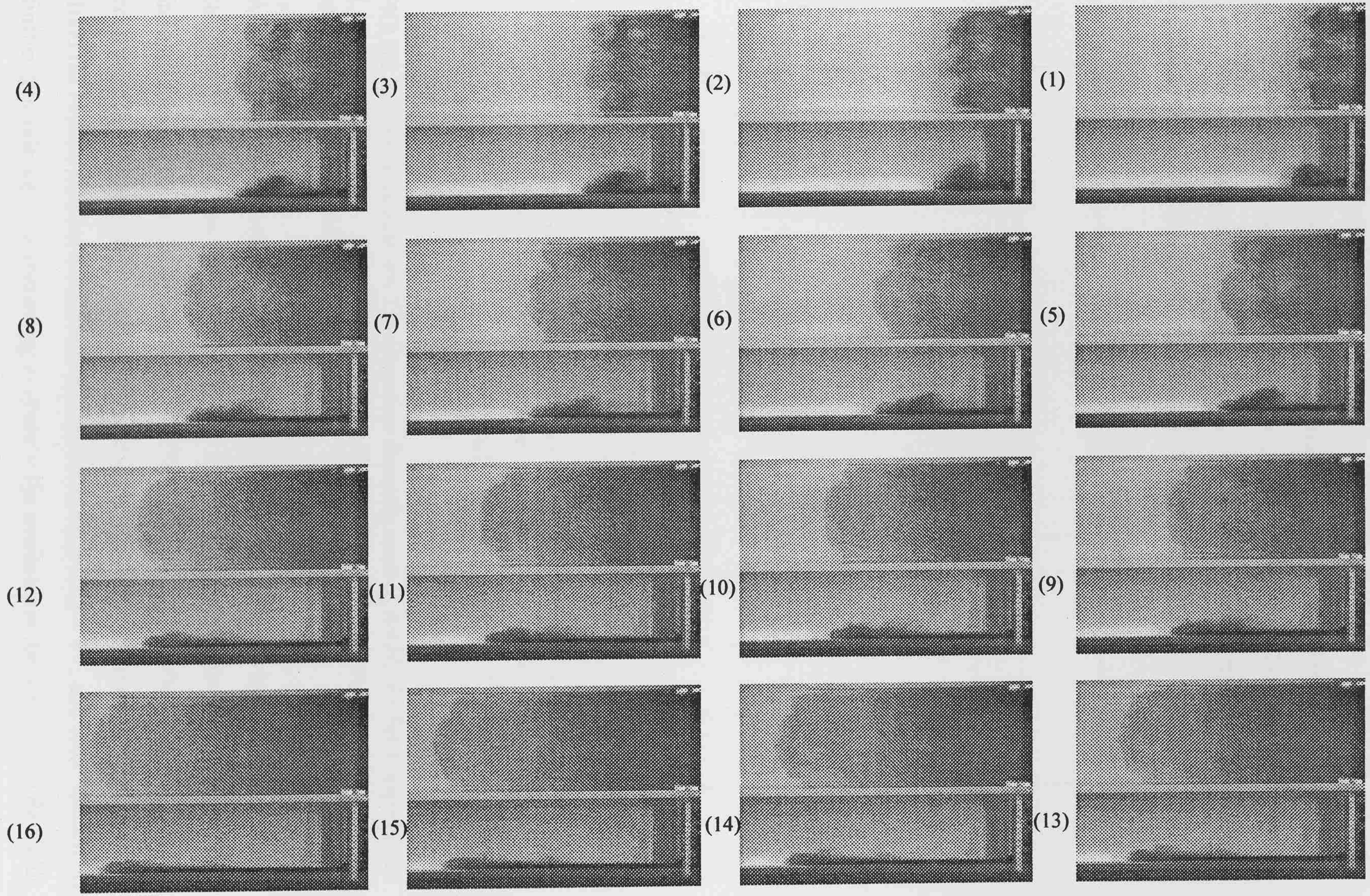

(4) (3) (2) (1)

(8) (7) (6) (5)

(12) (11) (10) (9)

(16) (15) (14) (13)

PLATE 5. Transition to viscous flow - $h_0/H_0 = 0.14$, $w/R(h_0) = 0$ and $Re(h_0) = 349$

Reynolds number on the front speed, the local Reynolds number at the head of the current, $Re(H_z)$, was plotted against the Froude number, based on upstream tail depth, $Fr(T)$,$_z$ (fig.7.2). The local Reynolds number and Froude number were used instead of one based on H_0, because they were more sensitive to the dynamics of the flow and to maintain consistency with previous experimental studies (Griffiths et al, 1983).

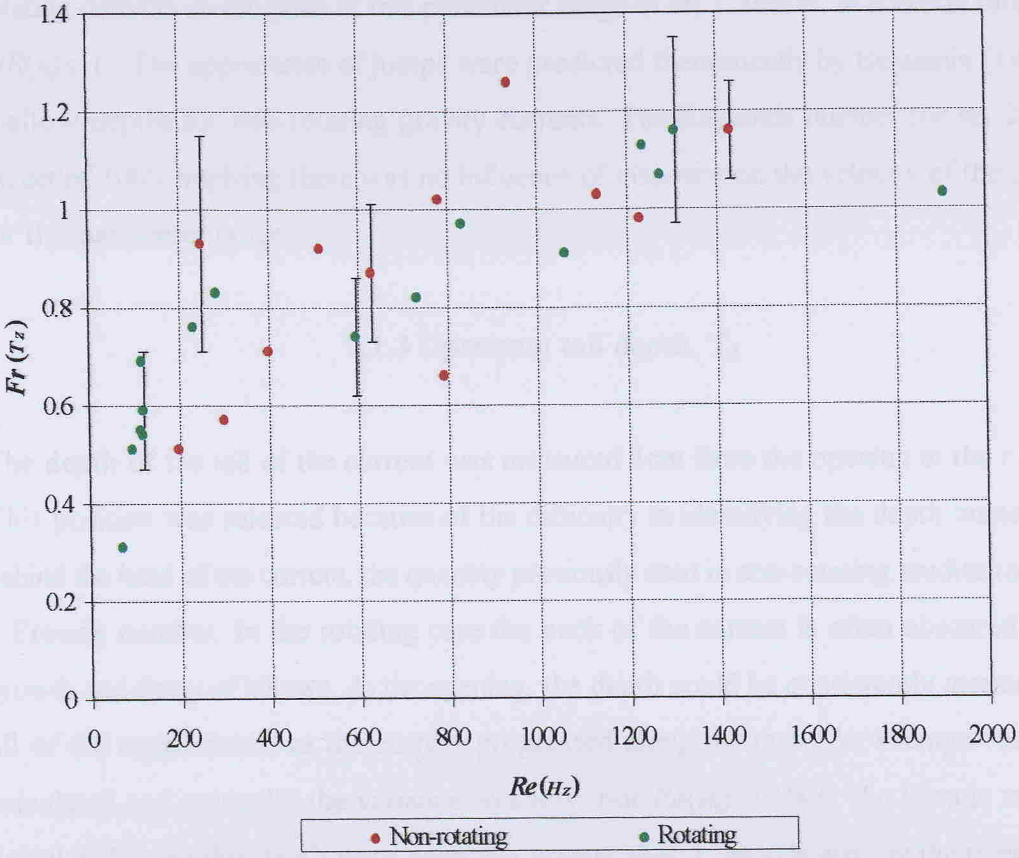

FIGURE 7.2 Froude number, $Fr(T_Z)$ versus local Reynolds number, $Re(H_Z)$ for Set 1 (experiments 1 to 28), where $h_0/H_0 \leq 0.2$ and $0 \leq w/R\ (h_0) \leq 10$. For Reynolds numbers below 1000 viscosity appears to affect the Froude number.

A correlation was found between shallow currents that showed viscous characteristics (laminar flow) and low Reynolds numbers. These viscous currents had $Re(H_z) \leq 500$, independent of the level of rotation. For $500 \leq Re(H_z) \leq 1000$, the Reynolds number continued to influence the Froude number, although the flow appeared turbulent. Above 1000 the Froude number levelled out at approximately $Fr(T_z) \sim 1.1$, and there seemed no further dependence. It is interesting to observe the similarity in the response to Reynolds number by the non-rotating and rotating gravity currents. Griffiths (1983) plotted a similar graph for shallow rotating gravity currents ($0.05 \leq h_0/H_0 \leq 0.1$). He also speculated that there was a dependence of front speed on $Re(H_z) \leq 1000$. The Froude numbers he observed were consistently higher than those in this study, for $Re(H_z) > 1000$, the $Fr(T_z) \sim (1.3$ +/- $0.2)$. This may be due to the smaller fractional depths he considered.

Undular bores occurred when $h_0/H_0 \leq 0.2$ at $Re(H_z) > 500$ for both rotating and non-rotating currents investigated at this parameter range in set 1, that is, at rotation rates, $0 \leq w/R(h_0) \leq 1$. The appearance of jumps were predicted theoretically by Benjamin (1968) at shallow depths for non-rotating gravity currents. The Reynolds number for set 2 flows exceeded 1000, implying there was no influence of viscosity on the velocity of the current for this parameter range.

7.1.3 Upstream tail depth, T_Z

The depth of the tail of the current was measured 1cm from the opening at the r.h.wall. This position was selected because of the difficulty in identifying the depth immediately behind the head of the current, the quantity previously used in non-rotating studies to define a Froude number. In the rotating case the neck of the current is often obscured by the growth and decay of billows. At the opening, the depth could be consistently measured for all of the experiments, as the current progressed along the tank. An average value was calculated and generally the variance was low. For $Re(H_z) > 1000$, the Froude numbers calculated using this depth were generally greater than 1, as indicated by the presence of the undular bores.

However the calculation of the Froude number using the front speed for supercritical flows is not fully appropriate, since the critical velocity occurs prior to the first crest. This could account for the experiments where bores were observed at $500 \leq Re(H_z) \leq 1000$, but the Froude numbers were less than 1. In set 2 all the currents are subcritical therefore the use of the front speed and upstream depth to calculate Froude number is acceptable.

The tail depth is non-dimensionalised by the height of the opening, T_z/h_0, and this is plotted against the fractional depth, h_0/H_0 (fig. 7.3). (The height of the opening, h_0 and the total depth of fluid ,H_0 were used to non-dimensionalise the parameters that characterised the flow because they were constant for each experiment and could be consistently measured.) The tail depth of deep non-rotating currents lies between $0.35 \leq T_z/h_0 \leq 0.6$. The influence of the approaching critical depth of the channel is again displayed, with all non-rotating gravity currents having a minimum between $0.2 \leq h_0/H_0 \leq 0.25$. This is followed by an increase in depth rising to above $T_z/h_0 = 0.6$ for very shallow currents.

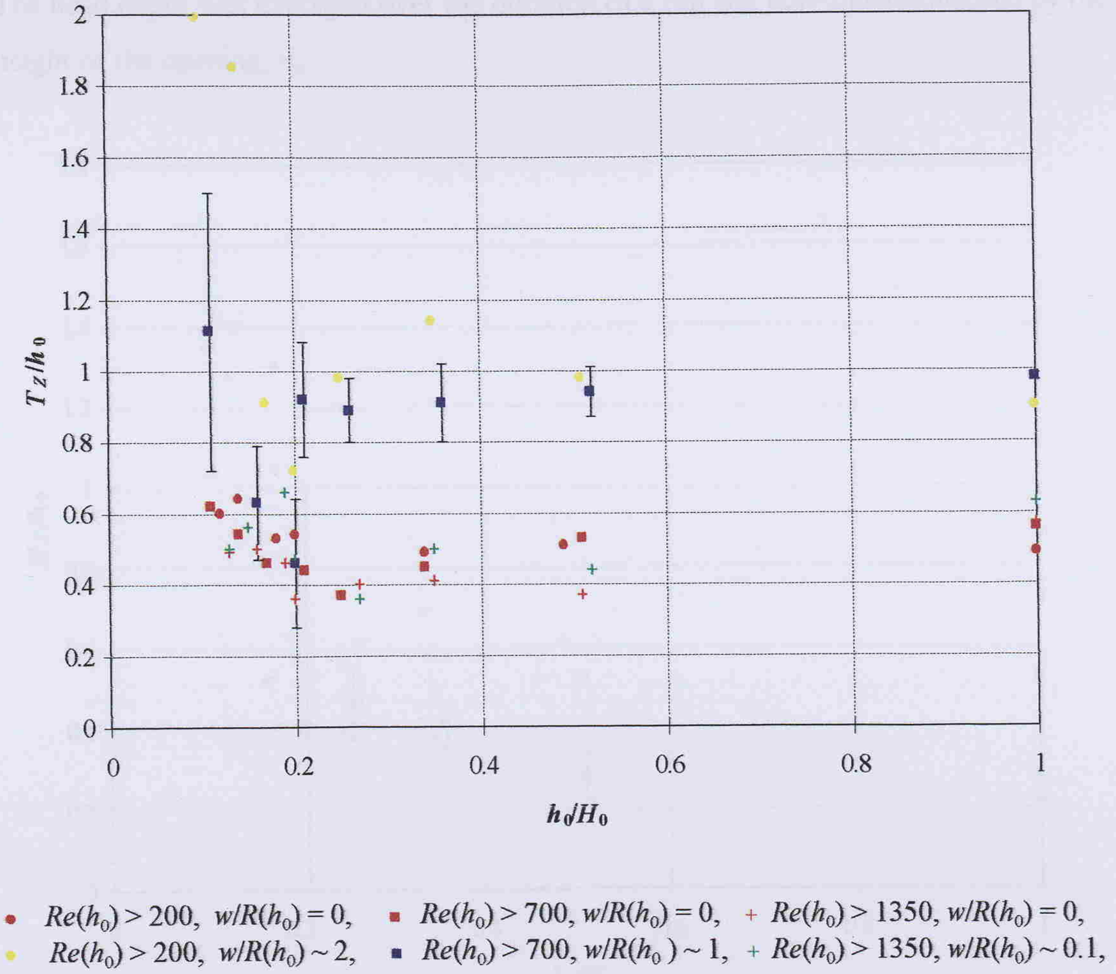

FIGURE 7.3 Sets 1 & 2 Tail depth (T_z/h_0) versus fractional depth (h_0/H_0). The tail depth was measured 1cm from the opening at the r.h. wall. The tail depth of non-rotating gravity currents is ≤ 0.65. Errors are largest for small values of h_0/H_0.

The tail depth deepens as rotation is increased, because of the fluid piling against the r.h. wall. Note the minimum at h_0/H_0 =0.25 this is thought to coincide with the critical depth of the channel and hence the transition from sub-critical to super-critical flow. For weak rotation rates ($w/R(h_0) \sim 0.1$) the depth has similar values to the non-rotating currents. As rotation is increased to $w/R(h_0) = 1$ the growth in depth is significant, almost doubling for deeper currents. Once again the minimum is observed at $h_0/H_0 \sim 0.2$. For stronger rotation, ($w/R(h_0) \sim 2$), the depth remains slightly higher than that measured at $w/R(h_0) \sim 1$. The minimum is seen at $h_0/H_0 \sim 0.2$ followed by a sharp increase in depth for very shallow currents.

7.1.4 Head depth, H_Z

The head depth was averaged over the duration of a run and non-dimensionalised by the height of the opening, h_0.

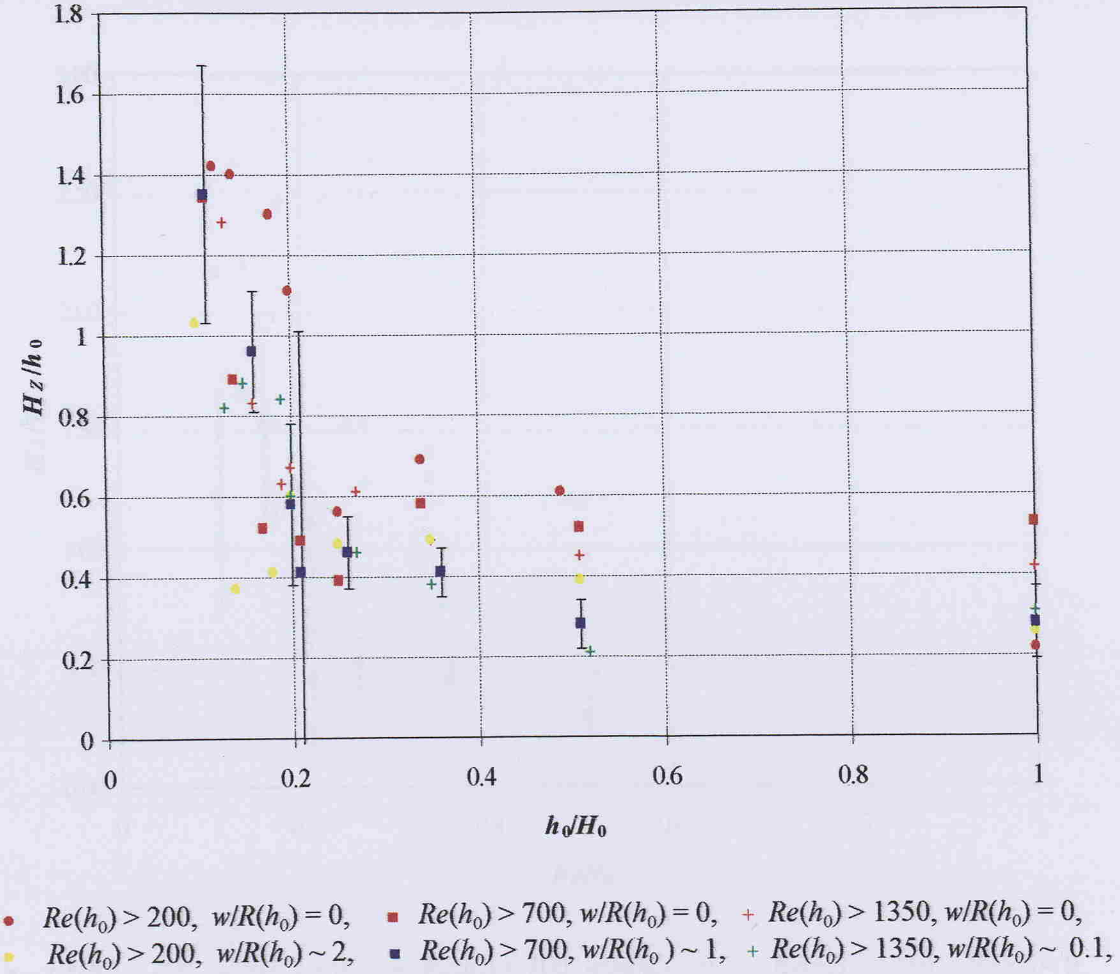

FIGURE 7.4 Sets 1 & 2 Head depth (H_z/h_0) versus fractional depth (h_0/H_0). The shallow currents show the greatest variability in H_z/h_0.

The head was found to vary significantly due to billows growing and peeling off periodically behind the nose. The plot of head depth versus fractional depth shows that overall the non-rotating gravity currents have deeper heads than the rotating currents (fig. 7.4). The influence of increasing rotation is not clear. This is probably due to the evolution of the head throughout an experiment. The use of the head depth by Stern in calculating the Froude number had been criticised previously by Griffiths, because of its variance. These results support that criticism.

7.1.5 Bore strength

The bore strength as defined by Simpson is the ratio of head to tail depth, H_z/T_z. It may be used to give an idea of the changing profile of the current as rotation increases, (fig. 7.5).

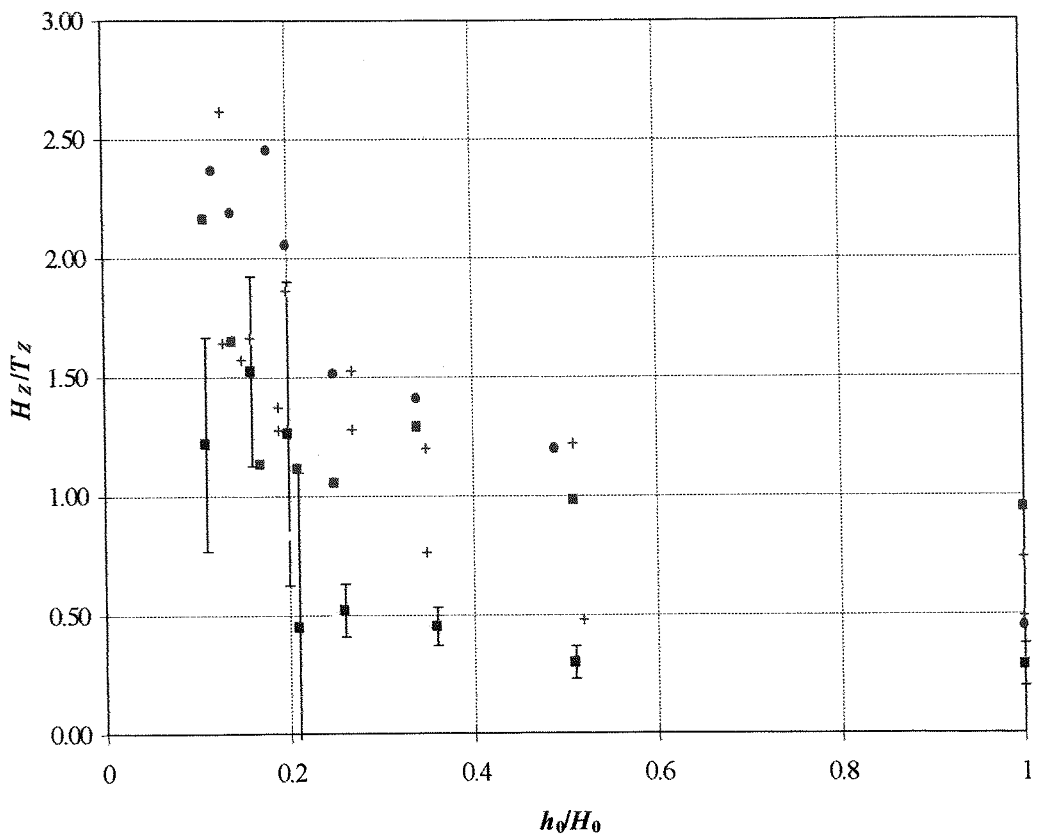

● $Re(h_0) > 200,\ w/R(h_0) = 0,$ ▪ $Re(h_0) > 700,\ w/R(h_0) = 0,$ + $Re(h_0) > 1350,\ w/R(h_0) = 0,$

$Re(h_0) > 200,\ w/R(h_0) \sim 2,$ ▪ $Re(h_0) > 700,\ w/R(h_0) \sim 1,$ + $Re(h_0) > 1350,\ w/R(h_0) \sim 0.1,$

FIGURE 7.5 Sets 1 & 2 Bore strength (H_z/T_z) versus fractional depth (h_0/H_0). For non-rotating currents the head is deeper than the tail depth. Rotation causes the bore strength to decrease.

For non-rotating currents the head is generally larger than the following flow, rising to double for very shallow currents ($h_0/H_0 \leq 0.2$). As rotation is increased the depth of the head relative to the tail decreases for deeper currents. What causes this change in profile? Is it a consequence of a lower mass flux to the head, due to the anticyclonic gyre effectively trapping fluid and decreasing the flux of fresh water from the lock? Plate 6 shows the evolution of a geostrophic eddy for a strongly rotating gravity current (exp.13). Perhaps the greater detrainment of fluid, due to the larger surface area of the gravity current in contact with the ambient fluid is responsible. Methods for quantifying and controlling detrainment are discussed in Chapter 8, where future work is considered.

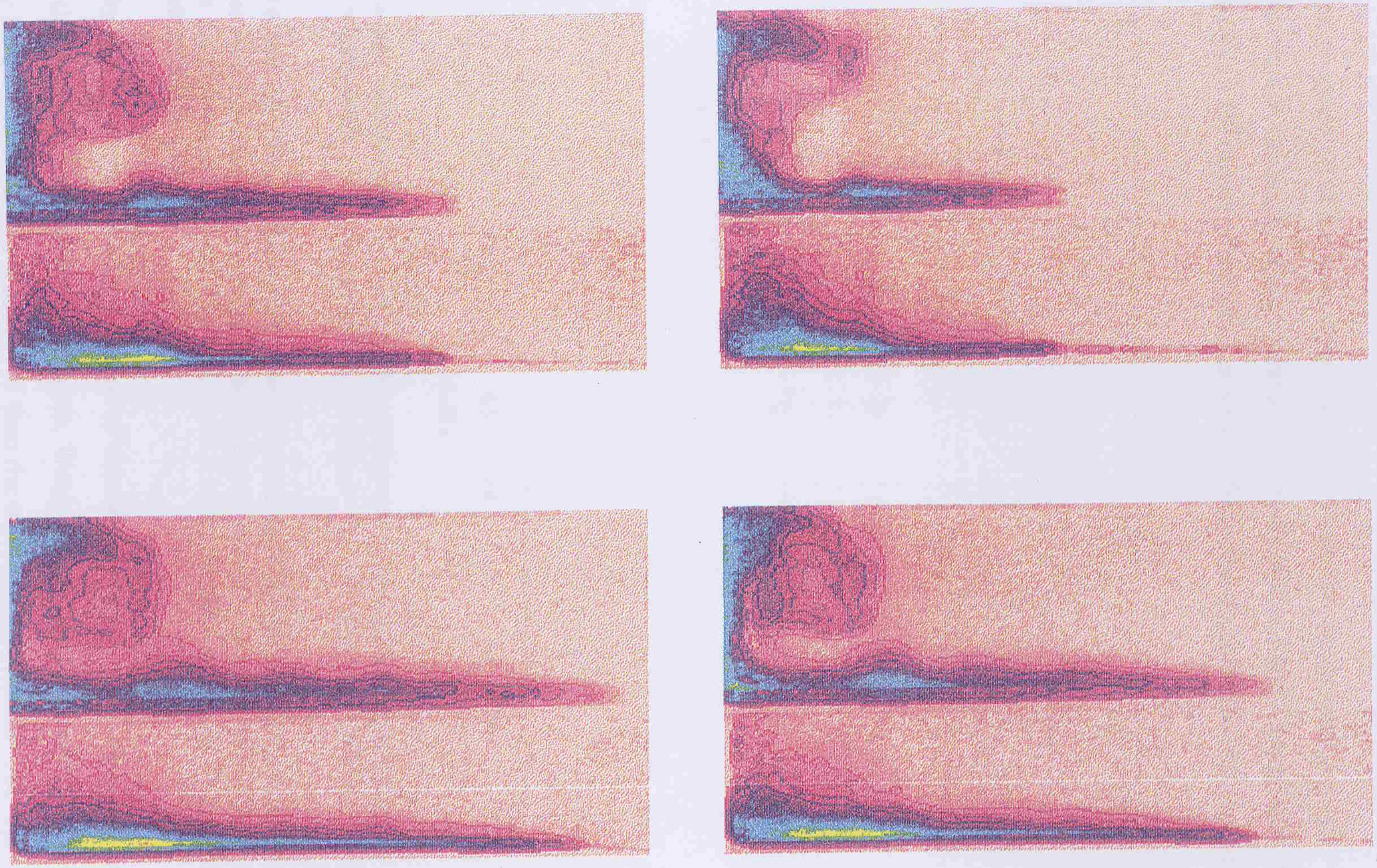

PLATE 6. Evolution of a geostrophic eddy (exp.13)- strongly rotating current, interval time/rotation period = 1.1.

7.1.6 Front speed

The speed of propagation of the nose along the channel was non-dimensionalised as $c = U/(g'h_0)^{\frac{1}{2}}$, where h_0 is the height of the opening. The results of sets 1 and 2 are plotted in figure 7.6, to give a full picture of the effect of varying fractional depth on the front speed.

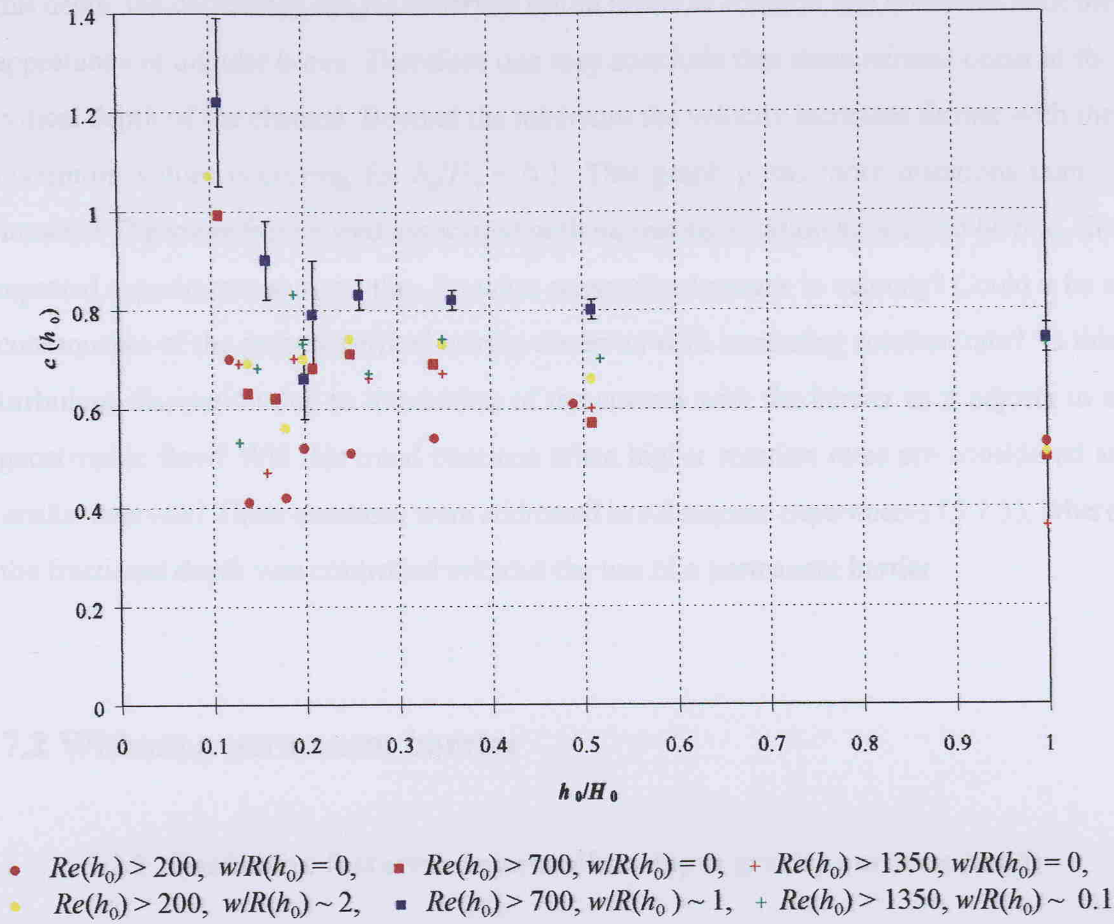

FIGURE 7.6 Sets 1 & 2 Front speed ($c\ (h_0)$) versus fractional depth (h_0/H_0). Initially the front speed increases as the level of rotation is increased. The maximum values are observed for $w/R(h_0) \sim 1$, above this the front speed decreases. The front speed is higher for shallow than for deep gravity currents, where $Re(H_Z) > 1000$.

The reader should bear in mind the influence of viscosity for $h_0/H_0 \leq 0.2$. Generally the non-rotating currents have lower front speeds. Weak rotating currents, $w/R(h_0) \sim 0.1$, generally have a slightly higher front speed than the non-rotating currents. The highest velocities are observed at moderate rotation rates, $w/R(h_0) \sim 1$, across the full range of fractional depths. For stronger rotation, $w/R(h_0) \sim 2$, the front speed is lower. Initially these experiments were performed at low values of $g' \sim 2.4\text{cms}^{-2}$, so to rule out any viscous effects they were repeated at $g' \sim 25\text{cms}^{-2}$. The results were found to be remarkably similar.

The trend of increasing front speed with decreasing fractional depth is apparent for both non-rotating and rotating currents. However, this is interrupted by a minimum in velocity at $0.1 < h_0/H_0 < 0.2$, for all currents. Although the front speed becomes more variable at this depth, the decrease in $c(h_0)$ is observed for all levels of rotation and coincides with the appearance of undular bores. Therefore one may conclude that these minima occur at the critical depth of the channel. Beyond the minimum the velocity increases further with the maximum values occurring for $h_0/H_0 \sim 0.1$. This graph poses more questions than it answers! The lower front speed associated with increasing rotation appears to be real, the repeated experiments support this. So what causes the decrease in velocity? Could it be a consequence of the greater vertical mixing observed with increasing rotation rate? Is this turbulent dissipation due to interaction of the current with the barrier as it adjusts to a geostrophic flow? Will this trend continue when higher rotation rates are considered at smaller intervals? These questions were addressed in subsequent experiments (§ 7.3), where the fractional depth was controlled without the use of a permanent barrier.

7.2 Without a permanent barrier

7.2.1 Qualitative features - Intermediate depth gravity currents (set 3)

Plate 7 illustrates the effect of increasing rotation on a gravity current of intermediate initial depth . In each image $h_0/H_0 \sim 0.5$, $Re(h_0) > 3000$, the only parameter varied is the rotation rate. The current has progressed approximately 2 lock lengths (50cm) along the channel. The position of the lock opening is marked by polystyrene strips either side of the tank, which are used to guide the barrier.

Plate 7a, is a non-rotating gravity current. The current fills the full width of the channel. Lobes and clefts as described in §1.2.1 are seen at the leading edge of the gravity current.

The frontal region is further advanced at the l.h. wall. Since the lamps attached to the apparatus were switched on immediately prior to the removal of the barrier, a temperature difference is unlikely to be the reason for this. Therefore it is thought to be a result of the unstable nature of the leading edge, due to the random growth and decay of lobes and clefts. The characteristic shape of the gravity current is observed with the large head and protruding nose. Behind the head Kelvin-Helmholtz billows are seen in the side view and the corresponding change in depth across the stream is just visible. In this case the depth at the head is approximately that at the opening, although immediately behind the head the tail depth is quite shallow.

Plate 7b - The current is exposed to moderate rotation ($w/R(h_0) = 0.92$). The current has detached from the left hand wall. The fluid is piled up against the right hand wall and its depth here has increased significantly. Billows are seen along the full length of the current and reach deep in to the lower ambient fluid. They are clearly observed on the free surface and are of significant magnitude. The head of the gravity current is now much smaller. It is less stable compared with the head of a non-rotating current, with the billows at the head periodically growing, breaking up and then replaced by smaller billows. Downstream the flow is approximately $R(h_0)$.

Plate 7c - The rotation rate has increased further ($w/R(h_0) = 1.88$). The width of the head and the flow immediately behind the head are narrower. Downstream the width is approximately that observed in plate 7b. This may be due to the growth of large billows obscuring the actual width. At the right hand wall the depth of the current has increased slightly and the head is similar to that observed for $w/R(h_0) \sim 1$. In the source region a geostrophic eddy is developing, the sense of rotation is anticyclonic. Griffiths & Hopfinger (1983) also observed the formation of an eddy in this region. They proposed that this vortex could effectively trap the remaining fluid in the lock. They also observed a Kelvin wave on the interface, propagating cyclonically around the lock and then along the current at the r.h. wall, which they believed caused the decay they observed in front speed after the current had progressed several lock lengths. Neither the Kelvin wave or the decay in front speed were observed in this investigation.

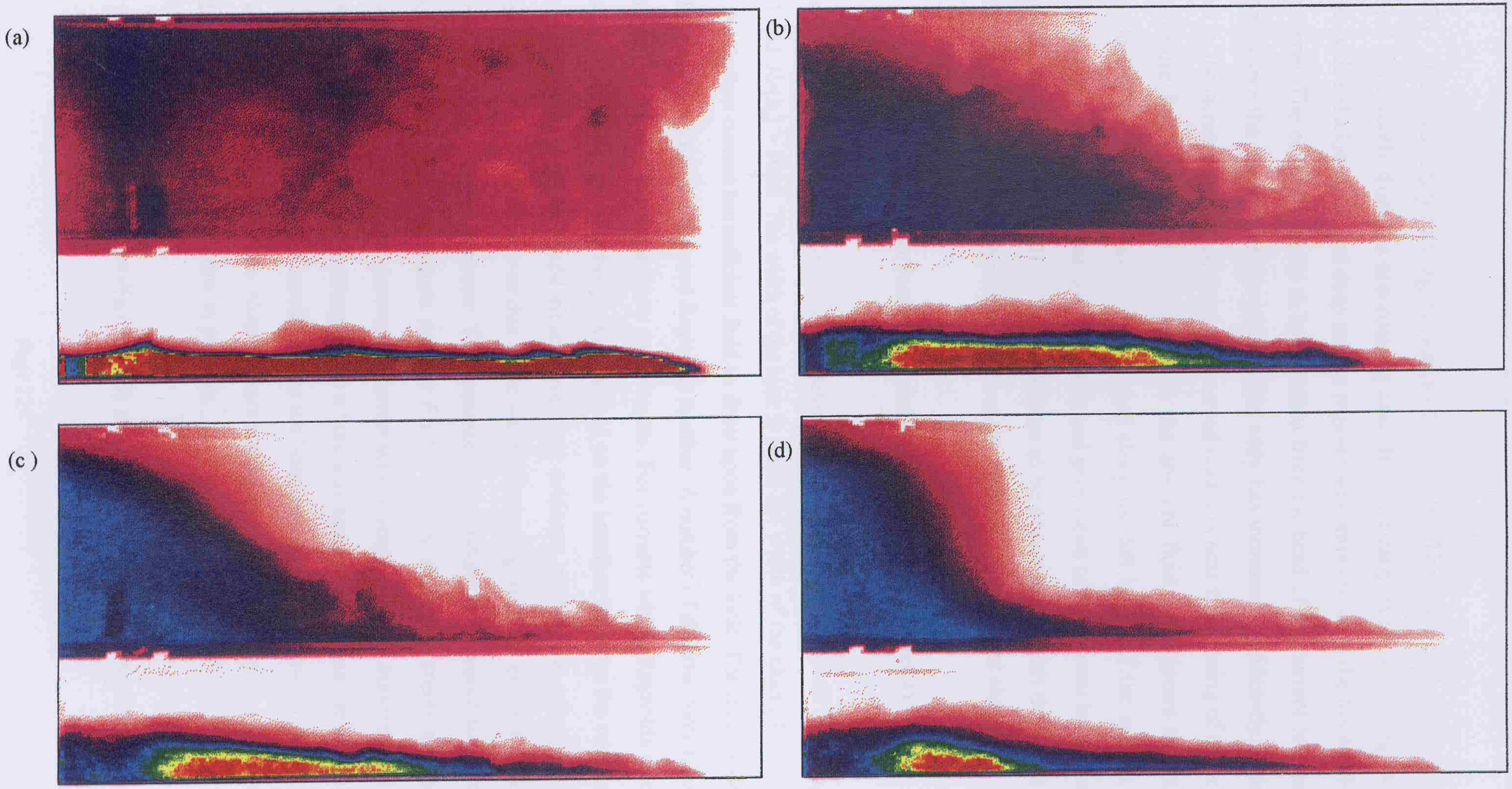

PLATE 7. Set 3 $h_0/H_0 \sim 0.5$, $Re(h_0) > 3000$ - (a) $w/R(h_0) = 0$, (b) $w/R(h_0) = 0.92$, (c) $w/R(h_0) = 1.88$, (d) $w/R(h_0) = 2.99$.

Plate 7d - This is a strongly rotating current ($w/R(h_0) = 2.99$). The shape of the current has changed significantly from the non-rotating case. It now clearly exhibits a 'wedge-like' profile, with a shallow head and deep source region that continues to fill the full width of the channel. The control appears to have shifted from the head of the current to source region, where the strength of the geostrophic eddy has increased significantly. This is shown by the increase in inferred depth and curved contours near the opening of the lock. This feature forms a domed interface with the ambient fluid and appears to rotate anticyclonically. The width has now decreased along the full length of the current, to approximately $\frac{1}{4}$ the width of the tank. The side and plan views of the current have similar length scales. Kelvin-Helmholtz billows continue to be observed but with the increased rotation their size has diminished. The depth at the opening has increased slightly.

7.2.2 Qualitative features - shallow gravity currents (set 4)

Plate 8 illustrates the effect of increasing rotation on a shallow current. In each image $h_0/H_0 = 0.1$ and $Re(h_0) > 1000$. The width of the lock is twice the width of the channel to ensure that the shallow current has sufficient fluid to draw upon from the lock. The shallow depth of the current results in a reduced Reynolds number. A number of shallow currents were examined in set 1 of the preliminary experiments. For currents with a Reynolds number greater than 1000 an undular bore was observed on the interface between the two fluids. The presence of the bore could either have been evidence of the flow adjusting from supercritical to subcritical flow or due to lee waves emanating from the interaction of the current with the permanent barrier. The presence of an undular bore would support the theory, which predicts a Froude number $Fr(T_Z) > 1$ for shallow currents and hence supercritical flow. In set 4 the permanent barrier was no longer used to control the depth of the current as it left the lock. Despite this a bore was again observed on the interface in the non-rotating current. This confirms that the bore was due to the flow adjusting from super-critical to sub-critical flow. Note the bars across the current in the plan view and the undular interface in the side view in plate 8a.

In plate 8b (weak rotation $w/R(h_0) = 0.98$) the interface has become smoother and the

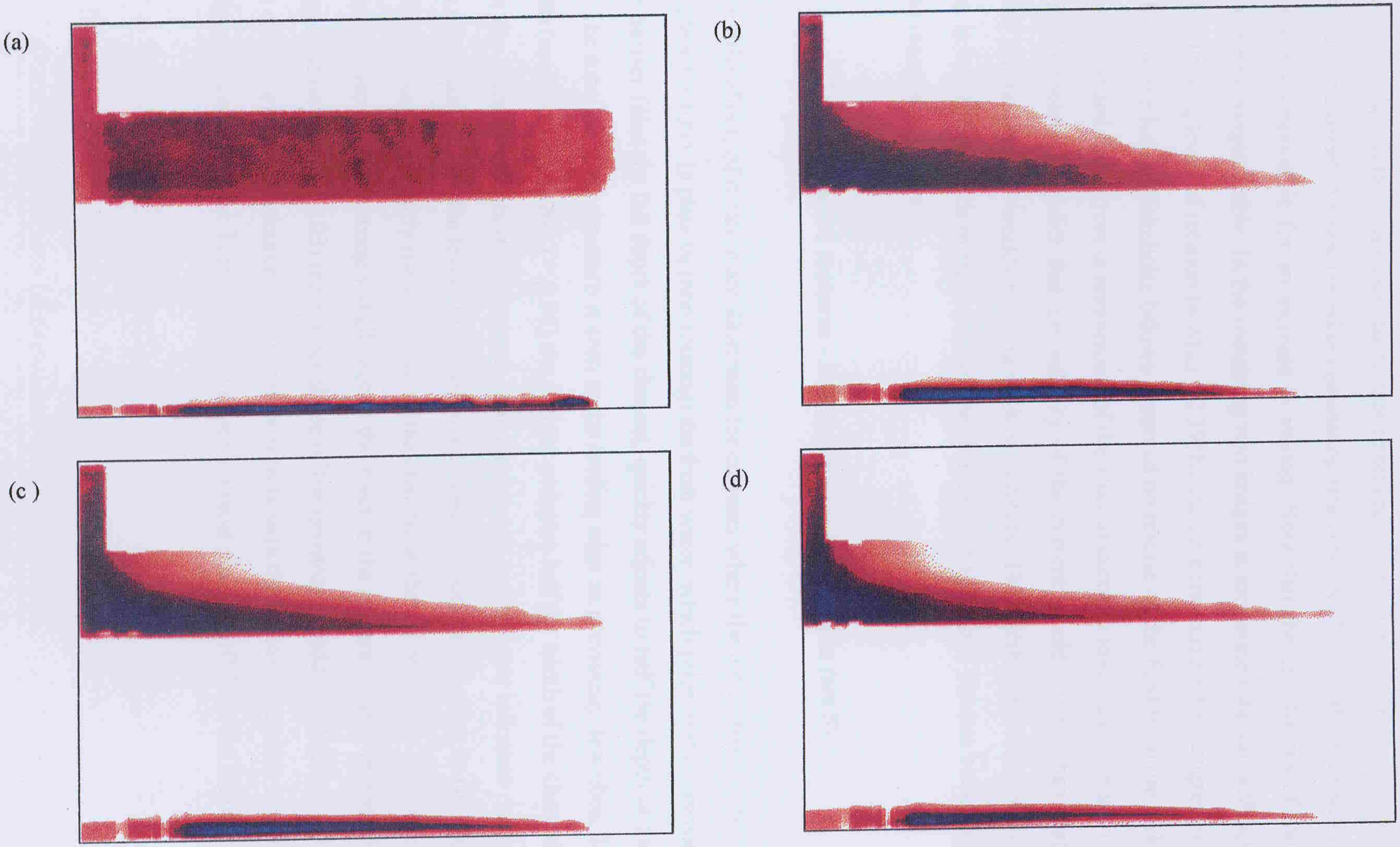

PLATE 8. Set 4 $h_0/H_0 \sim 0.1$, $Re(h_0) > 1200$ - (a) $w/R(h_0) = 0$, (b) $w/R(h_0) = 0.98$, (c) $w/R(h_0) = 1.92$, (d) $w/R(h_0) = 2.39$.

current has deflected towards the r.h. wall. The head of the current has become very shallow, whilst the width remains similar to that observed in set 3, i.e. approximately half the width of the channel. A stream of eddies emanating from corner of the L-shaped barrier were probably responsible for an increase in mixing. Note that the undulations of the interface are no longer visible. In the remaining two images at moderate rotation ($w/R(h_0)$ = 1.92) and strong levels of rotation ($w/R(h_0) = 2.39$) by the time the current has progressed 2 lock lengths the Kelvin-Helmholtz billows observed on release of the fluid from the lock have dissipated and the current is reminiscent of the viscous currents investigated in set 1. One would therefore predict that the velocity of the current would be less than that observed for the non and weakly rotating shallow currents. The width of the head of the current is less than 1/20th of the width of the channel and therefore viscous boundary stresses must be dominant.

7.2.3 Qualitative features - Full depth gravity currents (set 5)

In Plate 9 the effects of rotation are illustrated for currents where the initial depth $h_0/H_0 = 1$ and $Re(h_0) > 3000$. In plate 9a (non-rotating) the fresh water, which prior to the removal of the barrier filled the full depth of the channel, quickly adjusts to half the depth of the tank. The lobe and cleft structure is seen at the leading edge as previously described. In plate 9b (weak rotation $w/R(h_0) = 0.98$) the current occupies half the width of the channel. Again the fractional depth of the current seems to have an insignificant influence on the width of the current. As the level of rotation is increased to moderate in plate 9c ($w/R(h_0)$ = 1.99) the current is nearly the full depth of the channel at the r.h. wall near the source region, but becomes increasingly shallower at the head of the current. Finally in plate 9d (strong rotation $w/R(h_0) = 3.03$) the distinct shape of the geostrophic eddy is observed. The depth of the current at the source region now intersects with the bottom boundary and the head has become shallower. In fact the head appears almost pinched off from the following flow.

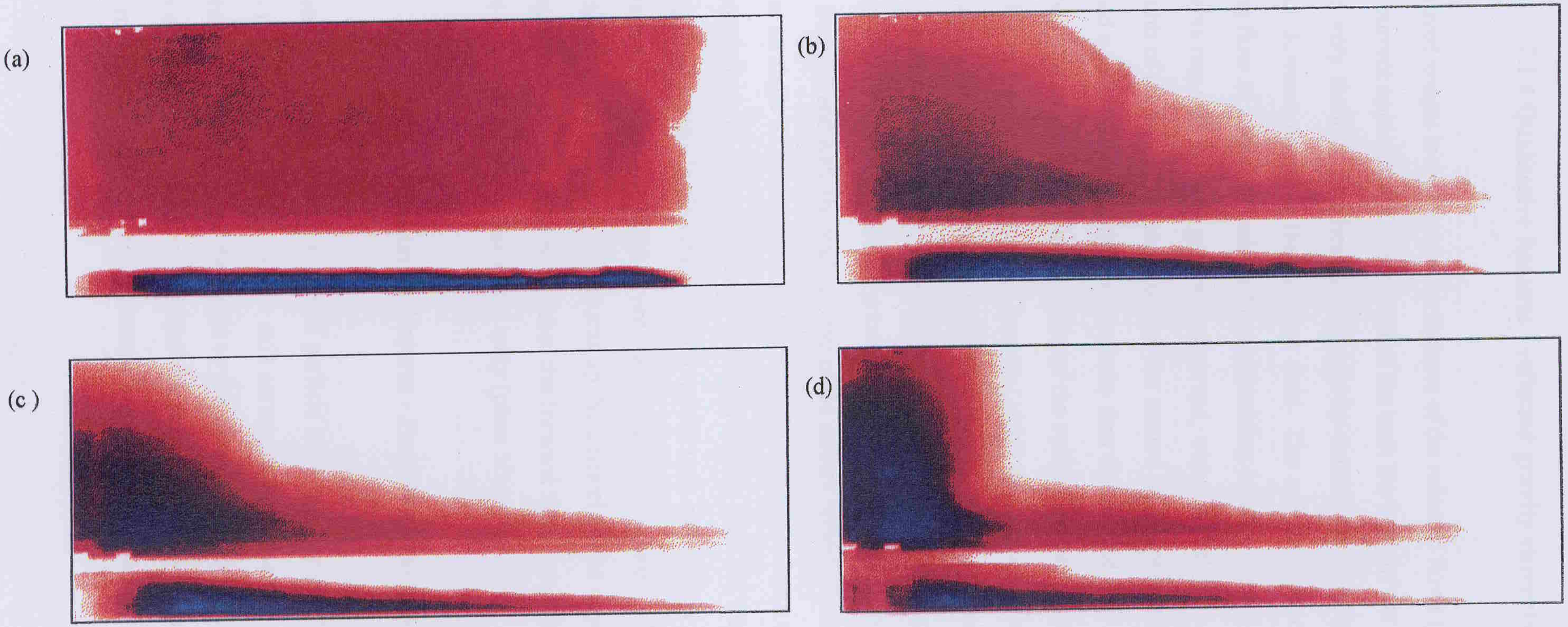

PLATE 9. Set 5 $h_0/H_0 \sim 1$, $Re(h_0) > 3000$ - (a) $w/R(h_0) = 0$, (b) $w/R(h_0) = 0.98$, (c) $w/R(h_0) = 1.99$, (d) $w/R(h_0) = 3.03$.

7.2.4 Qualitative features - reflected gravity currents (set 3)

The improved images in set 3 reveal the features of the reflected flows (plate 10). As a non-rotating current approaches the end wall of the tank the body of the current downstream becomes very shallow. The head of the gravity current on colliding with the end wall collapses downwards in to the ambient fluid. The reflected flow advances in to the oncoming flow as a smooth undular bore resembling a solitary wave (plate 10a). In these experiments two solitons were generally observed, with a wavelength which approximated to the width of the tank. The amplitude of the second soliton was less than the first. They maintained a constant but slightly lower velocity than the forward flow. Cross shaped shock waves were observed between the crests of the solitary waves. However these were not discernible in the digitised images. Chanson (1986) described similar features associated with undular bores. He proposed they were due to the fluid near the side wall being retarded by the boundary layer, causing critical conditions to develop there sooner than in the centre of the channel. When a gravity current at a low rotation rate $(w/R(h_0) \sim 0.5)$ reflects from the end wall, the leading edge of the current remains distinguishable as a series of bars at an angle to the left hand wall (plate 10b). The bore has a smaller amplitude and wavelength than the solitons seen in the non-rotating case. As the front progresses the following flow eventually fills the full width of the tank and solitary waves resembling the non-rotating reflected flow are observed. At strong rotation rates $(w/R(h_0) \sim 3)$ the current on reaching the end wall turns and returns up the channel on the opposite wall maintaining its integrity until it interacts with either the forward flow spreading laterally across the channel or eventually the geostrophic eddy (plate 10c).

7.2.5 Qualitative features - Particle tracking (set 6)

The final set of experiments involved particle tracking. The resulting velocity profile is shown in plates 11 a, b & c. The x axis corresponds to the distance along the channel measured from the barrier and the y axis to the width across the channel. The length of the arrows corresponds to magnitude of the velocity and that for 10 cm/s is shown in the top l.h. corner of the figure. A monochrome palette provides an indication of the vorticity

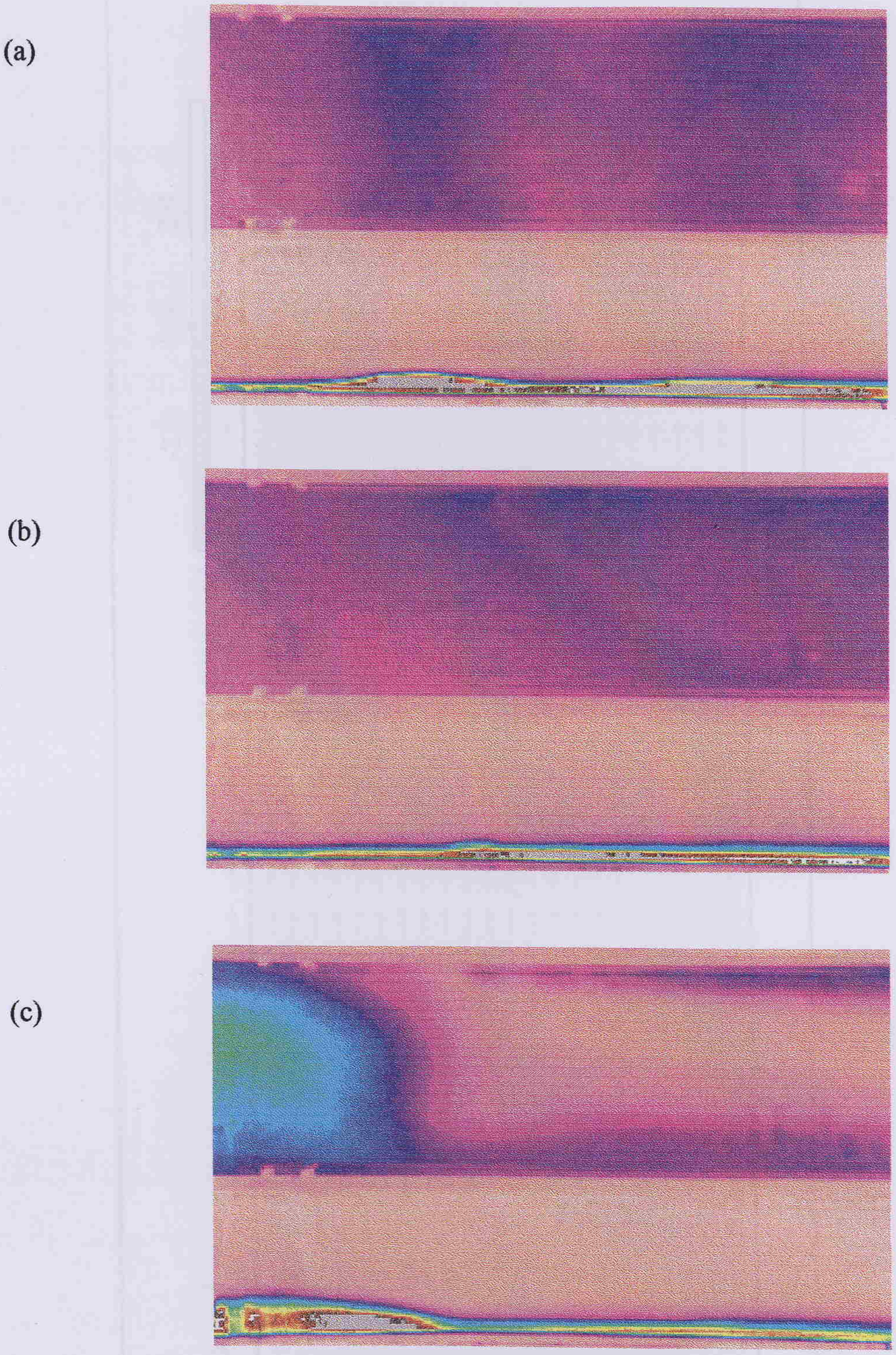

PLATE 10. Reflected flow $h_0/H_0 \sim 0.25$, $Re(h_0) > 3000$
- (a) $w/R(h_0) = 0$, (b) $w/R(h_0) = 0.5$, (c) $w/R(h_0) = 3.0$.

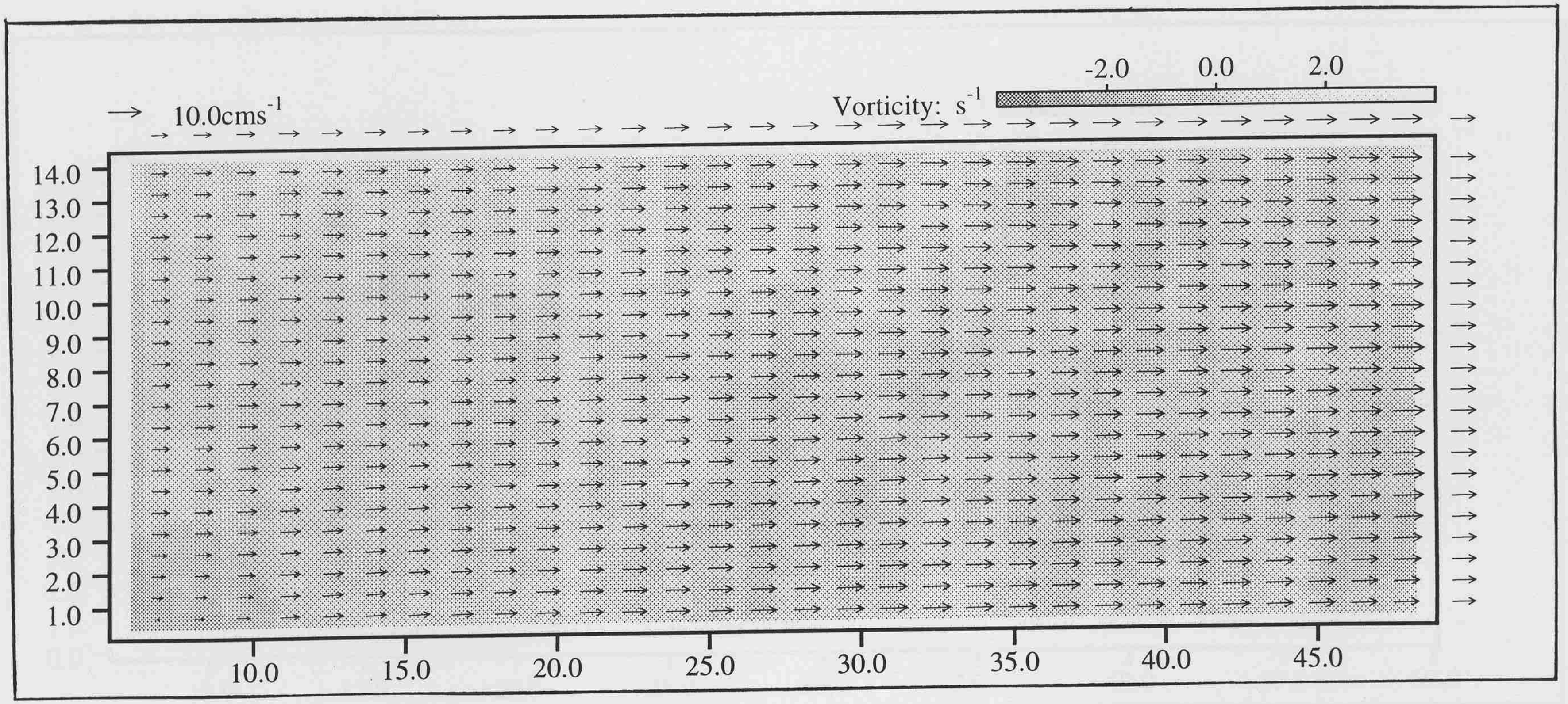

PLATE 11. Particle tracking (a) $h_0/H_0 = 0.25$, $w/R(h_0) = 0$ and $Re(h_0) = 3568$

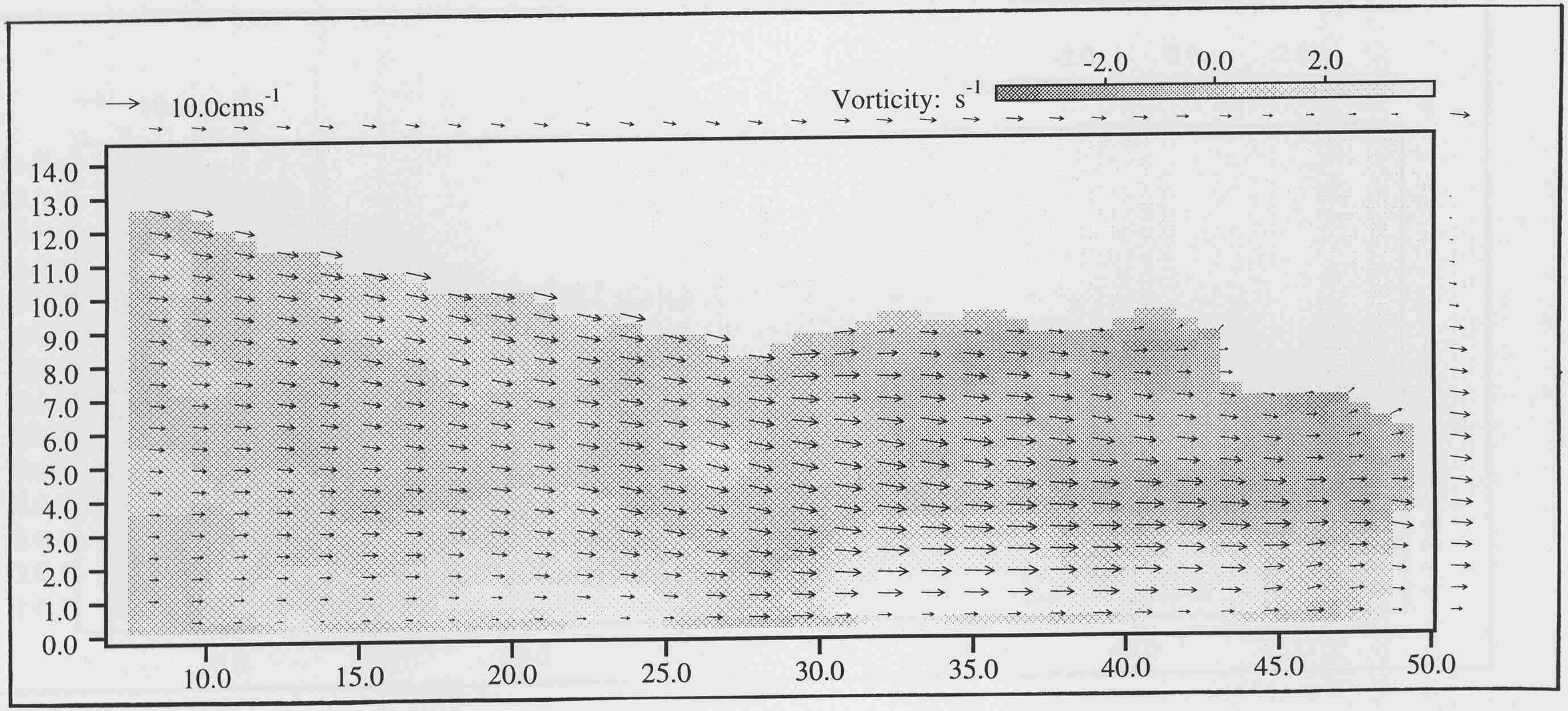

PLATE 11. Particle tracking (b) $h_0/H_0 = 0.25$, $w/R(h_0) = 0.99$ and $Re(h_0) = 3568$

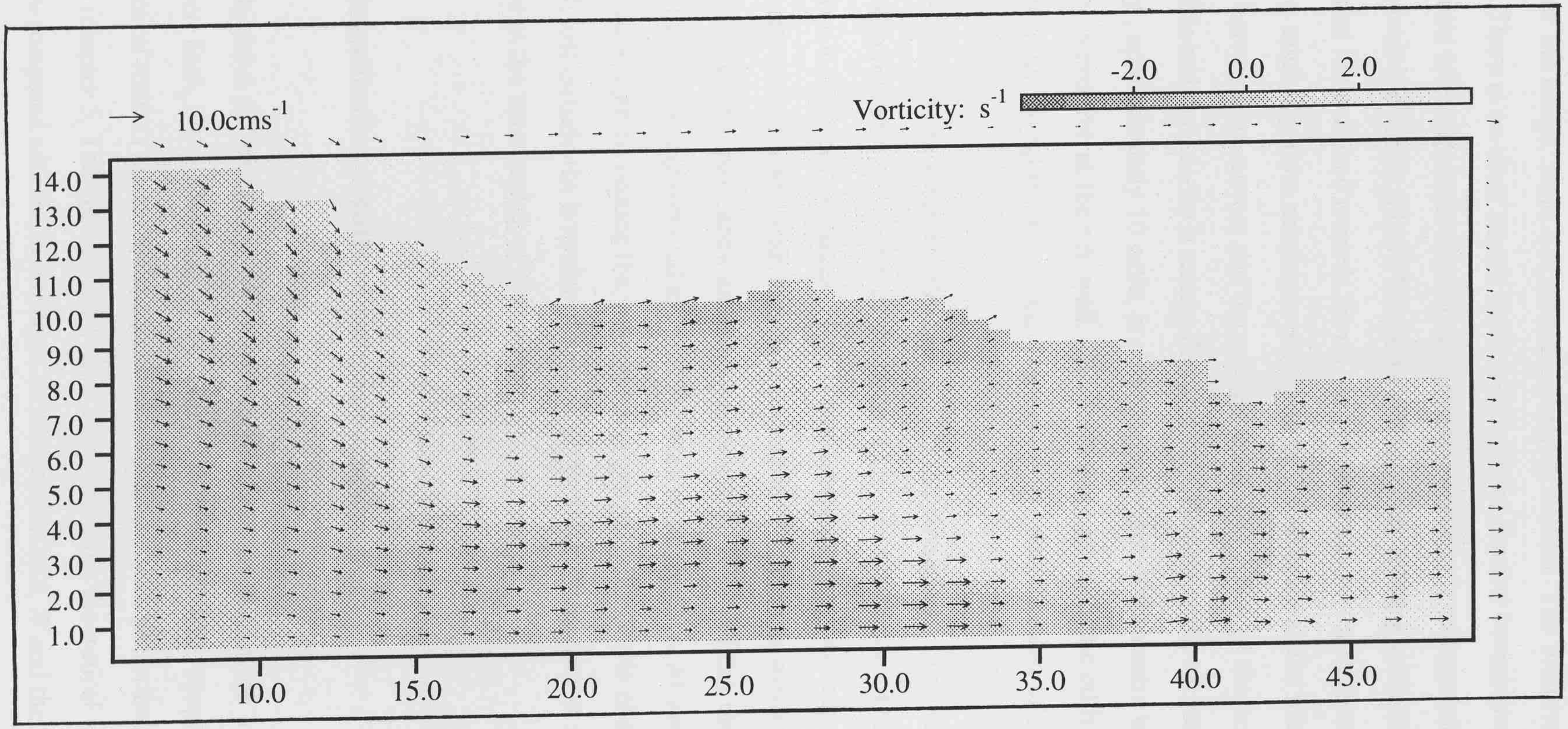

PLATE 11. Particle tracking (c) $h_0/H_0 = 0.25$, $w/R(h_0) = 2.11$ and $Re(h_0) = 3509$

profile across the surface of the current. The associated intensity scale is seen in the top r.h. corner of the image. Plate 11a, is a non-rotating current. The uniformity of the flow is striking. There is no shear across the current and the channel boundaries seem to have an insignificant effect upon the current. The relative vorticity is zero and therefore the depth of the current is constant. Plate 11b, shows a moderately rotating current ($w/R(h_0)$ ~ 0.99). The current has deflected towards the r.h. wall. A shear across the current is now apparent, with the opposing flow causing a reduction in the velocity at the interface on the free surface between the current and the ambient fluid. The effect of the boundary stresses is now visible and the velocity is seen to decrease considerably at the r.h. wall. The maximum velocity , approximately 10 cm/s, is observed just right of the centre of the current. The vorticity is positive at the r.h. wall. The developing geostrophic eddy is seen to extend approximately $2R(h_0)$ from the lock. The flow is towards the head of the current.

In Plate 11c (strong rotation $w/R(h_0) = 2.11$) the strength of the geostrophic eddy has increased considerably, as shown by the slope of the velocity vectors. The velocity however is less than in the previous images. There is now a considerable shear across the current and the velocity of the current tends to zero at the interface on the free surface between the two fluids. The geostrophic eddy extends approximately $2R(h_0)$ from the lock. Within the current the flow is unidirectional towards the head of the current. At the r.h.wall boundary stresses are seen to reduce the velocity. The greatest velocity is observed close to the r.h.wall just outside the boundary region. The vorticity is negative at the boundaries and positive in the inner region of the current.

7.3 Quantitative results of Sets 3, 4 and 5

The objective of the second series of experiments was to provide a direct comparison between both the predictions of the energy loss theory with simple flow (chapter 4, Theoretical results (1)) and the energy conserving theory with prescribed P.V. in the source region (chapter 5, Theoretical results (2)). There are three theoretical variables that can be directly compared with the experiments as the rotation rate, W and the fractional depth, η_0

(equivalent to the measured value of T_Z/H_0) are varied. These are the theoretical width of the current, *d*, front speed, *c* and Froude number, *Fr* which are equivalent to the laboratory measurements W_y/w, $c(H_0)$ and $Fr(T_Z)$ respectively. These variables are as defined in §1.2.3. To avoid confusion when discussing the results the theoretical notation will be used throughout this section.

A number of graphs are plotted for each of the three variables to illustrate the experimental results and to compare them with the two theories. Firstly, the experimental results of sets 3, 4 and 5 are contoured to show the effect of the fractional depth and rotation rate on the width, front speed and Froude no. These plots are compared with the results of the energy loss theory. Secondly, a further comparison with theory (1) is provided by a plot of the theoretical versus experimental values. Finally, experiments where the depth of the fresh water in the source region, $\delta = 0.5$ and 1.0 are contrasted with the predictions of theory (2).

7.3.1 Current Width, *d*

The width of the current is an important parameter. Hacker found the upstream width in better agreement with the theoretical curve than the head width, hence it is the upstream width that is discussed. The width was measured from the tank wall to the boundary between the geostrophic eddy and the boundary current. Unfortunately a billow was often found to develop here obscuring the boundary, therefore the upstream width is not as robust a length scale as the current depth.

Figure 7.8a shows a contour plot of the width of the current, *d* as the fractional depth and the rotation rate, *W*, are varied. Generally the fractional depth does not appear to influence the current width. This was my first impression on viewing the images. The initial response to weak rotation must be significant in that the current occupies approximately half the width of the channel when $W = 0.25$. At greater rotation rates the current width tends to the Rossby radius. Note that *W* is proportional to R^{-1}.

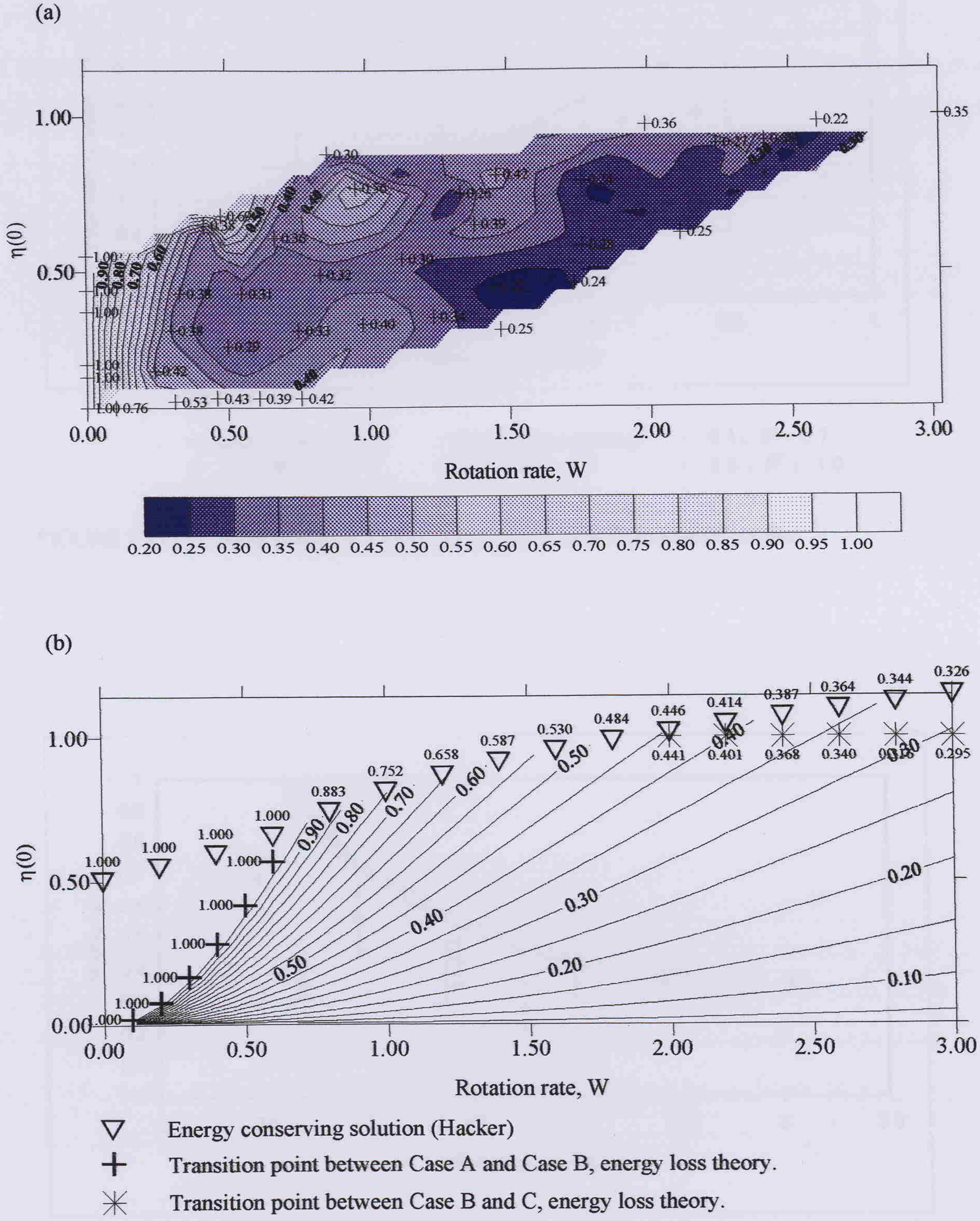

FIGURE 7.8 Current width, *d*, (a) experimental results, (b) energy loss theory.

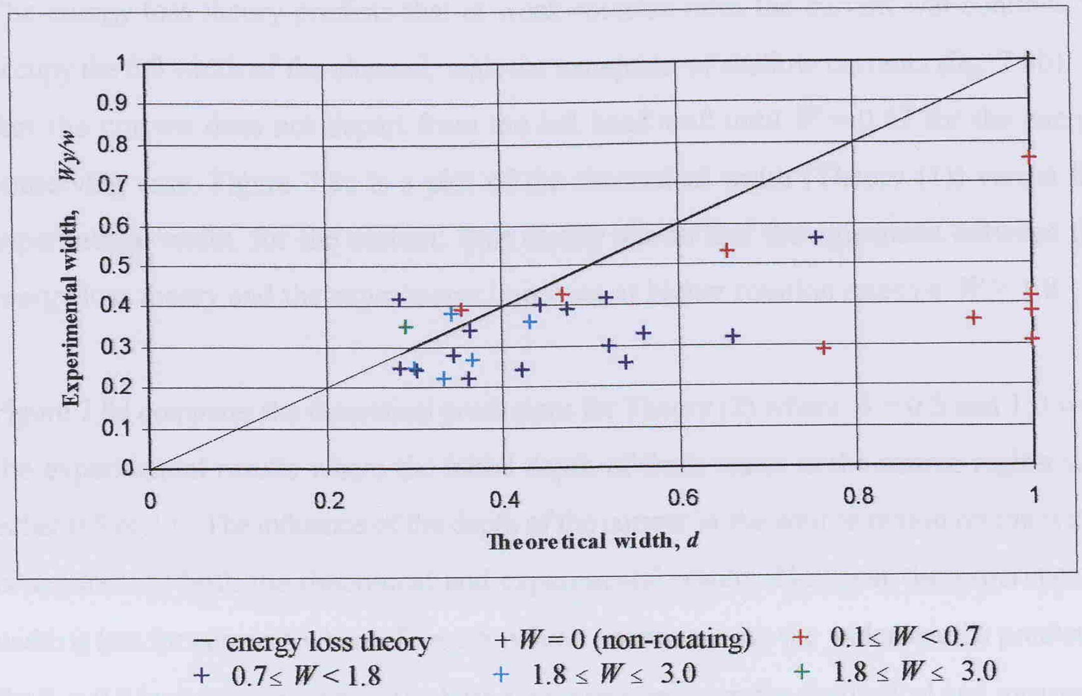

FIGURE 7.8 (c) Current width, *d*. Energy loss theory versus experimental results.

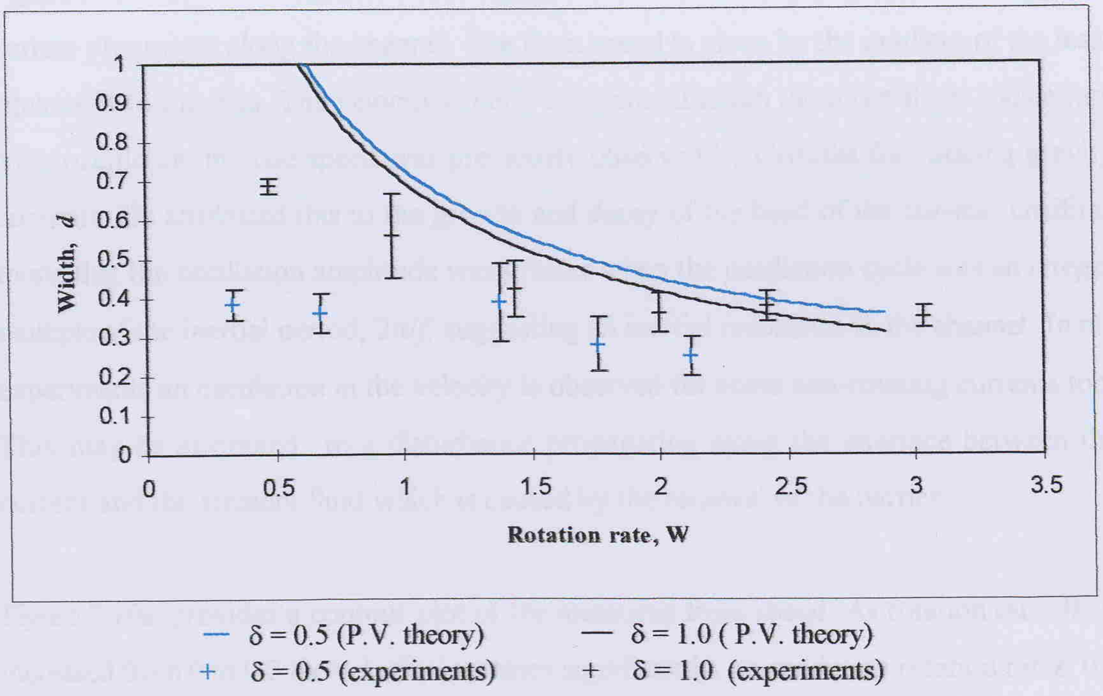

FIGURE 7.8 (d) Current width. Potential vorticity theory versus experimental results.

The energy loss theory predicts that at weak rotation rates the current will continue to occupy the full width of the channel, with the exception of shallow currents (fig. 7.8b). In fact the current does not depart from the left hand wall until $W = 0.67$ for the energy conserving case. Figure 7.8c is a plot of the theoretical width (Theory (1)) versus the experimental width, for the current. This clearly shows that the agreement between the energy loss theory and the experiments improves at higher rotation rates i.e. $W > 1.8$.

Figure 7.8d compares the theoretical predictions for Theory (2) where $\delta = 0.5$ and 1.0 with the experimental results where the initial depth of fresh water in the source region was either 0.5 or 1.0. The influence of the depth of the current in the source region on the width is apparent in both the theoretical and experimental results. However the experimental width is less for currents where $\delta = 0.5$, which contrasts with the wider widths predicted for $\delta = 0.5$ in the theory. Again the best agreement between the theoretical and measured widths is observed at strong rotation rates.

7.3.2 Front Speed, *c*

Figure 7.9, shows the non-dimensionalised position of the nose versus time as the gravity current progresses along the channel. The front speed is given by the gradient of the least squares fit to the data. The velocity is fairly constant although there is a slight oscillation. This oscillation in nose speed was previously observed by Griffiths for rotating gravity currents. He attributed this to the growth and decay of the head of the current. Griffiths found that the oscillation amplitude was greater when the oscillation cycle was an integer multiple of the inertial period, $2\pi/f$, suggesting an inertial resonance in the channel. In my experiments an oscillation in the velocity is observed for some non-rotating currents too. This may be attributed to a disturbance propagating along the interface between the current and the ambient fluid which is caused by the removal of the barrier.

Figure 7.10a provides a contour plot of the measured front speed. As rotation rate, W, is increased from 0 to 0.3 the velocity increases significantly. At moderate rotation rates, $0.5 \leq W \leq 1.5$, the velocity appears to plateau and as the rotation rate increases further it is

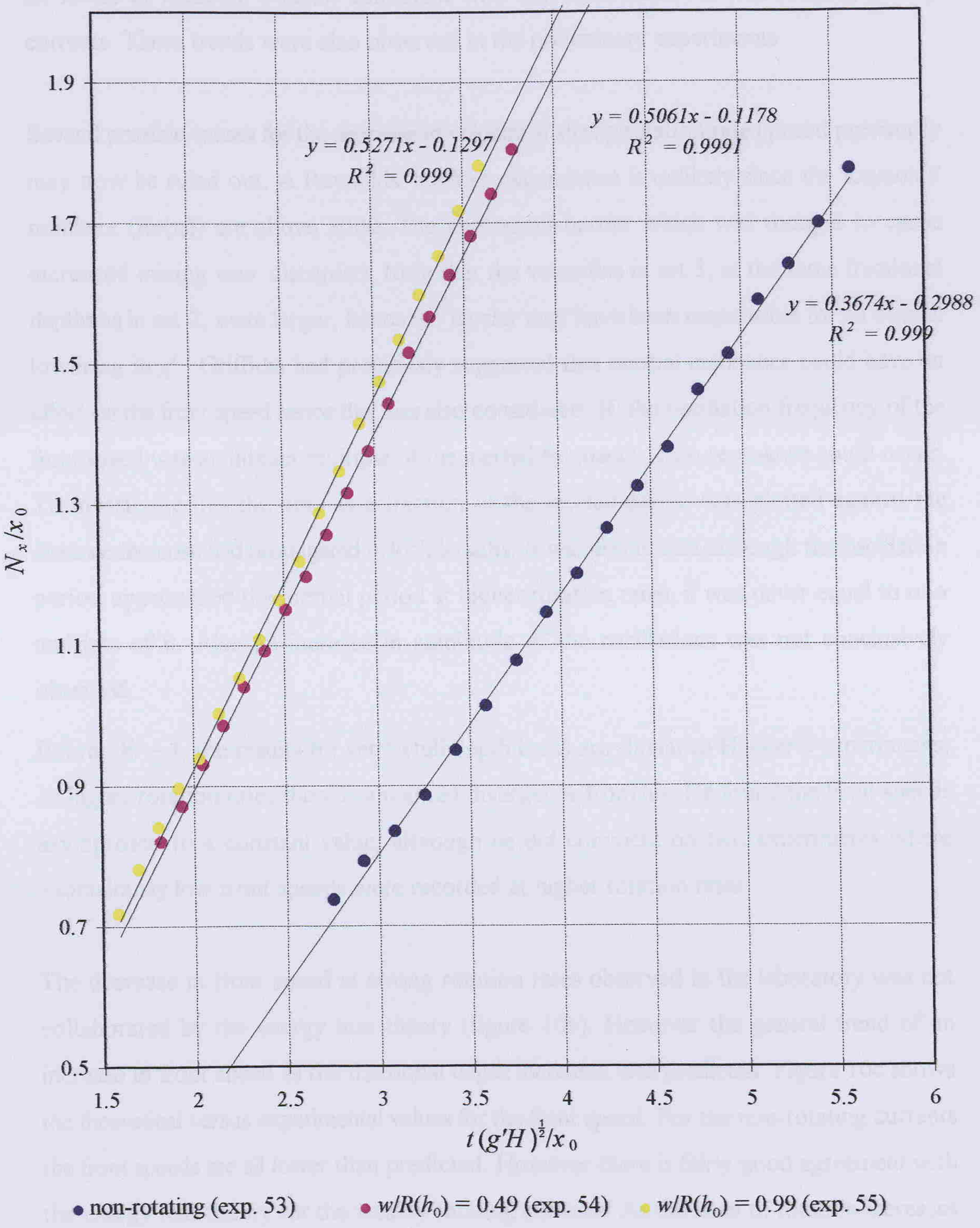

FIGURE 7.9. Non-dimensionalised nose position versus time for experiments 53, 54 and 55.

accompanied by a decrease in front speed. The velocity increases with fractional depth for all levels of rotation, a result consistent with that established for non-rotating gravity currents. These trends were also observed in the preliminary experiments.

Several possible causes for the decrease in velocity at strong rotation rates posed previously may now be ruled out. A Reynolds' number dependence is unlikely since the Reynolds' numbers ($Re(h_0)$) are above 3000. The permanent barrier which was thought to cause increased mixing was discarded. Note that the velocities in set 3, at the same fractional depths as in set 2, were larger, hence the barrier may have been responsible for an overall lowering in g'. Griffiths had previously suggested that inertial resonance could have an effect on the front speed hence this was also considered. If the oscillation frequency of the front speed was an integer multiple of the inertial frequency, then resonance could occur. To investigate this the time as a fraction of the inertial period was plotted against the distance the nose had propagated in lock lengths. It was found that although the oscillation period approached the inertial period at higher rotation rates, it was never equal to or a multiple of it. Also an increase in amplitude of the oscillations was not conclusively observed.

Below $W \sim 1$, the results for set 5 (full depth lock) are similar to Hacker's experiments. At higher rotation rates there is a marked divergence from his. He found the front speeds asymptoted to a constant value, although he did comment on two experiments where anomalously low front speeds were recorded at higher rotation rates.

The decrease in front speed at strong rotation rates observed in the laboratory was not collaborated by the energy loss theory (figure 10b). However the general trend of an increase in front speed as the fractional depth increases was predicted. Figure 10c shows the theoretical versus experimental values for the front speed. For the non-rotating currents the front speeds are all lower than predicted. However there is fairly good agreement with the energy loss theory for the weakly rotating currents. As the level of rotation increases the measured front speeds fall well below the predicted values.

Similar trends are identified when the experimental values for $\delta = 0.5$ and 1.0, are compared

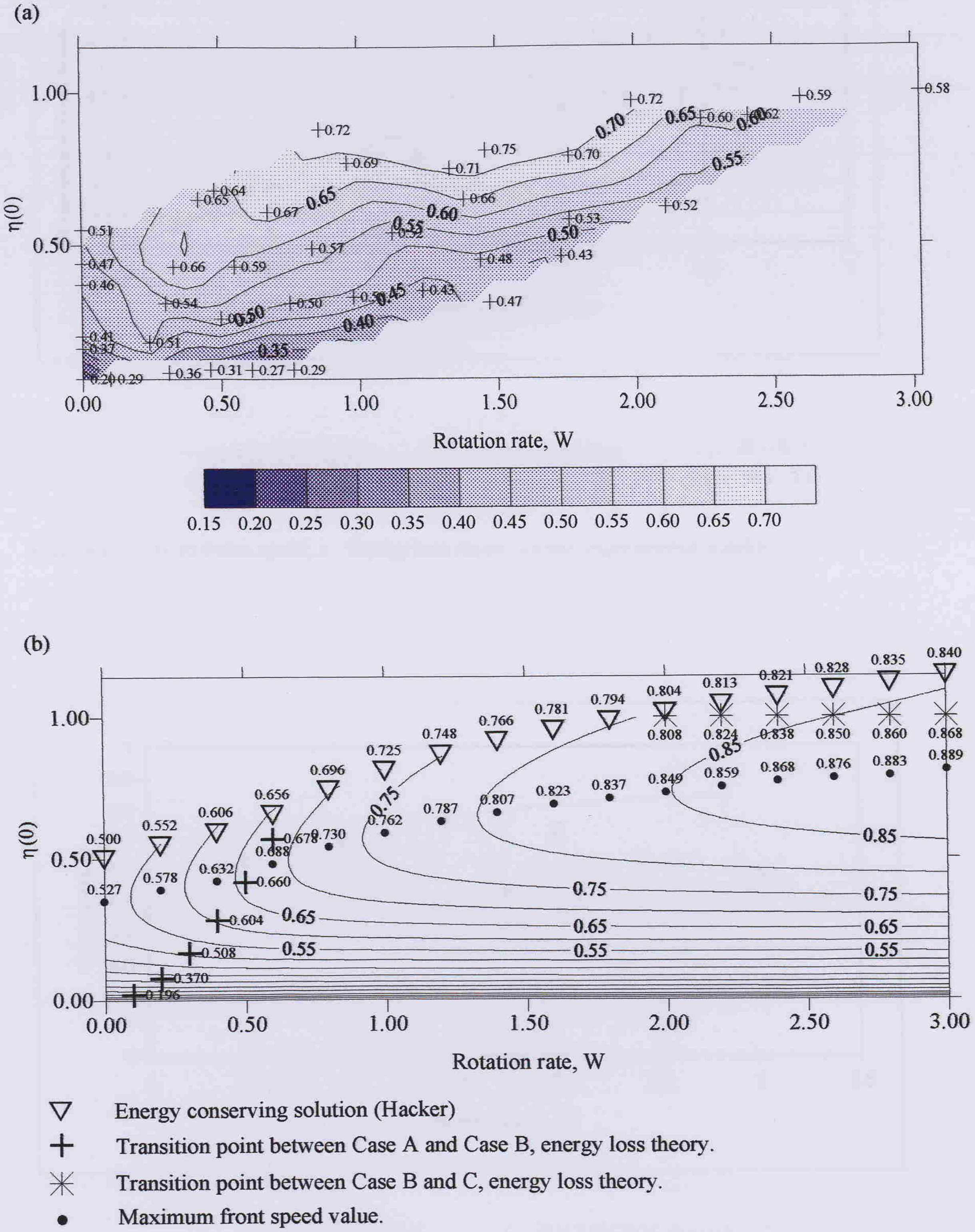

FIGURE 7.10 Front speed, c, (a) experimental results , (b) energy loss theory.

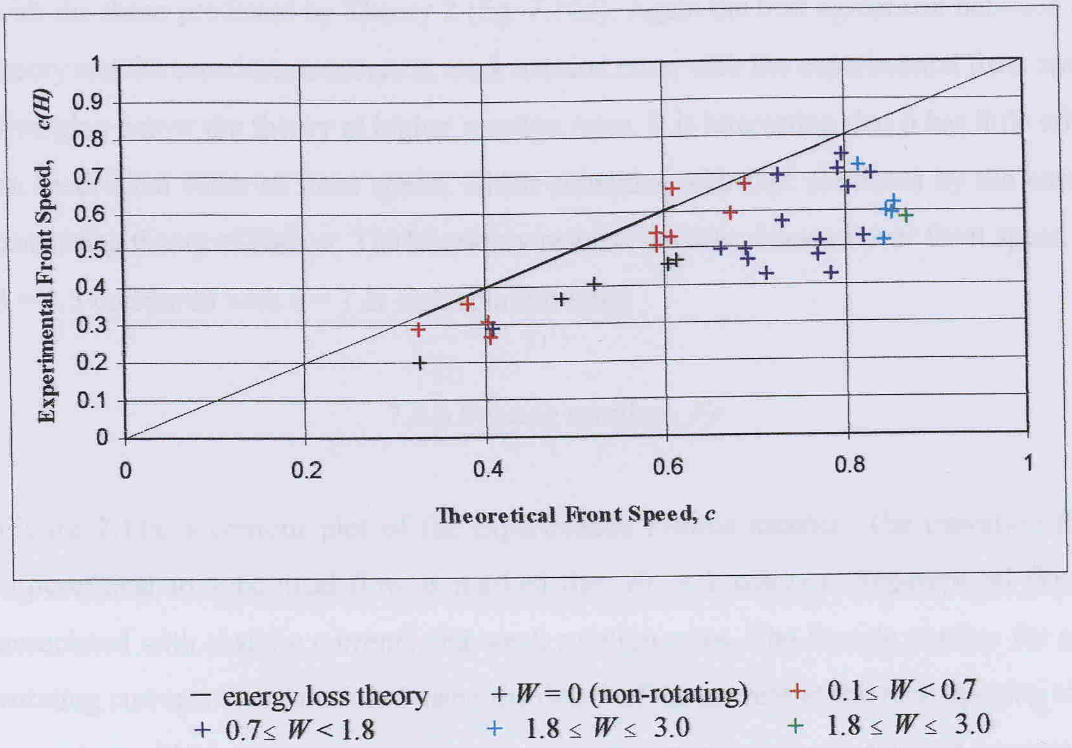

FIGURE 7.10 (c) Front speed, *c*. Energy loss theory versus experimental results.

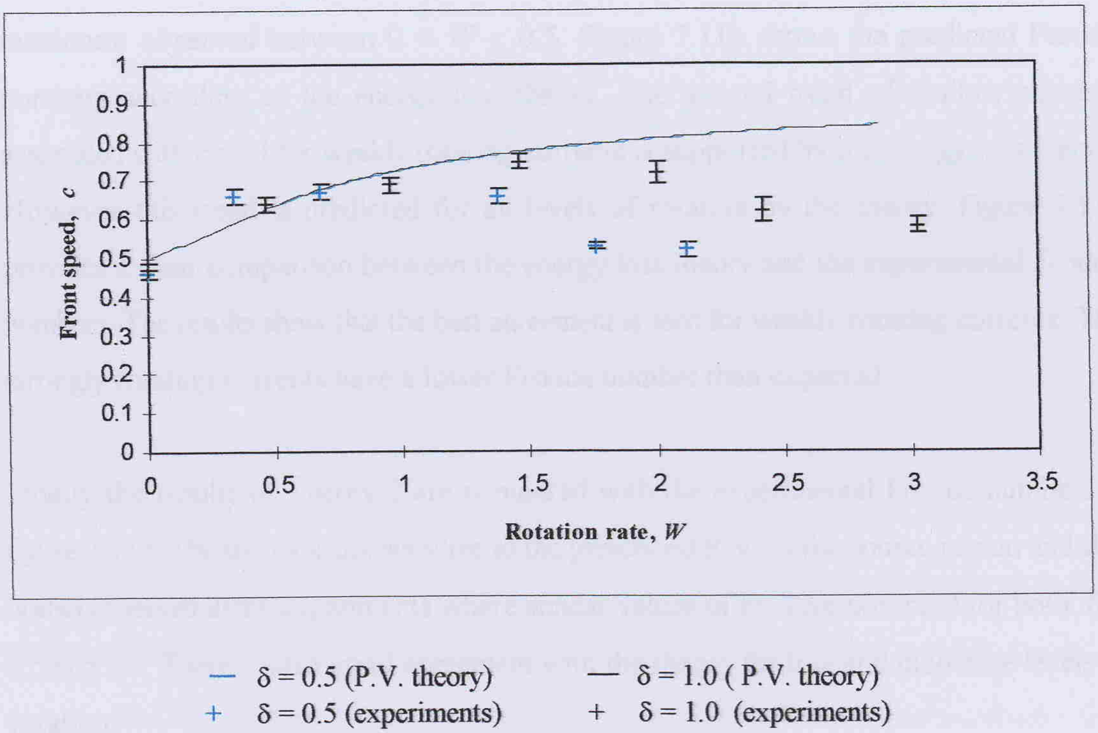

FIGURE 7.10 (d) Front speed. Potential vorticity theory versus experimental results.

with the those predicted by Theory 2 (fig. 7.10d). Again the best agreement between the theory and the experiments occurs at weak rotation rates, with the experimental front speed diverging below the theory at higher rotation rates. It is interesting that δ has little effect on theoretical value of front speed, which coincides with that predicted by the energy conserving theory of Hacker. The laboratory results however show a lower front speed for $\delta = 0.5$ compared with $\delta = 1$ at high rotation rates.

7.3.3 Froude number, *Fr*

Figure 7.11a is contour plot of the experimental Froude number. The transition from supercritical to subcritical flow is marked the $Fr = 1$ contour. Supercritical flow is associated with shallow currents and weak rotation rates. The Froude number for non-rotating currents was calculated using the depth of the current at the lock opening to be consistent with the measurements for the rotating currents. For non-rotating currents the depth immediately behind the head may be more appropriate. This depth which is generally shallower than that at the opening would imply a supercritical Froude number for shallow non-rotating currents, therefore in agreement with the observed bore described in section 7.2.2. As the level of rotation was increased the Froude number decreased from the maximum observed between $0 < W \leq 0.5$. Figure 7.11b shows the predicted Froude numbers according to the energy loss theory. The general trend of shallow currents associated with $Fr > 1$ for weakly rotating currents is supported by the energy loss theory. However this trend is predicted for all levels of rotation by the theory. Figure 7.11c provides a clear comparison between the energy loss theory and the experimental Froude numbers. The results show that the best agreement is seen for weakly rotating currents. The strongly rotating currents have a lower Froude number than expected.

Finally the results of Theory 2 are compared with the experimental Froude numbers in figure 7.11d. The theory is not sensitive to the prescribed P.V. in the source region and this is also observed in the experiments where similar values of Fr were observed for both $\delta = 0.5$ and 1.0. There is also good agreement with the theory for low and moderate levels of rotation.

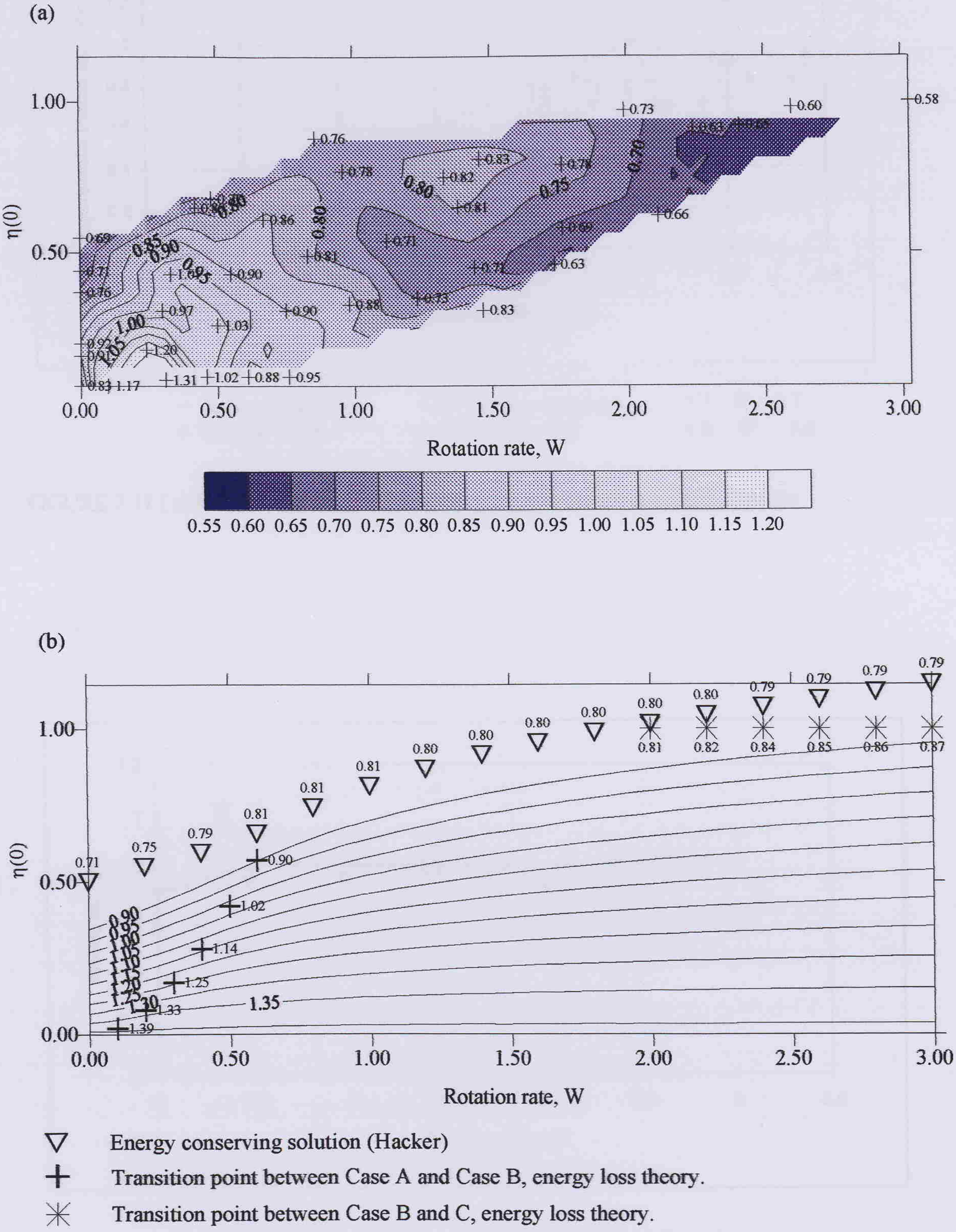

FIGURE 7.11 Froude number, *Fr*, (a) experimental results, (b) energy loss theory.

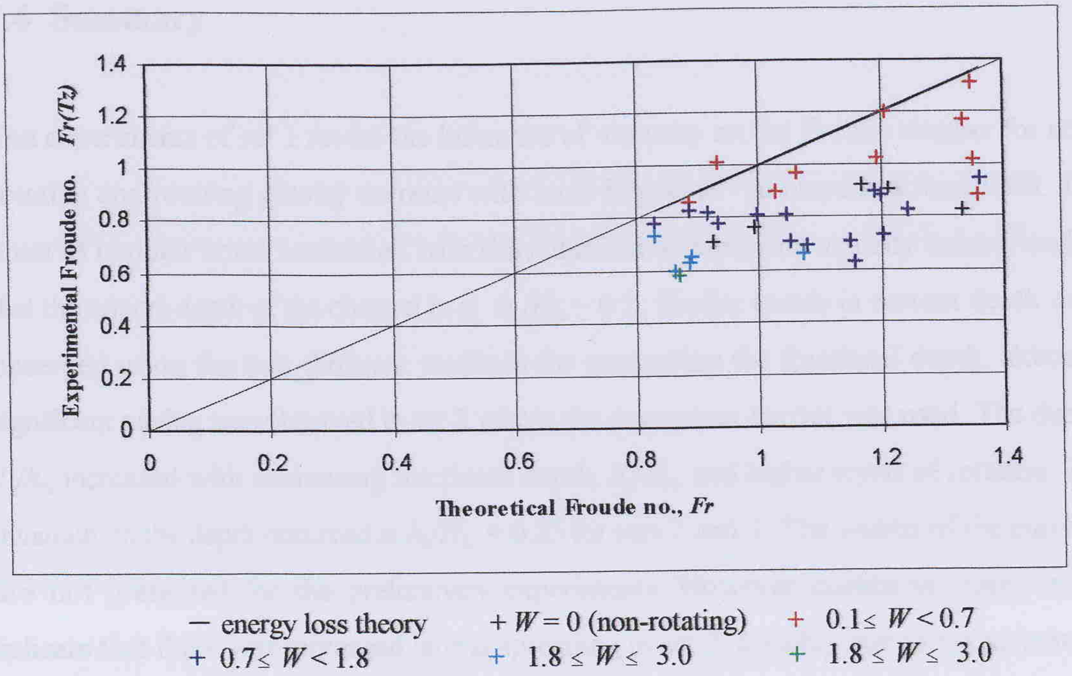

FIGURE 7.11 (c) Froude number, *Fr*. Energy loss theory versus experimental results.

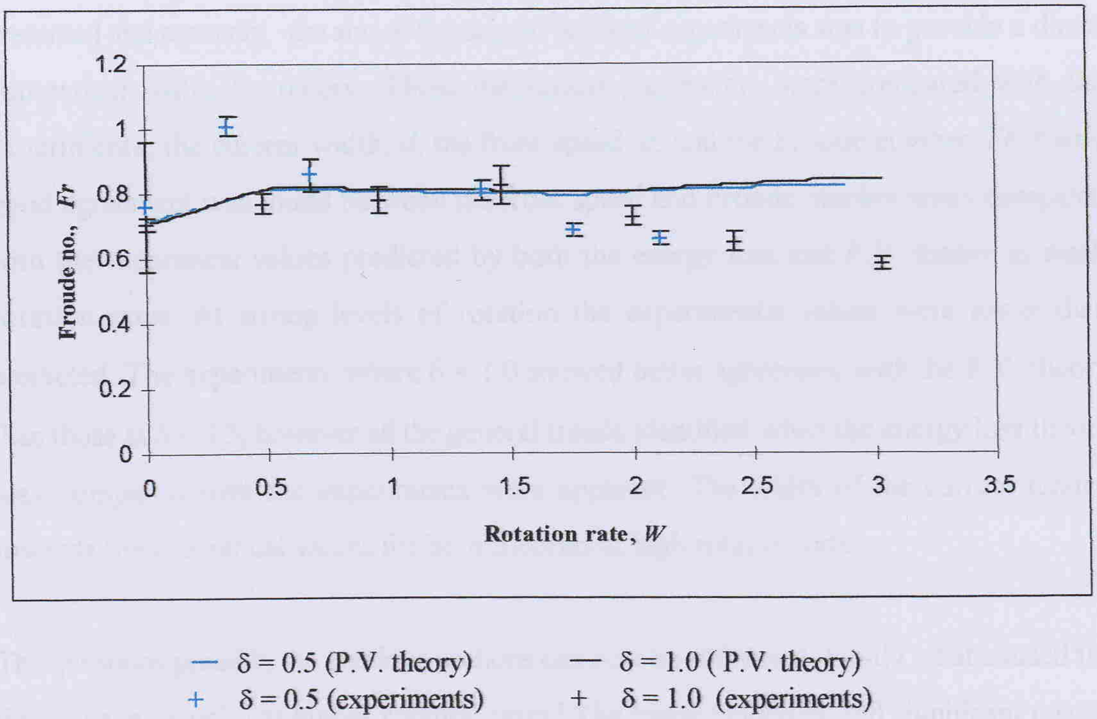

FIGURE 7.11 (d) Froude number, *Fr*. Potential vorticity theory versus experimental results.

7.4 Summary

The experiments of set 1 reveal the influence of viscosity on the Froude number for non-rotating and rotating gravity currents with local Reynolds' numbers less than 1000. The onset of undular bores associated with the minimum in depth and velocity values, implies that the critical depth of the channel is at $h_0/H_0 \sim 0.2$. Similar trends in current depth were observed using the two different methods for controlling the fractional depth, although significant mixing was observed in set 2 where the permanent barrier was used. The depth, T_z/h_0, increased with decreasing fractional depth, h_0/H_0, and higher levels of rotation. The minimum in the depth occurred at $h_0/H_0 = 0.25$ for sets 2 and 3. The widths of the currents are not presented for the preliminary experiments. However qualitative observations indicate that there was increased lateral spreading in set 2, possibly due to the permanent barrier. In the subsequent experiments, sets 3 to 5, the width seemed unaffected when the fractional depth was altered.

The experimental results of sets 3, 4 and 5 were presented alongside the equivalent theoretical values. This was because firstly, a full description of the behaviour of gravity currents had been provided in § 7.1 where the results of the preliminary experiments were presented and secondly, the aim of the second series of experiments was to provide a direct comparison with the theory. Three theoretical parameters were compared with the experiments, the current width, *d*, the front speed, *c*, and the Froude number, *Fr*. Fairly good agreement was found between the front speed and Froude number when compared with the theoretical values predicted by both the energy loss and P.V. theory at weak rotation rates. At strong levels of rotation the experimental values were lower than predicted. The experiments where $\delta = 1.0$ showed better agreement with the P.V. theory than those at $\delta = 0.5$, however all the general trends identified when the energy loss theory was compared with the experiments were apparent. The width of the current tended towards the theoretical values for both theories at high rotation rates.

The questions posed in the previous sections can now be addressed. Firstly what caused the decrease in velocity at higher rotation rates? The lower velocities and significant mixing observed in set 2 compared with sets 3, 4 and 5 indicate that the barrier was partly responsible, however since the same trend of lower velocity at stronger levels of rotation was observed in all the experiments there must be an additional forcing. The possibility of inertial resonance was investigated and rejected. Enhanced vertical mixing as rotation increased was observed in set 3, although to a lesser extent than in set 2. This could reduce the density difference which drives the flow and consequently the velocity. Since the surface area of the gravity current in contact with the ambient fluid has increased, detrainment of fluid is another possible cause. The increasing strength of the geostrophic gyre as rotation increased could trap fluid causing a lower mass flux to the head of the current. This could also account for the changing profile of the current. The lowering of the velocity at strong levels of rotation may be due to any one of these or some combination. It is interesting to note that both Griffiths and Hacker suggested the possibility of lower velocities at high rotation rates. In chapter 8 where future work is discussed methods of quantifying the mixing are discussed.

CHAPTER 8

Conclusion

8.1 Summary and Discussion

I have presented the results of an extensive theoretical and experimental study. The aim was to cover as large a parameter range as possible building on the work of Benjamin, 1968, (non-rotating theory) and Hacker, 1996, (rotating energy conserving theory). In reviewing Hacker's theory I have reworked his equations and I have presented his data in a manner in which it has not been previously presented i.e., 3-D surface plots of the interface depth profile, the across-stream velocity and the across stream pressure. Two substantial extensions to the previous theories have been achieved. In Chapter 4 the solutions for the energy loss theory with simple flow were presented. The smooth transitions of this theory from both Benjamin's non-rotating theory with dissipation and Hacker's rotating energy conserving solutions, as well as between each of the flow geometries, provide convincing solutions. These enable the velocity, depth and other quantities which characterise a flow to be predicted for rotating currents in channels for any given parameter. The main results of the energy loss rotating theory have a number of trends in common with Benjamin's non-rotating energy loss theory.

These include that the -

- maximum energy loss coincides with the maximum values for the front speed.
- maximum volume flux of the current occurs at the energy conserving depth.
- two alternative depths are possible for a each value of c within a certain range.
- Froude number tends to $2^{\frac{1}{2}}$ for shallow currents.

The two alternative depths for a certain value of front speeds were attributed by Benjamin to the adjustment from supercritical flow at the dissipationless depth to subcritical flow as energy is lost through a mechanism such as a hydraulic jump. Additional to these trends was that as rotation increased the maximum energy loss decreased.

The second theory I have presented considered the inclusion of a pre-set potential vorticity in the source region. This required an extra parameter δ i.e. the ratio between the reference depth of the current and the ambient fluid upstream in the source region. The assumption of zero velocity in the current was no longer made. This unfortunately further complicated the equations, but the governing equations were derived for each of the three cases. These were solved using a FORTRAN programme (Lane-Serff). The initial results reveal a fourth possible flow where the free surface current width, d, equalled zero and the current outcropped on the bottom boundary to a width of $y = b$. The velocity profile across the current was visualised using contour graphs for $\delta = 0.5$, 1.0 and 1.5. These showed the development of a complex circulation for $\delta = 0.5$, with cyclonic circulation at the r.h.wall and anticyclonic circulation close to the outer edge of the current. The boundary between the two occurred at $\eta(y) = 0.5$. For $\delta = 1.0$ and 1.5 the flow within the current was anticyclonic. The velocity in the ambient fluid showed similar behaviour to the energy conserving theory of Hacker with u_D tending to $2^{\frac{1}{2}}$ at the r.h. wall and 1 in the free stream as the rotation rate increased. An interesting result of the inclusion of a P.V. boundary condition in the source region was that the front speed remained the same as that for the energy conserving theory of Hacker. This was explained using a simple continuity argument based on the fact that the interface profile and the velocity of the ambient fluid were approximately that found in the energy conserving theory of Hacker. The fact that the interface profile remained almost unaltered irrespective of the value of δ implies that the upstream potential vorticity should have an insignificant effect upon the principle variables and indeed this was the case. The value of the P.V. theory lies in the fact that it gives an insight into the circulation within the current. However one wonders at the worth of pursuing this theory further to include dissipation, since it would be a major undertaking and these initial results suggest that the energy loss theory adequately models rotating gravity currents.

In the laboratory investigation the preliminary experiments considered the diversity of rotating gravity currents including viscous to inviscid flows and shallow to full depth locks. Different methods for controlling the fractional depth of the current were also investigated. The main experiments were primarily designed to support the theoretical study. Comparisons with the experiments have shown that their is reasonable agreement between the two theories and the laboratory results for the front speed and Froude number at weak rotation rates. At high levels of rotation the experimental speeds were found to be lower than expected. The measured current width, *d*, was found to tend towards the theoretical values at strong rotation rates, for weak rotation *d* was found to be less than expected. In comparing the theoretical and experimental studies one should remember their limitations. The theory assumes: the fluid is inviscid; the no-slip condition is not used at the boundary; energy loss is uniform across the channel; and potential vorticity is conserved. The theory does not include factors such as: the enhanced vertical mixing and the increased detrainment due to the larger surface area of the current in contact with the ambient fluid as W is increased. Also the role of the geostrophic eddy in effectively trapping fluid and the low Reynolds' number at the head of the current. All of these are associated with strong levels of rotation and would account for the divergence from the theory.

8.2 Future Work

There are a number of areas which require further attention as highlighted above in the discussion of the limitations of the theory. Firstly, an extension to the energy loss theory (Theory 1) could address the assumption of uniform energy loss across the channel. This is a unique case where energy is lost but potential vorticity is conserved. If the assumption of uniform energy loss was removed then there would be an associated loss of potential vorticity. Indeed in the environment it is unlikely that potential vorticity would be conserved. Hacker suggests that non-uniform energy and potential vorticity loss could be incorporated into the theory by prescribing $\Delta E(y)$ or $\Delta q(y)$, since there is insufficient information in equations (4.1.7a) and (4.1.7b) to describe the dissipation profiles.

Secondly, the potential vorticity theory could be extended to include energy loss in a similar manner to that described in chapter 4. A head loss term could be introduced to the Bernoulli equation together with the assumption of uniform energy loss across the stream. The continuity equation again could be used to side step the Bernoulli equations and therefore avoid the assumption of conservation of energy. The energy loss theory with prescribed P.V. would be dependent upon the three constants W, η_0 and δ, and would result in a unique solution for each of the principle variables. This would obviously further complicate the equations, and the value of this undertaking has already been questioned.

Finally, the importance of quantifying the mixing and detrainment that occurs at the head of the current through Kelvin-Helmholtz billows and lobe and cleft instabilities has already been stated. The theory assumes that the fluid is inviscid and it would be interesting to repeat the experiments using immiscible fluids for example an air intrusion, as envisaged by Benjamin in the non-rotating experiments. Simpson (1987) developed an ingenious apparatus to examine the mixing at the head of a gravity current by removing friction at the floor. This was achieved by pumping fluid at a steady rate on to a conveyor belt which was moving at the same rate. At the other end of the tank dense fluid was introduced. By adjusting the speed of the flow and the floor, he was able to bring the fluid to rest. This almost completely removed the lobe and cleft instability. The mixing rate due to the Kelvin-Helmholtz billows was simply determined by the rate of input of dense fluid required to maintain the steady front. Obviously this method will present difficulties in a rotating reference frame, but if these could be overcome it could provide valuable information regarding the supply of fluid to the head of the current for strong rotation rates and confirm whether the proposal that the geostrophic eddy traps fluid is correct

Another method which could be utilised is that described by Hacker et al (1996). This uses digital analysis to provide information about the mixing rates. The principle is based on the fact that light is attenuated as it passes through the dyed fluid and therefore areas of greater mixing and hence greater dilution will attenuate light to a lesser degree. Thus Hacker was able to quantify the amount and concentration of mixed fluid produced for a set of non-rotating gravity currents. The attenuation was determined by comparing the value of the light intensity of pixels in an image containing dye, i by one with out dye, i_0. The mean across channel dye concentration was estimated by dividing the integrated dye concentration by the width of the channel which was related to the attenuation ratio by the following expression,

$$C = C_0 f(i / i_0)$$

where f was a non-linear function determined by calibration. Hacker applied this method to three non-rotating gravity currents with different lock aspect ratios. An interesting finding was that although the digital imaging showed quite different dynamics within the currents i.e. areas of mixing and reduced concentration, the front speed seemed unaffected and remained close to the theoretical value predicted by Benjamin of $c = 0.5$.

There are many ways in which this work could be extended. Particularly the experimental study which I feel would benefit from simply being repeated in larger tanks, with different lock geometries. Then some of the questions which have arisen through this study and the respective explanations I have proposed could be examined further.

REFERENCES

Arnone, R.A. & La Violette, P.E. (1986). Satellite definition of the optical and thermal variation of coastal eddies associated with the African Current. *J. Geophys. Res.*, **91**, 2351-2364.

Baines, P.G. (1980). The dynamics of the southerly bluster. *Aus. Meteor. Mag.*, **28**, 175-200.

Benjamin, T.B. (1968). Gravity currents and related phenomena. *J. Fluid Mech.*, 31, 209-248.

Bowers, D.G. & Lennon, G.W. (1987). Observations of stratified flow over a bottom gradient in a coastal sea. *Conti. Shelf Res.*, 7, 1105-1121.

Bracalari, M., Salusti, E., Sparnocchia, S. & Zambianchi, E. (1989). On the role of the Froude number in geostrophic coastal currents around Italy. *Ocean. Acta.*, **12**, 161-166.

Bullock, D.A. (1975). The general circulation of Spencer Gulf, South Australia in the period February to May. *Trans. R. Soc. South Aust.*, **22**, 43-54, 1975.

Chabert d'Hières, G., Didelle, H. & Obaton, D. (1991). A laboratory study of surface boundary currents: application to the Algerian Current. *J. Geophys. Res.*, **96**, 12539-12548.

Chanson, H. & Montes, J.S. (1995). Characteristics of undular hydraulic jumps: experimental apparatus and flow patterns. *J. Hydraulic Eng.*, **121**, 129-143.

Colquhoun, J., Shepard, D., Coulman, C., Smith, R.K., & McInnes, K. (1985). The Southerly Burster of Eastern Australia. *Mon. Wea. Rev.*, **113**, 2090-2170.

Csanady, G.T. (1971). On the equilibrium shape of the thermocline in a shore zone. *J. Phys. Oceanogr.*, **1**, 263-270.

Dalziel, S.B. (1993). Decay of rotating turbulence: some particle tracking experiments. In: F.T.H Nieuwstadt (Editor), Flow Visualization and Image Analysis. Kluwer, Dordrecht.

Dalziel, S.B. (1994). *The Digimage manual.* Cambridge Environmental Research Consultants.

de Silva Samarasinghe, J.R. (1987). Dynamic and mixing processes in a tidal gulf of evaporation-enhanced salinity: Gulf St. Vincent, South Australia, *Ph.D. thesis, Flinders Univ. of S. Aust., Bedford Park.*

Dickson, R.R. & Brown, J. (1994). The production of North Atlantic Deep Water: Sources, rates and pathways. *J. Geophys. Res.*, **99**, 12375-12396.

Dickson, R.R., Gmitrowicz, E.M. & Watson, A.J. (1990). Deep water renewal in the northern North Atlantic, *Nature*, **344**, 848-850.

Geyer, R. (1983). Frazer River Salt Wedge Investigation. *Prelim. Report, University of Washington, Seattle.*

Gill, A.E. (1976). Adjustment under gravity in a rotating channel. *J. Fluid Mech.*, **77**, 603-621.

Gill, A.E. (1977). The hydraulics of rotating-channel flow. *J. Fluid Mech.*, **80**, **4**, 641-671.

Griffiths, R.W. (1983). Gravity currents moving along a lateral boundary in a rotating fluid. *J. Fluid Mech.*, **134**, 357-399.

Griffiths, R.W. (1986). Gravity currents in rotating systems. *Ann. Rev. Fluid Mech.* **18**, 59 - 89.

Griffiths, R.W. & Hopfinger, E.J. (1983). Gravity currents moving along a lateral boundary in a rotating fluid. *J. Fluid Mech.* **134**, 357-399.

Griffiths, R.W. & Linden, P.F. (1981a). The stability of buoyancy driven coastal currents. *Dyn. Atmos. Oceans.* **5**, 281-306.

Griffiths, R.W. & Linden, P.F. (1981b). The stability of vortices in a rotating, stratified fluid. *J. Fluid Mech.* **105**, 283-316.

Griffiths, R.W. & Linden, P.F. (1982). Laboratory experiments on fronts. Part 1: density-driven boundary currents. *Geophys. Astrophys. Fluid Dyn.* **19**, 159-87.

Griffiths, R.W. & Pearce, A.F. (1985). Satellite images of an unstable warm eddy derived from the Leeuwin Current. *Deep Sea Research*, **32**, 1371-1380.

Hacker, J. (1996). *Gravity currents in rotating channels.* PhD Thesis. DAMTP, University of Cambridge.

Hsueh, Y. & Cushman-Roisin, B. (1983). On the formation of surface to bottom fronts over steep topography. *J. Geophys. Res.* **88**, 743-750.

Kinder, T.H. & Parrilla, G. (1987). Yes, some of the Mediterranean Outflow does come from great depth. *J. Geophys. Res.*, **92**, 2901-2906.

Kubokawa, A. & Hanawa, K. (1984b). A theory of semigeostrophic gravity waves and its application to the intrusion of a density current along a coast. Part 2. Intrusion of a density current along a coast in a rotating fluid. *J. Oceanogr. Soc. Jpn.*, **40**, 260-270.

Lamb, H. (1932). *Hydrodynamics*, 6th ed. Cambridge University Press. (Dover edition, 1945)

Lennon, G.W., Bowers, D.G., Nunes, R.A., Scott, B.D., Ali, M., Boyle, J., Cai Wenju, Herzfeld, M., Johansson, G., Nield, S., Petrusevics, P., Stephenson, P., Suskin, A.A. & Wijffels, S.E.A. (1987). Gravity currents and the release of salt from an inverse estuary. *Nature*, **327**, 695-697.

Lilly, D.K. (1981). Doppler radar observations of upslope snowstorms. Preprints, 20th Conf. on Radar Meteorol., Boston. *Amer. Meteor. Soc.*, 638-645.

Mass, C.F. & Albright, M.D. (1987). Coastal Southerlies and Alongshore Surges of the West Coast of North America: evidence of mesoscale topographically trapped response to synoptic forcing. *Mon. Wea. Rev.*, **115**, 1707-1738.

McClimans, T.A., Vinger, A. & Mork, M. (1985). The role of Froude number in models of baroclinic coastal currents. *Ocean Modell*, **62**, 14-17.

Meincke, J. & Kvinge, T. (1978). On atmospheric forcing of overflow events, *ICES C.M. 1978/C:9*, Int. Counc. for the Explor. of the Sea, Copenhagen.

Millot, C., Taupier-Letage, I. & Benzohra, M. (1990). The Algerian eddies. *Earth Sci. Rev.*, **27**, 203-219.

Moncrieff, M.W. & So, D.W.K. (1989). A hydrodynamical theory of conservative bounded density currents. *J. Fluid Mech.*, **198**, 177-197.

Mysak, L.A. & Scott, F. (1977). Evidence of baroclinic instability off the Norwegian Current. *J. Geophys. Res.*, **82**, 2087-2095.

Nof, D. (1987). Penetrating outflows and the dam breaking problem. *J. Marine Res.*, **45**, 557-577.

Nunes, R.A. & Lennon, G.W. (1987). Episodic stratification and gravity currents in a marine environment of modulated turbulence. *J. Geophys. Res.*, **92**, 5465- 5480.

O'Brian, M.P. & Cherno, J. (1934). Model law for motion of salt water through fresh. *Trans. Am. Soc. Civil Eng.*, **99**, 576-594.

Orlanski, I. (1983). Orographically induced vortex centres. Proc. of 1st Sino-American workshop in mountain meteorology. Boston: Science press, Beijing and *Am. Met. Soc.*, 311-340.

Ou, H.W. (1983). Some two-layer models of shelf-slope front: geostrophic adjustment and its maintenance. *J. Phys. Oceanogr.*, **13**, 1798-1808.

Peterson, W.H. & Rooth, C.G.H. (1976). Formation and exchange of deep water in the Greenland and Norwegian Seas. *Deep Sea Res.*, **23**, 273-283.

Physick, W.L. & Smith, R.K. (1985). Observations and dynamics of sea-breezes in northern Australia. *Aust. Met. Mag.*, **33**, 51-63.

Rossby, C.G. (1938). On the mutual adjustment of pressure and velocity distributions in certain current systems. II. *J. Fluid Mech.*, **135**, 95-110.

Price, J.F., O'Neil Baringer, M., Lueck, R.G., Johnson, G.C., Ambar, I., Parrilla, G., Cantos, A., Kennelly, M.A. & Sanford, T.B. (1993). Mediterranean Outflow mixing and dynamics. *Science*, **259**, 1277-1282.

Rottman, J.W. & Simpson, J.E. (1983). Gravity currents produced by instantaneous releases of a heavy fluid in a rectangular channel. *J. Fluid Mech.*, **135**, 95-110.

Rutllant, J.C. (1981). Forced subsidence down the western Andean slope and its relationship with an air pollution episode of Santiago, Chile. *Tralka*, **2**, 57-76.

Seitter, K.L. & Muench, H.S. (1985). Observation of a cold front with rope cloud. *Mon. Wea. Rev.*, **113**, 840-848.

Shapiro, M.A., Hampel, T., Rotzoll, D. & Mosher, F. (1985). The frontal hydraulic head: A micro-α scale (~ 1 km) triggering mechanism for mesoconvective weather systems. *Mon. Wea. Rev.*, **113**, 1166-1183.

Simpson, J.E. (1972). Effects of the lower boundary on the head of a gravity current. *J. Fluid Mech.*, **53**, 759-768.

Simpson, J.E. (1982). Gravity currents in the laboratory, atmosphere and ocean. *Ann. Rev. Fluid Mech*, **14**, 213-234.

Simpson, J.E. (1987). Gravity currents in the environment and the laboratory. *Halsted*, New York.

Simpson, J.H. & Nunes, R.A. (1981). The tidal intrusion front: an estuarine convergence zone. *Estuarine, Coastal and Shelf Science*, **13**, 257-266.

Stern, M.E. (1980). Geostrophic fronts, bores, breaking and blocking waves. *J. Fluid Mech.*, **99**, 687-704.

Stern, M.E., Whitehead, J.A. & Hua, B.L. (1982). The intrusion of a density current along the coast of a rotating fluid. *J. Fluid Mech.* **123**, 237-265.

Stommel, H., Bryden, H. & Mangelsdorf, P. (1973). Does some of the Mediterranean outflow come from great depth? *Pure Appl. Geophys.*, **105**, 879-889.

Stommel, H. & Veronis, G. (1980). Barotrophic response to cooling. *J. Geophys. Res.*, **85**, 6661-6666.

Swift, J.H., Aagaard, K. & Malmberg, S.A. (1980). The contribution of the Denmark Strait Overflow to the deep North Atlantic. *Deep Sea Res.*, **27**, 29-42.

Tomczak, M. & Godfrey, J.S. (1994). *Regional Oceanography: an Introduction.* Pergamon.

Van Heijst, G.J.F. (1985). Geostrophic adjustment model of a tidal mixing front. *J. Phys. Oc.* **15**, 1182-1190.

Wadhams, P., Gill, A.E. & Linden, P.F. (1979). Transects by submarine of the East Greenland Polar Front. *Deep Sea Res.* **26A**, 1311-1327.

Whitehead, J.A. (1989). Giant ocean cataracts. *Sc. Am.* Feb.50-57.

Whitehead, J.A., Leetmaa, A., Knox, R.A. (1974). Rotating hydraulics of strait and sill flows. *Geophys. Fluid Dyn.* **6**, 101-25.

Worthington, L.V. (1969). An attempt to measure the volume transport of Norwegian Sea Overflow water through the Denmark Strait. *Deep Sea Res.*, **16**, 421-432.

Yamagata, T. (1980). A theory for the propagation of an oceanic warm front with application to Sagami Bay. *Tellus.* **32**, 73-76.

SOUTHAMPTON UNIVERSITY LIBRARY

USER'S DECLARATION

AUTHOR: Martin, J. R.

TITLE: Rotating gravity current and channel flows

DATE: 2000

I undertake not to reproduce this thesis, or any substantial portion of it, or to quote extensively from it without first obtaining the permission, in writing, of the Librarian of the University of Southampton.

To be signed by each user of this thesis

DATE	SIGNATURE	ADDRESS